

DAVI ÉBER SANCHES DE MENEZES

**Thermodynamic study on gas hydrates: experimental
determination of equilibrium data by high-pressure microcalorimetry and
modeling up to 100 MPa.**

São Paulo

2020

DAVI ÉBER SANCHES DE MENEZES

**Thermodynamic study on gas hydrates: experimental
determination of equilibrium data by high-pressure microcalorimetry and
modeling up to 100 MPa**

Revised Version

Thesis presented to the Polytechnic School
of the University of São Paulo, to obtain the
degree of Doctor of Science.

São Paulo

2020

DAVI ÉBER SANCHES DE MENEZES

**Thermodynamic study on gas hydrates: experimental
determination of equilibrium data by high-pressure microcalorimetry and
modeling up to 100 MPa**

Revised Version

Thesis presented to the Polytechnic School
of the University of São Paulo, to obtain the
degree of Doctor of Science.

Concentration area:

Chemical Engineering

Advisor:

Dra. María Dolores Robustillo Fuentes

São Paulo

2020

Autorizo a reprodução e divulgação total ou parcial deste trabalho, por qualquer meio convencional ou eletrônico, para fins de estudo e pesquisa, desde que citada a fonte.

Este exemplar foi revisado e corrigido em relação à versão original, sob responsabilidade única do autor e com a anuência de seu orientador.

São Paulo, _____ de _____ de _____

Assinatura do autor: _____

Assinatura do orientador: _____

Catálogo-na-publicação

Menezes, Davi Eber Sanches

Thermodynamic study on gas hydrates: experimental determination of equilibrium data by high-pressure microcalorimetry and modeling up to 100 MPa / D. E. S. Menezes -- versão corr. -- São Paulo, 2020.
269 p.

Tese (Doutorado) - Escola Politécnica da Universidade de São Paulo.
Departamento de Engenharia Química.

1.Equilíbrio Polifásico 2.Microcalorimetria de Alta Pressão 3.Hidratos de Gás 4.Entalpia de Dissociação 5.Inibidores de Hidratos I.Universidade de São Paulo. Escola Politécnica. Departamento de Engenharia Química II.t.

To my beloved father. (*in memoriam*)

ACKNOWLEDGEMENTS

First I must thank God, the one who has given me life, health and strength during hard times. To his Son, by whom I began this work and could conclude it.

I also owe thanks to people who supported me in many ways throughout my work:

Dr. María D. Robustillo Fuentes for being my advisor and doing so in an excellent manner. I thank Dr. Pedro de Alcântara Pessôa Filho for all the time he spent helping me with thermodynamics and other issues. These helpful and understanding mentors motivated me and facilitated the development of this research.

Dr. Amadeu K. Sum (Colorado School of Mines, USA) and Dr. Arnaud Desmedt (Université de Bordeaux, France) for the great opportunity to extend my work in their laboratories. The knowledge I gained through them has unquestionably improved my technical and personal skills. To Aline Melchuna, Xianwei Zhang, Yue Hu, Jeong-Hoon Sa, Claire Pétuya-Poublan and Morgane Lemaire. All of these colleagues from abroad were of great disposition and vital to my research.

The faculty and grad students in the Chemical Engineering Department from Polytechnic School at the University of São Paulo for the time we spent together.

Thanks to all my friends. They brightened my academic life even more and provided me with pleasant times during breaks and weekends.

To my family for all the love and support they gave during these times, specially my father, who passed away in the first year of my doctorate.

Finally, I thank to FAPESP (Fundação de amparo à pesquisa de São Paulo) for financial support I received in Brazil and abroad (processes: 2017/01351-2, 2015/23148-9, 2014/02140-7 and 2014/25740-0). All the requests approved by the agency were essential to the completion of this work.

ABSTRACT

MENEZES, D.E.S. **Thermodynamic study on gas hydrates: experimental determination of equilibrium data by high-pressure microcalorimetry and modeling up to 100 MPa.** 2020. 265 f. DSc. Thesis – Chemical Engineering, Polytechnic School, University of São Paulo, São Paulo, 2020.

Clathrate hydrates are crystalline structures formed by water molecules linked through hydrogen bonds. Regarding gas hydrates, the crystalline lattice hosts low molecular weight gases inside the cavities known as “cages”. These compounds are formed at low temperature and high pressure conditions, such as those characteristic of deep water regions. Many efforts have been made in research to avoid the formation of these structures during oil and gas exploitation and transport, as these compounds may clog the flowlines. Moreover, current studies are aimed at exploiting natural reservoirs of gas hydrates as an alternative energy resource or using them for capture and sequestration of carbon dioxide, among others. However, the technology and techniques required to extract them commercially are not yet available. For that purpose, a good knowledge about their thermodynamic equilibrium is needed to predict the conditions that may favor, delay or inhibit the formation of these structures. Nevertheless, few experimental data of gas hydrate dissociation over 20 MPa are found in the literature to assess the reliability of thermodynamic models and improve their accuracy due to the instrumental limitations at extreme conditions. In this context, this work presents new data up to 100 MPa obtained by High-Pressure micro Differential Scanning Calorimetry (HP- μ DSC), a relatively new technique of analysis whose application on gas hydrates studies is currently growing. Temperatures of dissociation are shown for single and double hydrates and compared to computational predictions from commercial software packages (CSMGem and Multiflash). Enthalpies of dissociation were estimated for CH₄, C₂H₆ and CO₂ single hydrates through the integration of dissociation curves from thermograms and compared to the results obtained by applying the Clapeyron equation. No data has been found so far in the literature for enthalpies of dissociation of ethane and carbon dioxide hydrates at the pressure and temperature ranges addressed in this work. Double hydrates composed of CH₄-C₂H₆, CH₄-C₃H₈ and CH₄-CO₂ were also studied, and the dissociation temperature profiles are discussed considering the occupancy degree of cages,

according to the gas phase composition, and the existence of empty cavities. In systems composed of CH₄-C₃H₈-H₂O, a secondary structure, likely metastable methane hydrate, was unexpectedly formed along with the methane-propane hydrate, emphasizing the importance of the experimental study. Moreover, experiments based on the isochoric method using a PVT cell and Raman spectroscopy analyses were performed to complement the results found by microcalorimetry. Finally, methanol and imidazolium-based ionic liquids were evaluated as methane hydrate inhibitors. Although methanol has shown better efficiency in mass fraction terms, the ionic liquids usually present a dual inhibition effect when used at appropriate concentrations, with respect to the thermodynamic and kinetic behavior of gas hydrates.

Keywords: High-pressure microcalorimetry (HP- μ DSC). Gas hydrates. Equilibrium data. Enthalpy of dissociation. Hydrate inhibitors.

RESUMO

MENEZES, D.E.S. **Estudo termodinâmico em hidratos de gás: determinação experimental de dados de equilíbrio por microcalorimetria de alta pressão e modelagem até 100 MPa.** 2020. 265 f. Tese de Doutorado em Ciências (Engenharia Química) – Escola Politécnica, Universidade de São Paulo, São Paulo, 2020.

Hidratos de clatratos são estruturas cristalinas formadas por moléculas de água ligadas através de ligações de hidrogênio. No caso dos hidratos de gás, a rede cristalina hospeda moléculas de gás de baixo peso molecular dentro de cavidades conhecidas como "gaiolas". Esses compostos são formados em condições de baixas temperatura e altas pressões, como em regiões de águas profundas. Muitas pesquisas têm sido realizadas a fim de evitar a formação dessas estruturas durante a exploração e transporte de petróleo e gás, visto que esses compostos podem obstruir os oleodutos. Além disso, estudos mais recentes têm como objetivo explorar reservatórios naturais de hidratos de gás como um recurso alternativo de energia ou utilizá-los para captura e armazenamento de dióxido de carbono, entre outros. No entanto, a tecnologia e as técnicas necessárias para extraí-los comercialmente ainda não estão disponíveis. Considerando tais aplicações, é necessário um profundo conhecimento sobre o equilíbrio termodinâmico dos hidratos de gás, de modo a prever as condições que favorecem, retardam ou inibem a formação dessas estruturas. Contudo, poucos dados experimentais de dissociação de hidratos de gás são encontrados na literatura acima de 20 MPa, devido a limitações de equipamentos em condições extremas. Nesse contexto, este trabalho apresenta dados inéditos de dissociação até 100 MPa através de uma configuração experimental baseada na microcalorimetria de alta pressão (HP- μ DSC), uma técnica relativamente recente que vem sendo cada vez mais aplicada em estudos de hidratos de gás. Temperaturas de dissociação são apresentadas para hidratos simples e compostos, e comparadas com previsões computacionais a partir de softwares comerciais (CSMGem e Multiflash). Entalpias de dissociação foram estimadas para hidratos simples de CH₄, C₂H₆ e CO₂ por meio de integração das curvas de dissociação nos termogramas gerados, e comparadas com cálculos aplicando a equação de Clapeyron. Nenhum trabalho foi encontrado na literatura até então que reportasse entalpias de dissociação de hidratos de etano e dióxido de carbono nas condições de pressão e temperatura abordadas

nesse trabalho. Hidratos duplos de $\text{CH}_4\text{-C}_2\text{H}_6$, $\text{CH}_4\text{-C}_3\text{H}_8$ e $\text{CH}_4\text{-CO}_2$ também foram estudados, e os perfis de temperatura de dissociação são discutidos considerando o grau de ocupação das gaiolas, de acordo com a composição da fase gasosa, e a existência de cavidades vazias. No sistema composto por $\text{CH}_4\text{-C}_3\text{H}_8\text{-H}_2\text{O}$, uma estrutura secundária de hidrato, provavelmente metaestável e constituída por metano, foi formada simultaneamente com o hidrato duplo de metano-propano, embora não prevista por simulações, o que ressalta a importância do estudo experimental. Além disso, experimentos usando o método isocórico em célula PVT e análises por espectroscopia Raman foram realizadas e complementam os resultados encontrados por meio da microcalorimetria. Finalmente, metanol e dois líquidos iônicos à base de imidazólio foram avaliados como inibidores de hidrato de metano. Embora o metanol tenha mostrado melhor eficiência em frações mássicas, os líquidos iônicos apresentam um efeito duplo de inibição quando em concentrações adequadas, com relação a abordagem termodinâmica e cinética dos hidratos de gás.

Palavras-chave: Microcalorimetria de alta pressão (HP- μ DSC). Hidratos de gás. Dados de equilíbrio. Entalpia de dissociação. Inibidores de Hidratos.

LIST OF FIGURES

1.1	Illustration of a phase diagram for a gas hydrate-forming system.....	29
1.2	Phase diagram for the methane-water system obtained using the software CSMGem.....	30
2.1	Main transitions observed in thermograms obtained by HP- μ DSC.....	51
2.2	Calorimetric transducer of μ DSC7 Evo apparatus (SETARAM).....	52
2.3	High-pressure cells used in microcalorimetric experiments.....	53
2.4	Experimental setup employed for gas hydrates studies based on high-pressure microcalorimetry.....	54
2.5	Calibration of pressure for isochoric experiments in the HP- μ DSC.....	55
2.6	Methodology applied to microcalorimetric analyses: A) Temperature profile throughout the analysis; B) Thermogram indicating usual transitions occurring during the analysis (...)	57
2.7	Determination of onset, peak and endset values for the CH ₄ -C ₃ H ₈ hydrate dissociation curve (sII, 39.3 MPa) using the data processing software Calisto (SETARAM).....	57
2.8	Establishment of baseline for calculating enthalpy of hydrate dissociation	60
2.9	Illustration of the multicycle method for higher conversion of ice to gas hydrate.....	68
2.10	Ultra-High-Pressure System used to analyze hydrates through the PVT-isochoric method.....	71
2.11	Commercial gas cylinder joined to the gas booster.....	72
2.12	Swagelok cylinder used for homemade gas mixtures (methane + propane) (A) and high-performance balance (B).....	72
2.13	Thermodynamic parameters calculated for gas transfer from the mixing cylinder to the PVT cell.....	73
2.14	Experimental stages followed in a methane hydrate analysis through the isochoric method in the PVT cell.....	75
2.15	Temperature and pressure profiles obtained for a methane-water system through the PVT - isochoric method	75
2.16	Light scatterings involved in Raman spectroscopy.....	76
2.17	Trajectory of the radiation along the Raman spectrometer (Labram UV)	77
2.18	Pumps employed for the preparation of gas mixtures and pressurization of the hydrate-forming systems A) Isco (260 cm ³); B) Top Industrie (100 cm ³).....	78
2.19	Schematic illustration of methane-propane mixtures preparation.....	79
2.20	High-Pressure cell used to prepare ex-situ gas hydrate samples.....	80

2.21	Optical cell (Linkam) used in the Raman spectroscopy of gas hydrates prepared ex-situ.....	80
2.22	Setup for Raman spectroscopy measurements of samples prepared ex-situ.....	81
2.23	Capillary cell (Linkam CAP500) used for in situ analysis of gas hydrates..	81
2.24	Illustration of the sample settled on the capillary cell (Linkam CAP500)..	82
2.25	Cylindrical cell (Linkam THMS600) used for in situ analyses of gas hydrates.....	83
2.26	Scheme of Raman spectroscopy analyses by placing the cell (THMS600) vertically.....	83
3.1	Vapor-liquid equilibrium lines (Aspen) for single gases and their respective critical points.....	89
3.2	Schematic illustration of possible phases during injection, pressurization and analysis performed by HP- μ DSC.....	90
3.3	Thermodynamic envelopes for CH ₄ -C ₂ H ₆ gaseous mixtures (...)	91
3.4	Thermodynamic envelopes for CH ₄ -C ₃ H ₈ gaseous mixtures (...)	91
3.5	Thermodynamic envelopes for CH ₄ -CO ₂ gaseous mixtures (...)	92
3.6	Influence of water content on dissociation temperature of of single hydrates composed of CH ₄ (A), C ₂ H ₆ (B), C ₃ H ₈ (C) and CO ₂ (D).....	93
3.7	Influence of water content on dissociation temperature of double hydrates (10 mol% CH ₄): CH ₄ -C ₂ H ₆ (A), CH ₄ -C ₃ H ₈ (B) and CH ₄ -CO ₂ (C).....	94
3.8	Influence of water content on dissociation temperature of double hydrates (90 mol% CH ₄): CH ₄ -C ₂ H ₆ (A), CH ₄ -C ₃ H ₈ (B) and CH ₄ -CO ₂ (C).....	95
3.9	(A) Methane densities by Peng-Robinson equation and from NIST; (B) Relative deviations of methane densities.....	96
3.10	(A) Methane-propane densities by Peng-Robinson equation and reported by Sage et al. (1934); (B) Relative deviations of methane-propane densities.....	97
3.11	Resultant heat flow on the calorimetric thermograms.....	98
3.13	Teflon transitions that occur in the sample and reference cells during heating in HP- μ DSC analyses	99
4.1	Heating thermograms of the CH ₄ -H ₂ O system at 1 K·min ⁻¹ and at different pressures (A). Ice melting and hydrate dissociation are expanded in B and C figures, respectively	106
4.2	Dissociation data of CH ₄ hydrates obtained by HP- μ DSC at 1 K·min ⁻¹ (...)	107
4.3	Overlapping of ice melting and CH ₄ hydrate dissociation curves at low pressures.....	111

4.4	Thermograms of cooling (A) and heating (B) indicating the effect of water sample size on the ice / CH ₄ hydrate formation and dissociation, respectively.....	112
4.5	Effect of the heating rate on the onset data corresponding to CH ₄ hydrate dissociation curves (A) and their respective absolute deviations (B).....	115
4.6	Effect of the heating rate on the peak data corresponding to CH ₄ hydrate dissociation curves (A) and their respective absolute deviations (B).....	115
4.7	Effect of the heating rate on the endset data corresponding to CH ₄ hydrate dissociation curves (A) and their respective absolute deviations (B).....	115
4.8	Absolute deviations of onset temperatures with respect to predictions for CH ₄ hydrates (...)	117
4.9	Thermograms of CH ₄ hydrates dissociation by the multicycles method..	118
4.10	Effect of H ₂ O sample size on the dissociation of CH ₄ hydrates by multicycles at 20 MPa.....	119
4.11	Effect of H ₂ O sample size on the conversion of ice to CH ₄ hydrate throughout 22 cycles at 20 MPa.....	119
4.12	Effect of pressure on the ice conversion to CH ₄ hydrate: A) 56.6 mg of water and B) 64.6 mg of water.....	120
4.13	Hydration number (n) for CH ₄ hydrates calculated through the iterative method (standard and multicycles methods) and by using CSMGem predictions.....	122
4.14	Enthalpies of CH ₄ hydrates dissociation determined by the Clapeyron equation based on experimental data: A) standard method; B) multicycles method.....	123
4.15	Enthalpies of CH ₄ hydrates dissociation determined by the integration of curves from calorimetric thermograms: A) standard method; B) multicycles method.....	123
4.16	Absolute deviations between enthalpies of CH ₄ hydrate dissociation by the Clapeyron equation and through the integration of the hydrate dissociation curve: A) standard method; B) multicycles method.....	124
4.17	Thermograms of the C ₂ H ₆ -H ₂ O system at 1 K·min ⁻¹ (A) and 0.2 K·min ⁻¹ (B). The pressure applied in this analysis was 3 MPa.....	126
4.18	Heating thermograms of the C ₂ H ₆ -H ₂ O system at 1 K·min ⁻¹ and at different pressures.....	126
4.19	Dissociation data of C ₂ H ₆ hydrates obtained by HP-μDSC at 1 K·min ⁻¹ .	127
4.20	Absolute deviations of onset temperatures with respect to predictions for C ₂ H ₆ hydrates (...)	128
4.21	Thermograms of C ₂ H ₆ hydrates dissociation by the multicycles method.	129
4.22	Ice conversion to C ₂ H ₆ hydrate throughout multicycles. The analyses were influenced by both effects of pressure and H ₂ O sample size.....	130

4.23	Hydration number (n) for C_2H_6 hydrates calculated through the iterative method (standard and multicycles methods) and by applying CSMGem predictions.....	132
4.24	Enthalpies of C_2H_6 hydrates dissociation determined by the Clapeyron equation based on experimental data: A) standard method; B) multicycles method.....	132
4.25	Enthalpies of C_2H_6 hydrates dissociation determined by the integration of curves from calorimetric thermograms (multicycles method): A) n from CSMGem predictions; B) n from the iterative method.....	133
4.26	Absolute deviations between enthalpies of C_2H_6 hydrate dissociation calculated by the Clapeyron equation and through the integration of the hydrate dissociation curve (multicycles method).....	133
4.27	Dissociation data of CO_2 hydrates obtained by HP- μ DSC (...)	135
4.28	Heating thermograms of the CO_2 - H_2O system at $1\text{ K}\cdot\text{min}^{-1}$ and at different pressures.....	136
4.29	Absolute deviations of dissociation temperatures with respect to predictions for CO_2 hydrates.....	137
4.30	Thermograms of CO_2 hydrate dissociation by the multicycles method....	138
4.31	Effect of pressure on the ice conversion to CO_2 hydrate: A) 48.9 mg of water and B) 53.4 mg of water.....	139
4.32	Hydration number (n) for CO_2 hydrates calculated through the iterative method: A) standard method; B) multicycles method (...)	140
4.33	Enthalpies of CO_2 hydrates dissociation by the Clapeyron equation based on experimental data: A) standard method; B) multicycles method (...)	141
4.34	Enthalpies of CO_2 hydrates dissociation determined by the integration of curves from calorimetric thermograms obtained by the multicycles method.....	142
4.35	Absolute deviations of CO_2 dissociation enthalpies calculated by the Clapeyron equation and integration of curves from thermograms.....	142
5.1	Cross-sections of ternary phase diagrams at constant water fractions. The temperature profiles are similar, following either trajectory.....	152
5.2	Dissociation data of CH_4 - C_2H_6 hydrates obtained by HP- μ DSC at different methane concentrations (...)	155
5.3	Overlapping transitions in thermograms, evidencing the heterogeneity of CH_4 - C_2H_6 hydrate structures.....	156
5.4	Ternary diagrams of dissociation temperatures of CH_4 - C_2H_6 hydrates...	158
5.5	Dissociation temperature profiles of CH_4 - C_2H_6 hydrates according to the gas phase composition (...)	159
5.6	Evolution of the cages occupancy for sl hosting CH_4 (blue) and C_2H_6 molecules (yellow) as methane fraction increases.....	160

5.7	Evolution of the cages occupancy for sII hosting CH ₄ (blue) and C ₂ H ₆ (yellow) molecules as methane fraction increases.....	160
5.8	Thermograms of CH ₄ -C ₃ H ₈ hydrates (20 MPa) at different gas phase compositions.....	162
5.9	Thermograms of CH ₄ -C ₃ H ₈ hydrates (87.5 mol% CH ₄) at different pressures.....	163
5.10	Dissociation data of CH ₄ -C ₃ H ₈ hydrates obtained by HP- μ DSC at different methane concentrations (...)	165
5.11	Evolution of absolute deviations (AD) of onset temperatures corresponding to sII (CH ₄ -C ₃ H ₈).....	166
5.12	Heat absorbed during ice melting and CH ₄ -C ₃ H ₈ hydrate dissociation according to the pressure.....	167
5.13	Dissociation temperature profiles of CH ₄ -C ₃ H ₈ hydrates according to the gas phase composition (...)	167
5.17	Ternary diagrams of dissociation temperatures of CH ₄ -C ₃ H ₈ hydrates...	168
5.15	Evolution of the cages occupancy for sII hosting CH ₄ (blue) and C ₃ H ₈ molecules (green) as methane fraction increases.....	169
5.16	Dissociation data of CH ₄ -CO ₂ dioxide hydrates obtained by HP- μ DSC at different methane concentrations (...)	172
5.17	Overlapping transitions in HP- μ DSC thermograms, evidencing the heterogeneity of CH ₄ -CO ₂ hydrate structures (3 mg H ₂ O).....	173
5.18	Influence of H ₂ O sample size on the hydrate fraction (...)	173
5.19	Dissociation temperature profiles of CH ₄ -CO ₂ hydrates according to the gas phase composition (...)	174
5.20	Ternary diagrams of dissociation temperatures of CH ₄ -CO ₂ hydrates...	175
5.21	Evolution of the cages occupancy for sI hosting CH ₄ (blue) and CO ₂ molecules (purple) as methane fraction increases.....	146
5.22	Dissociation temperature profiles of CH ₄ -C ₂ H ₆ -C ₃ H ₈ hydrates according to the ethane-propane ratio. Each plot presents a constant fraction of methane.....	177
5.23	Ternary diagrams of dissociation temperatures of CH ₄ -C ₂ H ₆ -C ₃ H ₈ hydrates.....	178
5.24	Equilibrium lines for CH ₄ , C ₂ H ₆ and C ₃ H ₈ single hydrates.....	179
5.25	Structural deformation of small cavities from sII due to the absence of methane molecules (...)	180
5.26	Evolution of the cages occupancy for sII hosting CH ₄ (blue), C ₂ H ₆ (yellow) and C ₃ H ₈ molecules (green) as ethane fraction increases.....	180
5.27	Evolution of the cages occupancy for sI hosting CH ₄ (blue) and C ₂ H ₆ molecules (yellow) as ethane fraction increases.....	180

6.1	Dissociation data of CH ₄ hydrates by PVT-isochoric method and microcalorimetry (...)	188
6.2	Effect of cooling degree (CD) on the equilibrium point and the amount of methane hydrate formed.....	190
6.3	Effect of mixing on the single methane hydrate-forming system.....	191
6.4	Dissociation data of CH ₄ -C ₃ H ₈ hydrates (92 mol% CH ₄) by the PVT-isochoric method and microcalorimetry (...)	192
6.5	Equilibrium data obtained by the PVT-isochoric method at different compositions (...)	193
6.6	Phenomenon of recrystallization just before the dissociation of sll in the CH ₄ -C ₃ H ₈ system at 67.7 MPa (92 mol% CH ₄).....	194
6.7	Diagram P vs T for the system CH ₄ -C ₃ H ₈ -H ₂ O (92 mol% CH ₄) by the PVT-isochoric method (...)	195
6.8	Dissociation profiles of CH ₄ -C ₃ H ₈ hydrate-forming systems (92 mol% CH ₄) at different heating rates by the PVT-isochoric method (...)	196
6.9	Thermograms of CH ₄ -C ₃ H ₈ hydrates (92.1 mol% CH ₄ , 67 MPa) at different heating rates.....	197
6.10	Effect of stirring on the dissociation profiles of CH ₄ -C ₃ H ₈ hydrates (92 mol% CH ₄) by the PVT-isochoric method, initially at 70 MPa (...)	198
6.11	Effect of stirring on the dissociation profile of CH ₄ -C ₃ H ₈ hydrate (92 mol% CH ₄) by the PVT-isochoric method, initially at 105 MPa (...)	199
6.12	Effect of multiple cycles heated up to ice melting, on CH ₄ -C ₃ H ₈ system at 67.7 MPa (92.3 mol% CH ₄) by microcalorimetry (...)	200
6.13	Effect of multicycles heated up to sl dissociation on CH ₄ -C ₃ H ₈ system at 68 MPa (92.1 mol% CH ₄) by microcalorimetry (...)	201
6.14	Effect of multicycles on the dissociation profile for CH ₄ -C ₃ H ₈ hydrate (92 mol% CH ₄) by the PVT-isochoric method (...)	203
6.15	Effect of gas phase composition on dissociation profile of CH ₄ -C ₃ H ₈ hydrates (...)	205
6.16	Effect of gas phase composition on CH ₄ -C ₃ H ₈ hydrate at 67.5 MPa by microcalorimetry (...)	206
7.1	Deconvolution of the peaks related to the CH ₄ molecules trapped in large and small cavities of structure I.....	214
7.2	Raman spectra of single CH ₄ and C ₃ H ₈ hydrates: assigned peaks for characterization of double hydrates.....	215
7.3	Raman spectra of CH ₄ -C ₃ H ₈ hydrate samples prepared under different gas compositions.....	216
7.4	Deconvolution of the peaks from the CH ₄ -C ₃ H ₈ hydrate (79.8 mol% CH ₄ in gas phase) formed at 8.7 MPa.....	216

7.5	Ratios between intensities of Raman bands corresponding to propane (P_A and P_B) and methane (M_A and M_B) in CH_4 - C_3H_8 hydrates with different gas compositions.....	217
7.6	Gas hydrate growth towards the aqueous phase in capillary cell visualized through the microscope coupled to the Raman spectrometer. Time elapsed after the first visually observed hydrate crystals: A) 2 min; B) 2min 17s; C) 3min 5s.....	218
7.7	Raman spectra of CH_4 hydrate (20 MPa) at different axial positions in the capillary cell.....	219
7.8	Visual inspection of CH_4 hydrate formation and growth in the cylindrical cell.....	220
7.9	Raman spectra of CH_4 hydrate in the cylindrical cell at 16.4 MPa.....	221
8.1	Cooling (A) and heating (B) thermograms of hydrate-forming systems composed of 5 mol% [BMIM][Br] at different pressures (...)	228
8.2	Effect of ionic liquid concentration on CH_4 hydrate formation and dissociation (20 MPa): A) Ionic liquid based on [BMIM][Br]; B) Ionic liquid based on [BMIM][Cl].....	229
8.3	Dissociation peak of CH_4 hydrate in the presence of [BMIM][Cl] at 10% wt. and 9.6 MPa: A) Comparison of both thermograms obtained at 0.01 and 1 $K \cdot min^{-1}$; B) Comparison of original thermogram obtained at 0.01 $K \cdot min^{-1}$ and the treated one to reduce noise.....	232
8.4	Dissociation peak of CH_4 hydrate in the presence of [BMIM][Br] at 10% wt. and 9.6 MPa: A) Comparison of both thermograms obtained at 0.01 and 1 $K \cdot min^{-1}$; B) Comparison of original thermogram obtained at 0.01 $K \cdot min^{-1}$ and the treated one to reduce noise.....	233
8.5	Inhibitor efficiency in reducing the hydrate dissociation temperatures....	238
8.6	Comparison of CH_4 hydrate dissociation by using different inhibition solutions (5 mol% inhibitor) at 20, 60 and 100 MPa.....	239
8.7	Comparison of CH_4 hydrate equilibrium lines by using different inhibitors (experimental data and predictions using Multiflash): A) Constant molar fraction (...); B) Constant mass fraction (...)	240

LIST OF TABLES

1.1	The main polyhedra-forming gas hydrate structures.....	27
1.2	Nomenclature of the main gas hydrate structures.....	27
1.3	Average radius (Å) of gas hydrate cavities in the main structures.....	28
2.1	Properties of gases used in microcalorimetric analyses.....	51
2.2	Assessment of the instrument calibration (temperature and enthalpy) considering reference substances.....	54
4.1	Dissociation data of ice melting preceding the CH ₄ hydrate dissociation by HP-μDSC and the respective absolute deviations (AD) from computational predictions.....	108
4.2	Dissociation data of CH ₄ hydrates by HP-μDSC and the respective absolute deviations (AD) from computational predictions.....	109
4.3	Dissociation data of CH ₄ hydrates at different heating rates and their respective absolute deviations (AD) from computational predictions.....	114
4.4	Dissociation data of CH ₄ hydrates by standard and multicycles methods, and their respective absolute deviations (AD) from computational predictions.....	115
4.5	Enthalpies of CH ₄ hydrates based on experimental data obtained by the standard method (...)	121
4.6	Enthalpies of CH ₄ hydrates based on experimental data obtained by the multicycles method (...)	121
4.7	Enthalpies of CH ₄ hydrates obtained in this work and found in the literature.....	125
4.8	Dissociation data of C ₂ H ₆ hydrates by HP-μDSC (1 K·min ⁻¹) and the respective absolute deviations (AD) from computational predictions.....	127
4.9	Dissociation data of C ₂ H ₆ hydrates by standard and multicycles methods, and their respective absolute deviations (AD) from computational predictions.....	128
4.10	Enthalpies of C ₂ H ₆ hydrates dissociation based on experimental data obtained by the standard method (...)	131
4.11	Enthalpies of C ₂ H ₆ hydrates dissociation based on experimental data obtained by the multicycles method (...)	131
4.12	Enthalpies of C ₂ H ₆ hydrates obtained in this work and found in the literature.....	134
4.13	Dissociation data of CO ₂ hydrates by HP-μDSC and the respective absolute deviations (AD) from computational predictions.....	135

4.14	Dissociation data of CO ₂ hydrates by standard and multicycles methods, and their respective absolute deviations (AD) from computational predictions	136
4.15	Enthalpies of CO ₂ hydrates based on experimental data obtained by the standard method (...).	139
4.16	Enthalpies of CO ₂ hydrates based on experimental data obtained by the multicycles method (...)	140
4.17	Enthalpies of CO ₂ hydrates obtained in this work and found in the literature.....	142
5.1	Ratio of guest and cavities diameters for structures sI and sII.....	153
5.2	Dissociation data of CH ₄ -C ₂ H ₆ hydrates obtained by HP- μ DSC and the respective absolute deviations (AD) from computational predictions.....	153
5.3	Dissociation data of CH ₄ -C ₃ H ₈ hydrates (sII) obtained by HP- μ DSC and the respective absolute deviations (AD) from computational predictions (...)	164
5.4	Dissociation data of likely CH ₄ hydrates (sI) formed in CH ₄ -C ₃ H ₈ systems through HP- μ DSC and the respective absolute deviations (AD) from computational predictions (...)	164
5.5	Dissociation data of CH ₄ -CO ₂ hydrates obtained by HP- μ DSC and the respective absolute deviations (AD) from computational predictions.....	171
6.1	Dissociation data of CH ₄ hydrates by HP- μ DSC at constant pressure and the PVT-isochoric method (...)	189
6.2	Dissociation data of CH ₄ -C ₃ H ₈ hydrates obtained by HP- μ DSC (...).....	194
6.3	Dissociation data of CH ₄ -C ₃ H ₈ hydrates obtained by the PVT-isochoric method (...)	194
6.4	Dissociation data for CH ₄ -C ₃ H ₈ hydrates obtained by single runs and after multiple cycles by HP- μ DSC (...)	202
8.1	Comparison between experimental data of CH ₄ hydrates dissociation in the absence and in the presence of ionic liquids obtained in this work and found in the literature.....	235
8.2	Ice melting temperatures (onset and peak) in the absence and presence of different inhibitors.....	236
8.3	Dissociation temperatures (onset and peak) of CH ₄ hydrates in the absence and presence of different inhibitors.....	237
A.1	Coefficients of equations fitted to the experimental data of CH ₄ hydrates..	259
A.2	Results from equations fitted to the experimental data of CH ₄ hydrates by the standard method.....	260
A.3	Results from equations fitted to the experimental data of CH ₄ hydrates by the multicycles method.	260

A.4	Coefficients of equations fitted to the experimental data of C ₂ H ₆ hydrates.....	260
A.5	Results from equations fitted to the experimental data of C ₂ H ₆ hydrates by the standard method.....	261
A.6	Results from equations fitted to the experimental data of C ₂ H ₆ hydrates by the multicycles method.....	261
A.7	Coefficients of equations fitted to the experimental data of CO ₂ hydrates..	261
A.8	Results from equations fitted to the experimental data of CO ₂ hydrates by the standard method.	261
A.9	Results from equations fitted to the experimental data of CO ₂ hydrates by the multicycles method.	262
A.10	Linear thermal expansivity coefficients for CH ₄ hydrates found in this work and reported in the literature.....	262
A.11	Methane hydrate volume by the standard method.	263
A.12	Methane hydrate volume by the multicycles method.....	263
A.13	Ethane hydrate volume by the standard method.	263
A.14	Ethane hydrate volume by the multicycles method.....	264
A.15	Carbon dioxide hydrate volume by the standard method.....	264
A.16	Carbon dioxide hydrate volume by the multicycles method.....	264
A.17	Volume change in CH ₄ hydrate dissociation by the standard method.....	265
A.18	Volume change in CH ₄ hydrate dissociation by the multicycles method..	265
A.19	Volume change in C ₂ H ₆ hydrate dissociation by the standard method...	265
A.20	Volume change in C ₂ H ₆ hydrate dissociation by the multicycles method	266
A.21	Volume change in CO ₂ hydrate dissociation by the standard method.....	266
A.22	Volume change in CO ₂ hydrate dissociation by the multicycles method..	266
A.23	Hydration number of CH ₄ hydrate by the standard method.....	267
A.24	Hydration number of CH ₄ hydrate by the multicycles method.....	267
A.25	Hydration number of C ₂ H ₆ hydrate by the standard method.....	268
A.26	Hydration number of C ₂ H ₆ hydrate by the multicycles method.....	268
A.27	Hydration number of CO ₂ hydrate by the standard method.....	268
A.28	Hydration number of CO ₂ hydrate by the multicycles method.....	269

TABLE OF CONTENTS

CHAPTER 1:	
INTRODUCTION, BACKGROUND AND STATE-OF-THE-ART.....	24
1.1 INTRODUCTION TO GAS HYDRATES AND SCIENTIFIC APPLICATIONS.....	24
1.2 STRUCTURAL CHARACTERISTICS OF GAS HYDRATES.....	26
1.2.1 Phase Transitions and Metastable Phases.....	28
1.3 BACKGROUND ON GAS HYDRATES THERMODYNAMICS.....	30
1.3.1 Thermodynamic Models for Describing Phase Equilibrium.....	31
1.3.2 Instrumental Techniques for Experimental Determination of Thermodynamic Properties of Gas Hydrates.....	35
1.4 MOTIVATION AND THESIS OBJECTIVES.....	38
1.5 OUTLINE OF THE WORK.....	39
REFERENCES.....	41
CHAPTER 2:	
MATERIALS AND METHODS.....	50
2.1 HIGH PRESSURE DIFFERENTIAL SCANNING CALORIMETRY: HP- μ DSC.....	50
2.1.1 Gas Hydrate-Forming Species.....	51
2.1.2 Experimental Configuration.....	51
2.1.3 Calibration of the Experimental Apparatus.....	54
2.1.4 Methods for Determining Thermodynamic Properties.....	56
2.1.4.1 Dissociation Temperature: Onset, Peak and Endset Points.....	56
2.1.4.2 Dissociation Enthalpy: Integration of Peaks.....	58
2.1.4.3 Dissociation Enthalpy: Equation of Clapeyron.....	61
2.1.4.4 Estimation of Hydration Number.....	64
2.1.4.5 Multicycles Method.....	68
2.1.4.6 Isobaric vs. Isochoric Method.....	69
2.1.4.7 Estimation of Overall and Gas-Phase Compositions.....	70
2.2 UHP SYSTEM: ISOCHORIC METHOD.....	71
2.2.1 Experimental Configuration.....	71
2.2.2 Preparation of Methane-Propane Mixture by Gravimetry.....	72
2.2.3 Determination of Equilibrium Data.....	74
2.3 RAMAN SPECTROSCOPY.....	76
2.3.1 Procedure for Mixing Gases.....	78

2.3.2	Procedures for ex-situ Analyses.....	79
2.3.3	Procedures for in situ Analyses.....	81
2.3.3.1	Capillary Cell.....	81
2.3.3.2	Cylindrical Cell (Linkam).....	82
	REFERENCES.....	84
CHAPTER 3:		
	PRELIMINARY STUDIES.....	88
	ABSTRACT.....	88
3.1	THERMODYNAMIC STUDY OF GASES.....	88
3.1.1	Single gases.....	89
3.1.2	Binary gaseous mixtures.....	90
3.2	INFLUENCE OF WATER FRACTION ON HYDRATE DISSOCIATION TEMPERATURE.	92
3.3	VALIDATION OF PENG-ROBINSON EOS AT HIGH PRESSURES.....	96
3.4	TRANSITIONS CONCERNING THE TEFLON RING.....	97
3.5	CONCLUSIONS.....	99
	REFERENCES.....	100
CHAPTER 4:		
	THERMODYNAMIC STUDY OF SINGLE-GUEST GAS HYDRATES.....	102
	ABSTRACT.....	102
4.1	INTRODUCTION.....	102
4.2	SPECIFIC EXPERIMENTAL CONDITIONS.....	104
4.3	METHANE-WATER SYSTEM.....	105
4.3.1	Equilibrium Data for CH ₄ Hydrates by Microcalorimetry.....	105
4.3.2	Effect of H ₂ O Sample Size.....	111
4.3.3	Effect of Cooling and Heating Rates.....	113
4.3.4	Effect of Multicycles.....	116
4.3.5	Enthalpy of Dissociation and Hydration Number.....	120
4.4	ETHANE-WATER SYSTEM.....	125
4.4.1	Equilibrium Data for C ₂ H ₆ Hydrates by Microcalorimetry.....	125
4.4.2	Effect of Multicycles.....	128
4.4.3	Enthalpy of Dissociation and Hydration Number.....	131
4.5	CARBON DIOXIDE-WATER SYSTEM.....	134
4.5.1	Equilibrium Data for CO ₂ Hydrates by Microcalorimetry.....	134

4.5.2	Effect of Multicycles.....	136
4.5.3	Enthalpy of Dissociation and Hydration Number.....	139
4.6	CONCLUSIONS.....	143
	REFERENCES.....	145
CHAPTER 5:		
	THERMODYNAMIC STUDY OF DOUBLE-GUEST GAS HYDRATES.....	149
	ABSTRACT.....	149
5.1	INTRODUCTION.....	149
5.2	SPECIFIC EXPERIMENTAL CONDITIONS.....	151
5.3	INFLUENCE OF CAGE OCCUPANCY ON STRUCTURAL STABILITY OF HYDRATES	152
5.4	METHANE-ETHANE-WATER SYSTEM.....	153
5.4.1	Equilibrium Data for CH ₄ -C ₂ H ₆ Hydrates by Microcalorimetry.....	153
5.4.2	Thermodynamic and Structural Analysis of CH ₄ -C ₂ H ₆ Hydrates by Simulations.....	157
5.5	METHANE-PROPANE-WATER SYSTEM.....	161
5.5.1	Coexistence of Structures I and II on CH ₄ -C ₃ H ₈ Hydrates.....	161
5.5.2	Equilibrium Data for CH ₄ -C ₃ H ₈ Hydrates by Microcalorimetry.....	163
5.5.3	Thermodynamic and Structural Analysis of CH ₄ -C ₃ H ₈ Hydrates by Simulations.....	167
5.6	METHANE-CO ₂ -WATER SYSTEM.....	170
5.6.1	Equilibrium Data for CH ₄ -CO ₂ Hydrates by Microcalorimetry.....	170
5.6.2	Thermodynamic and Structural Analysis of CH ₄ -CO ₂ Hydrates by Simulations.....	174
5.7	METHANE-ETHANE-PROPANE-WATER SYSTEM.....	176
5.8	CONCLUSIONS.....	181
	REFERENCES.....	183
CHAPTER 6:		
	GAS HYDRATES STUDIES BY ISOCHORIC METHOD IN A PVT CELL.....	185
	ABSTRACT.....	185
6.1	INTRODUCTION.....	185
6.2	SPECIFIC EXPERIMENTAL CONDITIONS.....	187
6.3	METHANE HYDRATE.....	187
6.3.1	Equilibrium Data for CH ₄ Hydrates: PVT-Isochoric Method vs Microcalorimetry.....	187

6.3.1.1	Effect of the Subcooling Degree.....	189
6.3.1.2	Effect of Mixing	190
6.4	METHANE-PROPANE HYDRATE.....	191
6.4.1	Equilibrium Data for CH ₄ -C ₃ H ₈ Hydrates: PVT-Isochoric Method vs Microcalorimetry.....	191
6.4.2	Coexistence of Structures I and II on CH ₄ -C ₃ H ₈ Hydrates (Isochoric Method).....	194
6.4.3	Impact of Experimental Factors on the Formation of sI and sII.....	195
6.4.3.1	Effect of Heating Rate.....	195
6.4.3.2	Effect of Mixing.....	197
6.4.3.3	Effect of Multiple Cycles.....	199
6.4.3.4	Effect of Gas phase composition.....	204
6.5	CONCLUSIONS.....	207
	REFERENCES.....	209
 CHAPTER 7:		
	STUDIES OF GAS HYDRATES BY RAMAN SPECTROSCOPY.....	212
	ABSTRACT.....	212
7.1	INTRODUCTION.....	212
7.2	SPECIFIC EXPERIMENTAL CONDITIONS.....	213
7.3	<i>EX SITU</i> ANALYSES.....	213
7.3.1	Methane Hydrate.....	214
7.3.2	Methane-propane Hydrates.....	214
7.4	<i>IN SITU</i> ANALYSES.....	218
7.4.1	Capillary Cell.....	218
7.4.2	Cylindrical Cell.....	219
7.5	CONCLUSIONS.....	222
	REFERENCES.....	222
 CHAPTER 8:		
	USE OF 1-BUTYL-3-METHYLIMIDAZOLIUM-BASED IONIC LIQUIDS AS HYDRATE INHIBITORS AT HIGH PRESSURE CONDITIONS.....	225
	ABSTRACT.....	225
8.1	INTRODUCTION.....	225
8.2	SPECIFIC EXPERIMENTAL CONDITIONS.....	227
8.3	EFFECT OF PRESSURE ON FORMATION AND DISSOCIATION OF SOLID PHASES..	228

8.4	EFFECT OF IONIC LIQUID CONTENT IN GAS HYDRATES FORMATION.....	228
8.3.1	Distance Between Onset and Peak Temperatures.....	231
8.3.2	Thermodynamic Inhibition Efficiency of [BMIM][Br] and [BMIM][Cl]...	237
8.3.3	Comparison with Methanol.....	238
8.4	CONCLUSIONS.....	241
	REFERENCES.....	242
CHAPTER 9:		
	SUMMARY OF CONCLUSIONS.....	249
9.1	SUMMARY OF CONCLUSIONS.....	249
9.2	RECOMMENDATIONS.....	253
CHAPTER 10:		
	SCIENTIFIC PRODUCTION.....	255
10.1	ARTICLES PUBLISHED IN SCIENTIFIC JOURNALS.....	255
10.2	ARTICLE ACCEPTED FOR PUBLICATION IN SCIENTIFIC JOURNAL.....	255
10.3	ARTICLES IN PROGRESS.....	255
10.4	WORKS IN SCIENTIFIC EVENTS.....	256
10.4.1	Full Works.....	256
10.4.2	Extended Abstracts.....	256
10.4.3	Abstracts.....	257
APPENDIX:		
	CALCULATION OF HYDRATE DISSOCIATION ENTHALPY BY THE CLAPEYRON EQUATION AND HIDRATION NUMBER BY THE ITERATIVE METHOD.....	259
A.1	EQUATIONS FITTED TO THE EXPERIMENTAL DATA.....	259
A.1.1	Methane Hydrates.....	259
A.1.2	Ethane Hydrates.....	260
A.1.2	Carbon Dioxide Hydrates.....	261
A.2	ESTIMATION OF THE HYDRATE VOLUME.....	262
A.2.1	Methane Hydrates.....	262
A.2.2	Ethane Hydrates.....	263
A.2.2	Carbon Dioxide Hydrates.....	264
A.3	CALCULATION OF THE VOLUME CHANGE.....	264
A.3.1	Methane Hydrates.....	265
A.3.2	Ethane Hydrates.....	265

A.3.2	Carbon Dioxide Hydrates.....	266
A.4	DETERMINATION OF THE HYDRATION NUMBER BY THE INDIRECT METHOD.....	266
A.4.1	Methane Hydrates.....	267
A.4.2	Ethane Hydrates.....	268
A.4.2	Carbon Dioxide Hydrates.....	268
	REFERENCES.....	269

CHAPTER 1

INTRODUCTION, BACKGROUND AND STATE-OF-THE-ART

1.1 INTRODUCTION TO GAS HYDRATES AND SCIENTIFIC APPLICATIONS

Clathrate hydrates or clathrates are inclusion compounds formed by low molecular mass molecules trapped in cavities or “cages” of different geometry constituted by water molecules linked through hydrogen bonds. When these structures host gas molecules, they are called gas hydrates, which are studied in this work.

Water in these high pressure and low-temperature environments added to natural gas, sometimes formed by anaerobic bacteria that decompose organic matter from the ocean floor, provide the necessary conditions for the formation of gas hydrates. Therefore, these crystalline structures can be generated in sediments on continental and insular slopes, as well as on continental shelves of polar regions and in deep water environments (> 300 m) in both lakes and seas, such as in the Brazilian Pre-Salt areas (CARDOSO et al., 2015; KVENVOLDEN, 1993).

These compounds have some properties similar to those of ice, such as physical appearance, refractive index and mechanical properties, since they present about 85 molar percent of water. However, other features may be quite different, such as viscosity and thermal conductivity. The thermodynamic stability of clathrate hydrate structures relies on van der Waals interactions between host lattice (water) and guest molecules (hydrocarbons). Hence, the molecular structure has an essential role in phase equilibria and thermal properties of hydrates (DURHAM et al., 2003; GABITO; TSOURIS, 2010).

The understanding of the mechanisms of formation or dissociation of such compounds has a great scientific interest because of the vast amount of hydrocarbons existing as gas hydrates and because of the significant impact on the Earth's ecosystem. The existence of large hydrate reservoirs promotes the potential of these compounds as an alternative energy resource. It is estimated that there is twice as much energy in clathrate hydrate deposits in Arctic and Oceanic regions as in available fossil fuel reservoirs (ALADKO et al., 2002). However, gas hydrates are unstable compounds and can dissociate rapidly due to a slight increase in temperature or

pressure drop. This also creates environmental hazards due to the risk of uncontrolled release of methane or other greenhouse gases contained in hydrates since the sudden release of the gas trapped in these compounds can generate explosions in hydrate reservoirs. The tragedy in the Gulf of Mexico in 2010 can be cited as an example, in which the *Deepwater Horizon* operational unit of drilling and exploration exploded and sank, releasing about 4.1 million barrels of oil from the Macondo well, in which the gas-to-oil ratio was 1600 standard cubic feet per petroleum barrel (MICHEL et al., 2013; REDDY et al., 2012).

The studies of the physical-chemical properties of gas hydrates also demand considerable attention because they can imply clogging oil and gas flowlines (SAMI et al., 2013; SLOAN et al., 2009). The Brazilian oil reservoirs discovered in the last two decades, known as Pre-Salt, present further features that corroborate to the hydrate formation during oil exploitation, such as colder regions, deeper waters and longer distances from shore (CARDOSO et al., 2015). Therefore, a significant part of published works on these compounds is related to the development of process conditions in which the hydrate formation is avoided by applying thermodynamic inhibitors, such as ionic salts, methanol and glycol, that displaces the thermodynamic equilibrium boundary of the involved fluid so that the safe operating zone is increased (HAGHIGHI et al., 2009; HU, et al., 2017a ; MOHAMMADI; RICHON, 2010). Besides, kinetic inhibitors are often applied in order to delay the hydrate growth and plugging processes while fluid goes within the pipeline (KELLAND et al., 2006; KOH et al., 2002; TARIQ et al., 2014). It is still possible to add anti-agglomerants agents along the flow path to prevent the adhesion between the hydrate particles formed (BUI et al., 2018; SLOAN et al., 2010; SLOAN; KOH, 2008).

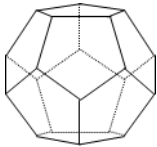
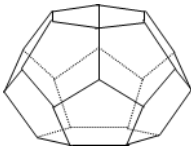
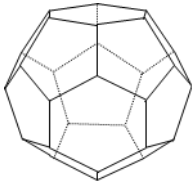
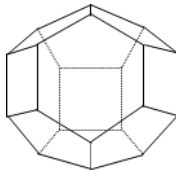
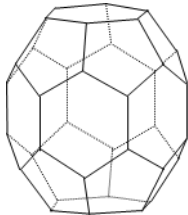
In addition, other technological applications reinforce the need of better understanding about these compounds and predict the conditions that may favor, delay or inhibit the formation of these structures, such as: a) storage of hydrogen in clathrate hydrate structures (TSUDA et al., 2010; XU et al., 2013), (b) purification / desalination of seawater or other fluids (LINJUN et al., 2013), c) gas hydrate forming compounds such as carbon dioxide applied as phase change materials or refrigeration fluids (MARINHAS et al., 2006) and d) capture / storage of carbon dioxide (XU et al., 2013)

Although gas hydrates are abundant around the earth and their applications are encouraging, there is still much more to learn about the formation and dissociation processes and the most relevant mechanisms in hydrate deposition. In addition, it is necessary to understand their growing process, interaction with sediments and how they could affect the environmental conditions during exploitation, especially at extreme conditions of high pressures and low temperatures such as in Brazilian pre-salt reserves. Finally, some particular gas hydrate-forming systems have not been exploited and their experimental data found in literature are scarce, mainly at high-pressure ranges due to instrumental limitations. Natural gas usually is composed mostly by methane and lower fractions of heavier hydrocarbons, such as ethane, propane, butane, isobutane and other gases, as carbon dioxide (TAN et al., 2012). Experimental data for gas hydrates formed in the presence of such mixtures need to be more deeply studied to evaluate the accuracy of predictions based on computational models and the effects of gas composition on the hydrate structural and physical-chemical properties. All these factors make evident the importance of studying these compounds.

1.2 STRUCTURAL CHARACTERISTICS OF GAS HYDRATES

The structure of gas hydrates consists of polyhedral arrangements working as host cavities that are formed by water molecules linked by hydrogen bonds. The terminology for each cavity is given based on the type and amount of polygons that constitute the polyhedron. For example, the pentagonal dodecahedron consists of 12 pentagons (5-sided polygon), ergo its nomenclature is 5^{12} . The cavities formed by different polygons follow the same logic: the hexadecahedron formed by 12 pentagons and 4 hexagons is called $5^{12}6^4$. The 5 most common types of polyhedra in gas hydrate formation are shown below:

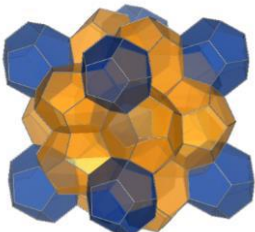
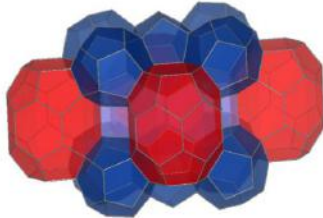
Table 1.1 – The main polyhedral-forming gas hydrate structures.

5^{12} (20 H ₂ O)	$5^{12}6^2$ (24 H ₂ O)	$5^{12}6^4$ (28 H ₂ O)	$4^{35}6^3$ (20 H ₂ O)	$5^{12}6^8$ (36 H ₂ O)
				
Pentagonal Dodecahedron	Tetradecahedron	Hexadecahedron	Irregular Dodecahedron	Icosahedron

Source: adapted from Sum et al. (2011).

The elementary structure of the gas hydrate crystalline lattice is composed of two or more types of cavities. Although other clathrate hydrate structures are mentioned in the literature, the most frequent ones are sI, sII and sH (Table 1.2). The unit cell for type sI and sII is composed of two polyhedra, whereas sH is formed by three distinct polyhedra. Table 1.3 shows the average radius of cavities in these three elementary structures. The guest molecule size is a factor that contributes to determining the hydrate structure to be formed, along with the thermodynamic conditions of the system. Chakoumakos et al. (2003) show the dependency of the polyhedron volume constituted of 12, 14 and 16 faces mainly on the temperature and type of the guest molecule.

Table 1.2 – Nomenclature of the main gas hydrate structures.

Structure I (sI)	Structure II (sII)	Structure H (sH)
		
$2(5^{12}) + 6(5^{12}6^2) : 46 \text{ H}_2\text{O} / a$ $= 12 \text{ \AA}$	$16(5^{12}) + 8(5^{12}6^4) : 136 \text{ H}_2\text{O} / a$ $= 17,3 \text{ \AA}$	$3(5^{12}) + 2(4^{35}6^3) + 1(5^{12}6^8) : 136$ $\text{H}_2\text{O} / a = 12,2 \text{ \AA}, c = 10,1 \text{ \AA}$

Source: adapted from Sum et al. (2011).

Table 1.3 – Average radius (Å) of gas hydrate cavities in the main structures.

Elementary Structure	sI		sII		sH		
Nomenclature	5 ¹²	5 ¹² 6 ²	5 ¹²	5 ¹² 6 ⁴	5 ¹²	4 ³ 5 ⁶ 6 ³	5 ¹² 6 ⁸
Average radius (Å)	3.95	4.33	3.91	4.73	3.94	4.04	5.79

Source: adapted from Sloan and Koh (2008).

1.2.1 Phase transitions and Metastable Phases

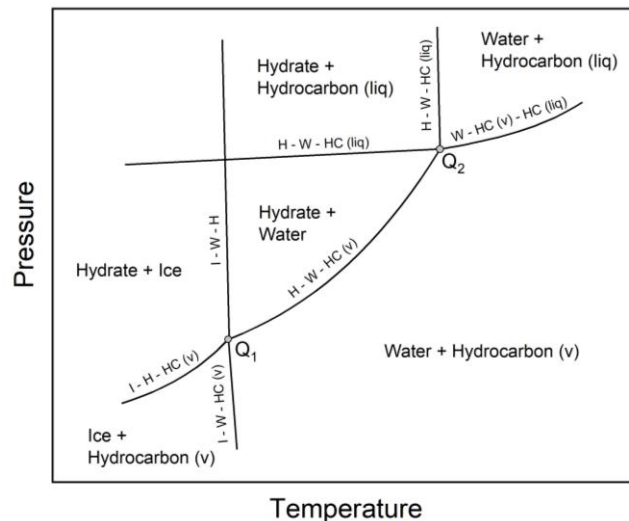
When the gas hydrate is under very high pressures, the structure can undergo a molecular rearrangement and evolve to a denser and more stable phase. The compression of methane hydrate was experimentally studied by Chou et al. (2000) and the group observed the transition from type sI to type II at 100 MPa and then to sH at 600 MPa. However, other studies have shown higher pressures are required for the same transitions, such as the work published by Hirai et al. (2000), which describes the transition of sI into sH at 0.8 GPa and then two new orthorhombic structures are formed at 2.1 GPa. However, the group suggests that the phase transition can be affected by compression rate and the initial conditions. In any case, these types of structures may be common in deeper regions of continental shelves or permafrost and may be facilitated when minimal amount of other larger guest molecules is present, such as ethane and propane. Sloan and Koh (2008) point out several studies describing phase transitions for different clathrate hydrates as a function of pressure and temperature, based mainly on techniques such as X-ray diffractometry and Raman spectroscopy.

Another point to be evaluated regarding clathrate hydrate structures is the occurrence of transient or metastable phases, considering that natural reservoir or clathrate-forming systems are not in constant equilibrium. Phase transitions can occur when a system containing clathrate hydrates is subjected to thermodynamic changes, either by undercooling or compression process, for example. Besides, the initial process of clathrate formation could lead to different structures by itself, since the formation of a metastable structure may be favored by kinetic factors, even it is not the most thermodynamically stable configuration (ALADKO et al., 2002; KLAPPROTH et al., 2019; SHIN et al., 2012). Another situation that may promote metastable phases is

the phenomenon known as self-preservation, in which the hydrate remains stable even when outside of the stability zone. In this case, an ice shell covers the first formed hydrate phase (metastable), separating it from a further but more stable hydrate layer (BAI et al., 2015; CHUVILIN et al., 2018; MAKOGON; GHASSEMI, 2010). The coexistence of different phases can be checked by calorimetry or structural analysis, that allow obtaining metastable phase diagrams for gas hydrates possibly not predictable by current models (ISTOMIN et al., 2006).

Although the analytical results for clathrate properties may slightly differ according to the technique and methodology employed, the previous knowledge of structural transitions and metastable phases is essential to characterize reservoirs, to calculate and manage the heat applied in these reservoirs for gas exploitation and to design and develop inhibitors for flow assurance applications (SLOAN et al., 2010; SLOAN; KOH, 2008; STERN et al., 2000). For all these applications, it is required to know in advance the phase diagram for the gas hydrate system concerned, as illustrated in Figure 1.1, in which quadruple points (Q_1 and Q_2) are indicated.

Figure 1.1 – Illustration of a phase diagram for a gas hydrate-forming system

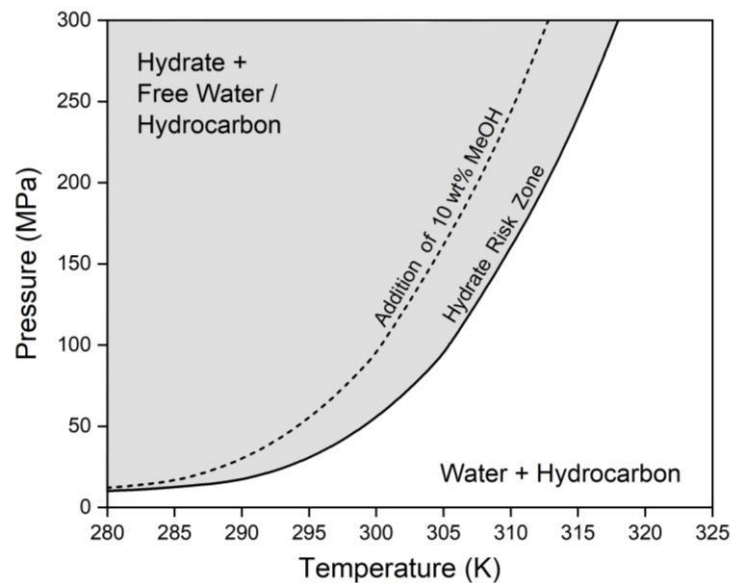


Source: Adapted from Lehmkuhler (2010) and Sloan and Koh (2008).

The quadruple points are characteristic for each hydrate-former system and represent the intersection of four three-phase lines. The lower quadruple end is constituted by ice, liquid water, hydrate and gaseous hydrocarbon (I-W-H- $HC_{(v)}$), while the upper quadruple point is composed of liquid water, hydrate, gaseous and liquid

hydrocarbon phases ($W-H-HC_{(v)}-HC_{(liq)}$). The upper intersection (Q_2) may not be attainable when the critical point of the gas concerned is too low, such as in the case of methane or nitrogen, for instance (SLOAN; KOH, 2008). Figure 1.2 shows a phase diagram for methane-water system and the effect of a thermodynamic inhibitor (methanol) in the hydrate equilibrium curve.

Figure 1.2 – Phase diagram for the methane-water system obtained using the software CSMGem.



1.3 BACKGROUND ON GAS HYDRATES THERMODYNAMICS

The main thermodynamic properties of gas hydrates, such as phase equilibrium, enthalpy and heat capacity have been studied by experimental methods and mathematic models. Unlike the kinetic approach, the hydrate phase equilibrium can be well-defined through statistical thermodynamic models designed in order to predict hydrate formation conditions, providing good accuracy and comprehensiveness (ALADKO et al., 2002; BALLARD; JAGER et al., 2013; LARIONOV et al., 2006; SLOAN, 2001; VINS et al., 2016; ZHDANOV et al., 2017). However, these models need to be corroborated with experimental data, that in some cases may be scarce in literature due to experimental limitations, mainly at extreme conditions of pressure and temperature (JAGER et al., 2005). This section briefly describes the progress of most applied models in thermodynamic studies of gas hydrates and the main instrumental

techniques used for experimentally determining thermodynamic properties of gas hydrates.

1.3.1 Thermodynamic Models for Describing Phase Equilibrium

More than one model is needed to describe all phases in systems consisting of water and hydrocarbons at favorable thermodynamic conditions to hydrate formation. However, some works have tried to develop a single equation of state that includes all the fluids present in the system (AVLONITIS; VAROTSIS, 1996).

The fluid phases are usually described by cubic equations of state, while the statistical thermodynamic model of van der Waals and Platteeuw (1959) or derivations is applied for the hydrate phase. This model is based on the chemical potential difference of water in empty hydrate lattice (β) and gas molecules-occupied lattice (H), as described below, where v_m is the number of cages of type m per water molecules in the structure unit cell and θ_{jm} refers to the occupation of cages m by the guest molecule j .

$$\Delta\mu_{\omega}^H = \mu_{\omega}^{\beta} - \mu_{\omega}^H \quad (1.1)$$

$$\frac{\mu_{\omega}^H}{RT} = \frac{g_{\omega}^{\beta}}{RT} + \sum_m^{cages} v_m \cdot \ln \left(1 - \sum_j^{guests} \theta_{jm} \right) \quad (1.2)$$

This model is based on the similarity between hydrate formation and Langmuir adsorption, in which molecules of an ideal gas are adsorbed on a uniform, simple, infinite and non-porous surface under isothermal condition. The Langmuir isotherm model uses the following assumptions: (a) the adsorption is monomolecular; (b) the surface is energetically homogeneous; (c) there is no interaction between the adsorbed particles and the adsorption does not depend on the occupation of the neighboring sites. In the Langmuir relationship below, f_j is the fugacity of molecule j in the fluid phase.

$$\theta_{mj}(T, P, y) = \frac{C_{mj}(T) \cdot f_j(T, P, y)}{1 + \sum_{i=1}^n C_{mj} \cdot f_i(T, P, y)} \quad (1.3)$$

It is assumed by the van der Waals and Platteeuw model that: (a) each cavity can be occupied by only one guest molecule; (b) the entrapped molecules do not distort the cavity; (c) the interactions between the guest molecules are negligible; (d) the cavity has spherical symmetry. Considering these assumptions, the Langmuir's constant (C_{mj}) can be calculated by the following equation. $W(r)$ defines the potential of the spherically symmetric cell, in which the functions of Lennard-Jones and Kihara are the most used ones (MARTÍN, 2010).

$$C_{mj} = \frac{4 \cdot \pi}{k \cdot T} \int_0^r \exp\left(-\frac{W(r)}{k \cdot T}\right) \cdot r^2 \cdot dr \quad (1.4)$$

Parrish and Prausnitz (1972) developed an interactive scheme for the computational calculation of equilibrium from equations developed by van der Waals and Platteeuw and Saito et al. (1964). The group applied an empirical equation to calculate the Langmuir's constant in the van der Waals model and developed a correlation of Kihara potential with experimental hydrate formation data. The simplified model provided more accurate results and was applied in industrial software as ASPEN HYSYS and PVTSIM (LI et al., 2017). However, the scheme developed by Parrish and Prausnitz does not explicitly incorporate the gas hydrate phase. The method determines the thermodynamic equilibrium of fluid phases and compares to the solid phase (gas hydrate), and then takes the temperature and pressure at the point in which the chemical potential of water converges to the same value in all phases, disregarding the influence of the guest type on the guest-lattice interactions (JAGER et al., 2013). Since then, the van der Waals and Platteeuw model has been improved for *flash* calculations in multiphase and closed systems, based on the minimum of the Gibbs free energy criterion (BALLARD, 2002; BISHNOI et al., 1989; GUPTA, 1990), considering by this way the hydrate distortion and allowing the equilibrium point calculation from any phase, including the hydrate. In a series of four parts, Ballard and Sloan (2002, 2004a, 2004b) and Jager et al. (2003) detail the progress of

implementing this new approach using the Gibbs energy minimization technique, using a different standard state for deriving the thermodynamic equations instead of the hypothetical empty hydrate lattice. In the last part, the multi-phase Gibbs energy minimization program (CSMGem), developed incorporating the new hydrate and aqueous phase models, is compared with four commercial programs: CSMHYD, DBRHydrate, Multiflash and PVTsim. According to the authors, the results are entirely satisfactory for non inhibited systems and favorable predictions are provided for inhibited systems (methanol and NaCl), giving credibility to the proposed models for hydrate and aqueous phases. Antunes et al. (2018) also compare predictions calculated by four different methods: Multiflash, PVTsim, CSGem and a homemade hydrate prediction program using the van der Waals and Platteeuw model (1959) coupled with the Peng-Robinson equation of state (PENG; ROBINSON, 1976). The group observed that the best results for one-guest systems were provided by CSMGem, while PVTsim showed best ones for more than one-guest systems. By considering inhibited systems, all the three commercial programs presented similar results for one-guest systems, but Multiflash performed better with gas mixtures.

Some works have pointed to a different approach in hydrate modeling, such as *ab initio* methods, which aim to extend fundamental calculations of quantum mechanics to macroscopic properties and even predict hydrate spectroscopic properties (ANDERSON, 2005; KLAUDA; SANDLER, 2003; SLOAN; KOH, 2008). According to Bandyopadhyay and Klauda (2011), water fugacity is used in this approach instead of chemical potential for hydrate phase modeling and it has the advantage of not using empiric data. The effect of lattice distortion, long-range guest-host and guest-guest interactions, as well as the cavity occupancy by more than one guest are all included in the fugacity-based model.

The heat of dissociation (ΔH_{diss}), or enthalpy, is a time-independent property defined as the energy required for gas hydrate to dissociate and turn back to a fluid phase formed by gas and liquid water (SLOAN; FLEYFELB, 1992). This physical property is used to calculate the energetic potential of gas hydrate reservoirs and to develop an adequate production system (SAW et al., 2012). Some equations allow the estimation of this property based on phase equilibrium data. The Clapeyron equation

is commonly used to determine the enthalpy of simple gas hydrates from easily measured properties, such as pressure and temperature, according to Eq. 1.5.

$$\frac{dP}{dT} = \frac{\Delta H}{T\Delta V} \quad (1.5)$$

This equation can be simplified considering that the volume change during phase transition (ΔV) is close to the gas phase volume (V_g). By this way, a reduced form of the Clapeyron equation (7) is obtained, known as Clausius-Clapeyron:

$$\Delta V = V_g = \frac{zRT}{P} \quad (1.6)$$

$$\frac{d \ln P}{d \left(\frac{1}{T} \right)} = - \frac{\Delta H}{zR} \quad (1.7)$$

Sloan and Fleyfelb (1992) examined previous works and proposed applying this equation only in univariate systems, considering three restrictions: (a) the composition of guest molecules in each cavity does not vary significantly; (b) the volume of hydrate approximates that of water in the hydrate formation reaction; (c) the gas phase composition remains constant. Several studies adopted this simplified version (LONG, 1994; YOON et al., 2003). However, the accuracy of this equation has been discussed by some authors. Anderson (2003, 2004) suggests using the Clapeyron equation instead of the simplified equation. According to the author, the Clausius-Clapeyron equation may be valid for some gas hydrates at relatively low pressures; however, a rigorous approach is required when working at higher pressures and especially at temperatures far from the lower quadruple point. Gupta et al. (2008) state that experimental data for methane hydrate heat of dissociation obtained by calorimetry do not agree with the predictions of the Clausius-Clapeyron equation, probably by neglecting the volume of water and hydrate phase, while Clapeyron equation provided predictions in agreement to experimental data up to 20 MPa.

Regarding the heat capacity of gas hydrates, Parsonage and Staveley (1958) applied statistical mechanics to calculate this property for the first time. For a system in which interaction between guest molecules is negligible and they do not distort the lattice or are coupled to it, the hydrate heat capacity can be calculated from the equation below, in molar terms:

$$C_p(\text{hydrate}) = C_p(\text{empty structure}) + C_p(\text{guest molecule}) \quad (1.8)$$

This model was used to predict the heat capacity of different clathrates, including N_2 and CH_4 , and the results revealed this property as a linear function of the composition (PARSONAGE; STAVELEY, 1984). Handa and Tse (1986) also applied this model in heat capacity analysis of xenon, krypton and methane. In 1994, Avlonitis proposed a computational scheme to calculate heat capacity of hypothetical empty structure and of the guest species involved. This script allowed to reduce the data obtained by Handa and Tse (1986) and predict the C_p for both simple and multicomponent gas hydrates. The results indicate that this thermodynamic property of hydrates is close but always greater than that of ice.

1.3.2 Instrumental Techniques for Experimental Determination of Thermodynamic Properties of Gas Hydrates

The main experimental methods currently used to study equilibrium and thermal properties of gas hydrates are based on isochoric experiments by using PVT cells and High-Pressure Differential Scanning Calorimetry (HP- μ DSC). The first experimental setup for studying hydrate equilibrium was designed by Deaton and Frost (1937) and came to be the prototype of PVT cells for further researches (MCLEOD; CAMPBELL, 1961; DALMAZZONE et al., 2002a; HU et al., 2017; MOHAMMAD-TAHERI et al., 2013; THAKORE; HOLDER, 1987; VERMA, 1974; WARD et al., 2015). This type of cell allows to set a homogeneous sampling due to the mixing in the liquid bulk and the analysis is usually performed through isochoric methods. On the other hand, the calorimetry came later not only for determining equilibrium data but also for obtaining other thermal properties such as enthalpy and heat capacity, with advantages such as

shorter analysis, simple experimental procedure and smaller amount of material required (DALMAZZONE et al., 2002b; GUPTA et al., 2008; HANDA et al., 1986; PARLOUËR et al., 2004). Nevertheless, hydrate growth inside the cell undergoes mass transfer issues since the hydrate layer is formed in the interface of gas and liquid phases due to the absence of mixing in most of μ DSC configurations. Recently, Delroisse et al. (2018) published new enthalpy data for cyclopentane hydrate by using a mechanically stirred calorimetric cell. The group points out a list of advantages by using *in situ* agitation: lower induction time, higher surface area for mass transfer between water and cyclopentane liquid phases and no interfacial hydrate shell usually formed in non-stirred systems. It is also stated that the whole experimental apparatus can work at up to 20 MPa, although the experiments were performed at atmospheric pressure. No work is found in literature so far applying μ DSC at high pressures in presence of continuous mixing.

In recent years, nevertheless, several studies have used high-pressure μ DSC to determine hydrate phase equilibrium or other thermal properties through non-mixed methods: Lachance et al. (2009) used this methodology to study hydrate kinetic inhibition in water-in-oil emulsions at 15 MPa and stated some advantages of such method, as less material required and shorter experimental time; Ohno et al. (2010) studied methane-ethane-propane hydrates at 4 MPa to evaluate some proteins as a new class of inhibitors by means of μ DSC temperature ramping and isothermal experiments; Later on, Daraboina et al. (2011) studied the same hydrate former system by applying chemical and biological inhibitors at 9 MPa; At the same time, Dalmazzone et al. (2011) patented a method for determining kinetic characteristics of gas hydrate formation by means of high-pressure μ DSC measurements; In 2012, Lafond et al. published a work studying the methane hydrate from 7 to 20 MPa through stepwise measurements in order to establish new hydrate phase boundaries in the presence of NaCl and methanol. In such method, several consecutive steps are performed in which the temperature is increased only a fraction of degree and then followed by an isothermal period, allowing to obtain the hydrate dissociation temperature more accurately; Daraboina et al. (2013) used the High-Pressure μ DSC up to 10 MPa to study methane hydrates and demonstrated that it can provide statistically reliable time-dependent results using both temperature-ramping and isothermal programs; In 2015,

Sabil et al. investigated ionic liquids as a new class of inhibitors for hydrate formation from 3.6 to 11.2 MPa; Chu et al. (2016) also used high-pressure microcalorimetry to evaluate the chain length effect of ionic liquids on the methane hydrate phase equilibrium, working at pressures from 5 to 35 MPa; Cha et al. (2016) applied both PVT-isochoric method and HP- μ DSC to investigate methane hydrate phase equilibria in aqueous salt solutions up to 11.5 MPa and the results showed good agreement.

The microcalorimetry allows the detection of phase transitions over time by means of isobaric, isochoric or isothermal methods. Energy transitions caused by phase changes or structural rearrangement can be observed through endothermic or exothermic peaks in thermograms, depending on the nature of the transition. Despite its enormous potential, few studies approach the determination of hydrate enthalpy and heat capacity through this equipment (DELROISSE et al., 2018; GUPTA, 2008; MU; SOLMS, 2018). Although the experimental procedure is simple, the methodology for determining heat capacity can be made difficult since it requires rigorous baselines for empty cells and all analyses must be carried out under the same conditions. In addition, the heating rate in these cases should be considerably low so that the kinetic effect on the heat flow signal is minimized. In the case of enthalpy, the difficulty concerns about determining the actual amount of hydrate formed, since it must be estimated considering the theoretical stoichiometry of the reaction. In addition, hydrate formation may occur along with ice melting during the heating process, making harder the integration of peaks. However, a multi-cycled methodology is presented in this work adapted from Marinhas et al. (2006) to calculate hydrates enthalpy and to expand the experimental database available in the literature at pressures up to 100 MPa. Besides, the cited limitations do not affect the determination of dissociation temperatures, whose results are obtained quickly and satisfactorily. Considering this work is focused mainly on gas hydrate characterization via high-pressure microcalorimetric measurements, this technique will be more extensively approached in the next chapters.

Several other works gather different methods and techniques to analyze more comprehensively the gas hydrates, considering the structural aspects. Desmedt et al. (2015) proposed a new way of studying the effects of ionic defects in lattice on hydrate physicochemical properties. The group performed calorimetric, X-ray diffraction and Raman scattering measurements along with computational structure relaxation in the

density functional theory approximation to better describe the new mixed synthesized hydrate. In particular, Raman spectroscopy has been used to study gas hydrate formation through specific signatures of vibrational modes in the spectra. More recently, Petuya et al. (2017) published a work about the guest partitioning in CO hydrate using high-resolution Raman spectroscopy and neutron powder diffraction. By the first time, the group unraveled Raman signatures of CO molecules trapped in both small and large cavities of structure I. They also studied the dependency of cage occupancy on temperature and pressure through Raman signatures and indicate that in some cases the occupancy is higher than 1, i.e., large cavities can be multiple occupied by CO molecules. Raman spectra are also presented in this work to complement the methane-propane hydrates characterization.

1.4 MOTIVATION AND THESIS OBJECTIVES

Although the equilibrium properties of any system are determined by phase diagrams, most hydrate diagrams available so far are based on simulations. The equilibrium equations for these simulations can deviate significantly from real data, especially as pressure increases (JAGER et al., 2005) and for inhibited systems, that may substantially influence the results depending on the activity coefficient model used and how its parameters are regressed (ANTUNES et al., 2018). Few experimental data in the literature for natural gas hydrates also limit the comparison of predictions (BALLARD; SLOAN, 2004b). Moreover, modeling may not predict metastable states occurring under specific thermodynamic conditions that may be common in hydrate reservoirs, as mentioned before (KLAPPROTH et al., 2019).

Phase diagrams for hydrate-forming systems based on experimental data are very scarce in the literature due to instrumental limitations or experimental difficulties, especially for gaseous mixtures. An exception is the work reported by Aladko et al. (2002), in which the methane-propane-water system was investigated by means of differential thermal analysis up to 1500 MPa. According to the group, this technique allows obtaining the topology of phase diagrams and hydrate decomposition temperatures based on high-pressure equipment, firstly employed by Dyadin et al. (1997). However, most hydrate studies at high pressures were carried out using

complex and heavy instrumentation coupled to a PVT cell with a visual sapphire window, that records temperature and pressure simultaneously. Moreover, variations in experimental conditions make hard the comparison of results obtained by different laboratories since hydrate structural properties and stability depends on several factors, such as hydrate stabilization-time, natural gas composition, solubility and salinity in aqueous phase (BANDYOPADHYAY; KLAUDA, 2011; SLOAN et al., 2010).

In spite of the difficulties mentioned above, it is relevant to investigate the phase diagrams for gas hydrate-forming systems. It is essential to understand the mechanisms of gas hydrates formation and dissociation as well as structural characteristics and thermal properties to effectively design industrial exploitation processes and operational conditions. In this context, the microcalorimetry appears as a very interesting alternative to accurately determine thermodynamic equilibrium data and other thermal properties, such as enthalpy and heat capacity of hydrates. However, few experimental data obtained by means of microcalorimetry above 20 MPa are found in the literature because of the analysis may be labor-intensive and require specific experimental configuration to work under such conditions.

Considering that the formation of gas hydrates on the ocean floor occurs at pressures much higher than previously studied by microcalorimetry, the main scope of this thesis is to present methodologies based on HP- μ DSC, providing reliable and reproducible experimental thermodynamic data for different hydrate systems up to 100 MPa. The experimental setup has been optimized during the work and new thermodynamic data were obtained at different pressures and gas-phase compositions. The thermodynamic properties studied were the equilibrium temperature (or dissociation point) and dissociation enthalpy of gas hydrates. In this way, this work contributes not only providing experimental data but also studying new hydrate-forming systems that collaborate to scientific interests in developing phase diagrams hereafter and growing the scientific knowledge in this area.

1.5 OUTLINE OF WORK

This thesis is composed of nine chapters written according to the motivation mentioned above. Following this first chapter, which deals with the scientific context

and the main references found in the literature related to this topic, the work is organized as the outline below.

Chapter 2 corresponds to the description of all experimental methods applied and developed during the work, including the preparation and characterization of samples, and the equations applied in modeling thermodynamic properties of gas hydrates.

Chapter 3 presents preliminary studies of gaseous systems by computational simulations. These studies were essential to determine the experimental conditions to be applied thereafter. For instance, it was avoided to work at pressures and compositions that could lead to gas liquefaction when working with gas mixtures. Besides, it was important to perform previous simulations on hydrate equilibrium, both for planning the experiments and for understanding the influence of overall and gas phase compositions on the hydrate dissociation temperature.

Chapter 4 is the first experimental section and contains the data obtained by using High-Pressure Differential Scanning microCalorimetry (HP- μ DSC). Several new thermodynamic data of dissociation are presented for single-guest hydrate-forming systems up to 100 MPa (CH_4 , C_2H_6 and CO_2 hydrates), along with the corresponding predictions from commercial software (Multiflash and CSMGem). Moreover, new data of dissociation enthalpy are presented for single hydrates, obtained by a direct method (integrations from thermograms) and an indirect method (Clapeyron equation).

Chapter 5 is similar to the previous one, presenting new dissociation data for double-guest hydrate-forming systems (CH_4 - C_2H_6 , CH_4 - C_3H_8 and CH_4 - CO_2 hydrates) and comparing them to the predictions. In this case, the dissociation temperature profiles are discussed by taking into account the likely occupancy degree of small and large cavities. The type of structure formed in each case and the possible coexistence of metastable phases are also addressed.

The next chapter (6) contains the results obtained through the isochoric method by using a PVT cell available in the *Phases to Flow Laboratory* at the Colorado School of Mines, in the United States of America. Chapter 7 also presents results from abroad, concerning to structural analysis by Raman spectroscopy carried out in the *Groupe Moléculaire Spectroscopie* at the Université de Bordeaux, France. These complementary studies performed abroad, along with some calorimetric studies, were

very elucidating mainly with respect to CH₄-C₃H₈ hydrates and resulted in a recently published scientific article (MENEZES et al., 2019).

Chapter 8 presents the studies performed by using two ionic liquids and methanol as gas hydrate inhibitors. The inhibitory character of such compounds is discussed by addressing thermodynamic and kinetic terms. A work containing the results presented in this chapter was also recently published in a scientific journal (MENEZES et al., 2020).

Chapter (9) is a summary of the main conclusions of this thesis and presents suggestions for further works. Finally, the last chapter (10) lists the scientific production, including the works presented in scientific events.

REFERENCES

ALADKO, E.Y.; DYADIN, YU.A.; MANAKOV, A.YU.; ZHURKO, F.V.; LARIONOV, E.G. Phase Diagrams of the Ternary Gas Hydrate Forming Systems at High Pressures. Part 1. Propane–Methane–Water System. *Journal of Supramolecular Chemistry*, v. 2, p. 369-376, 2002.

ANDERSON, B. Molecular modeling of clathrate-hydrate via ab initio, cell potential and dynamic methods, PhD Thesis, Massachusetts Institute of Technology, 2005.

ANDERSON, G.K. Enthalpy of dissociation and hydration number of carbon dioxide hydrate from the Clapeyron equation. *The Journal of Chemical Thermodynamics*, v. 35, p. 1171-1183, 2003.

ANDERSON, G.K. Enthalpy of dissociation and hydration number of methane hydrate from the Clapeyron equation. *The Journal of Chemical Thermodynamics*, v. 36, p. 1119, 2004.

ANTUNES, C.M.M.O.; KAKITANI, C.; NETO, M.A.M.; MORALES, R.E.M., SUM, A.K. An Examination of the Prediction of Hydrate Formation Conditions in the Presence of Thermodynamic Inhibitors. *Brazilian Journal of Chemical Engineering*. V. 35, p. 265-274, 2018.

AVLONITIS, D.; VAROTSIS, N. Modelling gas hydrate thermodynamic behavior: theoretical basis and computational methods. *Fluid Phase Equilibria*, v. 123, p. 107-130, 1996.

BAI, D.; ZHANG, D.; ZHANG, X.; CHEN, G. Origin of Self-preservation Effect for Hydrate Decomposition: Coupling of Mass and Heat Transfer Resistances. *Nature: Scientific Reports*, v. 5, p. 1-13, 2015.

BALLARD, A.L.; SLOAN, E.D. Hydrate phase diagrams for methane + ethane + propane mixtures. *Chemical Engineering Science*, v. 56, p. 6883-6895, 2001.

BALLARD, A.L.; SLOAN, E.D. The next generation of hydrate prediction: Part III. Gibbs energy minimization formalism. *Fluid Phase Equilibria*, v. 218, p. 15-31, 2004a.

BALLARD, A.L.; SLOAN, E.D. The next generation of hydrate prediction: an overview. *Journal of Supramolecular Chemistry*, v. 2, p. 385-392, 2002.

BALLARD, A.L.; SLOAN, E.D. The next generation of hydrate prediction IV: A comparison of available hydrate prediction programs. *Fluid Phase Equilibria*, v. 216, p. 257-270, 2004b.

BANDYOPADHYAY, A.A.; KLAUDA, J.B. Gas hydrate structure and pressure predictions based on an updated fugacity-based model with the PSRK equation of state. *Industrial and Engineering Chemistry Research*, v. 50, p. 148-157, 2011.

BISHNOI, P.R.; GUPTA, A.K.; ENGLEZOS, P.; KALOGERAKIS, N. Multiphase equilibrium flash calculations for systems containing gas hydrates. *Fluid Phase Equilibria*, v. 53, p. 97-104, 1989.

BUI, T.; SICARD, F.; MONTEIRO, D.; LAN, Q.; CEGLIO, M.; BURRESS, C.; STRIOLO, A. Antiagglomerants Affect Gas Hydrate Growth. *The Journal of Physical Chemistry Letters*, v. 9, p. 3491-3496, 2018.

CARDOSO, C.A.B.R.; GONÇALVES, M.A.L.; CAMARGO, R. M.T. Design Options for Avoiding Hydrates in Deep Offshore Production. *Journal of Chemical & Engineering Data*, v. 60, p. 330-335, 2015.

CHA, M., HU, Y., SUM, A.K. Methane hydrate phase equilibrium for systems containing NaCl, KCl, and NH₄Cl. *Fluid Phase Equilibria*, v. 413, p. 2-9, 2016.

CHAKOUMAKOS, B.C.; RAWN, C.J.; RONDINONE, A.J.; STERN, L.A.; CIRCONI, S.; KIRBY, S.H.; ISHII, Y.; JONES, C.Y.; TOBY, B.H. Temperature dependence of polyhedral cage volumes in clathrate hydrates. *Canadian Journal of Physics*, v. 81, p. 183-189, 2003.

CHOU, I-M.; SHARMA, A.; BURRUSS, R.C. SHU, J.; MAO, H.; HEMLEY, R.J.; GONCHAROV, A.F.; STERN, L.A.; KIRBY, S.H. Transformations in methane hydrates. *Proceedings of the National Academy of Sciences of the United States of America*, v. 97, p. 13484-13487, 2000.

CHU, C.; LIN, S.; CHEN, Y.; CHEN, P.; CHEN, L. Chain length effect of ionic liquid 1-alkyl-3-methylimidazolium chloride on the phase equilibrium of methane hydrate. *Fluid Phase Equilibria*, v. 413, p. 57-64, 2016.

CHUVILIN, E.; BUKHANOV, B.; DAVLETSHINA, D.; GREBENKIN, S.; ISTOMIN, V. Dissociation and Self-Preservation of Gas Hydrates in Permafrost. *Geosciences*, v. 8, 431, 2018.

DALMAZZONE, C.; DALMAZZONE, D.; HERZHAFT, B. Differential scanning calorimetry: a new technique to characterize hydrate formation in drilling muds. *Society of Petroleum Engineers Journal*, p. 196-202, 2002b.

DALMAZZONE, C.; HERZHAFT, B.; ROUSSEAU, L. Method of analyzing the kinetics of gas hydrate formation in fluids. US Patent 8,038,342 B2, 2011.

DALMAZZONE, D.; KHARRAT, M.; LACHET, V.; FOUCONNIER, B.; CLAUSSE, D. DSC and PVT measurements: Methane and trichlorofluoromethane hydrate dissociation equilibria, *Journal of Thermal Analysis and Calorimetry*, v. 70, p. 493-505, 2002b.

DARABOINA, N.; MALMOS, C.; SOLMS, N. Investigation of kinetic hydrate inhibition using a high-pressure micro differential scanning calorimeter. *Energy Fuels*, v. 27, p. 5779– 5786, 2013.

DARABOINA, N.; RIPMEESTER, J.; WALKER, V. K.; ENGLEZOS, P. Natural gas hydrate formation and decomposition in the presence of kinetic inhibitors. 1. High-pressure calorimetry. *Energy Fuels*, v. 25, p. 4392–4397, 2011.

DELROISSE, H.; PLANTIER, F.; MARLIN, L.; DICHARRY, C.; FROUTÉ, L.; ANDRÉ, R.; TORRÉ, J.P. Determination of thermophysical properties of cyclopentane hydrate using a stirred calorimetric cell. *The Journal of Chemical Thermodynamics*, v. 125, p. 136-141, 2018.

DESMEDT, A.; MARTIN-GONDRE, L.; NGUYEN, T.; PÉTUYA, C.; BARANDIARAN, L.; BABOT, O.; TOUPANCE, T.; GRIM, G.; SUM, A. K. Modifying the Flexibility of Water Cages by Co-Including Acidic Species within Clathrate Hydrate. *The Journal of Physical Chemistry*, v. 119, p. 8904–8911, 2015.

DURHAM, W.B.; STERN, L.A.; KIRBY, S.H. Ductile flow of methane hydrate. *Canadian Journal of Physics*, v. 81, p. 373-380, 2003.

DYADIN, YU.A.; LARIONOV, E. G.; MIRINSKIJ, D. S.; MIKINA, T. V.; ALADKO, E.YA.; STAROSTINA, L. I. Phase diagram of the Xe-H₂O system up to 15 kbar. *Journal of Inclusion Phenomena and Molecular Recognition in Chemistry*, v. 28, 271–285, 1997.

GABITTO, J.F.; TSOURIS, C. Physical Properties of Gas Hydrates: A Review. *Journal of Thermodynamics*, ID 271291, 12 pages, 2010.

GUPTA, A.K., Steady state simulation of chemical processes, Ph.D. Thesis, University of Calgary, Alberta, 1990.

GUPTA, A.; LACHANCE, J.; SLOAN, E. D.; KOH, C. A. Measurements of methane hydrate heat of dissociation using high pressure differential scanning calorimetry. *Chemical Engineering Science*, v. 63, p. 5848-5853, 2008.

HAGHIGHI, H.; CHAPOY, A.; BURGESS, R.; TOHIDI, B. Experimental and thermodynamic modelling of systems containing water and ethylene glycol: application to flow assurance and gas processing. *Fluid Phase Equilibria*, v. 276, p. 24–30, 2009.

HANDA, Y.P. Calorimetric determinations of the compositions, enthalpies of dissociation, and heat capacities in the range 85 to 270 K for clathrate hydrates of xenon and krypton. *The Journal of Chemical Thermodynamics*, v. 18, Pages 891-902, 1986.

HANDA, Y.P.; TSE, J.S.; Thermodynamic properties of empty lattices of structure I and structure II clathrate hydrates. *Journal of Physical Chemistry*, v. 90, p. 5917-5921, 1986.

HIRAI, H.; KONDO, T.; HASEGAWA, M.; YAGI, T.; YAMAMOTO, Y.; KOMAI, T.; NAGASHIMA, K.; SAKASHITA, M.; FUJIHISA, H.; AOKI, K. Methane hydrate behavior under high pressure. *The Journal of Physical Chemistry B*, v.104, p. 1429-1433, 2000.

HU, Y.; LEE, B.R.; SUM, A.K. Phase equilibrium data of methane hydrates in mixed brine solutions. *Journal of Natural Gas Science and Engineering*, v. 46, p. 750-755, 2017b.

HU, Y.; MAKOGON, T.Y.; KARANJKAR, P.; LEE, K.; LEE, B.; SUM, A.K. Gas hydrates phase equilibria and formation from high concentration NaCl brines up to 200 MPa. *Journal of Chemical & Engineering Data*, v. 62, p. 1910–1918, 2017a.

ISTOMIN, V.A.; KVON, V.G.; DUROV, V.A. Metastable states of gas hydrates. "Gas Industry of Russia", v. 4, p. 13-16, 2006.

JAGER, A.; VINS, V.; GERNERT, J.; SPAN, R.; HRUBY, J. Phase equilibria with hydrate formation in H₂O + CO₂ mixtures modeled with reference equations of state. *Fluid Phase Equilibria*, v. 338, p. 100–113, 2013.

JAGER, M.D.; BALLARD, A.L.; SLOAN, E.D. Comparison between experimental data and aqueous-phase fugacity model for hydrate prediction. *Fluid Phase Equilibria*, v. 232, p. 25-36, 2005.

JAGER, M.D.; BALLARD, A.L.; SLOAN, E.D. The next generation of hydrate prediction: II. Dedicated aqueous phase fugacity model for hydrate prediction. *Fluid Phase Equilibria*, v. 211, p. 85-107, 2003.

KELLAND, M.A. History of the development of low dosages hydrate inhibitors. *Energy and Fuels*, v. 20, p. 825-847, 2006.

KLAPPROTH, A.; PILTZ, R.O.; KENNEDY, S.J.; KOZIELSKI, K.A. Kinetics of sII and Mixed sI/sII, Gas Hydrate Growth for a Methane/Propane Mixture Using Neutron Diffraction. *The Journal of Physical Chemistry C*, v. 123, p. 2703-2715, 2019.

KLAUDA, J. B.; SANDLER, S. I. Phase Behavior of Clathrate Hydrates: A Model for Single and Multiple Gas Component Hydrates. *Chemical Engineering Science*, v. 58, p. 27–41, 2003.

KOH, C.A.; WESTACOTT, R.E.; ZHANG, W.; HIRACHAND, K.; CREEK, J.L.; SOPER, A.K. Mechanisms of gas hydrate formation and inhibition. *Fluid Phase Equilibria*, v. 194–197, p. 143-151, 2002.

KVENVOLDEN, K. A.; GINSBURG, G. D.; SOLOVIEV, V. A. Worldwide distribution of subaquatic gas hydrates. *Geo-Marine Letters*, v. 13, p. 32-40, 1993.

LACHANCE, J.W.; SLOAN, E.D.; KOH, C.A. Determining gas hydrate kinetic inhibitor effectiveness using emulsions. *Chemical Engineering Science*, v. 64, p. 180-184, 2009.

LAFOND, P. G.; OLCOTT, K. A.; SLOAN, E. D.; KOH, C. A.; SUM, A. K. Measurements of methane hydrate equilibrium in systems inhibited with NaCl and methanol. *Journal of Chemical Thermodynamics*, v. 48, p. 1–6, 2012.

LARIONOV, E.G.; DYADIN, YU.A.; ZHURKO, F.V.; MANAKOV., A.YU. Phase Diagrams of the Ternary Gas Hydrate Forming Systems at High Pressures. Part II. Ethane–Methane–Water System. *Journal of Inclusion Phenomena and Macrocyclic Chemistry*, v. 56, p. 303–308, 2006.

LEHMKUHLER, F. Formation of clathrate hydrates: an x-ray scattering study. 2010. 147 pages. PhD Dissertation, Technischen Universität Dortmund, Germany, March of 2010.

LI, Z.; YOU, J.; JIA, W.; HE, Y. An improved Parrish-Prausnitz (P-P) model to predict the hydrate formation condition of natural gas with a high volume content of CO₂, *Journal of Natural Gas Science and Engineering*, v. 37, p. 479-486, 2017.

LINJUN, W.; XUEMIN, Z.; HONGHUI, LI.; SHAO, L.; ZHANG, D.; JIAO, L. Theory research on desalination of brackish water using gas hydrate method. *Advanced Materials Research*, v. 616-618, p. 1202-1207, 2013.

LONG, J.P. Gas Hydrate Formation Mechanism and Kinetic Inhibition. PhD Thesis, Colorado School of Mines, 1994.

MAKOGON, Y. F.; GHASSEMI, A. Effects of Self-Preservation of Natural Gas-Hydrates. *American Rock Mechanics Association* 10-291, 2010.

MARINHAS, S.; DELAHAYEA, A.; FOURNAISONA, L.; DALMAZZONE, D.; FURST, W.; PETITET, J.P. Modelling of the available latent heat of a CO₂ hydrate slurry in an

experimental loop applied to secondary refrigeration. *Chemical Engineering and Processing*, v. 45, p. 184–192, 2006.

MARTÍN, A. A Simplified van der Waals-Platteeuw Model of Clathrate Hydrates with Multiple Occupancy of Cavities. *The Journal of Physical Chemistry B*, v. 114, p 9602–9607, 2010.

MCLEOD, H.O.J.; CAMPBELL, J.M. Natural Gas Hydrates at Pressures to 10,000 psia, *Journal of Petroleum Technology*, v. 222, p. 590-594, 1961.

MENEZES, D.E.S.; PESSÔA FILHO, P.A.; ROBUSTILLO, M.D. Use of 1-Butyl-3-methylimidazolium-based ionic liquids as methane hydrate inhibitors at high-pressure conditions. *Chemical Engineering Science*, v. 212, 115323, 2020.

MENEZES, D.E.S.; SUM, A.K.; DESMEDT, A.; PESSÔA FILHO, P.A.; ROBUSTILLO, M.D. Coexistence of sl and sll in methane-propane hydrate former systems at high pressures. *Chemical Engineering Science*, v. 208, 115149, 2019.

MICHEL, J.; OWENS, E.H.; ZENGEL, S.; GRAHAM, A.; NIXON, Z.; ALLARD, T.; HOLTON, W.; REIMER, P.D.; LAMARCHE, A.; WHITE M.; RUTHERFORD, N.; CHILDS, C.; MAUSETH, G.; CHALLENGER, G.; TAYLOR, E. Extent and Degree of Shoreline Oiling: *Deepwater Horizon Oil Spill*, Gulf of Mexico, USA. *Plos One*, v. 8, p. 1-9, 2013.

MOHAMMADI, A.H.; RICHON, D. Phase equilibria of methane hydrates in the presence of methanol and/or ethylene glycol aqueous solutions. *Industrial and Engineering Chemistry Research*, v. 49, p. 925–928, 2010.

MOHAMMAD-TAHERI, M.; MOGHADDAM, A.Z.; NAZARI, K.; ZANJANI, N.G. The role of thermal path on the accuracy of gas hydrate phase equilibrium data using isochoric method, *Fluid Phase Equilibria*, v. 338, p. 257-264, 2013.

MU, L.; SOLMS, N. Hydrate thermal dissociation behavior and dissociation enthalpies in methane-carbon dioxide swapping process. *The Journal of Chemical Thermodynamics*, v. 117, p. 33-42, 2018.

OHNO, H.; SUSILO, R.; GORDIENKO, R.; RIPMEESTER, J.; WALKER, V.K. Interaction of antifreeze proteins with hydrocarbon hydrates. *Chemistry - A European Journal*, v. 16, p. 10409-10417, 2010.

PARLOUËR, P. L.; DALMAZZONE, C.; HERZHAFT, B.; ROUSSEAU, L.; MATHONAT, C. Characterization of gas hydrates formation using a new high-pressure micro-DSC. *Journal of Thermal Analysis and Calorimetry*, v. 78, p. 165–172, 2004.

PARRISH, W.R.; PRAUSNITZ, J.M. Dissociation pressures of gas hydrates formed by gas mixtures. *Industrial Engineering Chemistry Process Design and Development*, v. 11, p. 27-35, 1972.

PARSONAGE, N.G.; STAVELEY, L.A.K. Thermodynamic properties of clathrates: The heat capacity and entropy of argon in the argon quinol clathrate. *Molecular Physics*, v. 2, p. 212-222, 1958.

PARSONAGE, N.G., STAVELEY, L.A.K. Thermodynamic studies of clathrates and inclusion compounds. In *Inclusion Compounds*, Academic Press: London, v. 3, chapter 1, 1984.

PENG, D.Y., ROBINSON, D.B., A new two-constant equation of state, *Industrial and Engineering Chemistry: Fundamentals*, v. 15, p. 59–64, 1976.

PETUYA, C.; DAMAY, F.; TALAGA, D.; DESMEDT, A. Guest Partitioning in Carbon Monoxide Hydrate by Raman Spectroscopy. *The Journal of Physical Chemistry*, v. 121, p. 13798–13802, 2017.

REDDY, C.M.; AREY, J.S.; SEEWALD, J.S.; SYLVA, S.P.; LEMKAU, K.L.; NELSON, R.K.; CARMICHAEL, C.A.; MCINTYRE, C.P.; FENWICK, J.; VENTURA, G.T.; VAN MOOY, B.A.S.; CAMILLI, R. Composition and fate of gas and oil released to the water column during the *Deepwater Horizon* oil spill. *Proceedings of the National Academy of Sciences*, v. 109, p. 20229-20234, 2012.

SABIL, K.M.; NASHED, O.; LAL, B.; ISMAIL, L.; JAPPER-JAAFAR, A. Experimental investigation on the dissociation conditions of methane hydrate in the presence of imidazolium-based ionic liquids. *The Journal of Chemical Thermodynamics*, v. 84, p.7-13, 2015.

SAITO, S.; MARSHALL, D.R.; KOBAYASHI, R. Hydrates at High Pressures. *American Institute of Chemical Engineers*, v. 10, p. 734, 1964.

SAMI, N.A.; SANGWAI, J.S.; SUBRAMANIAN, B. Gas hydrate Applications and problems in Oil and Gas Industry. *International Journal of Scientific & Engineering Research*, v. 4, 2013.

SAW, V.K.; AHMAD, I.; MANDAL, A.; UDAYABHANU, G.; LAIK, S. Methane hydrate formation and dissociation in synthetic seawater. *Journal of Natural Gas Chemistry*, v. 21, p. 625-632, 2012.

SHIN, W.; PARK, S.; RO, H.; KOH, D.Y.; SEOL, J.; LEE, H. Spectroscopic confirmation of metastable structure formation occurring in natural gas hydrates. *Chemistry – An Asian Journal*, v. 7, p. 2235-2238, 2012.

SLOAN, E.D.; FLEYFELB, F. Hydrate dissociation enthalpy and guest size. *Fluid Phase Equilibria*, v. 76, p. 123-140, 1992.

SLOAN, E.D.; KOH, C.A. *Clathrate hydrates of natural gases*, 3rd ed. Boca Raton: CRC Press, 2008.

SLOAN, E.D.; KOH, C.A.; SUM, A.K. Gas hydrate stability and sampling: the future as related to the phase diagram. *Energies*, v. 3, p. 1991-2000, 2010.

SLOAN, E.D.; KOH, C.A.; SUM, A.K. Natural Gas Hydrates in Flow Assurance. Gulf Professional Publishing (Elsevier), Oxford, U.K., 2010.

SLOAN, E.D.; KOH, C.A.; SUM, A.K.; BALLARD, A.L.; SHOUP, G.J.; MCMULLEN, N.; CREEK, J.L.; PALERMO, T. Hydrates: State of the Art Inside and Outside Flowlines. *Journal of Petroleum Technology*, v. 61. 89-94, 2009.

STERN, L.A.; KIRBY, S.H.; DURHAM, W.B.; CIRCONE, S.; WAITE, W.F. Laboratory synthesis of pure methane hydrate suitable for measurement of physical properties and decomposition behavior. Natural Gas Hydrate, in Oceanic and Permafrost Environments. M.D. Max, Ed. Kluwer Publ., chapter 25, p. 323-348, 2000.

SUM, A.; WU, D.; YASUOKA, K. Energy science of clathrate hydrates: Simulation-based advances. *Material Research Society Bulletin*, v. 36 (3), p. 205-210, 2011.

TAN, L.S.; LAU, K.K.; BUSTAM, M.A.; SHARIFF, A.M. Removal of high concentration CO₂ from natural gas at elevated pressures via absorption process in packed column. *Journal of Natural Gas Chemistry*, v. 21, p. 7-10, 2012.

TARIQ, M.; ROONEY, D.; OTHMAN, E.; APARICIO, S.; ATILHAN, M.; KHRAISHEH, M. Gas Hydrate Inhibition: A Review of the Role of Ionic Liquids. *Industrial and Engineering Chemistry Research*, v. 53, p. 17855-17868, 2014.

THAKORE, J. L.; HOLDER, G. D. Solid vapor azeotropes in hydrate forming systems. *Industrial and Engineering Chemistry Research*, v. 26, p.462-469, 1987.

TSUDA, T.; OGATA, K.; HASHIMOTO, S.; SUGAHARA, T.; SATO, H.; OHGAKI, K. Storage capacity of hydrogen in gas hydrates. *Journal of Physics: Conference Series* 215, 012061, 2010.

VAN DER WAALS, J.H.; PLATTEEUW, J.C. Clathrate solutions. *Advances in Chemical Physics*, v. 2, p. 1-55, 1959.

VERMA, V.K. Gas Hydrates from Liquid Hydrocarbon-Water Systems. Ph.D. Dissertation, University of Michigan: Ann Arbor, MI, 1974.

VINS, V.; JAGER, A.; SPAN, R.; HRUBY, J. Model for gas hydrates applied to CCS Systems Part I. Parameter study of the van der Waals and Platteeuw model. *Fluid Phase Equilibria*, v. 427, p. 268-281, 2016.

XU, C.G.; ZHANGA, S.H.; CAI, J.; CHENA, Z.Y.; LI, X.S. CO₂ (carbon dioxide) separation from CO₂ e H₂ (hydrogen) gas mixtures by gas hydrates in TBAB (tetra-n-butyl ammonium bromide) solution and Raman spectroscopic analysis. *Energy*, v. 59, p. 719-725, 2013.

WARD, Z.T.; MARRIOTT, R.A.; SUM, A.K.; SLOAN, E.D.; KOH, C.A. Equilibrium Data of Gas Hydrates containing Methane, Propane, and Hydrogen Sulfide. *Journal of Chemical & Engineering*, v.60, p.424-428, 2015.

YOON, J.H.; YAMAMOTO, Y.; KOMAI, T.; HANEDA, H. Rigorous Approach to the Prediction of the Heat of Dissociation of Gas Hydrates. *Industrial & Engineering Chemistry Research*, v. 42., p. 1111–1114, 2003.

ZHDANOV, R.K.; GETS, K.V.; BELOSLUDOV, R.V.; SUBBOTIN, O.S.; BOZHKO, Y.Y.; BELOSLUDOV, V.R. Theoretical modeling of the thermodynamic properties and the phase diagram of binary gas hydrates of argon and hydrogen. *Fluid Phase Equilibria*, v. 434, p. 87-92, 2017.

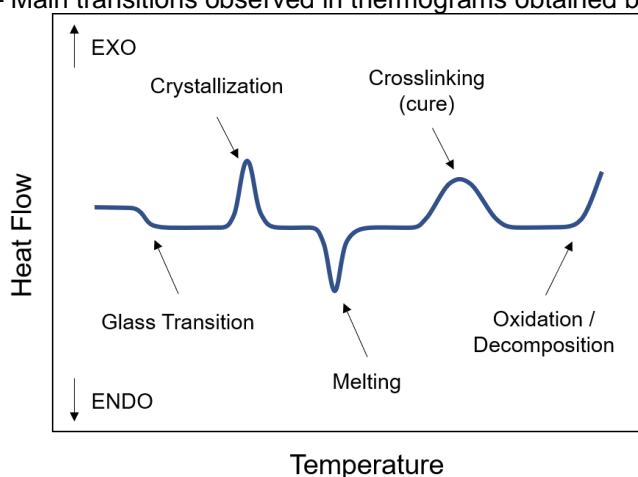
CHAPTER 2

MATERIALS AND METHODS

2.1 HIGH PRESSURE DIFFERENTIAL SCANNING CALORIMETRY: HP- μ DSC

Differential Scanning Calorimetry (DSC) is a thermal analytical technique applied to characterize the physical and chemical properties of a wide range of materials as a function of temperature. There are different types of differential scanning calorimeters according to the principle that is used to detect and transduce electric signals (KODRE et al., 2014). In the instrument used in this work (HP- μ DSC7 Evo - Setaram), the heat flow is detected by two plane flowmeters that surround each cell and generate a proportional electrical signal for each of them (SETARAM, 2016). In this way, it is possible to quantify the difference between the heat flow in the cell containing the sample and the reference cell, usually kept empty. Eventual energetic transitions occurring in the sample lead to a difference in the heats that flow through the sample and the reference cells. For this reason, thermal events occurring in the sample can be accurately detected through this technique due to the heat flow discrepancy between the two flowmeters. Common interferences in both cells are eliminated by subtracting the reference heat flow signal from the sample one.

The signal concerning the heat flow difference is plotted versus the temperature or time in graphs, usually known as thermograms, as illustrated in Figure 2.1. The thermal phenomena observed in thermograms are used to characterize the sample and can be classified as first or second-order transitions. Events that present enthalpy changes (endothermic or exothermic) are known as first-order transitions and give rise to the appearance of peaks in thermograms. Some endothermic events are melting, sublimation and desolvation, while the crystallization and decomposition are examples of exothermic phenomena. Solid-solid transitions and chemical reactions may also promote first order events. On the other hand, second-order events present heat capacity changes, although the enthalpy does not vary. Instead of peaks, these events are observed in thermograms as a displacement of the baseline and may be detected during a material glass transition or relaxation of polymeric chains processes, for instance.

Figure 2.1 – Main transitions observed in thermograms obtained by HP- μ DSC.

2.1.1 Gas Hydrate-Forming Species

Milli-Q water was used to prepare all samples for microcalorimetric analyses in this work. Some properties of the gases employed to form gas hydrates are given in Table 2.1, according to the data provided by the National Institute of Standards and Technology (NIST). Other substances used in this work are detailed in subsections related to specific materials and methods presented in the results section, according to the respective chapter.

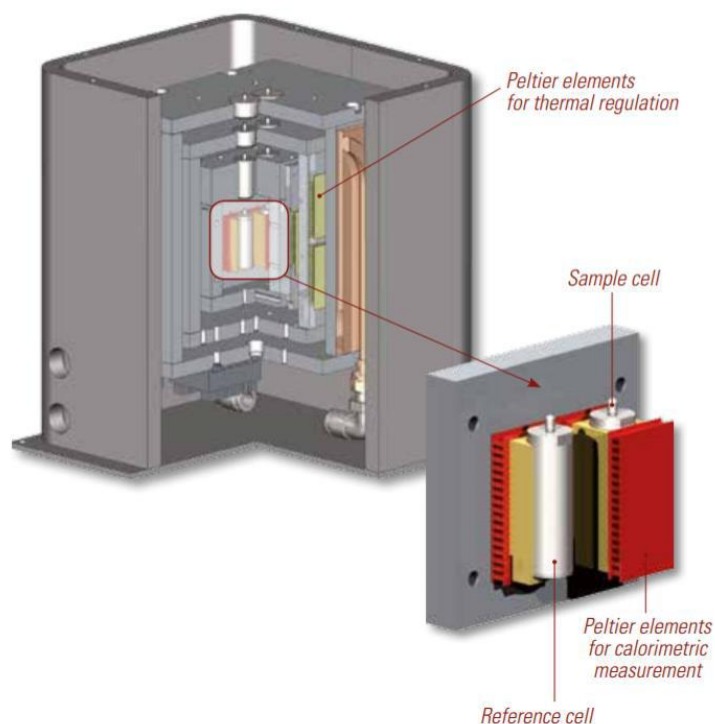
Table 2.1 – Properties of gases used in microcalorimetric analyses.

Properties (Supplier)	Methane (White Martins)	Ethane (Linde)	Propane (Gama)	Carbon Dioxide (Gama)
Purity (%)	99.5	99.95	99.5	99.99
T Melting (K)	90.5	101.0	85.4	216.6
T Boiling (K)	111.0	184.6	231.1	194.7
T Critical Point (K)	190.6	305.3	369.9	304.2
P Critical Point (MPa)	4.6	4.9	4.3	7.4

Source: NIST Chemistry WebBook (except purity).

2.1.2 Experimental Configuration

The main experimental configuration used in this work for studying gas hydrates consists of a high-pressure microcalorimeter (HP- μ DSC7 Evo - Setaram) equipped with a calorimetric transducer and a Calvet three-dimensional sensor for accurate and precise measurements. The main elements constituting the calorimetric transducer are shown in Figure 2.2.

Figure 2.2 – Calorimetric transducer of μ DSC7 Evo apparatus.

Source: Setaram (2016).

Basically, a calorimetric block holds the sample and the reference cells, and it is allocated inside three concentric chambers. The cells are surrounded by high-sensitivity Peltier elements that work in this case as heat flow detectors and as good thermal conductors, maintaining the same temperature in the cells and in the calorimetric block. Two other Peltier coolers constitute the external chambers for temperature regulation throughout the calorimetric transducer. This double-stage temperature control allows to work at temperatures from 228 K (aided by a cooler, Julabo F32) up to 393 K (LIN; KEDZIERSKI, 2018; SETARAM, 2016).

Two cylindrical containers made of an alloy of iron, nickel and chrome (known as Incoloy, or 1.4980, A-286) are employed as ‘sample’ and ‘reference’ high-pressure cells, that are placed inside the calorimetric transducer before the analysis. The reference cell was kept depressurized and empty in all the experiments performed in this work. Polymeric elements, shown in Figure 2.3, are used to seal the system and avoid any gas or liquid leakage. This configuration and combination of materials make the cells capable of withstanding pressures up to 100 MPa.

Figure 2.3 – High-pressure cells used in microcalorimetric experiments.

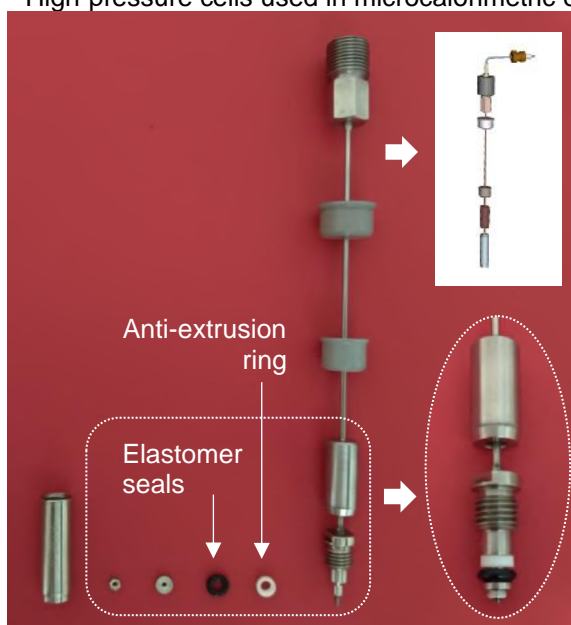
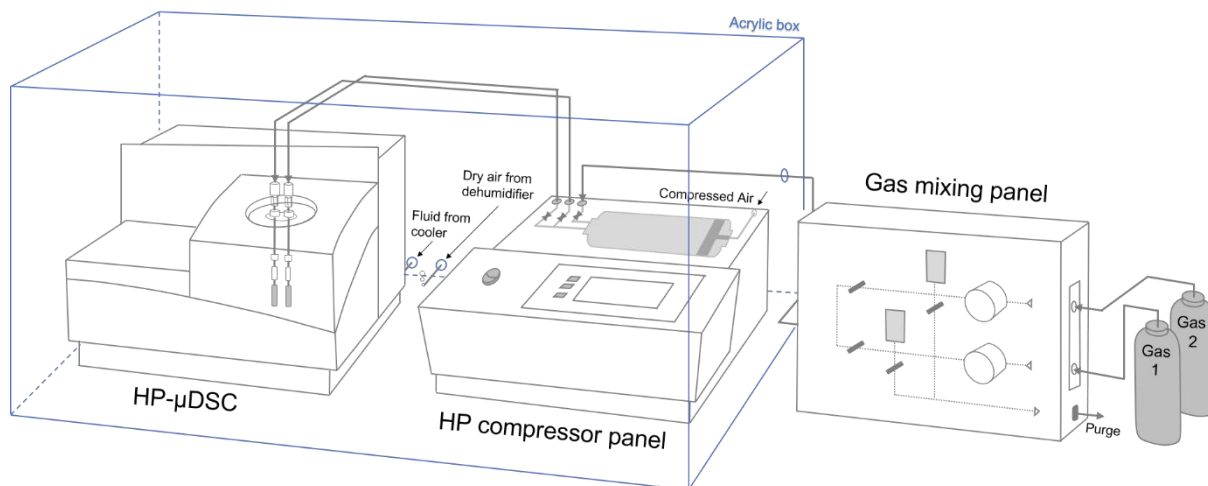


Figure 2.4 shows the instruments employed during the microcalorimetric analyses. A gas mixing panel (20 MPa, Gas Panel 2723 Top Industrie) and a high-pressure compressor (100 MPa, PMHP 1000 Setaram-V2) were coupled to the microcalorimeter to obtain gaseous binary mixtures of a desired composition and to work at constant volume or pressure modes, respectively. A maximum operation pressure of 100 MPa can be reached with an accuracy of 0.2 MPa. Before the pressurization, the gas is injected at low pressure (~ 0.5 MPa) from the mixing panel to the compressor chamber, and then the system is purged, including the sample cell. The procedure is repeated by at least three times in order to minimize the air in the system. In case of gaseous mixtures preparation, the gas with the lowest partial pressure in the mixture is injected first into the compressor chamber. Then, the second gas is injected, and the mixture is subjected to a couple of pressurization and depressurization cycles for homogenization before allowing the gas mixture to fill the cells inside the microcalorimeter.

Although nitrogen flows to the internal regions of the microcalorimeter during the analysis to protect the calorimetric transducer, water condensation over the DSC components must be avoided, mainly on the surface of the circuit boards near the cold tubes coming from the FP32 Julabo cooler. For this reason, the equipment was placed inside an acrylic box with a constant dry airflow coming from a dehumidifier (Cool 20 Dryer CHICAGO PNEUMATIC).

Figure 2.4 – Experimental setup employed for gas hydrates studies based on high-pressure microcalorimetry.



2.1.3 Calibration of the Experimental Apparatus

The microcalorimeter is calibrated from the factory with naphthalene (Setaram standard, purity $\geq 99.97\%$) by performing a Joule effect calibration. An annual procedure is performed by using hermetically sealed standard cells in order to verify the instrument calibration, as recommended by the manufacturer. Table 2.2 shows the reference substances used to check temperature and heat calibration and the comparison between the literature data and the experimental onset values obtained in this work through the software Calisto, provided by Setaram.

Table 2.2 – Assessment of the instrument calibration (temperature and enthalpy) considering reference substances.

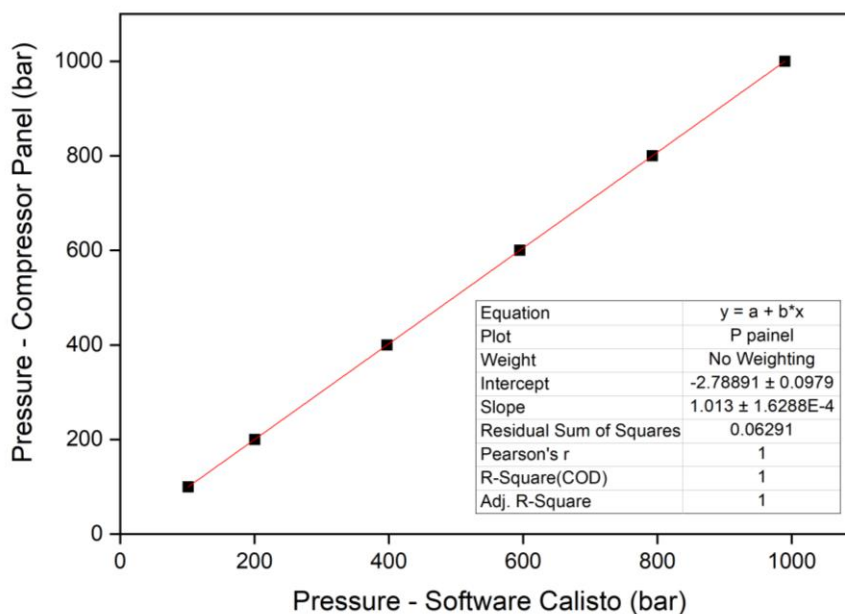
Substance	Purity (wt.%)	Rate (K·min ⁻¹)	T _{DSC} (K)	ΔH _{DSC} (J/g)	T _{Literature} (K)	ΔH _{Literature} (J/g)	ΔT (K)	Enthalpy relative error (%)
Decane	99.8	1	242.81	201.53			0.74	0.14
		0.5	243.19	201.33	243.55 ^a	201.81 ^a	0.36	0.24
		0.2	243.41	200.8			0.14	0.5
Cyclohexane	99.9	1	279.21	31.63			0.6	-0.41
		0.5	279.57	31.46	279.81 ^b	31.5 ^b	0.24	0.13
		0.2	279.76	31.18			0.05	1.01
Naphthalene	99.97	1	353.06	148.55			0.29	0.1
		0.5	353.3	148.75	353.35 ^b	148.7 ^b	0.05	-0.04
		0.2	353.43	147.15			-0.07	1.04

^a Rowley et al. (2003) ; ^b Sabbah et al. (1999).

The maximum temperature and enthalpy deviations from the literature data were 0.74 K at low temperatures (243.55 K) for a heating rate of 1 K·min⁻¹ and 1.5 J/g (1.04 %) at high temperatures (353.35 K) when using a heating rate of 0.2 K·min⁻¹, respectively. Thus, the factory-made calibration has been considered satisfactory.

As will be addressed in detail in section 2.1.4.6, isochoric method was used to study ternary systems by applying both the traditional PVT cell and the high pressure microcalorimeter, in order to compare and evaluate the reliability of both methods. In this case, a pressure variation occurs inside the cell during the experiments, mainly above 20 MPa. Thus, the dissociation pressure taken from microcalorimetric measurements was that belonging to the onset point of the hydrate dissociation curves obtained from thermograms according to the value recorded by the Calisto software, because the pressure displayed on the compressor panel is not recorded throughout the analysis. However, it was observed a discrepancy between the pressure provided by the software Calisto and the one displayed on the compressor panel since the pressure recorded by the software comes from an electrical signal and is not calibrated from the factory. For this reason, it was necessary to correct this dissociation pressure through a linear equation. The equation used in these cases is shown in Figure 2.5 and it is based on 59 experimental data, including binary and ternary systems from 10 to 100 MPa – equivalent to 100 and 1000 bar, according to the unit used by the software and the compressor panel.

Figure 2.5 – Calibration of pressure for isochoric experiments by HP- μ DSC.



2.1.4 Methods for Determining Thermodynamic Properties:

2.1.4.1 Dissociation Temperature: Onset, Peak and Endset Points

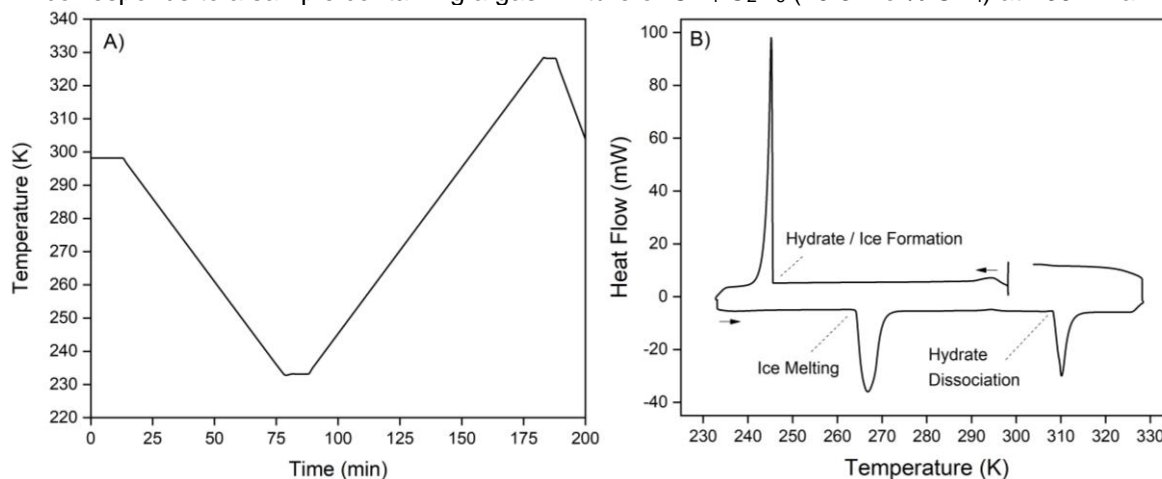
The experimental methodologies used in this work were adjusted according to the sample and the property to be studied. In general, the thermal sequence employed to determine the hydrate dissociation temperatures comprises the following steps:

- I – Stabilization of the system at 293 K during 10 min;
- II – Gas injection and compression of the system up to the setpoint pressure, followed by a 10 min isotherm for stabilization;
- III – Cooling the furnace down to 233 K at $1 \text{ K}\cdot\text{min}^{-1}$, followed by a 10 min isotherm;
- IV – Heating up to 353 K at $1 \text{ K}\cdot\text{min}^{-1}$, followed by a 10 min isotherm;
- V – Cooling the system back to 293 K.

Considering the absence of mixing inside the cell, the gas hydrate nucleation and crystal growth are limited by a mass transfer phenomenon. In order to favor hydrate formation in this condition, it is necessary a high cooling degree (DARABOINA et al., 2013), which is defined in this work as the difference between the hydrate equilibrium temperature obtained during heating and the minimum temperature reached when cooling the system. Therefore, the cooling zone was extended down to 233 K to guarantee the hydrate formation.

Figure 2.6 presents the usual thermal procedure (A), also known as temperature profile, and a typical thermogram (B) used in experiments based on differential scanning calorimetry. The thermogram indicates the thermal transitions usually obtained during cooling and heating processes. The heat flow in the vertical axis of figure B represents the difference of heat between the sample and the reference cells.

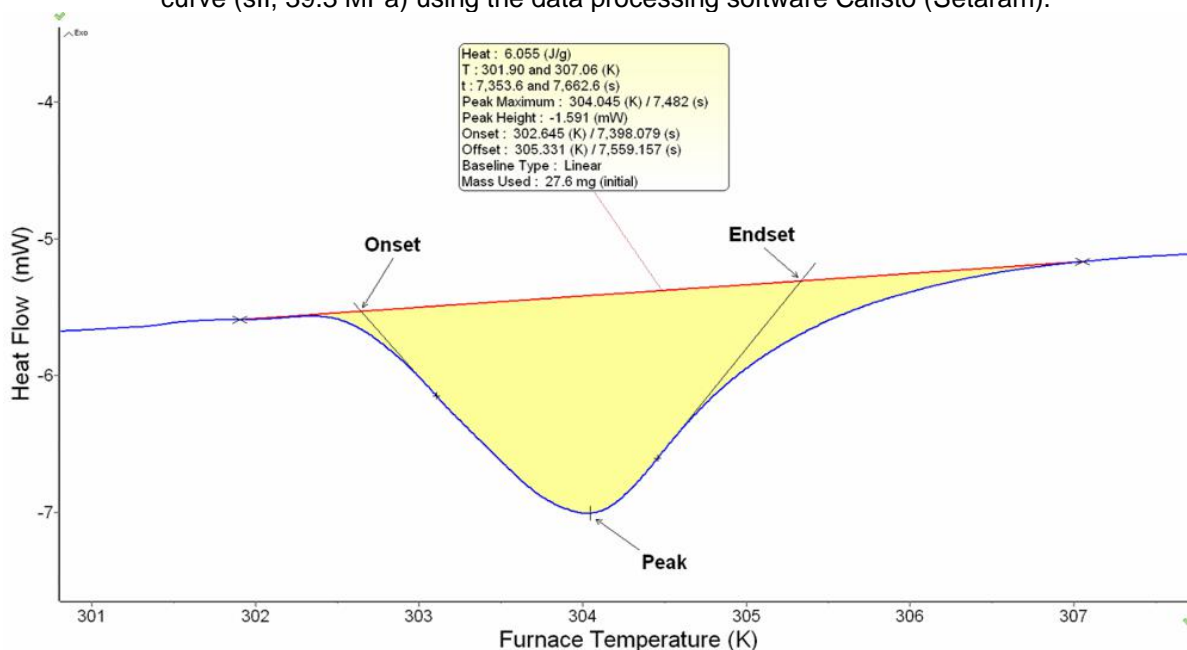
Figure 2.6 – Methodology applied to microcalorimetric analyses: A) Temperature profile throughout the analysis; B) Thermogram indicating usual transitions occurring during the analysis. The thermogram corresponds to a sample containing a gas mixture of CH₄-C₂H₆ (49.3 mol% CH₄) at 100 MPa.



Source: Adapted from Menezes et al. (2020).

The hydrate dissociation curves obtained by HP- μ DSC were characterized by the onset, peak and endset points provided by the Calisto software (the data processing program provided by Setaram), as illustrated in Figure 2.7.

Figure 2.7. Determination of onset, peak and endset values for the CH₄-C₃H₈ hydrate dissociation curve (sII, 39.3 MPa) using the data processing software Calisto (Setaram).



The so-called onset temperature is determined by the intersection between the baseline and the tangent line to the dissociation curve at the maximum slope point. It is widely used for estimating equilibrium points, since it represents the beginning of the thermal event and it should not be influenced by the heating rate or sample mass

(SAEED et al., 2016). However, determining onset values can be a difficult task and imprecise when there are very close or overlapped transitions caused by kinetic effects, irregularities in the crystal lattice (different cages occupancy degrees throughout the structure or empty cavities, in the case of hydrates), polymorphism or even external noises. The peak temperature, in turn, may be considered as an estimate when curves overlap or the onset is not well-defined, although it does not strictly represent an equilibrium point (MENEZES et al., 2019). Despite this method was chosen in this work because it is simple and provides good results, alternative methods are also found in the literature for accurate equilibrium properties measurements, developed specifically for non-constant temperature transitions such as hydrate melting (LIN et al., 2013; LIN et al., 2014).

2.1.4.2 *Enthalpy of Dissociation: Integration of Peaks*

The thermodynamic properties of hydrates, such as dissociation enthalpy and specific heat, are fundamental for determining the operating conditions during gas exploitation processes and predicting the production rate from hydrate reservoirs. For this purpose, heat must be provided to raise the temperature of the reservoir and induce the hydrate dissociation, which makes crucial the determination of hydrate thermal properties. These properties can be found in the literature only for specific systems, most based on simulations studies. There are few experimental data available due to instrumental limitations, especially under extreme pressure and temperature conditions. With the advent of high-pressure differential scanning calorimetry, it has been possible to obtain such properties from an indirect method by integrating thermogram peaks, which allows estimating the enthalpy of the hydrate during the transition.

The methodology applied in this work is similar to the one described by Gupta et al. (2008), extended in this case to higher pressures (up to 100 MPa). Considering Figure 2.6B, the analytical integration of the second peak (heating) provides the total heat absorbed during the hydrate dissociation phenomenon (\dot{Q} , $mW \cdot K$). Thus, the hydrate enthalpy of dissociation per mol of gas (ΔH_{diss} , $J \cdot mol^{-1}$) can be obtained according to equation 2.1, where \emptyset means the heating rate ($K \cdot min^{-1}$).

$$\Delta H_{diss} = \frac{\dot{Q}_{hydrate\ dissociation}}{n_{gas} \cdot \phi} \quad (2.1)$$

The main difficulty in determining the hydrate enthalpy is the estimation of the hydrate amount since it requires the amount of ice in the system and to assume a hydration number in order to establish the stoichiometry of the hydrate formation reaction. A considerable fraction of liquid water forms ice during the crystallization, and the remaining fraction forms hydrate. This effect is mainly due to the absence of mixing in the system, in addition to the subcooling below 273 K, required to induce hydrate formation. The first crystalline structure formed can be ice or hydrate, depending on the pressure of the system (DAVIES et al., 2009). In any case, it is necessary to calculate the amount of water that was not converted to hydrate by integrating the ice melting peak (equation 2.2). The theoretical heat of ice melting applied in the following equation was extrapolated from data found in the literature (BRIDGMAN, 1912; DENYS et al., 2001; FUKUSAKO et al., 1990; KARINO et al., 1994;).

$$n_{H_2O (ice)} = \frac{\dot{Q}_{Ice\ melting}}{\Delta H_{Ice\ melting (theoretical)} \cdot \phi} \quad (2.2)$$

The amount of water in the form of a hydrate, $n_{H_2O (hydrate)}$, can be obtained by the equation below since the total amount of water initially added in the cell is known:

$$n_{H_2O (hydrate)} = n_{H_2O (total)} - n_{H_2O (ice)} \quad (2.3)$$

Considering the methane hydrate, for instance, the reaction of formation is given according to the stoichiometry below, in which (n) is the hydration number:

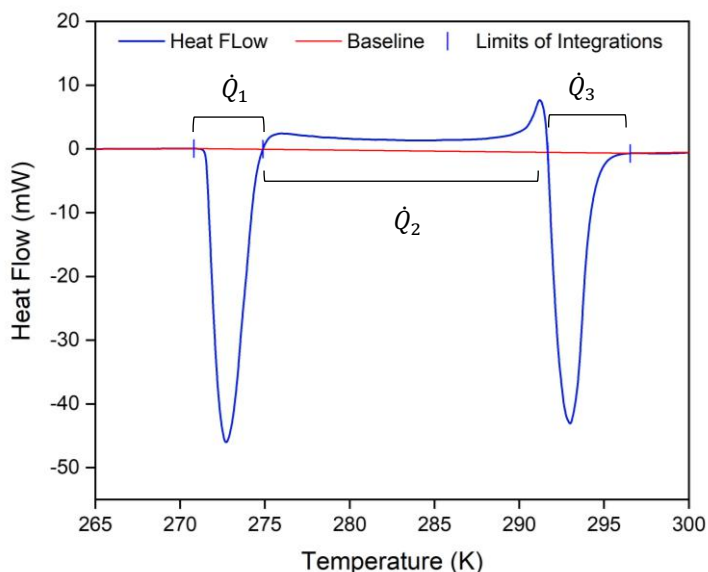


Estimations of the hydration number for different hydrates can be found in the literature (SLOAN; KOH, 2008; SUM, 1997). For methane hydrate, the value for n is usually close to 6 (CIRCONE et al., 2006; HANDA, 1986). However, the hydration number can vary significantly according to the pressure. For this reason, the values for

n used in integrations for enthalpy calculations were estimated according to two methods described in section 2.1.4.4.

Considering the amount of water in the form of hydrate (eq. 2.3) and the stoichiometric ratio (eq. 2.4), it is possible to estimate the amount of gas incorporated in the hydrate (n_{gas}). However, additional consideration is needed when determining the hydrate enthalpy: there may be the arrangement of the crystalline structure during the ice melting, leading to the recrystallization in the form of hydrate (GUPTA, 2007). This phenomenon likely is favored by the absence of mixing inside the HP- μ DSC cells and generates an exothermic band (\dot{Q}_2) between the ice melting and the hydrate dissociation (\dot{Q}_1 and \dot{Q}_3 , respectively), as shown in Figure 2.8.

Figure 2.8 – Establishment of baseline for calculating enthalpy of hydrate dissociation.



Therefore, the heat of dissociation to be considered in equation 2.1 should be concerned with the hydrate formed only during the cooling process. Thus, the heat delivered during the recrystallization (\dot{Q}_2) should be subtracted from the total heat absorbed during the hydrate dissociation (\dot{Q}_3). For this, a baseline is established along the heating process, as indicated in red in the thermogram of Figure 2.8, and it is considered that the energy above this line corresponds to the recrystallization phenomenon (\dot{Q}_2).

Ergo, the heat of dissociation is finally calculated according to equation 2.5, considering that the difference between (\dot{Q}_3) and (\dot{Q}_2) represents the hydrate formed during the cooling process.

$$\Delta H_{hydrate} = \frac{\dot{Q}_3 - \dot{Q}_2}{n_{gas} \cdot \phi} \quad (2.5)$$

Nevertheless, more accurate results for hydrate dissociation enthalpies are obtained by applying a multicycles method in order to convert most of ice to hydrate. In these cases, the recrystallization phenomenon mentioned above is not observed since most of the ice is converted to hydrate during consecutive cycles.

2.1.4.3 Dissociation Enthalpy: Equation of Clapeyron

The enthalpy values obtained from integrations of DSC-thermogram peaks are also compared in this work with enthalpies calculated by using the Clapeyron equation (2.6), often used in the literature for gas hydrate enthalpy estimation. The method developed in this work is similar, but not strictly the same, to the one reported by Anderson (2003, 2004), who calculated enthalpies of dissociation for carbon dioxide hydrates (ANDERSON, 2003) and methane hydrates (ANDERSON, 2004) based on the Clapeyron equation. In this work, enthalpies of dissociation for methane, ethane and carbon dioxide single hydrates were determined, and the improvements from Anderson's method are pointed out along the description of equations below.

$$\frac{dP}{dT} = \frac{\Delta H}{T\Delta V} \quad (2.6)$$

Firstly, the experimental data (temperature (T, K) and pressure (P, MPa)) were fitted to convenient equations for each system, as presented in the Appendix. Then, the respective equation was derived to obtain the factor dP/dT . The volume change, ΔV ($m^3 \cdot mol^{-1}$) is the sum of the partial molar volumes regarding the three phases involved in the dissociation reaction: hydrocarbon or CO_2 (V_{HC} or V_{CO_2} ; vapor or liquid), water (V_{H_2O} ; ice or liquid) and hydrate (V_{hyd} ; solid). The hydration number (n) was determined by two different methods, described in section 2.1.4.4.

$$\Delta V = \left(1 - \frac{n \cdot x_{HC}}{1 - x_{HC}}\right) \cdot V_{HC} + n \cdot \left(V_{H_2O} + \left(\frac{x_{HC}}{1 - x_{HC}}\right) \cdot V_{HC, H_2O}^{\infty}\right) - V_{hyd} \quad (2.7)$$

V_{HC} and V_{H_2O} were obtained from NIST Webbook database. The equations of state employed for methane, ethane, carbon dioxide and water were reported by Setzmann and Wagner (1991), Friend et al. (1991), Span and Wagner (1996) and Wagner and Pruss (2002), respectively. The volumes of the methane and ethane in water at “infinite dilution” (V_{HC,H_2O}^∞) were calculated according to temperature-dependent equations reported by Rettich et al. (1981). For carbon dioxide, the value used was reported by Anderson (2002). The equation above also considers the solubility of the hydrocarbon in water (x_{HC}). For methane and ethane, it was determined through the Krichevsky-Kasarnovsky equation (1935), usually employed for vapor-liquid solutions at high pressures:

$$\ln\left(\frac{f}{x_{HC}}\right) = \ln K_H + \frac{V_{HC,H_2O}^\infty(P - P^S)}{RT} \quad (2.8)$$

The fugacity (f) was calculated from thermodynamic data (enthalpy and entropy) available in NIST Webbook (<http://webbook.nist.gov>). Equations for determining the natural logarithm of Henry’s law constant (K_H) for both CH₄ and C₂H₆ are also reported by Rittich et al. (1981). Finally, P is the pressure of the system and P^S is the vapor pressure of water at the respective temperature, that can be calculate from Antoine’s equation or derivatives (ANTOINE, 1888). The solubility of carbon dioxide in water, in turn, was calculated by correlations from Diamond and Akinfiev (2003) throughout the hydrate equilibrium line above the upper quadruple point (Q_2), corresponding to the region addressed in this work.

The volume of hydrate containing one mole of hydrocarbon or CO₂ required by equation. 2.7, was calculated according to the equation below, (ANDERSON, 2004):

$$V_{hyd}(T, P) / (m^3 \cdot mol^{-1}) = \frac{6.0221 \cdot 10^{23} \cdot V_{uc} \cdot n}{46} \quad (2.9)$$

At this point, one could note the first improvement with respect to the works published by Anderson (2003, 2004). The author considers V_{hyd} of CO₂ hydrates is invariant with the temperature and pressure, since the data are relatively close to the lower quadruple point (Q_1). For CH₄ hydrate, changes in the hydrate volume are considered, but the isobaric expansivity and isothermal compressibility effects on the

hydrate lattice are both constant for all temperature and pressure points. In fact, the thermal expansion coefficient applied for methane hydrates (ANDERSON, 2004) refers to CO₂ hydrate.

The molar volume of the hydrate unit cell (V_{uc}) comes from the partial derivatives of the volume change at constant pressure and temperature:

$$dV_{uc} = \left(\frac{\partial V_{uc}}{\partial T} \right)_P \cdot dT + \left(\frac{\partial V_{uc}}{\partial P} \right)_T \cdot dP \quad (2.10)$$

These derivatives can be written in terms of volumetric coefficients of isobaric thermal expansivity ($\beta_{(v)}$) and isothermal compressibility ($\kappa_{T(v)}$) (BALLARD, 2001):

$$dV_{uc} = \beta_{(v)} \cdot V_{uc} \cdot dT - \kappa_{T(v)} \cdot V_{uc} \cdot dP \quad (2.11)$$

In this work, the linear or volumetric thermal expansion of the unit cell (β_l and β_v , respectively) were considered to vary with the temperature according to the equation below (HESTER et al., 2007):

$$\beta_{(l)} = \frac{1}{a_{uc}} \left(\frac{\partial a_{uc}}{\partial T} \right)_P = \alpha_{l1} + \alpha_{l2} \cdot (T - T_0) + \alpha_{l3} \cdot (T - T_0)^2 \quad (2.12)$$

$$\beta_{(v)} = \frac{1}{V_{uc}} \left(\frac{\partial V_{uc}}{\partial T} \right)_P = \alpha_{v1} + \alpha_{v2} \cdot (T - T_0) + \alpha_{v3} \cdot (T - T_0)^2 \quad (2.13)$$

Equation 2.12 was useful to obtain eq. 2.13, since only linear lattice parameters (a_{uc}) are reported at several temperatures in the literature, cited in the Appendix. The reported data were used to calculate the linear thermal expansion coefficients ($\alpha_{l1}, \alpha_{l2}, \alpha_{l3}$) by extrapolation. Then, by integrating both equations above we find that the linear coefficients from eq. 2.12 are the third part of the volumetric ones ($\alpha_{v1}, \alpha_{v2}, \alpha_{v3}$) since the latter equation is obtained by cubing the first (BALLARD, 2001).

Ergo, the inclusion of equation 2.13 in equation 2.10, followed by integration, gives the equation 2.14, used to calculate the volume of hydrate unit cell.

$$V_{uc}(T, P, x) = V_{uc_0} \cdot \exp \left[\begin{aligned} &\alpha_{v1} \cdot (T - T_0) + \frac{\alpha_{v2}}{2} \cdot (T - T_0)^2 + \frac{\alpha_{v3}}{3} \cdot (T - T_0)^3 \\ &- \kappa_{T(v)} \cdot (P - P_0) \end{aligned} \right] \quad (2.14)$$

One should note that the compressibility coefficient ($\kappa_{T(v)}$) is considered invariant with the pressure in this work, and the value used for each hydrate studied was taken as reported by Ballard (2001). More details about the references used (a_0, T_0) and the coefficients (α_v) found for eq. 2.13 are available in the Appendix.

Finally, another factor summed to the hydrate enthalpy calculated by the Clapeyron equation was the enthalpy of solution of the hydrocarbon or CO₂ in water, considered to be equivalent to the enthalpy of solution at infinite dilution ($\Delta H_{HC,H_2O}^\infty$), as proposed by Anderson (2004). Equation 2.15 was used to calculate the enthalpy of solution for methane-water and ethane-water systems.

$$\Delta H_{HC,H_2O}^\infty = R \cdot \frac{d \ln(K_H)}{d\left(\frac{1}{T}\right)} - V_{HC,H_2O}^\infty \cdot (p - p^s) \quad (2.15)$$

For carbon dioxide in water, Anderson (2002) has estimated the enthalpy of solution at infinite dilution according to the equation:

$$\Delta H_{CO_2,H_2O}^\infty / (J \cdot mol^{-1}) = \frac{22,83 \cdot n \cdot x_{CO_2}}{1 - x_{CO_2}} \quad (2.16)$$

2.1.4.4 Estimation of Hydration Number

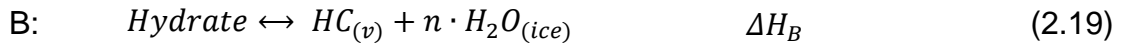
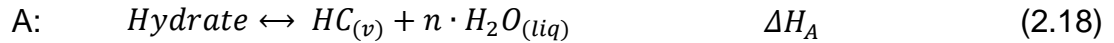
Both methods cited above require the hydration number (n), which describes the water to guest ratio, for the calculation of enthalpy. This factor is not negligible, and thereby, two methods were used to estimate n at each temperature and pressure point. The first method is based on the fractional cage occupancy of hydrate guests (Θ) provided by the software CSMGem. The calculations performed by the software are described in detail by Ballard (2001). The sum of filled cage fractions (Θ) times the total number of the respective cage (v) in the structure results in the total number of cages occupied per unit cell, which is equivalent to the number of guests per unit cell,

assuming one guest per cavity. Then, the hydration number is calculated according to the equation below:

$$n = \frac{H_2O \text{ molecules per unit cell}}{\nu_{small} \cdot \Theta_{small} + \nu_{large} \cdot \Theta_{large}} \quad (2.17)$$

In this work, the enthalpies were estimated for single hydrates known to form structure I. Ergo, the number of small and large cages (ν) are 2 and 6, respectively, for 46 molecules of water.

The second method proposed in this work is a modification of an indirect method, firstly suggested by de Forcrand (DE FORCRAND, 1902; SLOAN and KOH, 2008), which has been extensively used to estimate n based on the subtraction of equations which describe the reactions involving the hydrate, hydrocarbon (HC) or CO₂, liquid water and ice at the lower quadruple point (Q₁), indicated previously in Figure 1.1:



ΔH_A and ΔH_B are hydrate dissociation enthalpies and can be determined through the Clapeyron equation from equilibrium data, according to the method described in the previous section. Since the lower quadruple point of all natural gas hydrates approximates to the melting temperature of ice (SLOAN; KOH, 2008), the enthalpy of the reaction C (ΔH_C) can be considered proportional to the standard enthalpy for ice fusion ($\Delta H_{f \text{ H}_2\text{O}} = 6.01 \text{ kJ}\cdot\text{mol}^{-1} = 333.5 \text{ kJ/kg}$). Then, the hydration number can be obtained from equation 2.21:

$$n = \frac{\Delta H_A - \Delta H_B}{\Delta H_{f \text{ H}_2\text{O}}} \quad (2.21)$$

While many works simply extend this equation to calculate n at further points along the hydrate equilibrium lines, Anderson (2004) presents a method to calculate the hydration number (n) extended to T , P conditions away from Q_1 by a standard technique in which $\Delta H(T, P)$, calculated by the Clapeyron equation, is converted to the value (denoted by ΔH^*) that it would have at Q_1 (272.9 K and 2.563 MPa, for methane hydrate). The calculation is based on the enthalpy changes during hydrate dissociation represented by the reactions A and B mentioned before, in the vicinity of quadruple point Q_1 , where both reactions can occur simultaneously, as proposed by de Forcrand (DE FORCRAND, 1902; SLOAN; KOH, 2008). The correction for pressure and temperature is carried out in different steps, according to different thermodynamic cycles that satisfy Hess's Law.

In this thesis, a similar procedure was adopted to estimate the hydration number for the three single hydrates studied (methane, carbon dioxide and ethane hydrates) at any point of the equilibrium lines. Enthalpy variation of hydrate dissociation reaction (ΔH_{diss}) at any point (i) of the equilibrium line, with regard to pressure and temperature, is described by:

$$\Delta H_{diss(i)} = \left[\Delta H_{HC(i)}^0 + n_{(i)} \cdot \Delta H_{H_2O(i)}^0 - \Delta H_{Hyd(i)}^0 \right] \quad (2.22)$$

$$\Delta H_{X(i)}^0 = H_{X(i)} - H_{X(298.15 K)}^0 \quad (2.23)$$

Where H_X^0 in the equation 2.23 is the standard enthalpy of formation of the substance X at 298.15 K and 1 atm. Considering two points, 1 and 2, from the same equilibrium line defined by (T_1, P_1) and (T_2, P_2) , respectively, the enthalpy variation between point 1 and point 2 will be determined by the following expression:

$$\Delta H_{diss(1)} - \Delta H_{diss(2)} = \left[H_{HC(1)} + n_{(1)} \cdot H_{H_2O(1)} - H_{Hyd(1)} \right] - \left[H_{HC(2)} + n_{(2)} \cdot H_{H_2O(2)} - H_{Hyd(2)} \right] \quad (2.24)$$

By assuming that $n_{(1)} = n_{(2)}$, one can note that the standard enthalpies of formation are cancelled in the equation above. The enthalpy of the dissociation reaction at any point 1 ($\Delta H_{diss(1)}$) was initially calculated by the Clapeyron equation,

considering an initial value of n . The enthalpy of the hydrate dissociation reaction at point 2 was found for each system in the literature (ANDERSON, 2003; HANDA, 1986; KANG et al., 2001). The enthalpies of hydrocarbons and water (H_{HC} and H_{H_2O}) were taken directly from NIST Webbook, according to the equations available on the site (<http://webbook.nist.gov>). The difference of the hydrate enthalpies ($H_{Hyd(2)} - H_{Hyd(1)}$) was calculated considering the definition by partial derivatives:

$$dH_{hyd} = \left(\frac{\partial H_{hyd}}{\partial T} \right)_P \cdot dT + \left(\frac{\partial H_{hyd}}{\partial P} \right)_T \cdot dP \quad (2.25)$$

From thermodynamic correlations, we find the extended forms below for the partial contributions:

$$\left(\frac{\partial H_{hyd}}{\partial P} \right)_T = V_{hyd} - T \cdot \left(\frac{\partial V_{hyd}}{\partial T} \right)_P = V_{hyd} \cdot (1 - \beta_{(v)} \cdot T) \quad (2.26)$$

$$\left(\frac{\partial H_{hyd}}{\partial T} \right)_P = c_{p_{hyd}}(T) \quad (2.27)$$

The determination of the thermal expansivity parameter ($\beta_{(v)}$) and the molar volume of the hydrate (V_{hyd}) were described previously. The value of the specific heat ($c_{p_{hyd}}(T)$) of each hydrate was extrapolated by applying equations reported by Handa (1986), in case of methane and ethane hydrates, and Ning (2015), for carbon dioxide hydrate. Therefore, the integration of the equations 2.26 and 2.27 allows to determine the difference of the hydrate enthalpies between point 1 and 2:

$$H_{Hyd(2)} - H_{Hyd(1)} = \int_{P_1}^{P_2} V_{hyd} \cdot (1 - \beta_{(v)} T) \cdot dP + \int_{T_1}^{T_2} c_{p_{hyd}}(T) \cdot dT \quad (2.28)$$

Finally, by reorganizing the equation 2.24, the hydration number was estimated by equation 2.29 considering the enthalpies calculated previously. The new $n_{(1)}$ value

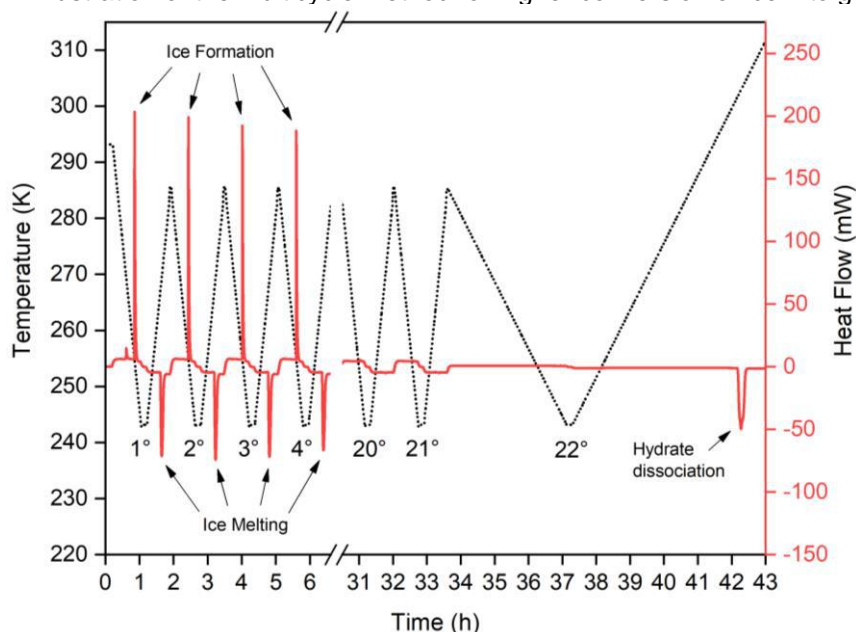
was used to recalculate ΔH_1 and this cycle was repeated through iterations until the output coincided with the input.

$$n = \frac{\Delta H_1 - \Delta H_2 + (H_{HC(2)} - H_{HC(1)}) + (H_{Hyd(1)} - H_{Hyd(2)})}{(H_{H_2O(1)} - H_{H_2O(2)})} \quad (2.29)$$

2.1.4.5 Multicycles Method

Studies developed in our laboratory have demonstrated that the use of a multicycle mode, as proposed by Marinha et al. (2006), improves the interactions between the compounds that are inside the sample cell of the microcalorimeter, reduces the ice fraction by promoting the hydrate formation, and reduces the error associated with the enthalpy calculation. Unlike the standard analysis described above, this methodology consists of subjecting the sample to several successive cooling-heating cycles, as shown in Figure 2.9.

Figure 2.9 – Illustration of the multicycle method for higher conversion of ice into gas hydrate.



Before the last cycle, in which the hydrate is dissociated, the sample is heated up to a temperature between the ice melting (T_{ENDSET}) and the hydrate dissociation (T_{ONSET}), depending on the pressure of the system. This intermediate temperature at which the sample is heated up during the cycles is previously estimated by performing a standard analysis before applying the multicycle method. The ice and the hydrate

peaks are sufficiently separated when pressure is higher than 9.8 MPa, then the sample is heated to 5 K or more from the ice melting endset temperature in these cases. For lower pressures, the difference between the mentioned points may be lower than 5 K, and the peaks may overlap each other, especially for methane and carbon dioxide hydrates, making necessary the deconvolution of them.

By using this method, the amount of non-converted ice is reduced at every cycle, and the water conversion into hydrate is over 97% after the last cycle. The number of cycles required for this conversion depends on several factors, ranging from 5 (carbon dioxide hydrate at 50 MPa) to 37 cycles (ethane hydrate at 20 MPa) in this work. Once the desired water conversion is obtained, the heating of the last cycle is extended so that the gas hydrate is completely dissociated, and the equilibrium properties are determined from the dissociation peak.

2.1.4.6 Isobaric vs. Isochoric Method

The HP- μ DSC allows working in isobaric or isochoric modes. Experiments with a single gas as a guest molecule were performed applying the isobaric method. In this case, the valve of the gas panel, which connects the gas chamber and the sample cell, was kept opened along the experiment. Thus, the constant addition or withdrawal of gas in the system compensate the pressure variation caused by temperature change or by hydrate formation / dissociation, allowing the pressure to be maintained throughout the analysis. The advantage of this method consists of having constant pressure for determining the dissociation points. This is not possible when using a traditional PVT cell since the pressure is initially reached by a booster and then the system is closed (isochoric system). Unlikely, hydrate-forming systems containing gas mixtures presented in chapter 5 were analyzed by applying the isochoric method in the microcalorimeter, in which the referred valve was kept closed in order to maintain constant the overall composition of the system and to make feasible the comparison of experimental data to computational predictions.

Although the amount of water itself does not affect the hydrate equilibrium significantly, the final gas-phase composition calculated by CSMGem predictions may be different from gas fractions entered as “input” when working with mixtures of gases, since the proportion of gas incorporated into the hydrate is not exactly the same as in the gas phase. The guest molecules are incorporated preferentially into small or large

cages according to their molecular size, then the fraction of each species taken from gas phase also depends on the availability of each cavity in the hydrate structure being formed. For this reason, it was initially considered important to keep the system closed during the analysis in these cases and to calculate the predictions considering the overall composition that there was inside the cell at the beginning of the experiment. However, the use of an isochoric method (HP- μ DSC) for such kind of samples implies a pressure variation inside the cell, and thereby, the dissociation pressure for these experiments was considered to be the one obtained at the onset of the hydrate dissociation curves. Thus, the pressure data registered by Calisto software were corrected according to a linear equation, as mentioned in section 2.1.3.

2.1.4.7 Estimation of Overall and Gas-Phase Compositions

In case of ternary systems, composed of two gaseous species and water, the gas phase composition inside the high-pressure cell of the microcalorimeter was estimated from the partial pressures indicated on the high-pressure panel. The ideal condition was considered to correlate the partial pressures with the gas molar fractions (x_1, x_2) of the gases injected into the chamber through the gas injection panel, according to the equation 2.30. P_B is the partial pressure of the second gas, and it refers to the difference between the total pressure (P) and the partial pressure of the first gas injected (P_A), according to Dalton's Law.

$$P_B = P - P_A = P_A \cdot \frac{x_B}{x_A} \quad (2.30)$$

In order to estimate the overall composition inside the cell, the Peng-Robinson equation of state (PR) was applied, considering the initial conditions of temperature and pressure, and the gas volume in the system. The latter was calculated by subtracting the volume of the water sample from the cell volume. Data regarding the water density were obtained from NIST Chemistry Webbook. The study regarding this topic is presented in Chapter 3.

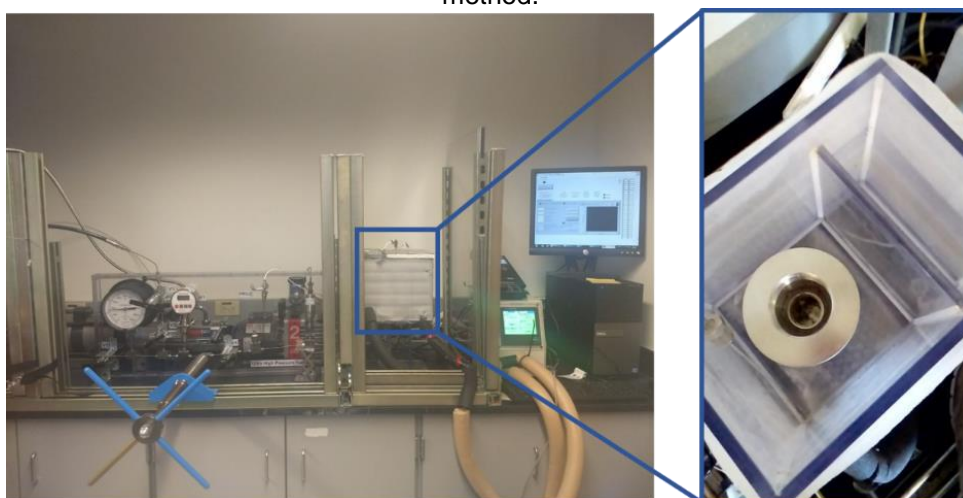
2.2 ULTRA HIGH PRESSURE SYSTEM: PVT-ISOCHORIC METHOD

2.2.1 Experimental Configuration

The PVT-isochoric experiments presented in this work were performed in the Ultra High Pressure system (UHP system) available at the Phases to Flow Laboratory of the Colorado School of Mines (USA). The configuration allows obtaining hydrate equilibrium data up to 200 MPa under temperature control (± 0.25 K and ± 0.3 MPa). The experimental configuration is comprised of a gas booster, a manual pressurizing pump, a magnetic stirrer (500 rpm) and a thermostatic bath where the PVT cell is placed (temperature range depends on the cooling fluid). Inside the PVT cell, there is a cylinder (50 mL), where deionized water sample (~ 15 mL) is added. A baffle is accoupled to this cylinder to break gas-liquid interface and promote mixing. Finally, the cell is closed using a screw-top lid and the system is pressurized with the help of the mentioned gas booster. Pressure and temperature data are recorded during the experimental procedure, allowing the measurement of hydrate equilibrium points.

Figures 2.10 and 2.11 show the experimental setup, including the PVT cell allocated inside the thermal bath and the gas cylinder.

Figure 2.10 – Ultra-High-Pressure System used to analyze hydrates through the PVT- isochoric method.



Source: Photos taken at the Phases to Flow laboratory, Colorado School of Mines.

Figure 2.11 – Commercial gas cylinder joined to the gas booster.

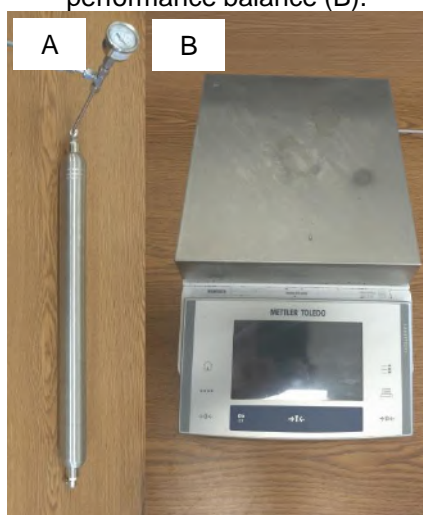


Source: Photo taken at the Phases to Flow laboratory, Colorado School of Mines.

2.2.2 Preparation of Methane-Propane Mixture by Gravimetry

A high-purity commercial gas cylinder was used for single gas hydrate analyses. However, some custom mixtures of methane and propane were gravimetrically prepared in the laboratory from pure gases by using a Swagelok cylinder (0.475 L) and a balance (Mettler Toledo) able to weight up to 8100 g with an accuracy of 0.1 g, shown in Figure 2.12.

Figure 2.12. Swagelok cylinder used for homemade gas mixtures (methane + propane) (A) and high-performance balance (B).



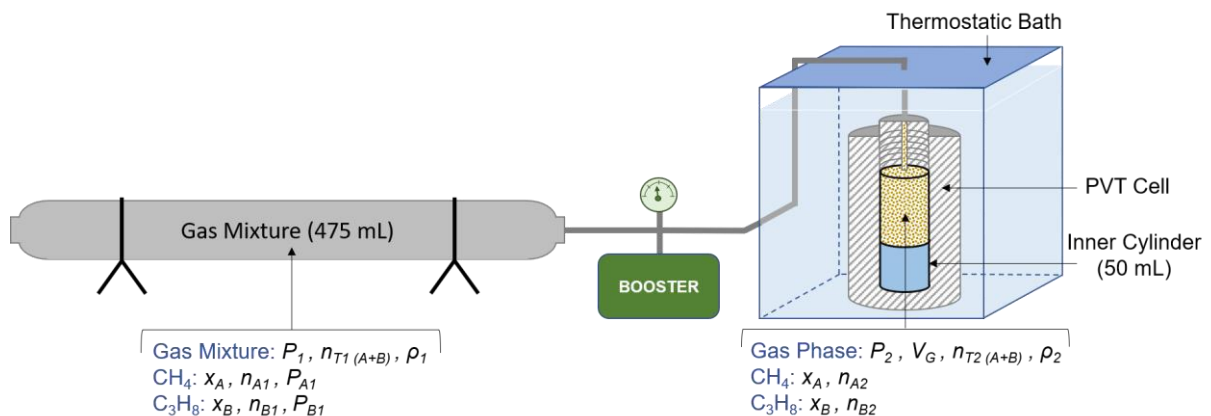
Source: Photo taken at the Phases to Flow laboratory, Colorado School of Mines.

The preparation of the mixtures followed the steps described below and the thermodynamic parameters are indicated in Figure 2.13:

- I – Stipulation of the molar fraction of methane (x_A) and propane (x_B) in the gas phase;
- II – Determination of the gas phase density (ρ_2) inside the PVT cell by using the software Aspen Hysys and the Peng-Robinson equation, considering the established composition (x_A and x_B), the pressure to be applied in the experiment (P_2) and the volume of gas-phase ($V_G \sim 35$ mL);
- III – Calculation of total gas amount (n_{T2}) required to reach the stipulated pressure inside the PVT cell (P_2), considering the gas density (ρ_2) determined previously and the volume of gas-phase ($V_G \sim 35$ mL);
- IV – Estimation of total gas amount (n_{T1}) required in the cylinder for the gas mixture so that enough gas could be available to be transferred from this one (at lower pressure) to the PVT cell until to reach the stipulated pressure. The amount of gas inside the cylinder for mixture should be greater than the one that is injected inside the PVT cell;
- V – Estimation of the partial pressures (P_{A1} and P_{B1}) required in the mixture cylinder, considering the total gas amount (n_{T1}) estimated in the last step and its corresponding composition (x_A and x_B).

By following these steps, each gas was injected inside the mixture cylinder and the weight was taken for each one so that the real composition was calculated based on gravimetric measurements.

Figure 2.13 – Thermodynamic parameters calculated for gas transfer from the mixing cylinder to the PVT cell.



2.2.3 Determination of Equilibrium Data

The experimental procedure to obtain equilibrium data via the PVT-isochoric method includes basically three stages described below (CHA; HU; SUM, 2016; HU et al., 2017;). Stepwise heating is required in order to make sure that the system is in state of equilibrium and to determine accurately the final pressure at which the solid phase is totally dissociated. Nevertheless, this stepwise procedure was not performed in experiments focused on checking the dissociation profile (P vs T) rather than the equilibrium points. In such cases, a fast heating stage was performed continuously at the same rate until complete hydrate dissociation.

- I – The first segment (AB) refers to a fast cooling of the system with a consequent drop in the pressure. A' refers to the point where hydrate formation starts, leading to gas consumption and a more accentuated drop in the pressure. Minimum temperature ranges between 278 K and 293 K, depending on the system, so that hydrate formation is induced, and the ice formation is avoided;
- II – The next stage (BC) is the fast heating of the system (5-10 K/h), during which the increase in pressure is mainly concerned with gas compression (higher molecular excitation);
- III – Finally, the last segment (CD) indicates the stepwise range, where the temperature is increased by 0.2 K every 2 hours. In this stage, the pressure increases in each step due to the gas release from hydrate phase until equilibrium is achieved again. The dissociation of remaining hydrate phase occurs in the last step and the equilibrium point is determined by the intersection of cooling and heating lines.

Figure 2.14 illustrates all the steps employed during analyses using a PVT cell through the isochoric method.

Figure 2.14 – Experimental stages followed in a methane hydrate analysis through the isochoric method in the PVT cell.

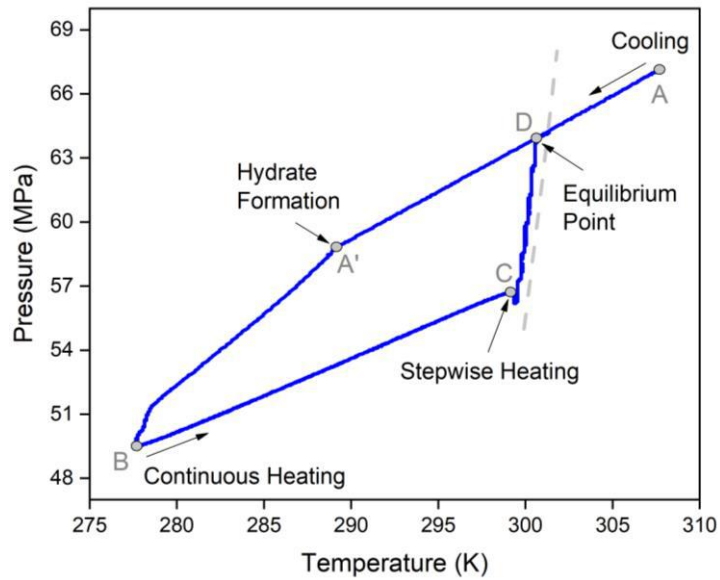
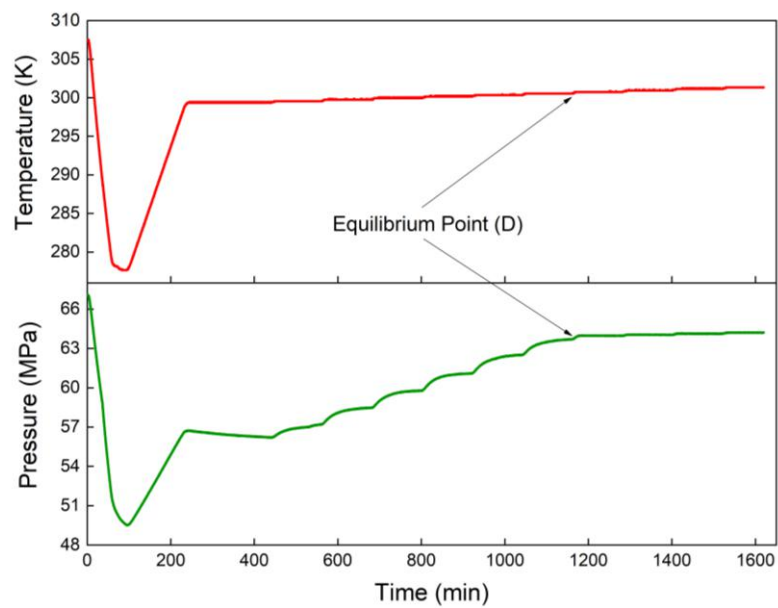


Figure 2.15 exhibits temperature and pressure versus time to provide a better view of each step established by the increase of 0.2 K every 2 hours. The arrows indicate the dissociation point (D), that provides the thermodynamic conditions at the point in which the last hydrate crystal dissociates.

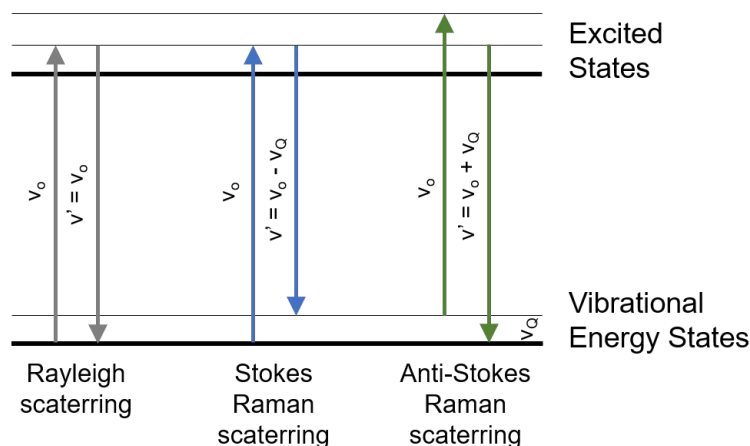
Figure 2.15 – Temperature and pressure profiles obtained for a methane-water system through the PVT - isochoric method.



2.3 RAMAN SPECTROSCOPY

Raman spectroscopy is a scattering technique usually used to identify molecules and chemical structures through vibrational, rotational and other low-frequency transitions in the system. It is based on the Raman effect, that involves the interaction of incident radiation (monochromatic light) with the molecules and the reemission of photons with a different vibration. This phenomenon is known as inelastic scattering since the frequency of incident light shifts up or down after its interaction with the sample, as illustrated in Figure 2.16. However, most of the reemitted monochromatic radiation (>99.99%) is scattered with the same frequency as the incident radiation, known as the elastic Rayleigh scattering. Hence, it is required to use special techniques and instruments to separate the Raman and Rayleigh scatterings (BUMBRAH; SHARMA, 2016).

Figure 2.16 – Light scatterings involved in Raman spectroscopy.

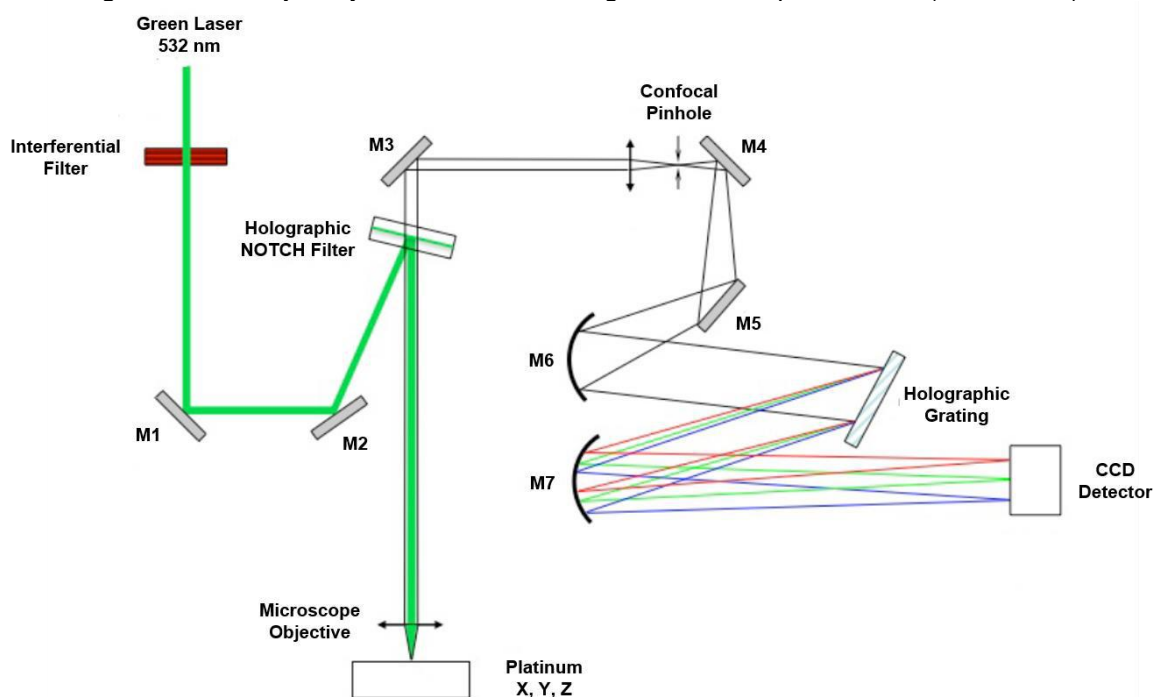


Source: Adapted from PETUYA, 2017.

Gas hydrate studies based on Raman spectroscopy were conducted at the platform SIV (“Spectroscopie et Imagerie Vibrionnelle”), in partnership with the “Groupe Spectroscopie Molléculaire” (GSM) at Université de Bordeaux (France), which is funded by the FEDER and the Region Aquitaine. In this work, a green laser (532 nm wavelength) was applied as the excitation source. This monochromatic light was focused on the sample by a confocal optical microscope, which makes it possible to improve the lateral and axial resolutions at micrometric spatial resolution. A 50x objective (Olympus) was used to focus the laser beam on the sample. The setup allows to analyze the sample by choosing different areas and depths of penetration and it is

described in detail by PETUYA (2017). Figure 2.17 illustrates the trajectory of radiation along the Raman spectrometer (*Labram UV*, Horiba Jobin Yvon, Villeneuve d'Asq, France). The radiation initially passes through an interferential filter, which suppresses stray lights from noisy sources, and then through a holographic notch filter that attenuates the Rayleigh line in a narrow bandwidth allowing to collect both Stokes and anti-Stokes Raman data (TEDESCO et al., 1993). A holographic grating of 1800 lines/mm disperses the Raman scattering providing a high spectral resolution. Finally, a Peltier-cooled CCD detector (Andor, UK) recovers the Raman scattering, transforming the light signal into an electrical signal. The spectra calibration was performed using the 520.7 cm^{-1} vibration mode of a silicon sample.

Figure 2.17 – Trajectory of the radiation along the Raman spectrometer (Labram UV).



Source: Adapted from PETUYA (2017).

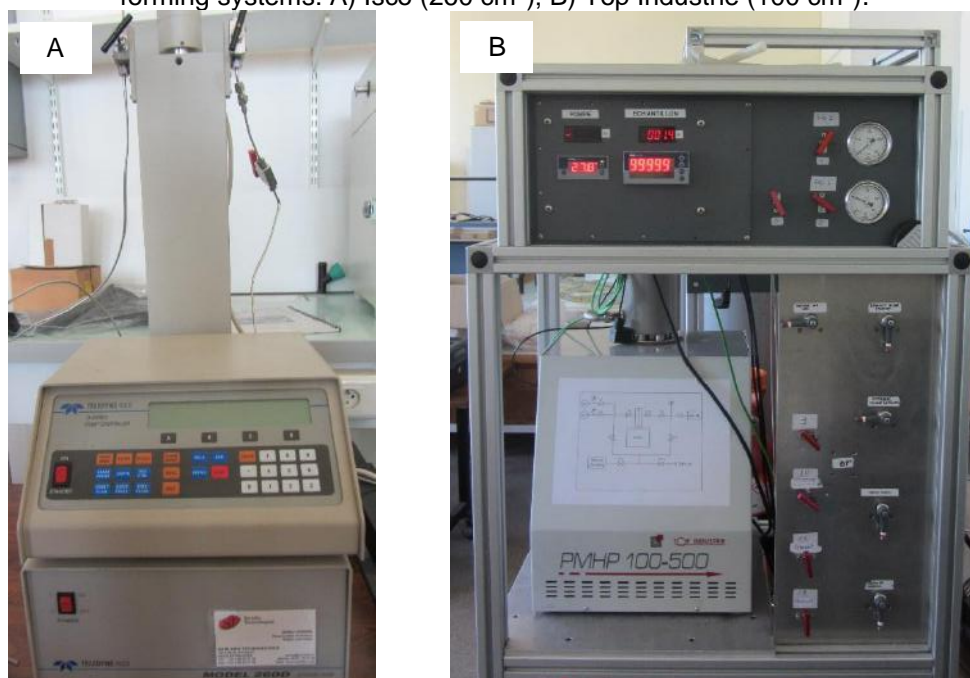
Different methodologies (*ex situ* and *in situ*) were applied in the preparation and analysis of gas hydrates in order to evaluate the most appropriate one for structural and compositional characterization. When working with gas mixtures, it was employed the procedure described in section 2.3.1 for both methods. The *ex situ* methodology was used to characterize methane-propane hydrates prepared at different gas phase compositions and it is presented in section 2.3.2. Although the results in this work indicate that the *in situ* methods are not the most suitable for a homogeneous characterization of gas hydrates, they were relevant to visualize and understand the

mechanisms of hydrate growth in static systems (in absence of mixing). For that reason, the *in situ* methodology is also described in the section 2.3.3. Results for both *ex situ* and *in situ* analyses are shown in chapter 7 of this work.

2.3.1 Procedure for Mixing Gases

A different methodology from the previous ones (HP- μ DSC and PVT-isochoric method) was employed in the preparation of methane-propane hydrates characterized by Raman spectroscopy. The gas mixtures were made by using a homemade setup composed of two pumps shown in Figure 2.18.

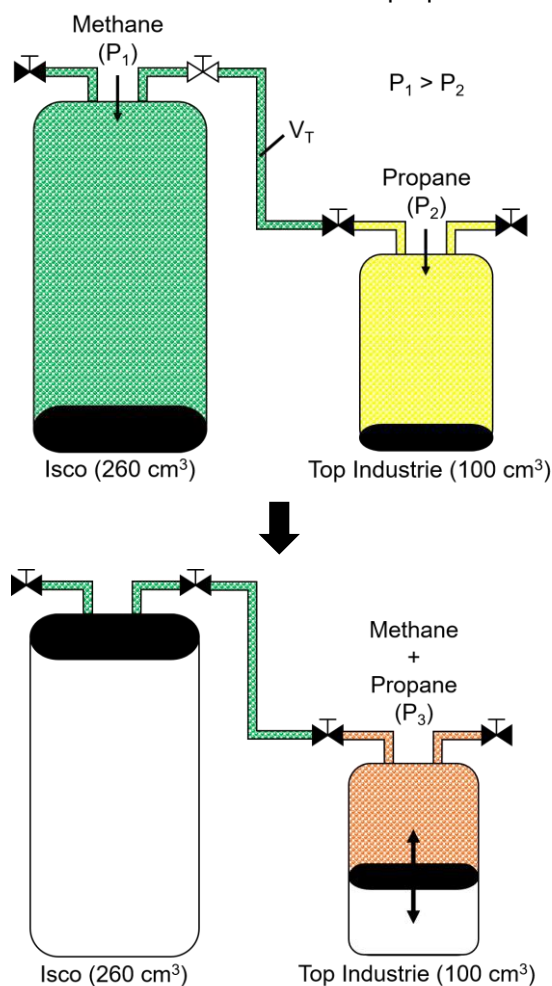
Figure 2.18 – Pumps employed for the preparation of gas mixtures and pressurization of the hydrate-forming systems: A) Isco (260 cm³); B) Top Industrie (100 cm³).



Source: Photos taken at the GSM laboratory, Université de Bordeaux

Methane is injected in the first pump (Isco) while propane is injected in an automatized one (Top Industrie). Such a setup allows us to measure both volume and pressure accurately for each gas, and then both are brought into contact by transferring the methane gas into the chamber of the second pump, as illustrated in Figure 2.19. The mixture is kept under a sinusoidal variation of pressure (± 30 MPa from the initial pressure) for 30 minutes in order to homogenize the gas mixture. A similar procedure is described with details by Petuya et al. (2018).

Figure 2.19 – Schematic illustration of methane-propane mixtures preparation.



2.3.2 Procedures for ex situ Analyses

Ex situ analyses were performed on hydrates samples prepared from ice powder. The advantage of this method is based on the formation of a more homogeneous hydrate sample since ice powder provides greater surface area and interstitial gaps that favor diffusion of gas molecules and restructuring of crystalline lattice. Thus, this method was the main one applied to prepare gas hydrate samples in order to obtain compositional analyses by Raman spectroscopy.

For the preparation of samples, ice is crushed in a mortar until to obtain a fine powder, and then it is transferred to stainless steel cells (Figure 2.20). This procedure is performed at about 195K in a chamber filled with pellets of dry ice. Next, the cells containing ice powder are pressurized with the respective gas at 8.7 MPa and kept at 253K for 3 days aided by a thermostatic bath. The temperature control in this step is also essential to lead to the formation of hydrate structures while avoiding the

condensation of the gas phase. Posteriorly, the hydrate samples are depressurized and immediately transferred to a vessel under inert atmosphere and liquid nitrogen ($\sim 77\text{K}$) so that the gas hydrates remain stable.

Figure 2.20 – High-Pressure cell used to prepare *ex situ* gas hydrate samples.



Source: Photos taken at the GSM laboratory, Université de Bordeaux

For Raman measurements, a fraction of the sample is inserted into a metal surface of a modified optical cell (Linkam CAP500, Figure 2.21) with the aid of a quartz capillary tube also cooled in liquid nitrogen. The optical cell is maintained at 140 K all over the analysis thanks to a laboratory-modified temperature-controlled stage (based on the Linkam THMS600 stage), which pumps nitrogen inside the cell according the specified temperature.

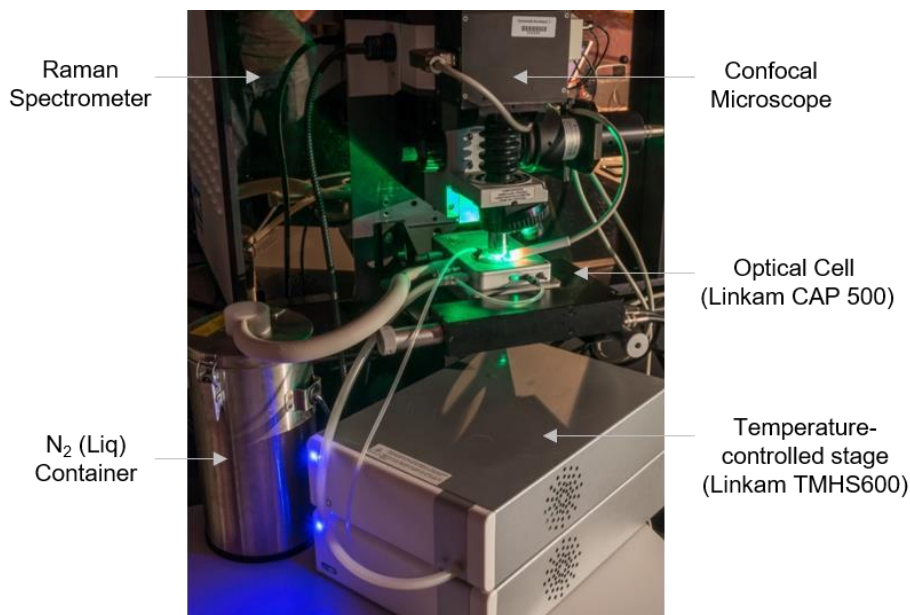
Figure 2.21 – Optical cell (Linkam) used in the Raman spectroscopy of gas hydrates prepared *ex situ*.



Source: PETUYA, 2017.

A container stores and supplies liquid nitrogen to this device throughout the experiment. The setup is shown in Figure 2.22.

Figure 2.22 – Setup for Raman spectroscopy measurements of samples prepared *ex situ*.



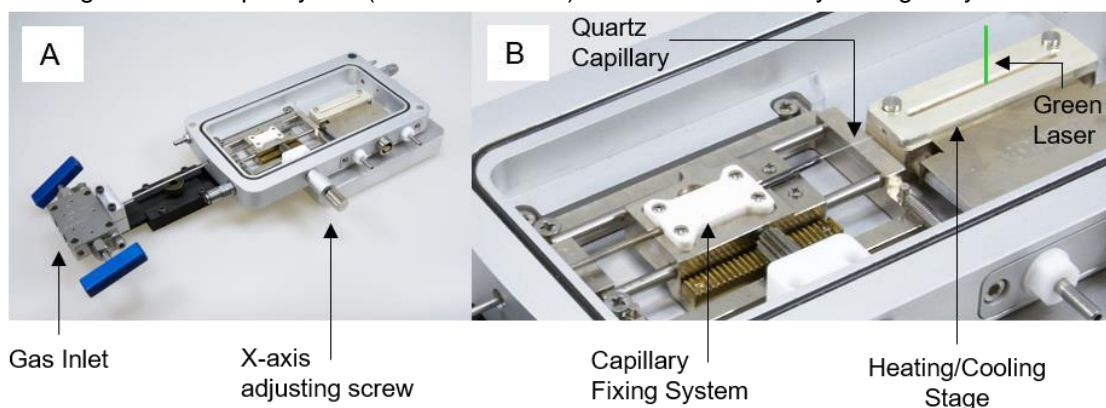
Source: PETUYA, 2017.

2.3.3 Procedures for in situ Analyses

2.3.3.1 Capillary Cell

The purpose of the analyses, according to this method, was to obtain Raman spectra of the hydrate structures during the formation process. The first method employed to analyze gas hydrates formation *in situ* is based on a modified Capillary Pressure Stage (Linkam CAP500) designed to heat and cool high-pressure quartz capillaries. Figure 2.23 indicates the main features of the apparatus that allows visual monitoring of the hydrate growth and the obtaining of Raman spectra.

Figure 2.23. Capillary cell (Linkam CAP500) used for *in situ* analysis of gas hydrates.

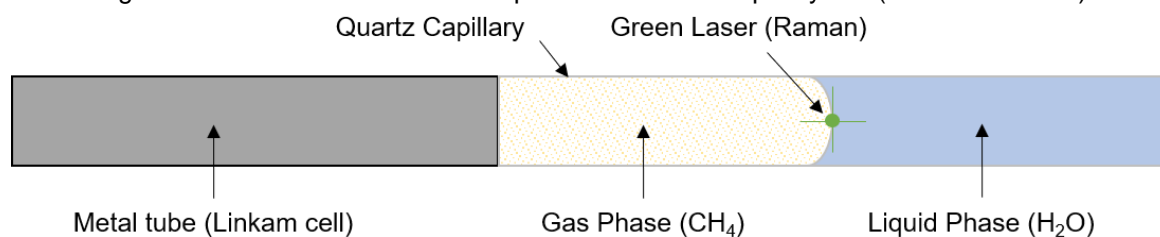


Source: Photos from GSM collection, Université de Bordeaux.

The samples preparation procedure is the same employed by Petuya et al. (2018) and it is described below in detail. The quartz capillary is illustrated in Figure 2.24.

- I – A square-shape quartz capillary (inner diameter = 200 μm) was partially filled with Milli-Q water via capillary suction;
- II – The dry end of the tube was sealed by using a propane blowtorch, and the capillary was subjected to centrifugation (13000 rpm for 45 minutes) in order to push the column of water to the sealed end;
- III – The quartz capillary was attached to the metal tube of the Linkam cell (Figure 2.25) and fixed by a high-performance glue. The system was maintained at rest overnight;
- IV – Methane gas was slowly injected through the cell until it reached 20 MPa. The valve was closed to check for leaks;
- V – The green laser beam was focused on the interface of gas and liquid phases (meniscus). Finally, the system was cooled down to 278K to induce hydrate formation.

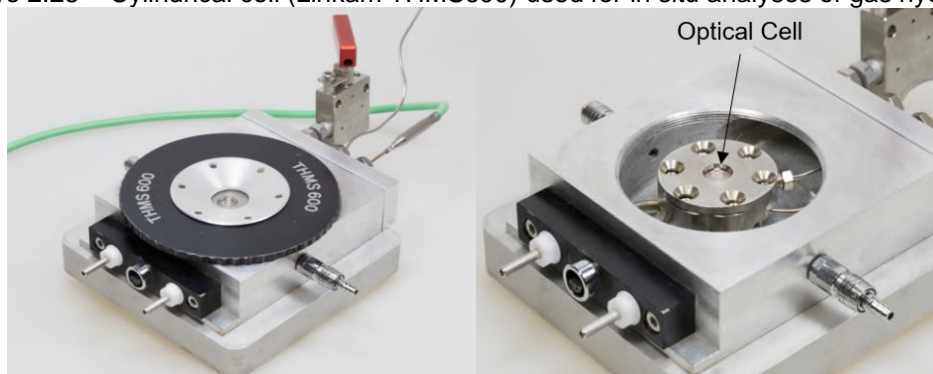
Figure 2.24 – Illustration of the sample settled on the capillary cell (Linkam CAP500)



2.3.3.2 Cylindrical Cell (Linkam)

The following configuration employed for studying gas hydrates *in situ* features a modified cell (Linkam THMS600) that includes an optical cell inside and allows Raman measurements thanks to a sapphire window (2 mm) resistant to high pressures, as shown in Figure 2.25.

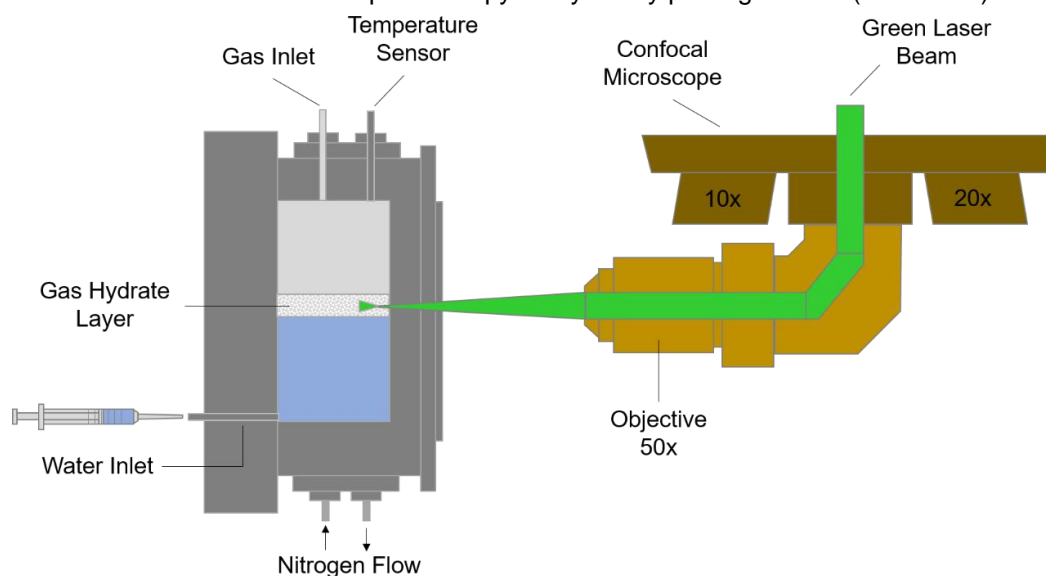
Figure 2.25 – Cylindrical cell (Linkam THMS600) used for in situ analyses of gas hydrates.



Source: Adapted from PETUYA, 2017.

The cell was placed vertically, and the microscope objective was adapted, as showed in Figure 2.26, so that the light beam could be directed straightly to the solid phase. Methane molecules in the gas phase have very similar vibrational modes to the molecules in the hydrate structure. Thus, if the light beam passes through the gas phase, the methane content trapped in the hydrate cavities is overestimated. For this reason, it was necessary to avoid interference of the gas phase in the spectra.

Figure 2.26 – Scheme of Raman spectroscopy analyses by placing the cell (THMS600) vertically.



In this case, the sample was prepared by injecting 0.5 mL of Milli-Q water into the cell in the vacuum. Then, the cell was pressurized slowly with methane gas up to 16.4 MPa by the Top Industrie pump shown in Figure 2.18b. The optical cell was cooled down to 263 K at 1 K·min⁻¹ and kept at this temperature throughout the analysis by using the same temperature-controlled stage mentioned in the latter section, which manages the nitrogen flow in the outer region of the optical cell.

REFERENCES

- ANDERSON, G.K. Enthalpy of dissociation and hydration number of carbon dioxide hydrate from the Clapeyron equation. *The Journal of Chemical Thermodynamics*, v. 35, p. 1171-1183, 2003.
- ANDERSON, G.K. Enthalpy of dissociation and hydration number of methane hydrate from the Clapeyron equation. *Journal of Chemical Thermodynamics*, v. 36, p. 1119-1127, 2004.
- ANDERSON, G.K. Solubility of Carbon Dioxide in Water under Incipient Clathrate Formation Conditions. *Journal of Chemical and Engineering Data*, v. 47, p. 219-222, 2002.
- ANTOINE, C. Tensions des vapeurs: nouvelle relation entre les tensions et les températures. *Comptes Rendus de l'Académie de Sciences*, v. 107, p. 681-684, 1888.
- BALLARD, A.L. A non-ideal hydrate solid solution model for a multi-phase equilibria program. Ph.D. Thesis, Colorado School of Mines, 2001.
- BRIDGMAN, P.W. Water, in the liquid and five solid forms, under pressure. *Proceedings of the American Academy of Arts and Sciences XLVII*, v. 13, p. 439-558, 1912.
- BUMBRAH, G.S.; SHARMA, R.M. Raman spectroscopy – Basic principle, instrumentation and selected applications for the characterization of drugs of abuse. *Egyptian Journal of Forensic Sciences*, v. 6, p. 209-215, 2016.
- CHA, M., HU, Y., SUM, A.K. Methane hydrate phase equilibrium for systems containing NaCl, KCl, and NH₄Cl. *Fluid Phase Equilibria*, v. 413, p. 2-9, 2016.
- CIRCONE, S., S. H. KIRBY, AND L. A. STERN. Thermodynamic calculations in the system CH₄-H₂O and methane hydrate phase equilibria. *The Journal of Physical Chemistry B*, v. 110, p. 8232–8239, 2006.
- DARABOINA, N.; MALMOS, C.; SOLMS, N. Investigation of kinetic hydrate inhibition using a high pressure micro differential scanning calorimeter. *Energy Fuels*, v. 27:10, p. 5779– 5786, 2013.
- DAVIES, S.R.; HESTER, K.C.; LACHANCE, J.W.; KOH, C.A.; SLOAN, E.D. Studies of hydrate nucleation with high pressure differential scanning calorimetry. *Chemical Engineering Science*, v. 64, p. 370-375, 2009.
- DE FORCRAND, R. *Comptes Rendus*, v. 135, p. 959–961, 1902.
- DENYS, S.; SCHLÜTER, O.; HENDRICKX, M.E.G.; KNORR, D. Effects of High Pressure on Water-Ice Transitions in Foods. In: Hendrickx M.E.G., Knorr D., Ludikhuyze L., Van Loey A., Heinz V. (eds) *Ultra High Pressure Treatments of Foods*, chapter 8, p. 242. *Food Engineering Series*. Springer, Boston, MA, 2001.

DIAMOND, L.W.; AKINFIEV, N.N. Solubility of CO₂ in water from -1.5 to 100 °C and from 0.1 to 100 MPa: evaluation of literature data and thermodynamic modelling. *Fluid Phase Equilibria*, v. 208, p. 265-290, 2003.

FRIEND, D.G.; INGHAM, H.; ELY, J.F. Thermophysical properties of ethane. *Journal of Physical and Chemical Reference Data*, v. 20, p. 275-347, 1991.

FUKUSAKO, S. Thermophysical properties of ice, snow, and sea ice. *International Journal of Thermophysics*, v. 11, p. 353-372, 1990.

GUPTA, A. Methane Hydrate Dissociation Measurements and Modeling: The Role of Heat Transfer and Reaction Kinetic, Ph.D. thesis, Colorado School of Mines, Golden, Colorado, USA, 2007.

GUPTA, A.; LACHANCE, J.; SLOAN, E. D.; KOH, C. A. Measurements of methane hydrate heat of dissociation using high pressure differential scanning calorimetry. *Chemical Engineering Science*, v. 63, p. 5848-5853, 2008.

GUTT, C.; ASMUSSEN, B.; PRESS, W; JOHNSON, M.R.; HANDA, Y.P.; TSE, J.S. The structure of deuterated methane-hydrate. *Journal of Chemical Physics*, v. 113, p. 4713-4721, 2000.

HANDA, Y.P. Compositions, enthalpies of dissociation, and heat capacities in the range 85 to 270 K for clathrate hydrates of methane, ethane, and propane, and enthalpy of dissociation of isobutane hydrate, as determined by a heat-flow calorimeter. *Journal of Chemical Thermodynamics*, v. 18, p. 915- 921, 1986.

HESTER, K.C.; HUO, Z.; BALLARD, A.L.; KOH, C.A.; MILLER, K.T.; SLOAN, E.D. Thermal Expansivity for sl and sII Clathrate Hydrates. *Journal of Physical Chemistry B*, v. 111, p. 8830-8835, 2007.

HU, Y.; LEE, B.R.; SUM, A.K. Phase equilibrium data of methane hydrates in mixed brine solutions. *Journal of Natural Gas Science and Engineering*, v. 46, p. 750-755, 2017.

HUO, Z. Hydrate Phase Equilibria Measurements by X-ray Diffraction and Raman Spectroscopy. Ph.D. Thesis, Colorado School of Mines, 2002.

IKEDA, T.; YAMAMURO, O.; MATSUO, T.; MORI, K.; TORII, S.; KAMIYAMA, T.; IZUMI, F.; IKEDA, S.; MAE, S. Neutron diffraction study of carbon dioxide clathrate hydrate. *Journal of Physics and Chemistry of Solids*, v. 60, p. 1527-1529, 1999.

KANG, S.-P.; LEE, H.; RYU, B.-J. Enthalpies of dissociation of clathrate hydrates of carbon dioxide, nitrogen, (carbon dioxide + nitrogen), and (carbon dioxide + nitrogen + tetrahydrofuran). *Journal of Chemical Thermodynamics*, v. 33, p. 513-521, 2001.

KARINO, S.; HANE, H.; MAKITA, I. Behavior of water and ice at low temperature and high pressure. In R. Hayashi, S. Kunugi, S. Shimada, & A. Suzuki (Eds.), *High Pressure Bioscience* (p. 2-9). Kyoto: San-Ei Suppan. 1994.

KLAPPROTH, A.; GORESHNIK, E.; STAYKOVA, D.; KLEIN, H.; KUHS, W. Structural studies of gas hydrates. *Canadian Journal of Physics*, v. 81, p. 503–518, 2003.

KODRE, K.V.; ATTARDE, S.R.; YENDHE, P.R.; PATIL, R.Y.; BARGE, V.U. Differential scanning calorimetry: a review. Research and Reviews: *Journal of Pharmaceutical Analysis*, v. 3, p. 11-22, 2014.

KRICHEVSKY, I.R.; KASARNOVSKY, J.S. Thermodynamical Calculations of Solubilities of Nitrogen and Hydrogen in Water at High Pressures. *Journal of the American Chemical Society*, v.57, p. 2168-2171, 1935.

LIN, L.; KEDZIERSKI, M.A. Specific heat of aluminum-oxide nanolubricants. *International Journal of Heat and Mass Transfer*, v. 126, p. 1168-1176, 2018.

LIN, W.; DALMAZZONE, D.; FÜRST, W.; DELAHAYE, A.; FOURNAISON, L.; CLAIN, P. Accurate DSC measurement of the phase transition temperature in the TBPB–water system. *The Journal of Chemical Thermodynamics*, v. 61, p. 132-137, 2013.

LIN, W.; DALMAZZONE, D.; FÜRST, W.; DELAHAYE, A.; FOURNAISON, L.; CLAIN, P. Thermodynamic properties of semiclathrate hydrates formed from the TBAB+TBPB+water and CO₂+TBAB+TBPB+water systems. *Fluid Phase Equilibria*, v. 372, p. 63-38, 2014.

LINSTROM, P.J.; MALLARD, W.G. (Eds.). NIST Chemistry WebBook, NIST Standard Reference Database Number 69, July 2001, National Institute of Standards and Technology, Gaithersburg MD, 20899 (<http://webbook.nist.gov>).

MARINHAS, S.; DELAHAYEA, A.; FOURNAISONA, L.; DALMAZZONE, D.; FURST, W.; PETITET, J.P. Modelling of the available latent heat of a CO₂ hydrate slurry in an experimental loop applied to secondary refrigeration. *Chemical Engineering and Processing*, v. 45, p. 184–192, 2006.

MENEZES, D.E.S.; SUM, A. K.; DESMEDT, A.; PESSOA FILHO, P. A.; ROBUSTILLO, M.D. Coexistence of sl and sll in methane-propane hydrate former systems at high pressures. *Chemical Engineering Science*, v. 208, 115149, 2019.

MENEZES, D.E.S.; PESSÔA FILHO, P.A.; ROBUSTILLO, M.D. Use of 1-Butyl-3-methylimidazolium-based ionic liquids as methane hydrate inhibitors at high-pressure conditions. *Chemical Engineering Science*, v. 212, 115323, 2020.

NING, F.L.; GLAVATSKIY, K.; JI, Z.; KJELSTRUP, S.; VLUGTE, T.J.H. Compressibility, thermal expansion coefficient and heat capacity of CH₄ and CO₂ hydrate mixtures using molecular dynamics simulations. *Physical Chemistry Chemical Physics*, v. 17, p. 2869, 2015.

PETUYA, C. Étude de la stabilité, de l'occupation des cages et de la sélectivité moléculaire des hydrates de gaz par spectroscopie Raman. PhD Thesis, Université de Bordeaux, Bordeaux, France, 2017.

PETUYA, C.; DAMAY, F.; CHAZALLON, B.; BRUNEEL, J.-L.; DESMEDT, A. Guest Partitioning and Metastability of the Nitrogen Gas Hydrate. *The Journal of Physical Chemistry C*, v. 122, p. 566-573, 2018.

RETTICH, T.R.; HANDA, Y.P.; BATTINO, R.; WILHELM E. Solubility of gases in liquids. 13. High-precision determination of Henry's constants for methane and ethane in liquid water at 275 to 328 K. *The Journal of Physical Chemistry*, v. 85, p. 3230-3237, 1981.

ROWLEY, R.L.; WILDING, W.V.; OSCARSON, J.L.; YANG, Y.; ZUNDEL N.A.; DAUBERT, T.E.; DANNER, R.P. "DIPPR Data Compilation of Pure Compound Properties," Design Institute for Physical Properties. *American Institute of Chemical Engineers*, New York, 2003.

SABBAH, R.; XU-WU, A.; CHICKOS, J.S.; PLANAS LEITÃO, M.L.; ROUX, M.V.; TORRES, L.A. Reference materials for calorimetry and differential thermal analysis. *Thermodynamic Acta*, v. 331, p. 93-204, 1999.

SAEED, R.M.; SCHLEGEL, J.P.; CASTANO, C.; SAWAFTA, R. Uncertainty of thermal characterization of phase change material by differential scanning calorimetry analysis. *International Journal of Engineering Research and Technology*, v. 5, p. 105-412, 2013.

SETARAM Instrumentation, Brochure of micro DSC 7 evo, Caluire, France, 2016.

SETZMANN, U.; WAGNER, W. A new equation of state and tables of thermodynamic properties for methane covering the range from the melting line to 625 K at pressures up to 1000 MPa. *Journal of Physical and Chemical Reference Data*, v. 20, p. 1061-1151, 1991.

SLOAN E.D.; KOH, C. Clathrate hydrates of natural gases, 3rd ed. Boca Raton: CRC Press, 2008.

SPAN, R.; WAGNER, W. A new equation of state for carbon dioxide covering the fluid region from the triple-point temperature to 1100 K at pressures up to 800 MPa. *Journal of Physical and Chemical Reference Data*, v. 25, p. 1509-1596, 1996.

SUM, A.K.; BURRUSS, R.C.; SLOAN, E.D. Measurement of clathrate hydrates via Raman spectroscopy. *The Journal of Physical Chemistry B*, v. 101 (38), p. 7371-7377, 1997.

TEDESCO, J.M.; OWEN, H.; PALLISTER, D.M.; MORRIS, M.D. Principles and spectroscopic applications of volume holographic optics. *Analytical Chemistry*, v. 65, p. 441A-449A, 1993.

UDACHIN, K.A.; RATCLIFFE, C.I.; RIPMEESTER, J.A. Structure, composition and thermal expansion of CO₂ hydrate from single crystal x-ray diffraction measurements. *Journal of Physics Chemistry B*, v. 105, p. 4200-4204, 2001.

WAGNER, W.; PRUSS, A. The IAPWS formulation 1995 for the thermodynamic properties of ordinary water substance for general and scientific use, *Journal of Physical and Chemical Reference Data*, v. 31, p. 387-535, 2002.

CHAPTER 3

PRELIMINARY STUDIES

ABSTRACT

This chapter introduces preliminary topics evaluated before studying gas hydrate phases by high-pressure microcalorimetry. The thermodynamic study of the gases used in this work and the influence of water fraction on hydrate dissociation temperatures were studied by commercial simulation software. The Peng-Robinson equation was also validated in order to estimate the overall composition of microcalorimetric analyses. Finally, unexpected transitions concerned to Teflon, the material of which anti-extrusion rings for high-pressure cells are made of, were found within the temperature range applied for gas hydrate studies. The considerations below were important to a better understanding of each system and for planning experiments.

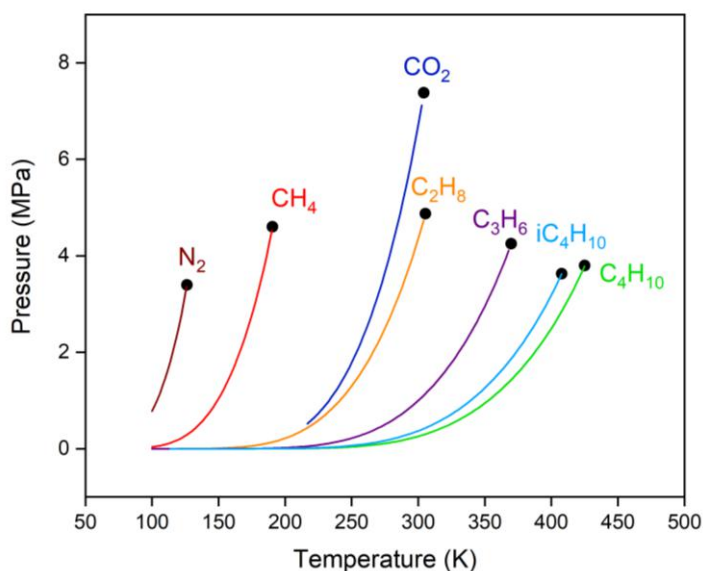
3.1 THERMODYNAMIC STUDY OF GASES

Methane, ethane, propane and carbon dioxide were used as guest species in different hydrate-forming systems. Prior to the study of hydrates itself, it is important to predict the thermodynamic behavior of these substances during injection into the high-pressure panel and throughout the analyses. Such knowledge is necessary because the pressure and temperature ranges applied could lead to heterogeneous systems containing hydrocarbon (or carbon dioxide) in a gaseous-liquid equilibrium, apart from the aqueous phase. Consequently, transitions corresponding to vapor-liquid changes could be observed. The possibility of two-phases coexistence is even greater in case of double guest systems. Therefore, simulations were performed by using the software ASPEN to obtain equilibrium curves that indicate the phases present in different thermodynamic conditions and compositions. Predictive computational results for single and binary mixtures, containing the hydrocarbons cited above and / or carbon dioxide, are presented in sections 3.1.1. and 3.1.2, respectively.

3.1.1 Single Gases

Figure 3.1 shows the respective liquid-vapor equilibrium lines for different gases studied in this work and their critical points, above which the phase obtained, known as “plasma”, is homogeneous and presents a density similar to that of liquid but with other gas characteristics (HITCHEN; DEAN, 1993). Considering that the gas is injected at 273.15 K, greater attention needs to be given to substances which may have two phases at this temperature and relatively low pressures (below 4 MPa), such as carbon dioxide, ethane and propane. It is assumed that in these cases the vapor-liquid transition and even their coexistence during injection and pressurization are very probable. The same behavior should be observed in thermograms from analyses performed below the critical pressure. Nevertheless, a homogeneous supercritical phase condition is assumed to be reached for analyses above the critical point. This makes essential the stabilization period before cooling the oven and starting the analysis.

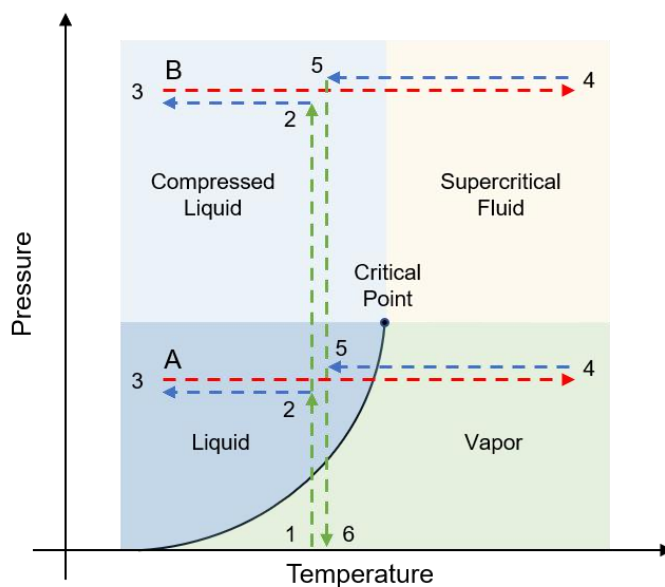
Figure 3.1 – Vapor-liquid equilibrium lines (Aspen) of single gases and their respective critical points.



In the next chapter, single methane, ethane and carbon dioxide hydrates are particularly evaluated. With regard to methane, a single supercritical phase must be present throughout the temperature range of the analysis, whatever the pressure. On the other hand, ethane and carbon dioxide at pressures below critical pressure should present transitions related to vapor-liquid phases along the cooling and heating

process, as illustrated by sequence A in Figure 3.2. This figure indicates the thermodynamic steps used in calorimetric analysis. Line 1-2 represents the hydrocarbon (s) / carbon dioxide injection and pressurization, and it is followed by a cooling step (2-3) for the hydrate formation, a heating (3-4) for the hydrate dissociation, a second cooling down to the initial temperature (4-5) and, finally, the depressurization (5-6). Otherwise, analyses at pressures above the critical pressure should not present any thermal transitions with respect to compressed liquid and supercritical fluid (sequence B). The physical-chemical features from this phase do not change suddenly and, in practice, only the terminology is different.

Figure 3.2 – Schematic illustration of possible phases during injection, pressurization and analysis performed by HP- μ DSC.



3.1.2 Binary Gaseous Mixtures

Unlike single gases, where the conditions for two-phase coexistence are defined by an equilibrium line, the presence of liquid-vapor phases in gaseous mixtures is delimited by an area known as equilibrium envelope. This means that the heterogeneous region covers a temperature range for each pressure rather than just one point, and therefore, the possibility of two-phase coexistence is greater. Thus, the envelopes for each binary mixture studied in this work (methane-ethane, methane-propane and methane-carbon dioxide) were sketched from the equilibrium data obtained by the software Aspen. The figures below show the envelopes obtained for each mixture, considering molar fractions of methane from 0.1 to 0.99. It is noteworthy

that the fraction of methane in hydrate-forming systems is usually higher than other substances.

Figure 3.3 – Thermodynamic envelopes for CH₄-C₂H₆ gaseous mixtures. Solid lines refer to saturated liquid, while dashed lines refer to saturated vapor.

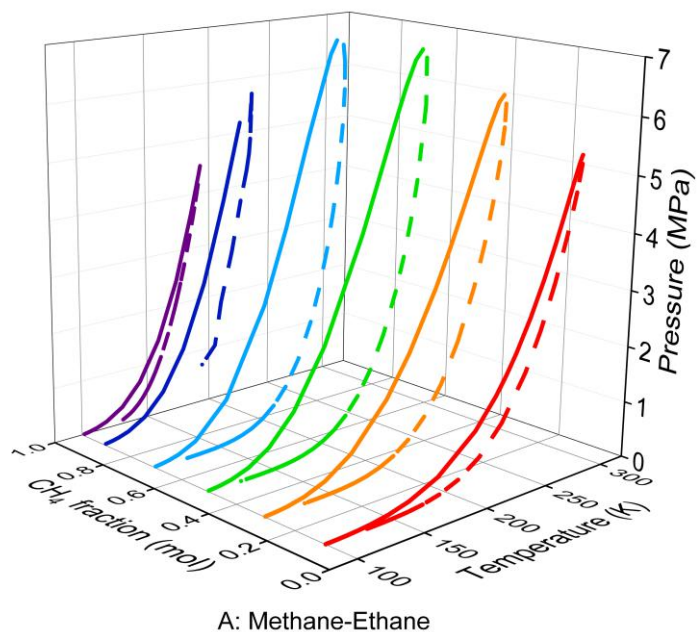


Figure 3.4 – Thermodynamic envelopes for CH₄-C₃H₈ gaseous mixtures. Solid lines refer to saturated liquid, while dashed lines refer to saturated vapor.

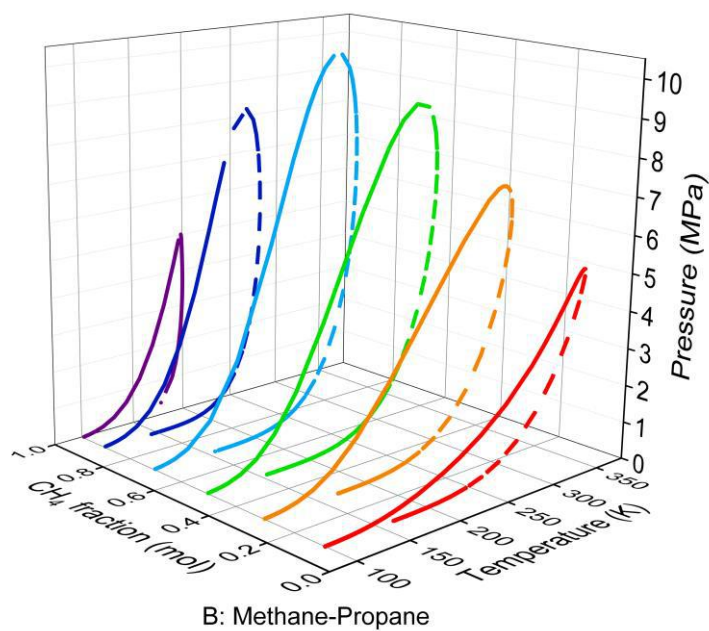
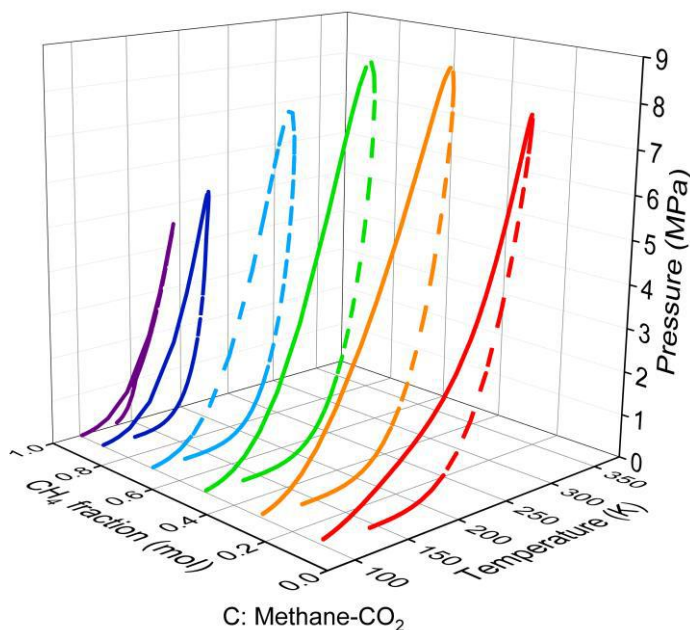


Figure 3.5 – Thermodynamic envelopes for CH₄-CO₂ gaseous mixtures. Solid lines refer to saturated liquid, while dashed lines refer to saturated vapor.



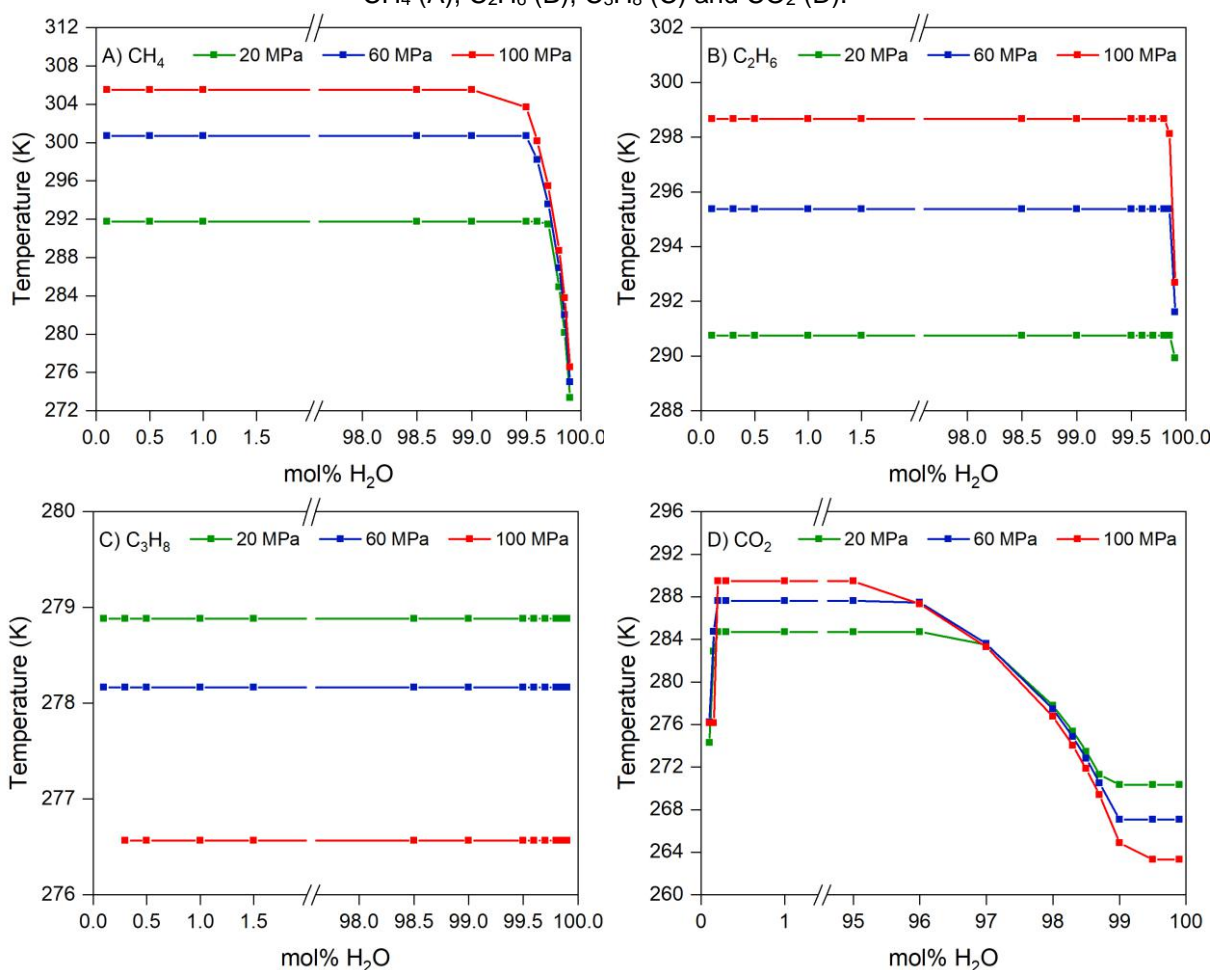
According to the simulations results presented in Figures 3.3, 3.4 and 3.5, compositions of mixtures that imply the liquid-vapor coexistence were avoided when studying gas hydrates since the composition of the hydrocarbon phase (or CO₂) in contact with the aqueous phase influences hydrate composition, and this variable cannot be measured by the experimental apparatus. Although the pressure applied for the analyses was higher than found in the envelopes above, a heterogeneous gaseous phase likely forms during the injection and pressurization inside the high-pressure panel, making necessary a time for stabilizing the system at the final pressure before the analysis.

3.2 INFLUENCE OF WATER FRACTION ON HYDRATE DISSOCIATION TEMPERATURE

Unlike the gas mixture ratio, the influence of water content on the hydrate dissociation temperature is usually neglected by most works in literature. This factor was studied in this work by evaluating the temperature profiles obtained by CSMGem predictions, according to the pressure and water fraction in different systems. This was done to estimate the proper size of water sample to be placed inside the HP- μ DSC cell. Indeed, the water fraction may have some influence on hydrate properties when there is a shortage of gas molecules, in which just traces of hydrate are formed.

The profiles presented in Figure 3.6, at 20, 60 and 100 MPa, indicate that the dissociation temperatures of single hydrates composed of methane and ethane are affected only at extremely high fraction of water (above 99 mol% H₂O). In such conditions, the hydrate dissociation temperatures drop significantly since most of the cavities in the hydrate structure are likely empty. Propane hydrates, in turn, do not present any temperature variation in the composition range studied.

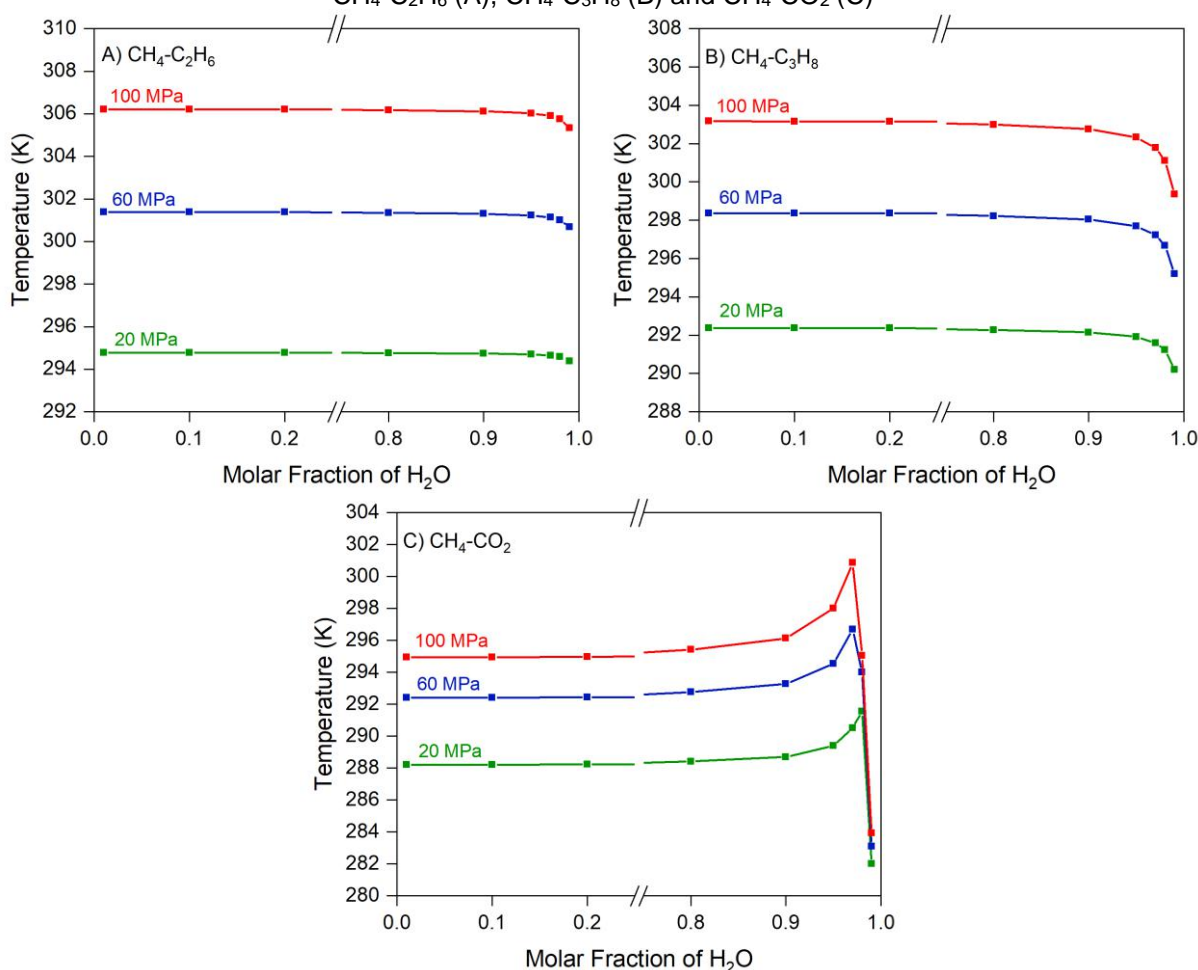
Figure 3.6 – Influence of water content on dissociation temperature of single hydrates composed of CH₄ (A), C₂H₆ (B), C₃H₈ (C) and CO₂ (D).



The most affected system in the figure above is the one forming carbon dioxide hydrate, in which the dissociation temperature decreases when the water content is above 95 mol%. For this system, the presence of small content of water (below 0.2 mol% H₂O) also leads to lower dissociation temperatures. All cases have demonstrated that the most significant changes are observed at higher pressures.

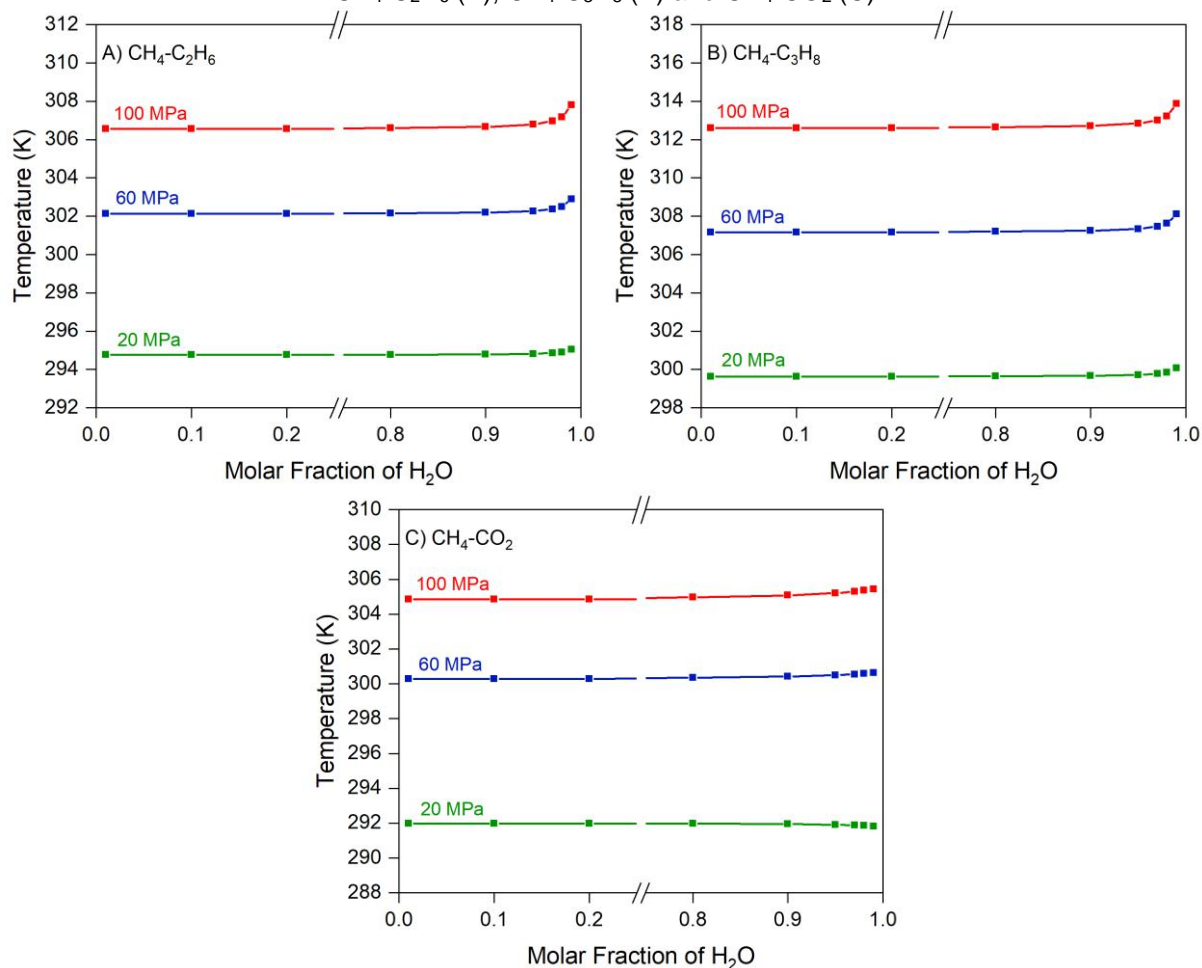
One could note in Figure 3.6 that the hydrate dissociation temperatures at gas shortage conditions tend to decrease to values approaching ice melting temperature for single guest systems. The same can be observed for double guest systems at low fractions of methane, shown in Figure 3.7, in which the systems contain 10 mol% CH₄. However, the profiles for methane-CO₂ hydrates, at this gas phase composition, are unexpectedly different since the temperature initially increases reaching the higher value at 0.97 molar fraction of water and suddenly decreases.

Figure 3.7 – Influence of water content on dissociation temperature of double hydrates (10 mol% CH₄): CH₄-C₂H₆ (A), CH₄-C₃H₈ (B) and CH₄-CO₂ (C)



The dissociation temperature profiles obtained for double guest systems at high methane fraction in gas phase (90 mol% CH₄) were also unexpected. For any system in Figure 3.8, except CH₄-CO₂ at 20 MPa, the dissociation temperature increases, mainly at gas shortage conditions, i.e, when water fraction is higher than 0.95.

Figure 3.8 – Influence of water content on dissociation temperature of double hydrates (90 mol% CH₄): CH₄-C₂H₆ (A), CH₄-C₃H₈ (B) and CH₄-CO₂ (C)

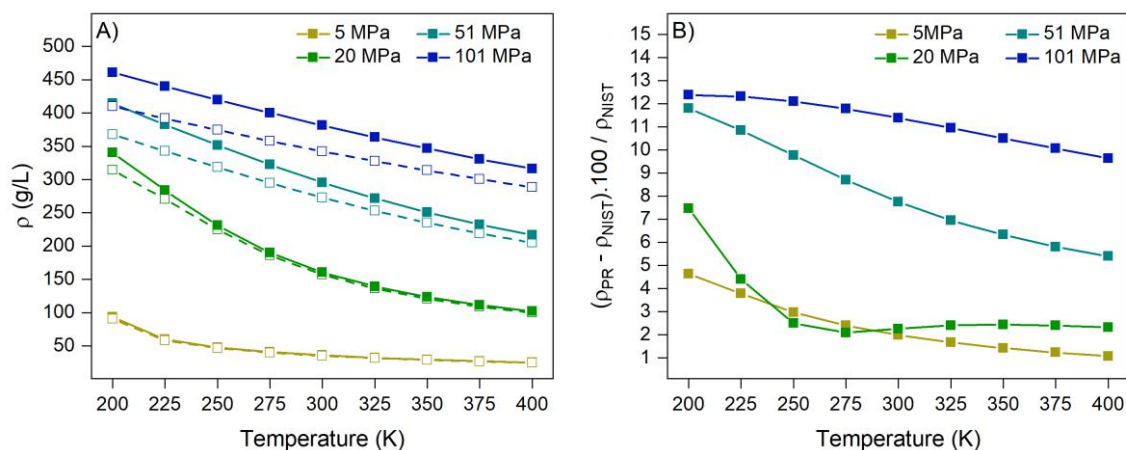


The results for all systems above reveal a slight influence of water content on equilibrium temperatures (< 0.5 K) for fractions of water lower than 0.9. In practice, higher fractions of water can be considered irrelevant for studies considering the main applications of hydrates. The system must contain enough gas molecules to form a considerable amount of hydrate and, indeed, to become a risk to the exploitation of gas and oil or promoting commercial interest. Unlike water fraction, the gas phase composition substantially affects the hydrate equilibrium temperatures along all the composition range due to the influence of guest-cavity fitting on the structure stability (NIXDORF; OELLRICH, 1997). Therefore, 0.5 molar fraction of water was chosen to design temperature-gas composition diagrams in order to evaluate the effect of gas composition on the hydrate equilibrium for all systems addressed in this work.

3.3 VALIDATION OF PENG-ROBINSON EOS AT HIGH PRESSURES

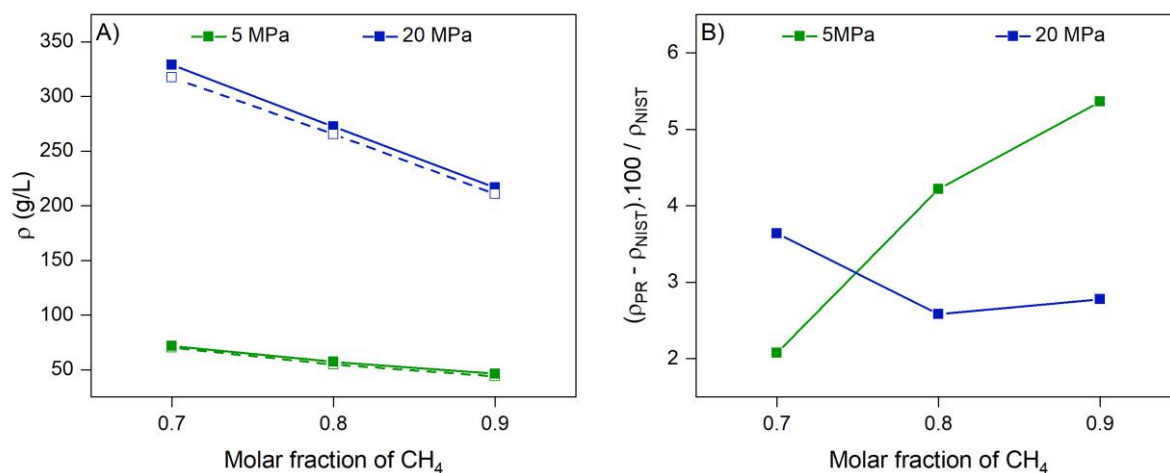
The composition of the system is a factor of significant influence on the properties of the gas hydrate formed, as discussed along this work. Although the water content does not affect the hydrate dissociation temperature when a reasonable amount of gas is present, the overall compositions of isochoric experiments (by HP- μ DSC) with binary gaseous mixtures were calculated in order to be used as “input” in calculations of equilibrium by the software (Multiflash and CSMGem). In fact, it is not possible to determine gravimetrically the exact amount of gas inside the sample cell in order to obtain the overall composition. Therefore, the total amount of gas was estimated using the Peng-Robinson equation of state (PR), considering the initial conditions of temperature and pressure and the volume occupied by the gas phase in the system (MENEZES et al., 2018). The reliability of this equation at different pressures was studied by comparing the calculated density with data reported in the literature (NIST Chemistry Webbook; SAGE et al., 1934). The van der Waals rule was applied for the binary gas mixtures, and the numerical resolution method proposed by Hoyos (2000) was used to solve the PR equation. The critical temperature, critical pressure, critical density, compressibility factor and molar mass of each gas are required for this numerical resolution, and they were obtained from the NIST database. For methane densities in Figure 3.9, the Peng-Robinson equation showed better results for higher temperatures and relatively low pressures. Considering that the gas is injected at 293.15 K, the deviation of the methane gas density can reach 12%, when comparing to the values calculated by Peng-Robinson and those from NIST at 101 MPa.

Figure 3.9 – (A) Methane densities by Peng-Robinson equation (■) and from NIST (□); (B) Relative deviations of methane densities.



The Peng-Robinson equation also provided slightly higher density values than those obtained experimentally for the binary mixture (methane and propane) at 293.15 K. However, the deviations tend to be lower at 20 MPa than at 5 MPa, as shown in Figure 3.10B.

Figure 3.10 – (A) Methane-propane densities by Peng-Robinson equation (■) and reported by Sage et al. (1934) (□); (B) Relative deviations of methane-propane densities.



Considering that the hydrate dissociation temperature remains practically unchangeable by density deviations in the order of magnitude presented in the figures, the Peng-Robinson equation is proved to be adequate to estimate the amount of gas inside the cells. However, the estimation of the overall composition may be affected by some intrinsic limitations: the volume of the cells is not perfectly known (0.19 ml according to the supplier, however, dead volumes are included and temperature variations may affect the size of polymeric materials used for sealing during the analysis); although the tubes connecting the high-pressure panel and the microcalorimeter have been coated with insulation material, there may still be heat loss and a temperature gradient between both instruments.

3.4 TRANSITIONS CONCERNING THE TEFLON RING

Some of the thermograms shown in this work, especially in chapter 6, present specific transitions of the anti-extrusion ring, a polymeric component of the microcalorimetric high-pressure cell (100 MPa), shown in Figure 2.3. This component is made of Teflon, which presents different structures in the ranges of pressure and temperature applied in this work (RAE; DATTELBAUM, 2004; RIGBY; BUNN, 1949).

This difference in the molecular arrangement and crystalline symmetry leads to transitions detected by microcalorimetry.

The resultant heat flow signal shown in thermograms is the difference between the heat flows through the sample and the reference cells, as illustrated in Figure 3.11. One could expect that the transitions occurring in both cells would be canceled in the resultant heat flow signal. However, the latter is kept empty during the experiments and thereby there is a difference in pressure between the cells, which leads the Teflon transitions to happen at different temperatures for each cell. Both transitions are endothermic, but the one from the reference cell appears as an exothermic event because it is subtracted from sample heat flow signal.

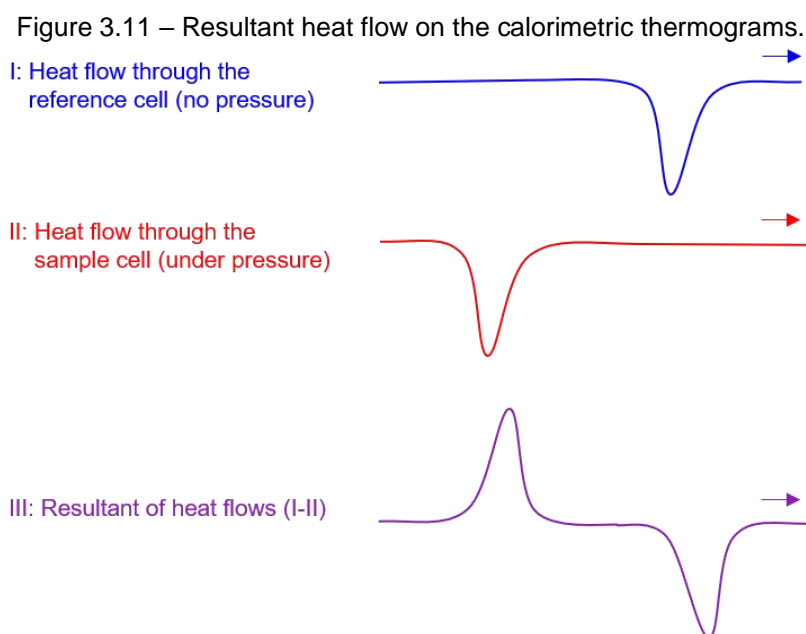
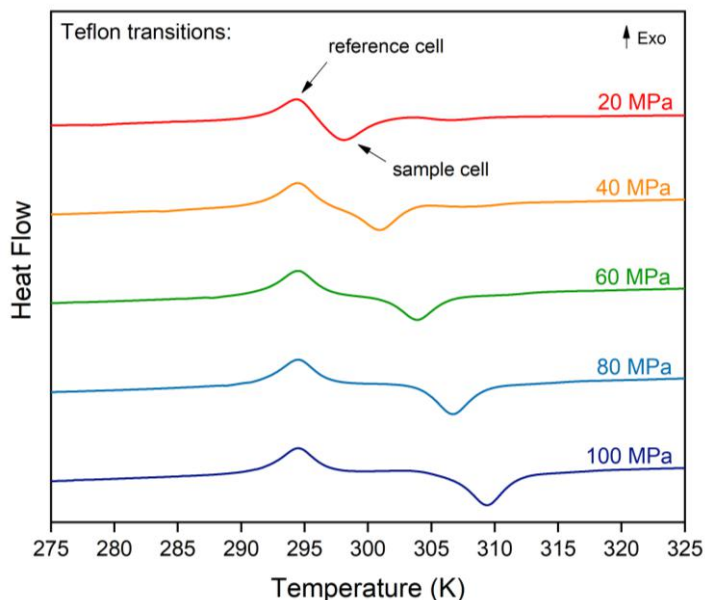


Figure 3.12 indicates the transitions observed in thermograms of heating, in the absence of water. The one related to the reference cell is always at the same position (peak at 294 K), considering this cell is kept at atmospheric pressure in all experiments. On the other hand, the Teflon peak in the sample cell is shifted to higher temperatures as the pressure of the experiments is incremented. Although the magnitude of these Teflon transitions is generally negligible in hydrate dissociation thermograms, high concentrations of inhibitors may lead to the formation of small fractions of hydrate, whose signal could be of the same magnitude of Teflon transitions, making it essential to distinguish each one to avoid misinterpretation of results.

Figure 3.12 – Teflon transitions during heating in microcalorimetric analyses: peak related to the transition in the sample cell moves according to the pressure.



Source: Menezes et al. (2020).

3.5 CONCLUSIONS

The topics addressed in this chapter are important to introduce the gas hydrates studies presented onward. The factors summarized below were considered by planning the experiments and analyzing the thermograms:

- Equilibrium lines were drawn by computational predictions for single gases and binary mixtures used in this work. Transitions concerned to phase-change of hydrocarbon and carbon dioxide should be observed in thermograms for experiments containing C_2H_6 or CO_2 below their respective critical pressures. The coexistence of heterogeneous phases in double guest systems would make difficult the estimation of the phase composition in contact with water. Therefore, pressures above the maximum one found in the envelopes were applied in order to avoid the coexistence of vapor-liquid phases composed of hydrocarbons / carbon dioxide;
- Considering that hydrocarbons or carbon dioxide should present phase change during injection and pressurization, a stabilization time is required to assure a homogeneous system before the analysis using the μ DSC apparatus;
- Equilibrium temperatures were obtained by computational predictions for hydrate-forming systems with different water contents. Although the water fraction does play a role in the hydrate dissociation temperature when there is a

shortage of gas, a negligible effect is observed (< 0.5 K) for water fractions varying below 0.9. The most affected systems are the ones containing carbon dioxide. However, a considerable amount of gas is required for practical studies on gas hydrates, thereby, the amount of water placed in the high-pressure cell should be irrelevant;

- The use of Peng-Robinson EoS was evaluated to estimate the overall composition in closed systems (applied for systems containing gas mixtures). The density of methane and methane-propane mixtures were calculated according to the pressure and compositions. The deviations obtained from the literature data represent negligible changes in the gas hydrate dissociation temperature. Thus, the PR equation was considered applicable;
- Transitions corresponding to Teflon structural changes are expected to be observed in thermograms from HP- μ DSC, especially when inhibitors are added to the system. These thermal events must be considered to avoid misinterpretation of the results.

REFERENCES

HITCHEN S.M., DEAN J.R. Properties of supercritical fluids. In: Dean J.R. (eds) *Applications of Supercritical Fluids in Industrial Analysis*. Springer, Dordrech, 1993.

HOYOS, B. Cálculo del Volumen Específico de Líquidos Puros con Ecuaciones de Estado Cúbicas. *Dyna.*, v. 129, p. 85-92, 2000.

LINSTROM, P.J.; MALLARD, W.G. (Eds.). NIST Chemistry WebBook, NIST Standard Reference Database Number 69, July 2001, *National Institute of Standards and Technology*, Gaithersburg MD, 20899 (<http://webbook.nist.gov>).

MENEZES, D.E.S.; PESSÔA FILHO, P.A.; ROBUSTILLO, M.D. Use of 1-Butyl-3-methylimidazolium-based ionic liquids as methane hydrate inhibitors at high-pressure conditions. *Chemical Engineering Science*, v. 212, 115323, 2020.

MENEZES, D.E.S.; RALHA, T.W.; FRANCO, L.F.M., PESSÔA FILHO, P.A.; ROBUSTILLO, M.D. Simulation and experimental study of methane-propane hydrate dissociation by high-pressure differential scanning calorimetry. *Brazilian Journal of Chemical Engineering*, v. 35, p. 403-414, 2018.

NIXDORF, J.; OELLRICH, L.R. Experimental determination of hydrate equilibrium conditions for pure gases, binary and ternary mixtures and natural gases. *Fluid Phase Equilibria*, v. 139, p. 325-333, 1997.

RAE, P.J.; DATTELBAUM, D.M. The properties of poly(tetrafluoroethylene) (PTFE) in compression. *Polymer*, v. 45, p. 7615-7625, 2004.

RIGBY, H.A.; BUNN, C.W. A room-temperature transition in polytetrafluoroethylene. *Nature*, v. 164, p. 583, 1949.

SAGE, B. H., LACEY, W.N., SCHAAF SMA, J. G., Phase Equilibria in Hydrocarbon Systems II. Methane – Propane System. *Industrial and Engineering Chemistry*, v. 26, 214-217, 1934.

CHAPTER 4

THERMODYNAMIC STUDY OF SINGLE-GUEST GAS HYDRATES

ABSTRACT

Binary systems formed by a single gas and water, that are susceptible to form hydrate, are studied in this chapter by HP- μ DSC and modeling. Experimental dissociation data for CH₄, C₂H₆, and CO₂ hydrates are compared to predictions from CSMGem and Multiflash software packages up to 100 MPa. Deviations of onset, peak, and endset temperatures from predictions and their representativeness as equilibrium data are evaluated. Onset temperatures have provided good reproducibility and the most accurate results for these systems, when compared to predictions. Dynamic effects on gas hydrates formation are also evaluated by varying experimental factors, such as water-sample size, cooling-heating rate, and running multicycles. Enthalpies of dissociation were determined by applying the Clapeyron Equation and by the integration of hydrate dissociation curves on thermograms and both show good agreement. New approaches were applied for the calculation of hydrate volume variation and hydration number estimation, and improvements are presented with respect to equations used in the literature. The experimental method based on multicycles was found to make the integrations easier and more accurate than the standard method since most of ice is converted to hydrate.

4.1 INTRODUCTION

Methane is the major hydrate-forming hydrocarbon because it is the most abundant in natural gas reservoirs. In addition, the methane molecular size is small enough to fit into all cages of well-known hydrate structures already identified in literature (structure I, structure II and structure H). Thereby, this hydrocarbon is the first one studied in this work up to 100 MPa, and it was used to develop most of the methodologies employed. In addition, single hydrates of ethane and carbon dioxide were also studied up to 80 and 90 MPa, respectively. Propane was not included in this chapter because it was not possible to reach pressures higher than 0.8 MPa during the gas injection into the cell. In fact, propane likely liquefies during injection into the compression chamber, as seen in section 3.1.1. For ethane and carbon dioxide

hydrate-forming systems, transitions regarding phase changes are observed for pressures below their critical points, as expected: vapor-liquid transition during the cooling and liquid-vapor during the heating. Transitions related to compressed liquid and supercritical fluid are not observed for pressures above the critical point, even occurring within the temperature range of the analysis. This is due to the absence of a sudden change in density or in other structural properties that could produce a heat flow variation in the microcalorimeter.

Computational simulation on gas hydrates is a powerful tool used to predict the amount of exploitable energy in reservoirs and, nowadays, mainly to define operational conditions based on hydrate thermodynamic properties for flow assurance applications. Also, simulations can be useful to an intrinsic understanding of thermodynamic behavior for specific systems. In this chapter, reliability and accuracy of two commercial software packages, CSMGem and Multiflash, are evaluated against experimental data obtained by high-pressure microcalorimetry, which has been widely used in studies of gas hydrates. As mentioned before, this technique allows to obtain the temperature and enthalpy of gas hydrate formation and dissociation or any process involving a transition with energy transfer.

Dissociation enthalpy of single hydrates was determined by the integration of the thermograms and the Clapeyron equation, according to the methods described in section 2.1.4.2. The first method, based on the works from Gupta et al. (2007, 2008), consists of estimating the hydrate enthalpy by integrating the heat absorbed during ice melting and hydrate dissociation. The amount of water consumed by the ice formation is subtracted from the total volume of water added to the sample cell in order to find the amount of water consumed by the hydrate formation. Then, the enthalpy per mol of CH_4 is given by the stoichiometric balance of the hydrate reaction. On the other side, an alternative method was applied in this work for estimating the enthalpy of hydrate dissociation using the Clapeyron equation. Sloan and Fleyfel (1992, 1994) suggest that the heat of dissociation depends mainly on the type and proportion of cavities occupied in the hydrate structure and is practically independent of the gas species and composition. This relation is demonstrated based on the Clausius-Clapeyron equation (1.7). The slope of the hydrate dissociation line ($\ln P$ vs $1/T$) is similar for different hydrates whose guest molecules occupy the same cavity type (SLOAN; KOH, 2008). From this equation, therefore, it is possible to determine the relation between the type of cavity occupied with the calculated dissociation heat, regardless of the species of

the guest molecule. However, this simplified equation does not provide accurate results due to restrictions cited in section 1.3.1: the composition of guest molecules in each cavity does not vary significantly; the volume variation between the condensed and gaseous phases is negligible; the gas phase composition remains constant. Thereby, the method applied here is based on the work reported by Anderson (2004) and accounts for the finite volumes of all phases, the non-ideality of the vapor phase, and the solubility of hydrocarbons in water. Some mathematical improvements are presented mainly concerning to the hydrate volume estimation so that the method could also be appropriately used for carbon dioxide and ethane hydrates. The equations used to describe the dissociation data, the fit parameters, and volume changes are shown in the Appendix. In this work, the gas species shows somehow affect the enthalpy of dissociation of gas hydrates.

Lastly, some experimental factors are evaluated in order to verify their possible effects on the hydrate properties. Considering the Gibbs phase rule, a binary system in a three-phase equilibrium state presents only one degree of freedom. Therefore, only one independent coordinate (pressure, temperature, or composition) is required to define the thermodynamic state of the system. Ergo given a specified pressure, the temperature at which the three phases coexist is also determined, regardless of the water/gas ratio. Nevertheless, considering a non-equilibrium state of the system and the absence of mixing, dynamics effects may interfere in the equilibrium and homogeneity of the structure, affecting the hydrate properties, including the dissociation temperature. Thus, three experimental factors, which may affect the mass transfer and the hydrate homogeneity, are addressed in this work: i) amount of H₂O; ii) cooling-heating rates; iii) multicycles.

4.2 SPECIFIC EXPERIMENTAL CONDITIONS

Computational Analysis: Two software packages were used to calculate equilibrium state of gas hydrates: the CSMGem code Version 1.10 (January 1, 2007), that uses the SRK equation of state, and the Multiflash 6.0, that applies the cubic plus association (CPA) equation of state for liquid and vapor phases. Both use the van der Waals and Platteeuw model for the hydrate phase, described in equation 1.3.1.

Experimental Configuration: Milli-Q water was used in all experiments performed by high-pressure microcalorimetry. The gases applied in the analysis were

methane (99.5%), ethane (99.95%), and carbon dioxide (99.99%). The reference cell was kept empty, whereas water was added into the sample cell. The experimental procedures used in this chapter are based on methodologies described in section 2.1.4 of this work. Some of the experiments were performed at different heating rates in order to verify the possible influence of kinetic factors on the dissociation data.

4.3 METHANE-WATER SYSTEM

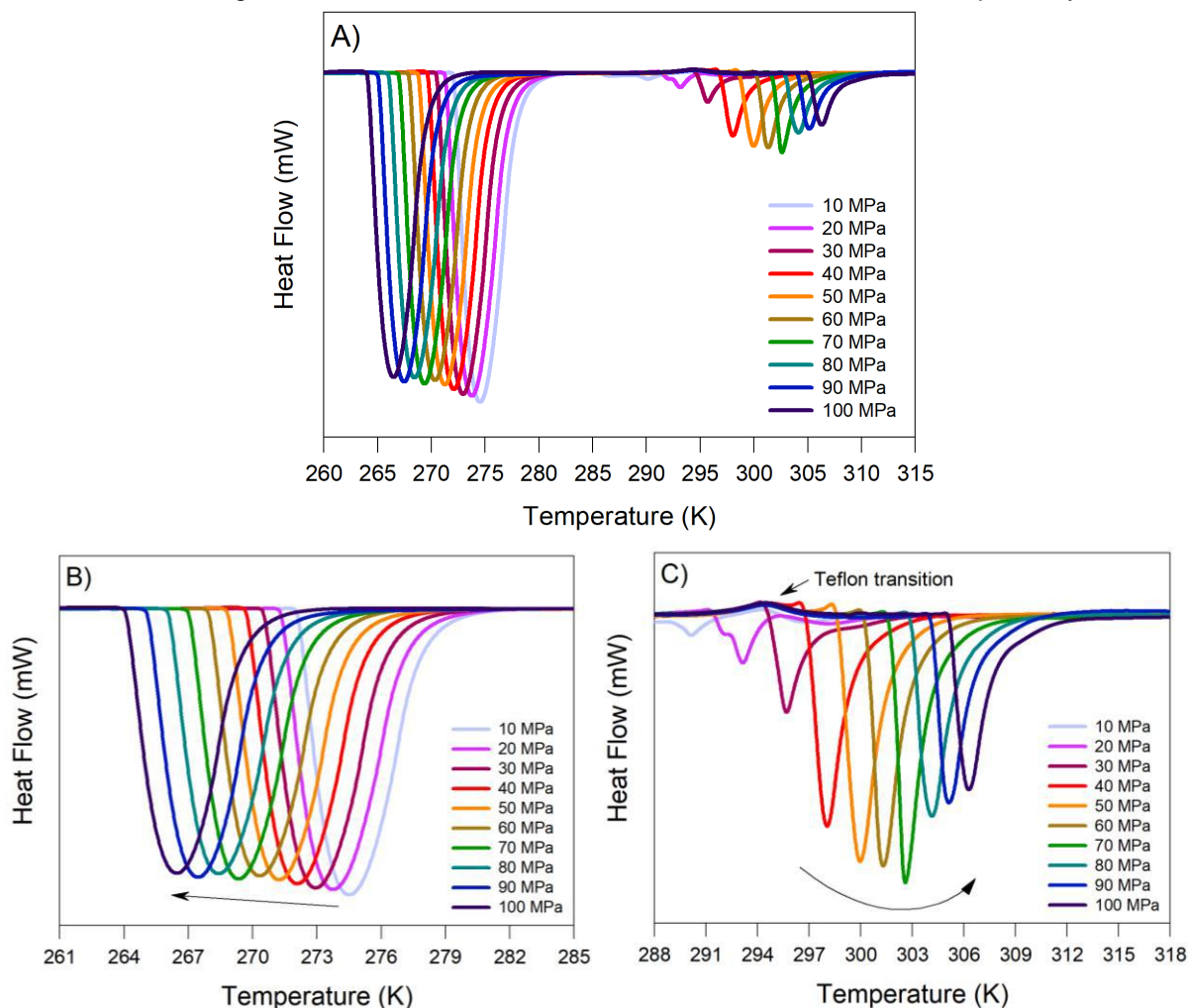
4.3.1 Equilibrium Data for CH₄ Hydrates by High Pressure Microcalorimetry

Figure 4.1 shows the thermograms of the analyses performed at 1 K·min⁻¹ at different pressures by using the standard method. Regarding the ice melting, one can note that the curve shifts to the left at higher pressures (Figure 4.1B). This phenomenon is explained by a crystalline rearrangement while the hexagonal ice approaches to the region of ice III, as can be checked in water phase diagrams (SAHLE et al., 2013; SANZ et al., 2004). The hydrate dissociation, in turn, shifts to higher temperatures as the pressure increases, which agrees to the literature results (SLOAN; KOH, 2008). The break of hydrogen bonds and the delivery of gas from the hydrate phase become harder under higher pressures, requiring higher temperatures for the structure to be dissociated.

Considering that the heat flow measured by the microcalorimeter is an extensive property, Figure 4.1 suggests that an increase in pressure favors hydrate rather than ice formation since the diffusivity of the gas molecules in water is enhanced as the pressure of the system increases. In other words, higher pressure leads to more gas molecules available in the aqueous phase, favoring hydrate formation and, consequently, decreasing the ice fraction. However, the amount of hydrate formed above 70 MPa surprisingly lessens in the figure. One possible reason for this is that there may have been a gas leak through the sealing elastomer, which may not have been noticeable because methane was continuously supplied. This may have implied that a fraction of the water was also dragged out of the cell during pressurization. On the other hand, the decrease in the area corresponding to the ice melting may be related to the lower enthalpy of ice dissociation at pressures relatively close to the change in the crystal structure (DENYS et al, 2001). Nevertheless, the dissociation temperatures from these analyses agree to others made by using different water

samples. Finally, one can clearly observe in Figure 4.1C the exothermic transition from the Teflon ring, as discussed in Chapter 3.4.

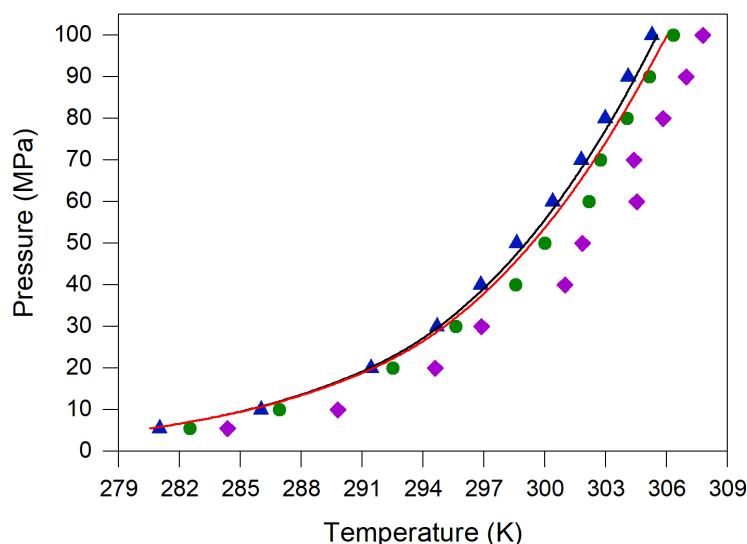
Figure 4.1 – Heating thermograms of the CH₄-H₂O system at 1 K·min⁻¹ and at different pressures (A). Ice melting and hydrate dissociation are expanded in B and C figures, respectively.



Essays for equilibrium determination were performed in triplicate (except to 30 and 70 MPa), and the data for ice melting and methane hydrate dissociation from 5.5 to 100 MPa are presented in Table 4.1 and 4.2, respectively. Figure 4.2 represents the average values for onset, peak and endset points of the dissociation curves. The predictions obtained for methane hydrates from the CSMGem and Multiflash software are also indicated in Figure 4.2. The onset temperature obtained from thermograms not only marks the beginning of the dissociation process but, in absence of polymorphism or overlapped transitions, it is usually the point that approaches to the equilibrium more accurately than peak and endset temperatures, mainly because it is less susceptible to the heating rate and sample mass. Sample size and crystalline

heterogeneity caused by a non-uniform distribution of nuclei and different growth rates lead to the obtention of broader curves, which affect peak and endset values. These factors explain the lower absolute deviations obtained from CSMGem predictions for onset temperatures.

Figure 4.2 – Dissociation data of CH₄ hydrates obtained by HP- μ DSC at 1 K·min⁻¹: (▲) onset temperatures; (●) peak temperatures; (◆) endset temperatures. Black lines refer to CSMGem predictions and red lines, to Multiflash.



Experimental data and absolute deviations from computational predictions are shown in Tables 4.1 and 4.2 for ice melting and hydrate dissociation, respectively. Standard deviations from ice melting data tend to be slightly lower than hydrate dissociation data. This may be due to impurities in the gas phase and/or heterogeneity of the hydrate structure. The hydrate onset temperatures are slightly lower than predictions likely due to a more significant presence of empty cavities throughout the structure, considering that the absence of mixture limits the mass transfer into the liquid phase. Nevertheless, all standard and average absolute deviations of onset temperatures are within the experimental uncertainty, thus proving the efficiency of this methodology in providing equilibrium data for gas hydrates. On the other hand, Multiflash predictions seem to deviate from CSMGem predictions as pressure increases and approach to peak temperatures.

The determination of methane hydrate dissociation points by HP- μ DSC at lower pressures than 5.5 MPa has shown to be inaccurate, mainly at 1 K·min⁻¹. As can be verified in Figure 4.3, the hydrate dissociation curve overlaps the ice melting curve

Table 4.1 – Dissociation data of ice melting preceding the CH₄ hydrate dissociation by HP- μ DSC and the respective absolute deviations (AD) from computational predictions

P (MPa)	CSMGem (K)	HP- μ DSC – Ice – T _{MELTING} (K)					
		Onset	AD	Peak	AD	Endset	AD
5.5	272.74	272.46	0.28	275.50	2.76	279.73	6.99
		272.46	0.28	274.85	2.11	278.90	6.16
		272.47	0.27	275.06	2.32	278.72	5.98
	<i>Avg.</i>	272.46	0.28	275.14	2.39	279.12	6.37
	<i>Std. (σ)</i>	0.00		0.27		0.44	
10	272.4	272.14	0.26	274.51	2.11	277.89	5.49
		272.33	0.07	273.66	1.26	275.88	3.48
		272.13	0.27	274.46	2.06	277.47	5.07
	<i>Avg.</i>	272.20	0.20	274.21	1.81	277.08	4.68
	<i>Std. (σ)</i>	0.09		0.39		0.87	
20	271.61	271.38	0.23	273.76	2.15	277.17	5.56
		271.38	0.23	273.52	1.91	276.04	4.43
		271.37	0.24	273.67	2.06	276.89	5.28
	<i>Avg.</i>	271.38	0.23	273.65	2.04	276.70	5.09
	<i>Std. (σ)</i>	0.00		0.10		0.48	
30	270.8	270.58	0.22	272.94	2.14	276.25	5.45
		270.74	0.06	271.99	1.19	274.14	3.34
	<i>Avg.</i>	270.66	0.14	272.47	1.66	275.20	4.39
	<i>Std. (σ)</i>	0.08		0.47		1.06	
40	269.96	269.77	0.19	272.10	2.14	275.32	5.36
		269.73	0.23	271.37	1.41	274.39	4.43
		269.65	0.31	272.67	2.71	276.04	6.08
	<i>Avg.</i>	269.72	0.24	272.05	2.09	275.25	5.29
	<i>Std. (σ)</i>	0.05		0.53		0.68	
50	269.08	268.90	0.18	271.23	2.15	274.40	5.32
		268.90	0.18	271.12	2.04	275.11	6.03
		268.83	0.25	270.67	1.59	274.78	5.70
	<i>Avg.</i>	268.88	0.20	271.01	1.93	274.76	5.68
	<i>Std. (σ)</i>	0.03		0.24		0.29	
60	268.18	268.01	0.17	270.34	2.16	273.50	5.32
		267.88	0.30	270.77	2.59	273.56	5.38
		267.92	0.26	270.48	2.30	274.25	6.07
	<i>Avg.</i>	267.94	0.24	270.53	2.35	273.77	5.59
	<i>Std. (σ)</i>	0.05		0.18		0.34	

Continues

Continuation

P (MPa)	CSMGem (K)	HP- μ DSC – Ice – T _{MELTING} (K)						
		Onset	AD	Peak	AD	Endset	AD	
70	267.25	267.09	0.16	269.34	2.09	272.50	5.25	
		267.11	0.14	269.41	2.16	272.99	5.74	
		<i>Avg.</i>	<i>267.10</i>	<i>0.15</i>	<i>269.38</i>	<i>2.13</i>	<i>272.75</i>	<i>5.50</i>
		<i>Std. (σ)</i>	<i>0.01</i>	<i>0.04</i>		<i>0.25</i>		
80	266.30	266.13	0.17	268.43	2.13	271.59	5.29	
		266.06	0.24	267.82	1.52	270.03	3.73	
		266.10	0.20	268.03	1.73	272.44	6.14	
		<i>Avg.</i>	<i>266.10</i>	<i>0.20</i>	<i>268.09</i>	<i>1.79</i>	<i>271.35</i>	<i>5.05</i>
		<i>Std. (σ)</i>	<i>0.03</i>	<i>0.25</i>		<i>1.00</i>		
90	265.31	265.14	0.17	267.46	2.15	270.48	5.17	
		265.09	0.22	267.41	2.10	270.74	5.43	
		265.10	0.21	266.97	1.66	270.71	5.40	
		<i>Avg.</i>	<i>265.11</i>	<i>0.20</i>	<i>267.28</i>	<i>1.97</i>	<i>270.64</i>	<i>5.33</i>
		<i>Std. (σ)</i>	<i>0.02</i>	<i>0.22</i>		<i>0.12</i>		
100	264.29	264.12	0.17	266.47	2.18	269.47	5.18	
		264.06	0.23	265.78	1.49	268.24	3.95	
		264.13	0.16	266.29	2.00	268.76	4.47	
		<i>Avg.</i>	<i>264.10</i>	<i>0.19</i>	<i>266.18</i>	<i>1.89</i>	<i>268.82</i>	<i>4.53</i>
		<i>Std. (σ)</i>	<i>0.03</i>	<i>0.29</i>		<i>0.50</i>		

Conclusion

Table 4.2 – Dissociation data of CH₄ hydrates by HP- μ DSC and the respective absolute deviations (AD) from computational predictions.

P (MPa)	HP- μ DSC – CH ₄ Hydrate – T _{DISSOCIATION} (K)									
	Onset	AD		Peak	AD		Endset	AD		
		CSMGem	Multiflash		CSMGem	Multiflash		CSMGem	Multiflash	
5.5	281.42	0.86	0.90	282.21	1.65	1.69	283.31	2.75	2.79	
	280.85	0.29	0.33	282.70	2.14	2.18	284.91	4.35	4.39	
	280.76	0.20	0.24	282.61	2.05	2.09	284.85	4.29	4.33	
	<i>Avg.</i>	<i>281.01</i>	<i>0.45</i>	<i>0.49</i>	<i>282.51</i>	<i>1.95</i>	<i>1.98</i>	<i>284.36</i>	<i>3.80</i>	<i>3.83</i>
	<i>Std. (σ)</i>		<i>0.29</i>		<i>0.21</i>		<i>0.74</i>			
10	285.81	0.25	0.34	286.95	0.89	0.80	291.46	5.40	5.31	
	286.27	0.21	0.12	286.48	0.42	0.33	287.47	1.41	1.32	
	285.94	0.12	0.21	287.40	1.34	1.25	290.45	4.39	4.30	
	<i>Avg.</i>	<i>286.01</i>	<i>0.19</i>	<i>0.22</i>	<i>286.94</i>	<i>0.88</i>	<i>0.79</i>	<i>289.79</i>	<i>3.73</i>	<i>3.64</i>
	<i>Std. (σ)</i>		<i>0.19</i>		<i>0.38</i>		<i>1.69</i>			

Continues

Continuation

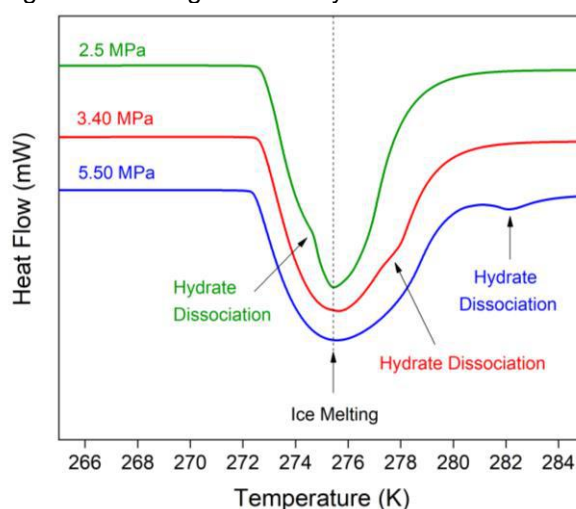
HP- μ DSC – CH ₄ Hydrate – T _{DISSOCIATION} (K)									
P (MPa)	Onset	AD		Peak	AD		Endset	AD	
		CSMGem	Multiflash		CSMGem	Multiflash		CSMGem	Multiflash
20	291.40	0.36	0.56	292.18	0.42	0.22	294.26	2.50	2.30
	291.49	0.27	0.47	292.97	1.21	1.01	294.97	3.21	3.01
	291.42	0.34	0.54	292.44	0.68	0.48	294.54	2.78	2.58
<i>Avg.</i>	291.44	0.32	0.52	292.53	0.77	0.57	294.59	2.83	2.63
<i>Std. (σ)</i>		0.04			0.33			0.29	
30	294.65	0.28	1.50	295.67	0.74	2.52	297.12	2.19	3.97
	294.72	0.21	1.57	295.56	0.63	2.41	296.63	1.70	3.48
	294.69	0.25	1.54	295.62	0.69	2.47	296.88	1.94	3.73
<i>Avg.</i>	294.69	0.25	1.54	295.62	0.69	2.47	296.88	1.94	3.73
<i>Std. (σ)</i>		0.04			0.06			0.25	
40	297.01	0.22	0.50	298.15	0.92	0.64	299.68	2.45	2.17
	296.79	0.44	0.72	298.19	0.96	0.68	301.10	3.87	3.59
	296.74	0.49	0.77	299.37	2.14	1.86	302.20	4.97	4.69
<i>Avg.</i>	296.85	0.38	0.67	298.57	1.34	1.06	300.99	3.76	3.48
<i>Std. (σ)</i>		0.12			0.57			1.03	
50	298.68	0.42	0.72	299.96	0.86	0.56	301.73	2.63	2.33
	298.57	0.53	0.83	299.73	0.63	0.33	301.61	2.51	2.21
	298.55	0.55	0.85	300.33	1.23	0.93	302.20	3.10	2.80
<i>Avg.</i>	298.60	0.50	0.80	300.01	0.91	0.60	301.85	2.75	2.44
<i>Std. (σ)</i>		0.06			0.25			0.25	
60	300.39	0.30	0.63	301.30	0.61	0.28	303.02	2.33	2.00
	300.24	0.45	0.78	302.55	1.86	1.53	304.94	4.25	3.92
	300.53	0.16	0.49	302.73	2.04	1.71	305.63	4.94	4.61
<i>Avg.</i>	300.39	0.30	0.63	302.19	1.50	1.17	304.53	3.84	3.51
<i>Std. (σ)</i>		0.12			0.64			1.10	
70	301.82	0.26	0.63	302.59	0.51	0.14	304.30	2.22	1.85
	301.73	0.35	0.72	302.72	0.64	0.27	304.44	2.36	1.99
	301.78	0.30	0.67	302.66	0.58	0.21	304.37	2.29	1.92
<i>Avg.</i>	301.78	0.30	0.67	302.66	0.58	0.21	304.37	2.29	1.92
<i>Std. (σ)</i>		0.04			0.07			0.07	
80	303.00	0.34	0.74	304.13	0.79	0.39	305.82	2.48	2.08
	303.01	0.33	0.73	304.02	0.68	0.28	305.48	2.14	1.74
	302.91	0.43	0.83	304.01	0.67	0.27	306.16	2.82	2.42
<i>Avg.</i>	302.97	0.37	0.76	304.05	0.71	0.32	305.82	2.48	2.08
<i>Std. (σ)</i>		0.04			0.05			0.28	

Continues

Continuation

HP- μ DSC – CH ₄ Hydrate – T _{DISSOCIATION} (K)									
P (MPa)	Onset	AD		Peak	AD		Endset	AD	
		CSMGem	Multiflash		CSMGem	Multiflash		CSMGem	Multiflash
90	304.17	0.31	0.75	305.12	0.64	0.20	306.82	2.34	1.90
	304.04	0.44	0.88	305.33	0.85	0.41	307.05	2.57	2.13
	304.10	0.38	0.82	305.04	0.56	0.12	307.03	2.55	2.11
Avg.	304.10	0.38	0.81	305.16	0.68	0.25	306.97	2.49	2.05
Std. (σ)		0.05			0.12			0.10	
100	305.19	0.34	0.82	306.27	0.74	0.26	307.21	1.68	1.20
	305.25	0.28	0.76	306.60	1.07	0.59	308.55	3.02	2.54
	305.35	0.18	0.66	306.16	0.63	0.15	307.60	2.07	1.59
Avg.	305.26	0.27	0.74	306.34	0.81	0.34	307.79	2.26	1.78
Std. (σ)		0.07			0.19			0.56	

Conclusion

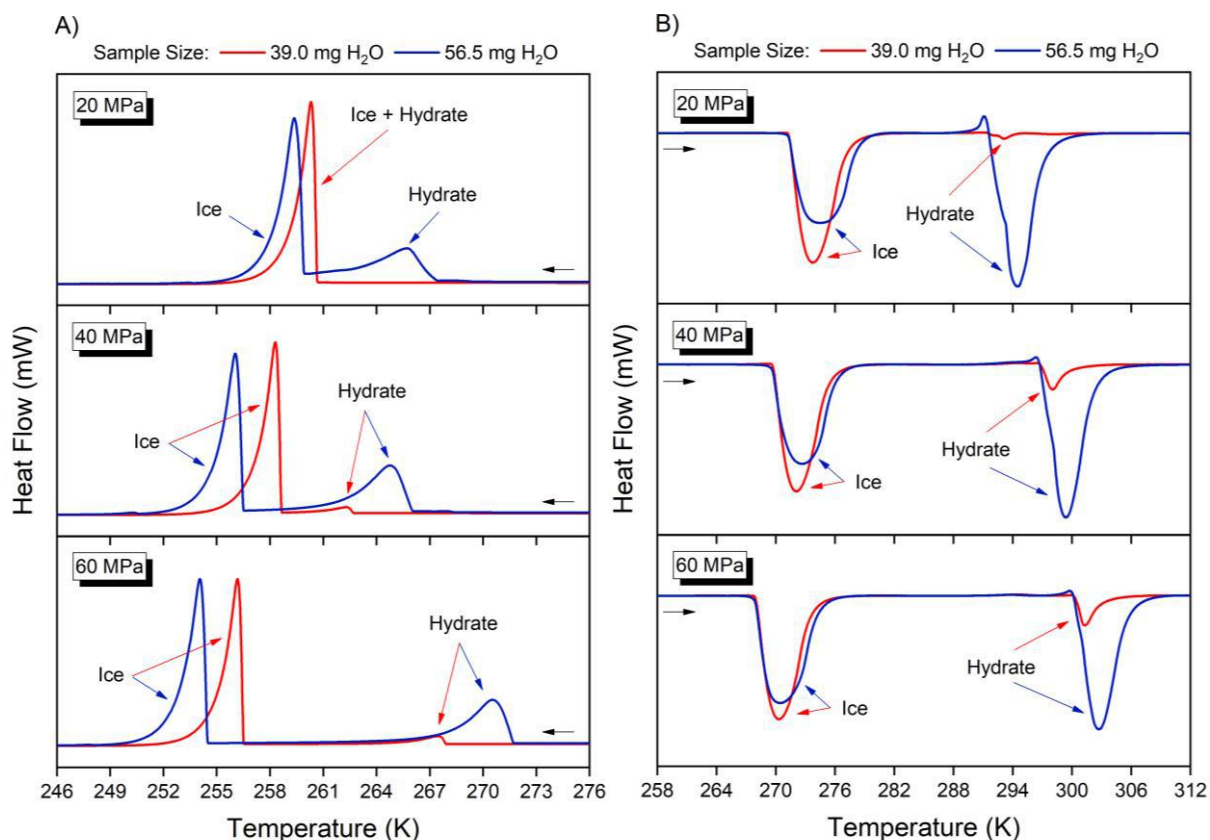
Figure 4.3 – Overlapping of ice melting and CH₄ hydrate dissociation curves at low pressures.

4.3.2 Effect of H₂O Sample Size

The onset temperatures from Table 4.2 were obtained using different amounts of water and still present low standard deviation values and excellent agreement to predictions. H₂O content seems not to affect the hydrate thermodynamic properties of binary systems, but the results below indicate that this factor plays a role in the kinetics and the proportion of ice/hydrate formed. Figure 4.4 compares the thermograms of formation (A) and dissociation (B) of two hydrates containing different amounts of water inside the cell. Davies et al. (2009) reported a tendency for hydrate nucleation prior to ice formation at pressures above 15 MPa and suggested a higher activation energy

barrier between ice and hydrate compared to water and hydrate under certain conditions.

Figure 4.4 – Thermograms of cooling (A) and heating (B) indicating the effect of water sample size on the ice / CH₄ hydrate formation and dissociation, respectively.



The distance between hydrate and ice formation peaks, for any case of Figure 4.4A, is noticeably longer in the sample containing the largest amount of water (blue thermograms). The smaller blue peaks (56.4 mg H₂O), related to the hydrate formation, tend to precede the corresponding red peaks (39.0 mg H₂O), from right to left. At the same time, the larger blue peaks, related to the ice formation, appear after the red peaks. Therefore, larger sample of water (blue lines) seems to favor the hydrate formation kinetics and retard the formation of ice.

The heating plots (Figure 4.4B) unquestionably indicate that the sample containing the largest amount of water (56.5 mg) led to higher fractions of hydrates than the one containing 39 mg H₂O. Despite this, ice fractions were expected to be even larger than hydrate fractions when water content is higher, assuming that hydrate formation is limited to the interface area between the gas and aqueous phases (initially assuming the same area in this case) due to the low methane solubility and no mixing

within the cell. A possible reason for the opposite effect observed is that the gas injection and pressurization may cause the liquid phase to spread into smaller droplets over the cell walls so that the total interfacial area (water – gas molecules) is enhanced due to droplets disposal and size. Thus, the hydrate fraction may be favored by the more numerous droplets available in the system as larger the sample of water. On the other hand, if the aqueous phase covers the entire base of the cell, the area of the concave water meniscus may be related to the amount of water, i.e., the meniscus may be higher if the volume of water is larger, thus increasing the interfacial area. In this case, the hydrate fraction also may be favored as larger the water content due to the greater contact between gas and water molecules. Anyway, the onset points of dissociation curves in Figure 4.4B are very similar, although the hydrate and ice fractions depend on the H₂O sample size. As mentioned above, the water content should not be relevant to the thermodynamic properties of single hydrates, except in cases of gas shortage, as seen in section 3.2.

4.3.3 Effect of Cooling and Heating Rates

Dissociation points related to methane hydrates obtained at different cooling/heating rates by HP- μ DSC are shown in Table 4.3, as well as their deviations from CSMGem predictions. It is worth to mention that, although onset temperature of melting generally is not affected by the heating rate, it could be slightly changed in cases of chemical reactions, impurities or structural heterogeneity. Interestingly, the onset temperatures tend to decrease as faster the heating (Figure 4.5A). It is believed that this phenomenon is not related to the heating process itself, but to the cooling. As it is known, smaller crystals are formed when higher cooling rates are applied (CONLEY et al., 2000). Thus, it is reasonable to suppose that structural irregularities, such as empty cavities and intergranular defects, are also magnified at higher cooling rates. In other words, the structure may become more heterogenous when the driving force induces the crystals to grow more rapidly. This assumption is consistent since the gas hydrate is formed from distinct phases in absence of mixing. Several works in the literature point out that the cooling / heating rate interferes on the formation of several materials, including hydrates and inclusion compounds (CHROSTEK, 2016; KE; SVARTAAS, 2011; ZHANG et al., 2019; WELLEN et al., 2015). Therefore, a higher heterogeneity of the hydrate lattice could explain the slightly lower dissociation

temperature by cooling / heating the system faster. Nevertheless, this difference between the onset points is negligible in practice.

Table 4.3 – Dissociation data of CH₄ hydrates at different heating rates and their respective absolute deviations (AD) from computational predictions.

P (MPa)	Ø (K·min ⁻¹)	HP-µDSC – CH ₄ Hydrate – T _{DISSOCIATION} (K)					
		Onset	AD	Peak	AD	Endset	AD
10	0.2	286.28	0.22	286.46	0.4	287.2	1.14
	0.5	286.15	0.09	287.24	1.18	288.66	2.60
	1	285.93	0.13	287.40	1.34	290.46	4.40
20	0.2	291.74	0.02	292.92	1.16	293.91	2.15
	0.5	291.66	0.10	293.00	1.24	294.29	2.53
	1	291.49	0.27	292.97	1.21	294.97	3.21
40	0.2	296.98	0.25	298.39	1.16	299.31	2.08
	0.5	296.96	0.27	298.40	1.17	299.38	2.15
	1	297.01	0.22	298.15	0.92	299.68	2.45
60	0.2	300.50	0.19	301.03	0.34	301.64	0.95
	0.5	300.44	0.25	301.44	0.75	302.35	1.66
	1	300.24	0.45	302.55	1.86	304.94	4.25
80	0.2	303.21	0.13	303.73	0.39	304.38	1.04
	0.5	303.14	0.20	304.07	0.73	305.18	1.84
	1	303.01	0.33	304.02	0.68	305.48	2.14
100	0.2	305.48	0.05	305.91	0.38	306.57	1.04
	0.5	305.40	0.13	306.17	0.64	307.34	1.81
	1	305.25	0.28	306.60	1.07	308.55	3.02

All the onset temperature deviations are within the experimental uncertainty, and they are lower at 0.2 K·min⁻¹, except at 10 and 40 MPa (Figure 4.5B). This indicates that this heating rate provides more accurate results than higher ones. However, while these analyses last about 13 hours, those performed at 1 K·min⁻¹ last less than 5 hours, and the onset results are still satisfactory. In contrast, the peak and endset temperatures are noticeably influenced by the heating rate, and their absolute deviations from the predictions are relevant. Figures 4.6 and 4.7 show that both the peak and endset temperatures and their respective AD tend to increase as higher the heating rate, due to its effect on the width of the curves.

Figure 4.5 – Effect of the heating rate on the onset temperatures corresponding to CH₄ hydrate dissociation curves (A) and their respective absolute deviations (B).

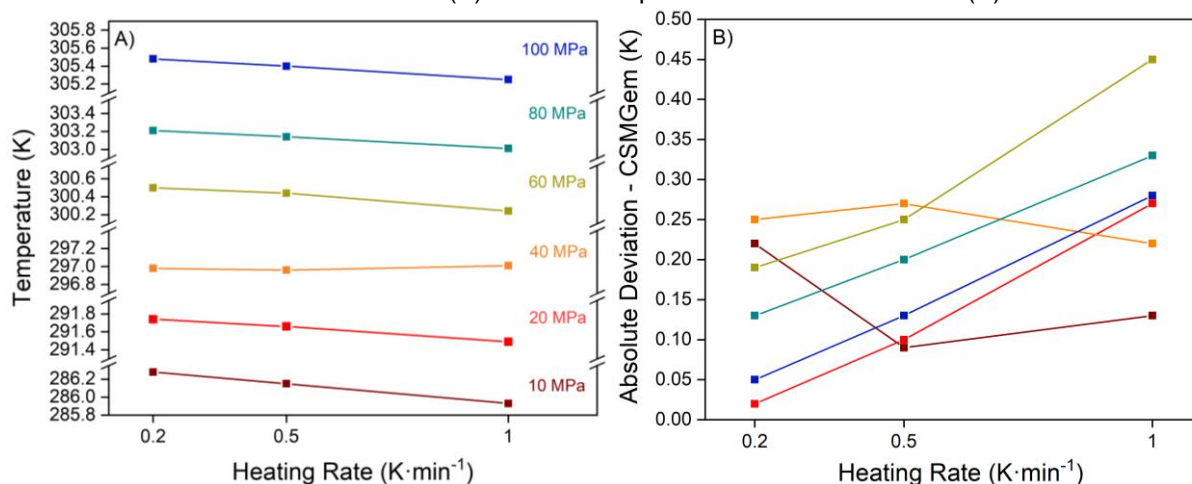


Figure 4.6 – Effect of the heating rate on the peak temperatures corresponding to CH₄ hydrate dissociation curves (A) and their respective absolute deviations (B).

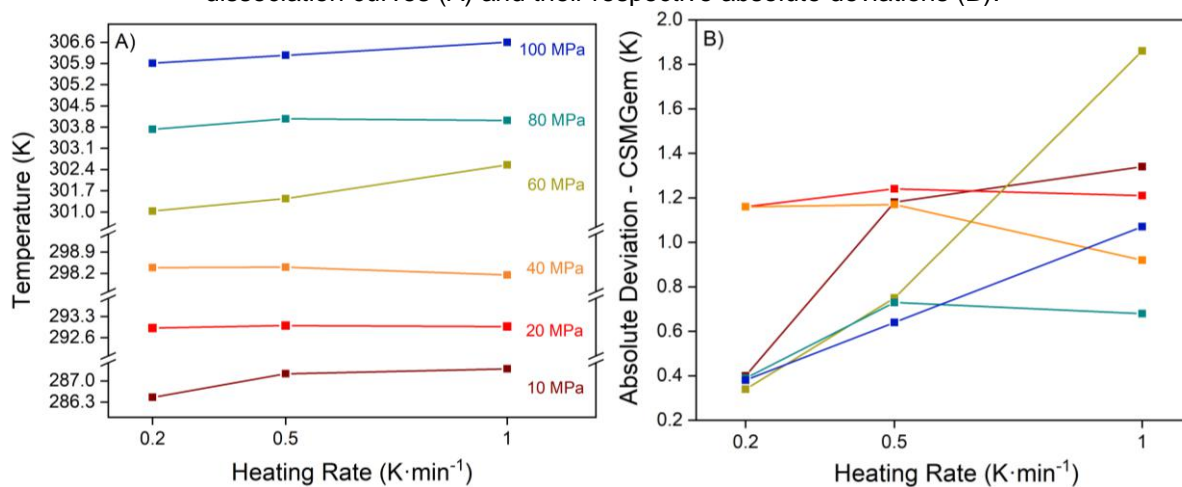
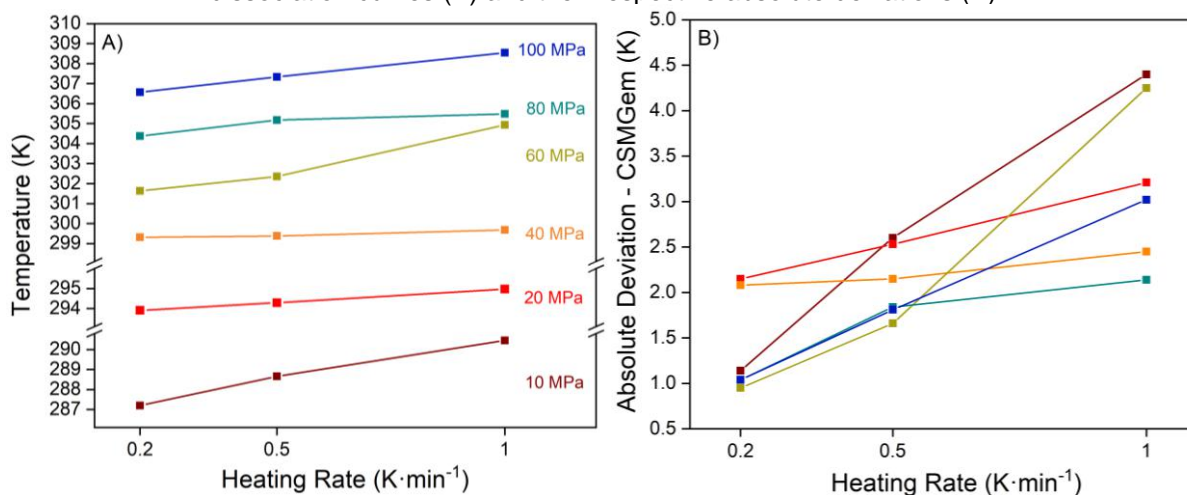


Figure 4.7 – Effect of the heating rate on the endset temperatures corresponding to CH₄ hydrate dissociation curves (A) and their respective absolute deviations (B).



Taking into account all the considerations above, the onset point of the dissociation curve by running analyses at $1 \text{ K}\cdot\text{min}^{-1}$ was chosen as the primary method for determining hydrate equilibrium in this work, based on the evaluation of the time of analysis required and the absolute deviations obtained. However, the determination of the onset temperature may be hampered by overlapping curves, polymorphism, or heterogeneity of the structure in some cases that will be discussed forward, especially for ternary diagrams in Chapter 5.

4.3.4 Effect of Multicycles

In Table 4.4, dissociation data obtained after multicycles are compared to the ones by the standard method, in which only one cycle is run.

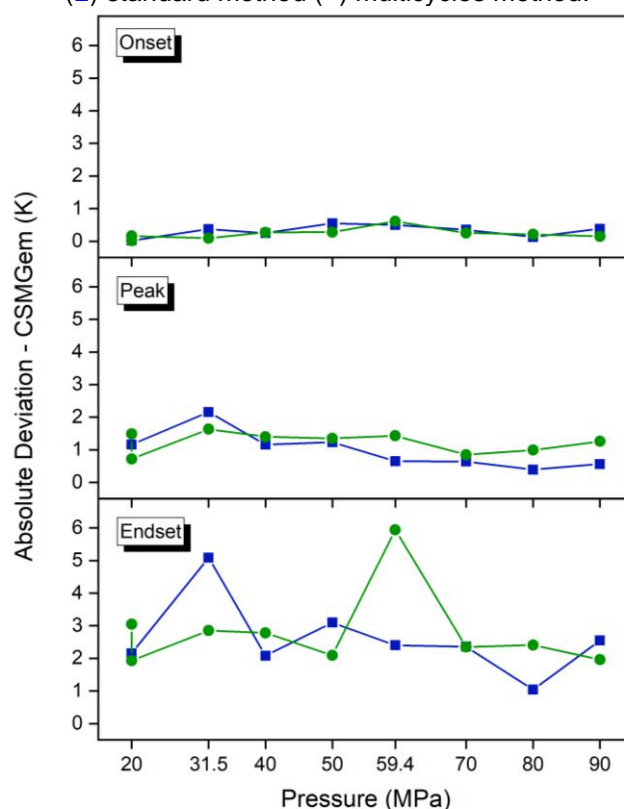
Table 4.4 – Dissociation data of CH_4 hydrates by standard and multicycles methods, and their respective absolute deviations (AD) from computational predictions.

P (MPa)	n° Cycles	\emptyset ($\text{K}\cdot\text{min}^{-1}$)	H_2O (mg)	Ice Conv. (%)	HP- μ DSC – CH_4 Hydrate – $T_{\text{DISSOCIATION}}$ (K)					
					Onset	AD (CSMGem)	Peak	AD (CSMGem)	Endset	AD (CSMGem)
20	1	0.2	31.0	-	291.74	0.02	292.92	1.16	293.91	2.15
	22	0.2	56.5	98.50	291.74	0.02	293.25	1.49	294.81	3.05
	22	0.2	41.6	98.99	291.60	0.16	292.48	0.72	293.69	1.93
31.5	1	1.0	56.5	-	294.95	0.37	297.48	2.16	300.41	5.09
	17	0.2	56.5	96.02	295.23	0.09	296.95	1.63	298.17	2.85
40	1	0.2	31.0	-	296.98	0.25	298.39	1.16	299.31	2.08
	20	0.2	56.5	97.33	296.96	0.27	298.63	1.40	300.01	2.78
50	1	1.0	64.6	-	298.55	0.55	300.33	1.23	302.20	3.10
	22	0.2	64.6	97.38	298.82	0.28	300.45	1.35	301.19	2.09
59.4	1	1.0	41.6	-	300.10	0.50	301.25	0.65	303.00	2.40
	22	1.0	41.6	99.84	299.99	0.61	302.03	1.43	306.54	5.94
70	1	1.0	51.7	-	301.73	0.35	302.72	0.64	304.44	2.36
	22	0.2	51.7	99.83	301.83	0.25	302.93	0.85	304.43	2.35
80	1	0.2	31.1	-	303.21	0.13	303.73	0.39	304.38	1.04
	20	0.2	64.6	99.96	303.13	0.21	304.33	0.99	305.75	2.41
90	1	1.0	64.6	-	304.10	0.38	305.04	0.56	307.03	2.55
	15	0.2	64.6	99.97	304.33	0.15	305.74	1.26	306.44	1.96

Multicycles method was applied at several pressures in order to maximize the ice fraction conversion to methane hydrate. The onset points from both methods agree even when the standard experiments were carried out at different heating rates. The deviations of onset temperatures with respect to predictions are similar for both standard and multicycles methods, as shown in Figure 4.8, and they are within the experimental uncertainty.

Figure 4.8 – Absolute deviations of onset temperatures with respect to predictions for CH₄ hydrates:

(■) standard method (●) multicycles method.



The standard analyses present slightly lower onset temperatures than multicycles analyses when heating rates differ (31.5, 50, 70 and 90 MPa in Table 4.4.). It may be related to the cooling/heating effect mentioned in the previous section, in which higher cooling rates led to lower onset temperatures. In contrast, the onset temperatures from multicycles experiments are slightly lower when both methods were performed at the same heating rate (20, 40 and 80 MPa at 0.2 K·min⁻¹; 59.4 MPa at 1 K·min⁻¹). Considering this evidence, multicycles method seems to induce a little more heterogeneous structure due to the difficulty of gas molecules diffusion implied by the hydrate layer initially formed above the aqueous phase, which hampers the contact between gas and free water molecules during the subsequent cycles. Therefore,

hydrate fractions formed in deeper sections of the droplets may contain more empty cavities, so that the dissociation temperatures of these fractions are lower. This phenomenon is resumed in section 4.5.2, in which all the standard and multicycle analyses for CO₂ hydrates were performed at the same heating rate (1 K·min⁻¹), and this behavior is also observed.

The heterogeneity of methane hydrates by the multicycles method can also be observed in the thermograms of Figure 4.9. Nevertheless, the onset temperatures from multicycles experiments are still reliable and present very good accuracy. Besides, this method has provided much better results for calculations of dissociation enthalpy than the standard method, as discussed below in section 4.3.5.

Figure 4.9 – Thermograms of CH₄ hydrates dissociation by the multicycles method.

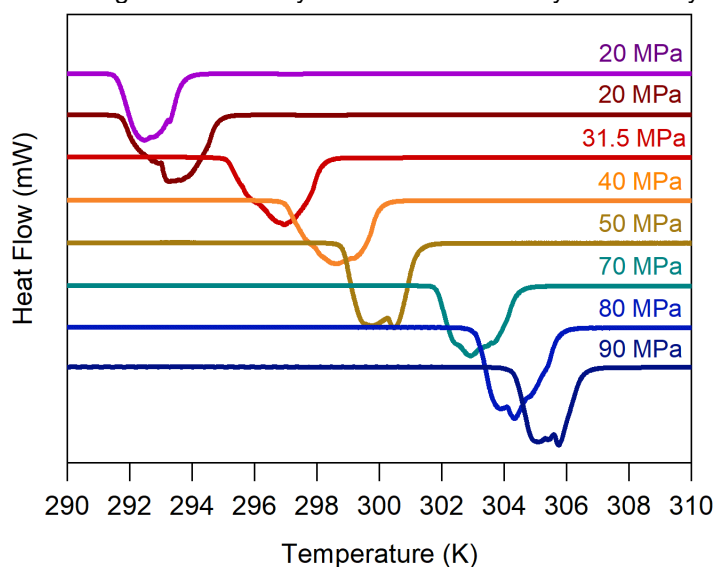
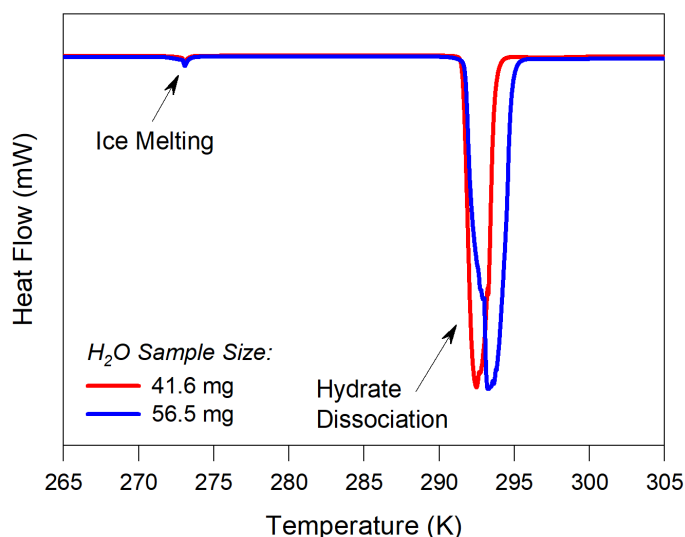
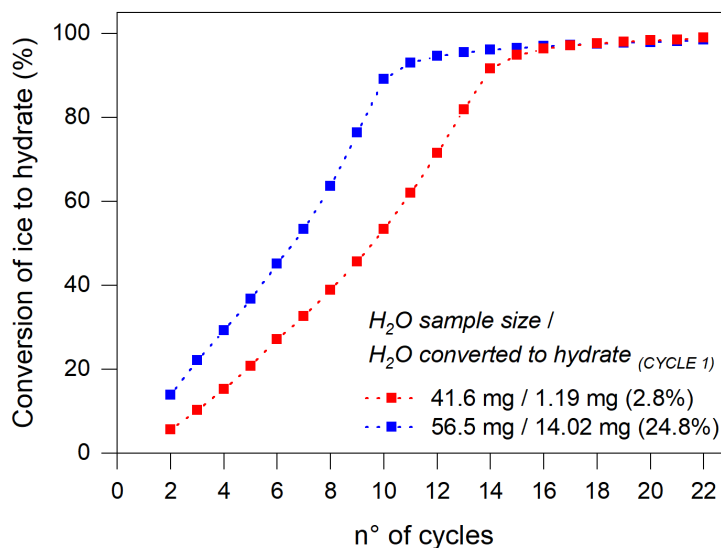


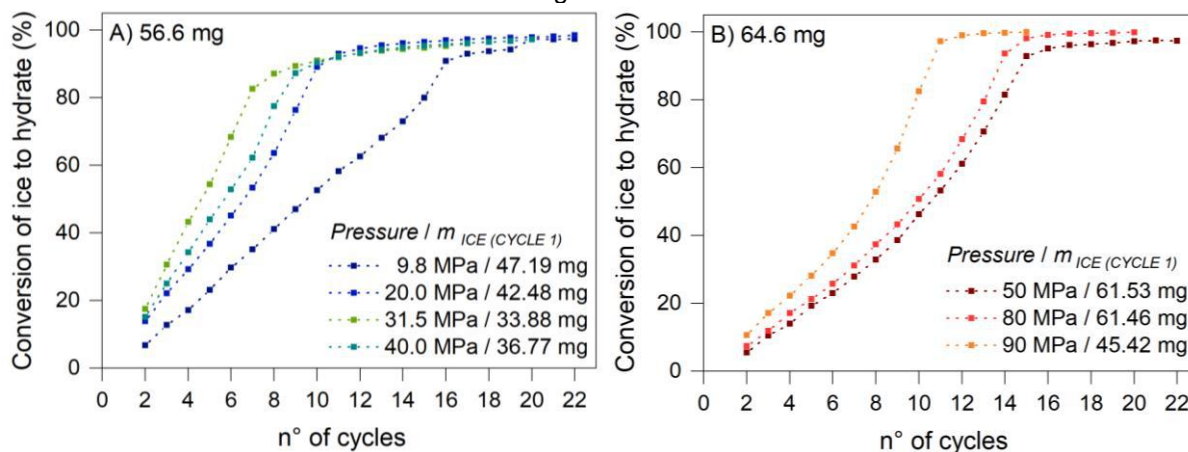
Figure 4.10 reveals the effect of the water content placed inside the cell on the width of the hydrate dissociation curve. However, the onset temperatures are very similar for both experiments (as shown in Table 4.4), again in agreement with the results of section 4.3.2. Water content may also affect the ice-to-hydrate conversion profile according to Figure 4.11, where two samples at the same pressure are compared. The percentage of water converted to hydrate in the first run is notably higher for the sample containing 56.5 mg of water (24.8%). Besides, this sample took 12 cycles for 95% ice conversion, while 41.6 mg took 15 cycles. This evidence supports again that samples containing a higher amount of water favor hydrate rather than ice formation, as discussed in section 4.3.2.

Figure 4.10 – Effect of H₂O sample size on the dissociation of CH₄ hydrates by multicycles at 20 MPa.Figure 4.11 – Effect of H₂O sample size on the conversion of ice to CH₄ hydrate throughout 22 cycles at 20 MPa.

The effect of pressure on the conversion rate of ice to hydrate was evaluated by gathering experiments containing the same water content so that the initial amount of ice can be comparable. Figures 4.12 refers to samples initially containing 56.6 and 64.6 mg of liquid water. Higher pressures tend to lessen the formation of ice in this system and to result in a faster conversion to hydrate. The value of m_{Ice} indicates the mass of ice melted in the first run, thus corresponding to the amount of ice initially formed. One can note that the conversion profiles constitute two distinct stages: a faster conversion up about 90% is followed by a slower one. The lower m_{Ice} , the faster the ice conversion in the first stage i.e., a lower number of cycles is required to reach the second stage. Therefore, both the amount of ice initially formed and the conversion

rate appear to depend on pressure. This was also found in Figure 4.1B and may be related to higher methane diffusivity in water at higher pressures, favoring hydrate over ice formation, as discussed in section 4.3.1.

Figure 4.12 – Effect of pressure on the ice conversion to CH₄ hydrate: A) 56.6 mg of water and B) 64.6 mg of water.



4.3.5 Enthalpy of Dissociation and Hydration Number

At first, it is worth to mention that n is close to 5.75 in the hypothetical case of all cages are filled with guest molecules. However, the estimation of a more realistic hydration number at each temperature / pressure condition is essential for determining the enthalpy. The hydration number is related to the hydrate volume, consequently, both temperature and pressure indirectly affect the occupancy of hydrate cages. The thermal expansion counteracts the compressibility effect caused by increasing the pressure. In other words, the temperature favors the hydration number, while the pressure decreases it. Thereby, the balance between these two factors play a role in the size of cavities and, consequently, in the occupancy degree of the structure. Therefore, the hydration number at each point was estimated by two ways: i) according to predictions of fractional cage occupancy provided by CSMGem, ii) an iterative method adapted from the one proposed by de Forcrand in 1902, currently used by many researchers (SLOAN; KOH, 2008).

Tables 4.5 and 4.6 present the results based on experiments run by the standard and multicycles methods, respectively. Different equations were used to fit each set of data, and thereby, it is expected to observe a small difference between standard and multicycles methods. In both cases, the enthalpy was estimated considering the hydration number (n) calculated by CSMGem predictions and by the iterative method, as mentioned above.

Table 4.5 – Enthalpies of CH₄ hydrates based on experimental data obtained by the standard method. The hydration number (n) was estimated based on the fractional occupancy degree provided by CSMGem software and by the iterative method.

P (MPa)	T (K)	\emptyset (K·min ⁻¹)	CSMGem				Iterative Method			
			n	$\Delta H_{Clap.}$	$\Delta H_{Integ.}$	AD	n	$\Delta H_{Clap.}$	$\Delta H_{Integ.}$	AD
				(kJ/mol CH ₄)				(kJ/mol CH ₄)		
20	291.74	0.2	5.93	55.59	55.00	0.59	6.12	54.91	56.80	1.89
40	296.98	0.2	5.87	55.62	55.31	0.30	6.01	54.65	55.01	0.37
60	300.5	0.2	5.83	56.72	54.24	2.48	6.03	54.95	56.76	1.81
80	303.21	0.2	5.81	58.56	52.71	5.85	6.10	55.37	58.16	2.79
100	305.48	0.2	5.79	62.09	51.22	10.88	6.26	55.97	53.79	2.18

Table 4.6 – Enthalpies of CH₄ hydrates based on experimental data obtained by the multicycles method. The hydration number (n) was estimated based on the fractional occupancy degree provided by CSMGem software and by the iterative method.

P (MPa)	T (K)	\emptyset (K·min ⁻¹)	CSMGem				Iterative Method			
			n	$\Delta H_{Clap.}$	$\Delta H_{Int.}$	AD	n	$\Delta H_{Clap.}$	$\Delta H_{Int.}$	AD
				(kJ/mol CH ₄)				(kJ/mol CH ₄)		
20.0	291.74	0.2	5.93	55.83	53.61	2.22	6.17	54.97	55.75	0.78
31.5	295.23	0.2	5.89	55.78	53.96	1.82	6.08	54.73	55.67	0.95
40.0	296.96	0.2	5.87	56.28	53.49	2.79	6.09	54.77	55.51	0.75
50.0	298.82	0.2	5.85	56.97	52.99	3.98	6.10	54.92	55.31	0.39
59.4	299.99	1.0	5.83	58.03	53.12	4.91	6.15	55.07	56.06	0.98
70.0	301.83	0.2	5.82	57.98	53.29	4.69	6.09	55.20	55.81	0.62
80.0	303.13	0.2	5.81	58.66	53.05	5.61	6.11	55.37	55.78	0.41
90.0	304.33	0.2	5.80	59.68	-	-	6.13	55.77	-	-

Figure 4.13 shows that n based on CSMGem predictions are slightly lower than by the iterative method. The latter method accounts for experimental data, and thereby, it is reasonable that the cages occupancy is lower for real hydrates than that based on simulations, even because of the mass transfer limitations on HP- μ DSC. On the other hand, choosing the equation to fit the experimental data may imply decimal variations in the calculation of the number of hydration and enthalpies (Appendix). One can also see a trend of slightly higher n as pressure increases, a phenomenon not observed for ethane and carbon dioxide hydrates, addressed forward. This is likely because the compressibility factor (κ_T) is found to be higher for methane hydrates so that it overcomes the lattice thermal expansion effect (BALLARD, 2001). It is not observed for n obtained from CSMGem predictions.

Figure 4.13 – Hydration number (n) for CH₄ hydrates calculated through the iterative method (standard and multicycles methods) and by using CSMGem predictions.

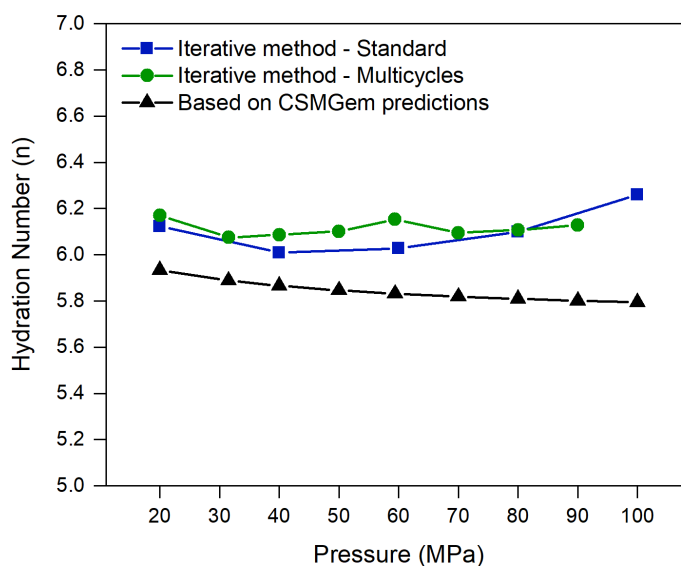


Figure 4.14 shows the enthalpies of dissociation obtained by the Clapeyron equation. The enthalpies calculated using n from CSMGem predictions present notable changes as the pressure increases, for both standard and multicycles methods. Such variation is not expected, and no similar results are found in the literature for dissociation enthalpy of methane hydrate. In fact, the results obtained from iterations are more consistent and comparable to the data reported by Anderson (2004).

Figure 4.14 – Enthalpies of CH₄ hydrates dissociation determined by the Clapeyron equation based on experimental data: A) standard method; B) multicycles method. The black line regards to the calculus of hydrate dissociation using n calculated from the cages occupancy obtained by CSMGem predictions.

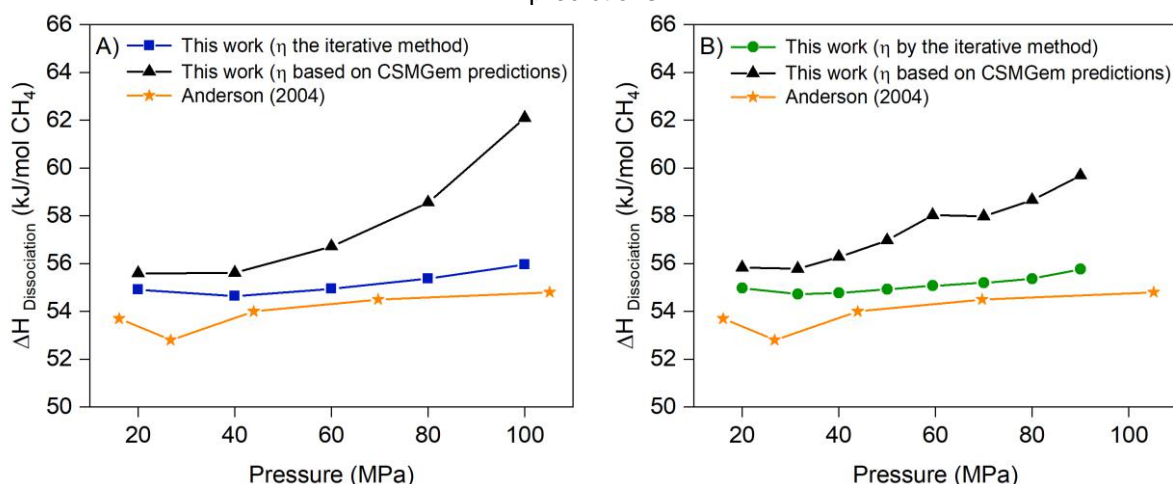
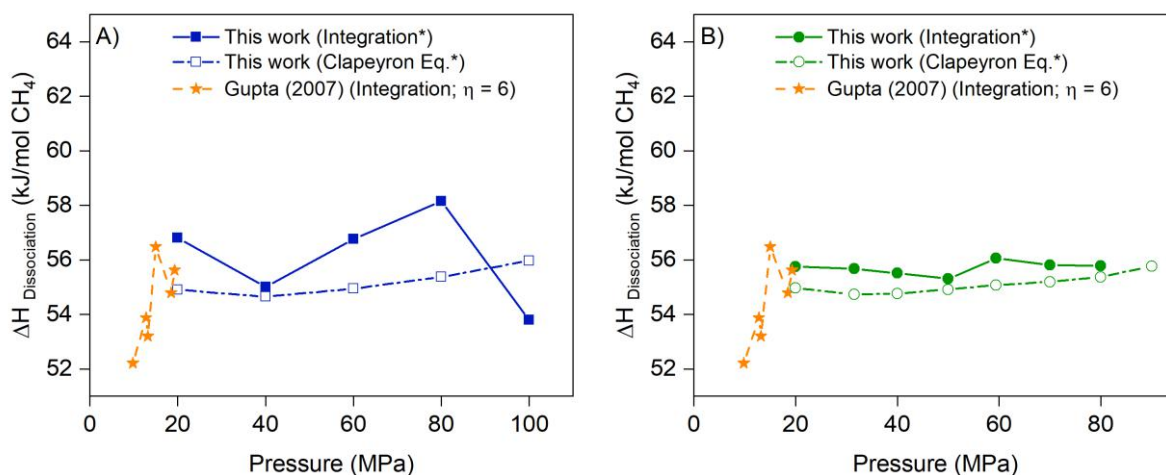


Figure 4.15 presents the enthalpies obtained by the integration of the dissociation curves from thermograms. The only enthalpies found in literature for methane hydrates at high pressures by the integration of thermograms were reported by Gupta (2007). Nevertheless, these data were obtained at lower pressures than in this work and present relatively high deviations, since the standard method was used.

Figure 4.15 – Enthalpies of CH₄ hydrates dissociation determined by the integration of curves from calorimetric thermograms: A) standard method; B) multicycles method. (*) n by the iterative method.

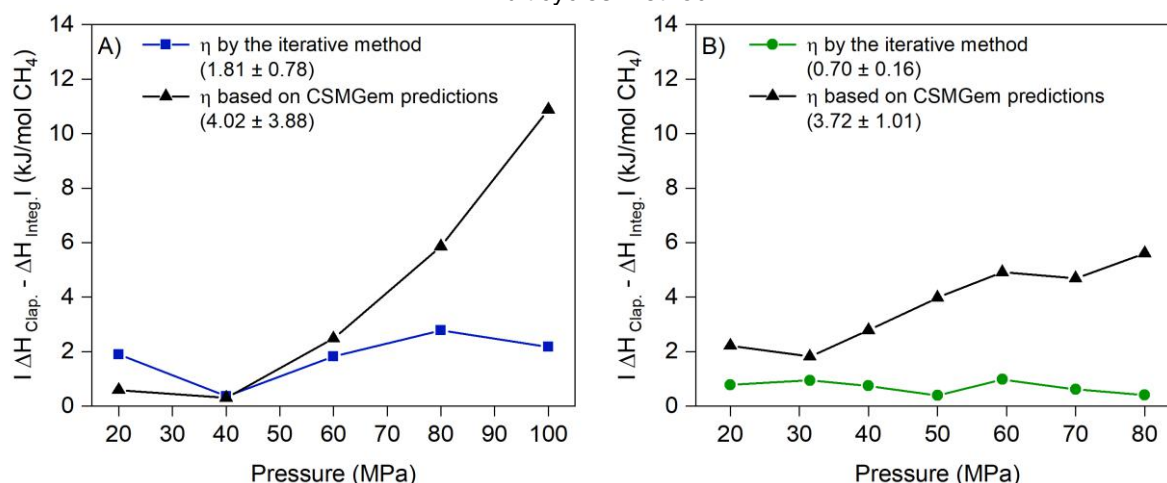


The multicycles method was used to determine the enthalpies by integration throughout this work. However, methane hydrate thermograms obtained by standard method at 0.2 K·min⁻¹ were also used for comparison. The great advantage of multicycles method is that integrations are much more accurate since the final amount of ice is too low (or inexistent) and no recrystallization process is observed. In contrast,

the results from the standard method are not accurate. Moreover, one can note that enthalpies obtained through integrations from thermograms are slightly higher than those obtained by the Clapeyron equation, considering the multicycles method. The uncertainty of enthalpies calculated from Clapeyron method relies mainly on the determination of dP/dT and the hydrate volume. Therefore, the equation chosen to fit the experimental data and the extrapolation of the lattice parameter (a) may partially explain this deviation. On the other hand, the integration also can be affected by minor errors caused when determining the baseline.

Accuracies of standard and multicycles methods are compared by estimating the absolute deviations between enthalpies calculated by the Clapeyron equation and from DSC thermograms, as shown in Figure 4.16. The average deviations and the respective confidence intervals (95%) indicate that the multicycles method and the use of n from iterations provide the most reliable results. This is more remarkable at higher pressures, confirming that the trend of the hydration number obtained from CSMGem prediction does not agree to the experimental trend. The same result was observed for ethane and carbon dioxide hydrates, as discussed forward.

Figure 4.16 – Absolute deviations between enthalpies of CH_4 hydrate dissociation by the Clapeyron equation and through the integration of the hydrate dissociation curve: A) standard method; B) multicycles method.



In sum, the results of methane hydrate enthalpy of dissociation are validated by comparing both Clapeyron and integration methods. The average of enthalpies obtained in this work and the respective confidence interval (95%) are shown in Table 4.7. Besides the good agreement found between them, the results are also consistent with enthalpies found in the literature.

Table 4.7 – Enthalpies of CH₄ hydrates obtained in this work and found in the literature.

Reference	Method	T (K)	P (MPa)	ΔH (kJ/mol CH ₄)
This work	HP-μDSC	291.74 - 303.13	20 - 80	55.70 ±0.18
	Clapeyron	291.74 - 304.33	20 - 90	55.10 ±0.24
Sun et al. (2018)	Clausius-Clapeyron	284.4 - 289.5	9.2 - 16	59.1
Nasir et al. (2014)	Clausius-Clapeyron	Q ₁ *		55.26
Kerkar et al. (2013)	Clausius-Clapeyron	-	10.44	54.5 - 57.79
Nakagawa et al. (2008)	Calorimeter	279 - 282	5.0	55.3
Gupta (2007)	HP-μDSC	285.65	9.8	52.21
		288.15	12.8	53.87
		288.45	13.2	53.2
		289.85	15.0	56.48
		291.65	18.5	54.79
	Clapeyron	292.16	19.3	55.62
		290	16.06	53.86
		298	43.92	53.98
		306	105.18	54.89
		306	105.18	54.8
Anderson (2004)	Clapeyron	Q ₁ *		52.9
		286	9.88	55.7
		298	43.92	54
		302	69.68	54.50
		306	105.18	54.8
Kang et al. (2001)	Microcalorimeter	274.15	-	56.84
Yoon et al. (2003)	Clausius-Clapeyron	Q ₁ *		53.81
Handa (1986)	Calorimeter	273.15	0.1	54.19

* Q₁: Quadruple point (272.9K; 2.563 MPa)

4.4 ETHANE-WATER SYSTEM

4.4.1 Equilibrium Data for C₂H₆ Hydrates by High Pressure Microcalorimetry

As discussed in chapter 3, the liquid-vapor equilibrium of ethane occurs within the temperature range covered by HP-μDSC analysis for pressures up to 4.9 MPa (ethane critical pressure). For this reason, liquid-vapor transitions were clearly observed in thermograms at 3, 4 and 5 MPa. Figure 4.17 shows the thermogram for an ethane hydrate-forming system in which such transition is observed. In this case, it was necessary to run the analysis at 0.2 K·min⁻¹ in order to separate hydrate dissociation peak from ethane vaporization. Figure 4.18 presents thermograms of heating for ethane hydrates from 9.8 to 80 MPa.

Figure 4.17 – Thermograms of the $C_2H_6-H_2O$ system at $1\text{ K}\cdot\text{min}^{-1}$ (A) and $0.2\text{ K}\cdot\text{min}^{-1}$ (B). The pressure applied in this analysis was 3 MPa.

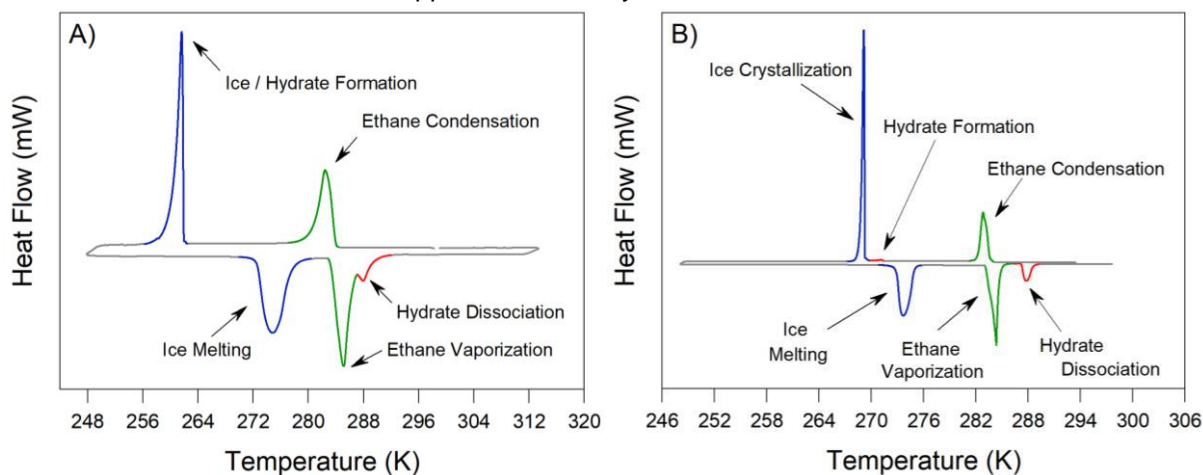
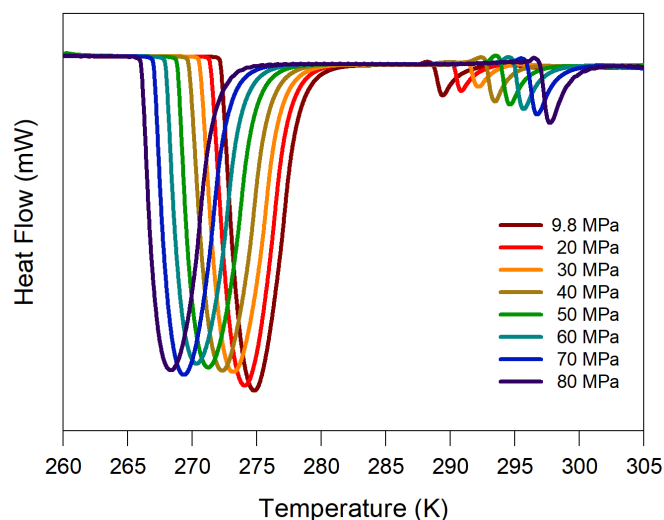


Figure 4.18 – Heating thermograms of the $C_2H_6-H_2O$ system at $1\text{ K}\cdot\text{min}^{-1}$ and at different pressures.

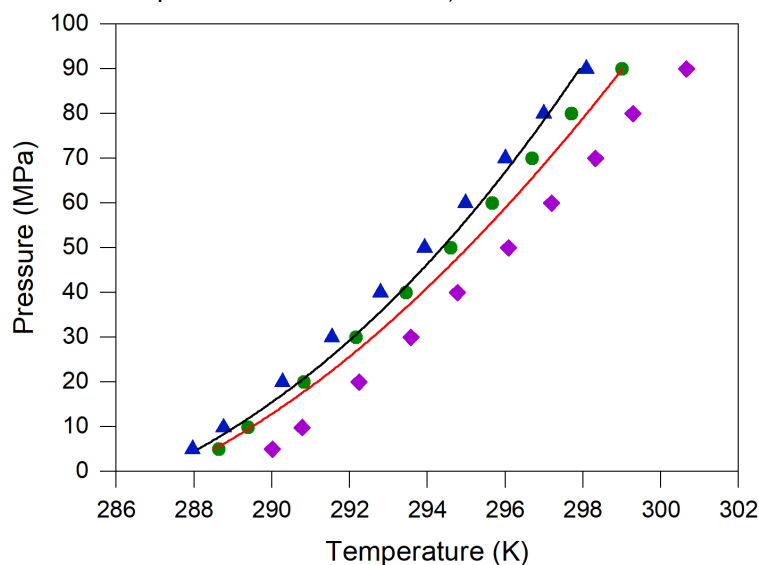


Dissociation data for ethane hydrates from 3 to 90 MPa are presented in Table 4.8 and Figure 4.19. Analogous to methane hydrate, Multiflash predictions move away from CSMGem results as the pressure increases. The predictions for ethane hydrates consider that a fraction of small cavities (sl) are filled, even the ethane diameter being slightly larger than the small cavity size (details in Table 5.1). However, the filling of such cavities can be hampered in real systems, leading to lower dissociation temperatures. Thus, the lower values of onset temperatures may be explained by a more significant presence of empty cavities throughout the hydrate than considered by predictions. The same phenomenon was mentioned for methane hydrates, but in lower magnitude, since methane molecules fit into both cavities of sl.

Table 4.8 – Dissociation data of C₂H₆ hydrates by HP- μ DSC (1 K·min⁻¹) and the respective absolute deviations (AD) from computational predictions.

P (MPa)	HP- μ DSC – C ₂ H ₆ Hydrate – T _{DISSOCIATION} (K)								
	Onset	AD		Peak	AD		Endset	AD	
		CSMGem	Multiflash		CSMGem	Multiflash		CSMGem	Multiflash
3	286.16	0.88	1.30	287.84	0.80	0.38	289.82	2.78	2.36
4	287.67	0.19	0.60	288.44	0.58	0.17	289.95	2.09	1.68
5	287.96	0.14	0.55	288.65	0.55	0.14	290.01	1.91	1.50
9.8	288.76	0.32	0.74	289.4	0.32	0.10	290.78	1.70	1.28
20	290.27	0.49	0.94	290.83	0.07	0.38	292.24	1.49	1.03
30	291.55	0.57	1.07	292.17	0.05	0.45	293.57	1.45	0.95
40	292.8	0.52	1.09	293.46	0.14	0.43	294.78	1.46	0.89
50	293.93	0.46	1.12	294.6	0.21	0.45	296.09	1.70	1.04
60	294.98	0.39	1.15	295.66	0.29	0.47	297.19	1.82	1.06
70	296	0.28	1.14	296.7	0.42	0.44	298.32	2.04	1.18
80	296.99	0.13	1.11	297.71	0.59	0.39	299.28	2.16	1.18
90	298.09	0.17	0.93	299	1.08	0.02	300.66	2.74	1.64

Figure 4.19 - Dissociation data of C₂H₆ hydrates obtained by HP- μ DSC at 1 K·min⁻¹: (\blacktriangle) onset temperatures; (\bullet) peak temperatures; (\blacklozenge) endset temperatures. Black lines refer to CSMGem predictions and red lines, to Multiflash.



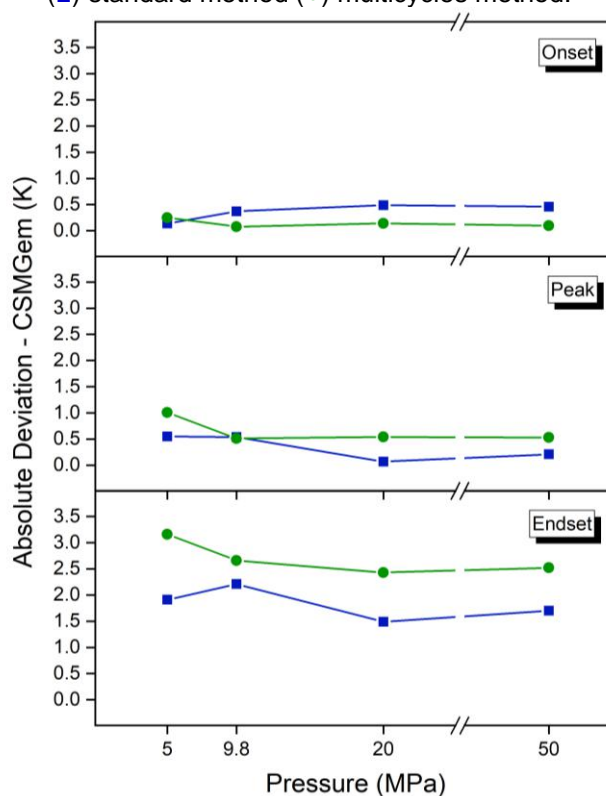
4.4.2 Effect of Multicycles

Multiple cycles were also performed for ethane hydrate systems at 5, 9.8, 20 and 50 MPa. The results are shown in Table 4.9 and the absolute deviations are compared to those of the standard method in Figure 4.20.

Table 4.9 – Dissociation data of C₂H₆ hydrates by standard and multicycles methods, and their respective absolute deviations (AD) from computational predictions.

P (MPa)	n° Cycles	Ø (K·min ⁻¹)	H ₂ O (mg)	Ice Conv. (%)	HP-µDSC – C ₂ H ₆ Hydrate – T _{DISSOCIATION} (K)					
					Onset	AD (CSMGem)	Peak	AD (CSMGem)	Endset	AD (CSMGem)
5	1	1.0	53.3	-	287.96	0.14	288.65	0.55	290.01	1.91
	38	0.2	53.3	97.19	288.35	0.25	289.11	1.01	291.26	3.16
9.8	1	1.0	42.3	-	288.71	0.37	289.62	0.54	291.29	2.21
	32	0.2	42.3	98.63	289.00	0.08	289.59	0.51	291.74	2.66
20	1	1.0	53.3	-	290.27	0.49	290.83	0.07	292.24	1.49
	42	0.2	53.9	99.80	290.61	0.14	291.29	0.54	293.18	2.43
50	1	1.0	53.3	-	293.93	0.46	294.60	0.21	296.09	1.70
	41	0.2	51.9	99.05	294.49	0.10	294.92	0.53	296.91	2.52

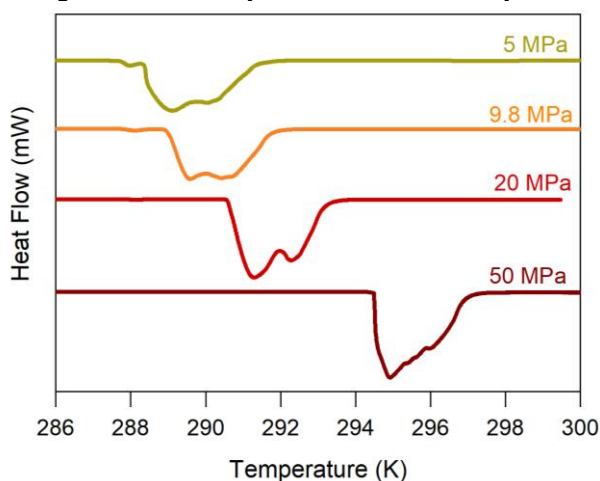
Figure 4.20 – Absolute deviations of onset temperatures with respect to predictions for C₂H₆ hydrates: (■) standard method (●) multicycles method.



The onset temperatures from multicycles method tend to be lower than those from the standard method. However, this should not be related to the multicycles method itself, but to the lower cooling / heating rate employed in these experiments, that leads to lower dissociation temperatures as resumed below. On the other hand, deviations of peak and endset temperatures from CSMGem predictions are verified to be higher for multicycles data. The main reason for this is the amount of hydrate formed, which is considerably larger than in the standard analyses.

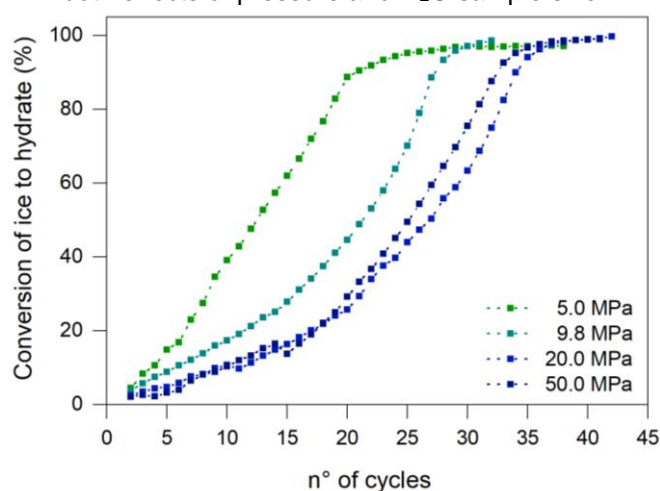
Figure 4.21 shows that the hydrate dissociation curves obtained through the multicycles method present distinct peaks, indicating heterogeneous structures. As previously mentioned, the hydrate formation is limited by the gas diffusion into the solid phase. Therefore, it is reasonable to say that the occupancy degree varies throughout the hydrate structure when multiple cycles are run, hence affecting the shape of the dissociation curve. In fact, even the onset temperature slightly changes according to the occupancy degree. The reason for this is that deeper regions could present more empty cavities than interfacial areas, leading to slightly lower dissociation temperatures, as observed for methane hydrates. However, the multicycles method does not give lower onset temperatures in this case likely because standard analyses were performed at a higher heating rate ($1 \text{ K}\cdot\text{min}^{-1}$), which may have led to lower dissociation temperatures than multicycles analyses ($0.2 \text{ K}\cdot\text{min}^{-1}$). It means that the same effect of heating rate on methane hydrates, observed in Figure 4.5 of section 4.3.3, may have occurred for ethane hydrates. The trend of lower onset temperatures for multicycles experiments is resumed in section 4.5.2, in which both methods were performed at the same heating rate for CO_2 hydrates.

Figure 4.21 – Thermograms of C_2H_6 hydrates dissociation by the multicycles method.



Another distinct point from the methane hydrate results is about the ice conversion rate. Methane hydrates took less than 16 cycles for 90% of ice conversion, whereas Figure 4.22 shows that at least 21 cycles were required for ethane hydrates in order to reach the same conversion rate. It has not to do with the difference of gas solubilities in water since ethane is more soluble than methane, and it should favor the hydrate formation (SCHARLIN et al., 1998). The reason indeed may be the same one why lower onset temperatures than predictions are obtained, as mentioned in the previous section. The size of ethane molecules is larger than methane, and it makes harder the diffusion and incorporation of such molecules into the cavities so that the hydrate structure takes longer to be finally formed. This phenomenon could contribute to the heterogeneity of structures observed in multicycles thermograms, mentioned above. However, despite the ethane molecules be geometrically more challenging to fill most of cages from structure I, mainly the small ones, ethane hydrate (sI) is still more thermodynamically stable than methane hydrate (sI) as guest molecules keep closer to the water lattice and chemical interactions are stronger.

Figure 4.22 – Ice conversion to C_2H_6 hydrate throughout multicycles. The analyses were influenced by both effects of pressure and H_2O sample size.



At last, one could suggest a trend of slower ice conversion as the pressure increases, unlike observed in methane hydrates. However, the sizes of water samples are different in these experiments and, thereby, the effect of pressure on ice conversion cannot be analyzed singularly and are not conclusive in this case.

4.4.3 Enthalpy of Dissociation and Hydration Number

The enthalpies of dissociation were also calculated for ethane hydrates by both Clapeyron and integration methods. Tables 4.10 and 4.11 present the enthalpies obtained by the standard and multicycles methods. The standard method was used to calculate the enthalpy changes only through the Clapeyron equation, since this method does not provide accurate results, as discussed for methane hydrates.

Table 4.10 – Enthalpies of C₂H₆ hydrates dissociation based on experimental data obtained by the standard method. The hydration number (*n*) was estimated based on the fractional occupancy degree provided by CSMGem software and by the iterative method.

P (MPa)	T (K)	Ø (K·min ⁻¹)	CSMGem		Iterative Method	
			<i>n</i>	ΔH _{Clapeyron} (kJ/mol C ₂ H ₆)	<i>n</i>	ΔH _{Clapeyron} (kJ/mol C ₂ H ₆)
5	287.96	1	7.74	69.75	8.22	65.74
9.8	288.76	1	7.72	65.72	7.79	65.06
20	290.27	1	7.68	63.44	7.56	64.78
30	291.55	1	7.65	62.38	7.45	64.76
40	292.8	1	7.62	61.87	7.40	64.85
50	293.93	1	7.59	61.15	7.33	64.91
60	294.98	1	7.56	60.35	7.26	64.95
70	296.00	1	7.51	59.61	7.19	65.00

Table 4.11 – Enthalpies of C₂H₆ hydrates dissociation based on experimental data obtained by the multicycles method. The hydration number (*n*) was estimated based on the fractional occupancy degree provided by CSMGem software and by the iterative method.

P (MPa)	T (K)	Ø (K·min ⁻¹)	CSMGem				Iterative Method			
			<i>n</i>	ΔH _{Clap.}	ΔH _{Int.}	AD	<i>n</i>	ΔH _{Clap.}	ΔH _{Int.}	AD
			(kJ/mol C ₂ H ₆)							
5	288.35	0.2	7.74	74.79	57.00	17.79	8.69	66.41	64.00	2.41
9.8	289.00	0.2	7.72	67.35	64.85	2.49	7.95	65.31	66.70	1.39
20	290.61	0.2	7.68	62.20	65.51	3.31	7.44	64.72	63.45	1.28
50	294.49	0.2	7.59	55.76	71.89	16.12	6.92	64.46	65.53	1.06

The experimental enthalpy change used as a reference for iterations in this case was 71.8 kJ/ mol C_2H_6 , as reported by Handa (1986) at standard condition of temperature and pressure. Figure 4.23 presents the hydration number according to the pressure. A higher deviation is observed for the multicycles method likely due to the few points available to find a more suitable equation describing the experimental data. Although the equation chosen to fit data affects the hydration number, the enthalpy changes found through the Clapeyron equation are very close for both standard and multicycles methods, as shown in Figure 4.24 (A and B).

Figure 4.23 – Hydration number (n) for C_2H_6 hydrates calculated through the iterative method (standard and multicycles methods) and by applying CSMGem predictions.

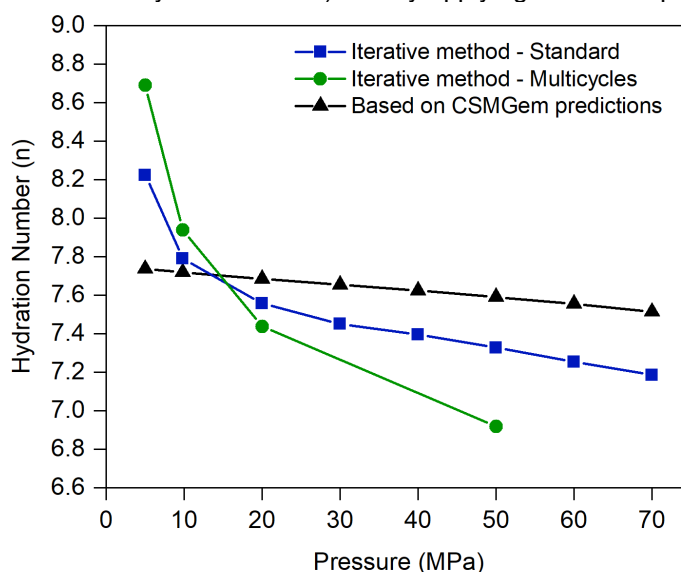
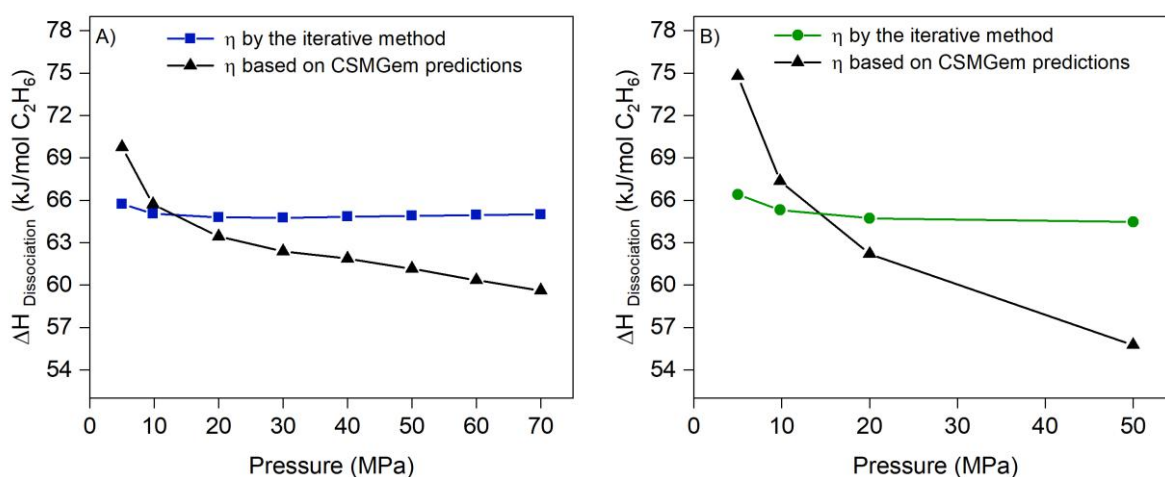


Figure 4.24 – Enthalpies of C_2H_6 hydrates dissociation determined by the Clapeyron equation based on experimental data: A) standard method; B) multicycles method. The black line regards to the calculus of hydrate dissociation using n calculated from the cages occupancy obtained by CSMGem predictions.



Although the dissociation temperature from CSMGem predictions can slightly deviate from the experimental one, the variation of the hydration number based on fractional cages occupancy (from CSMGem) is negligible for such small deviations. However, Figure 4.24 shows that using the hydration number based on CSMGem predictions again does not provide consistent results when applying the Clapeyron equation. The same is observed in the results of integrations in Figure 4.25. At last, a better convergence of enthalpies from Clapeyron equation and integration is obtained by using n from iterations than based on CSMGem predictions, as shown in Figure 4.26. The average deviations and the respective confidence intervals (95%) indicate that using the iterative method provides the most reliable results.

Figure 4.25 – Enthalpies of C_2H_6 hydrates dissociation determined by the integration of curves from calorimetric thermograms (multicycles method): A) n from CSMGem predictions; B) n from the iterative method.

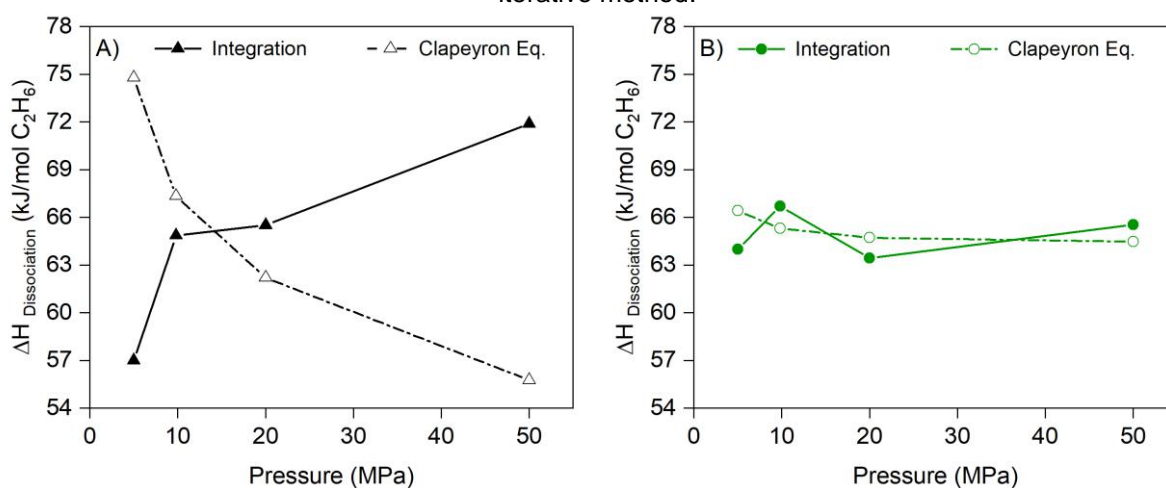
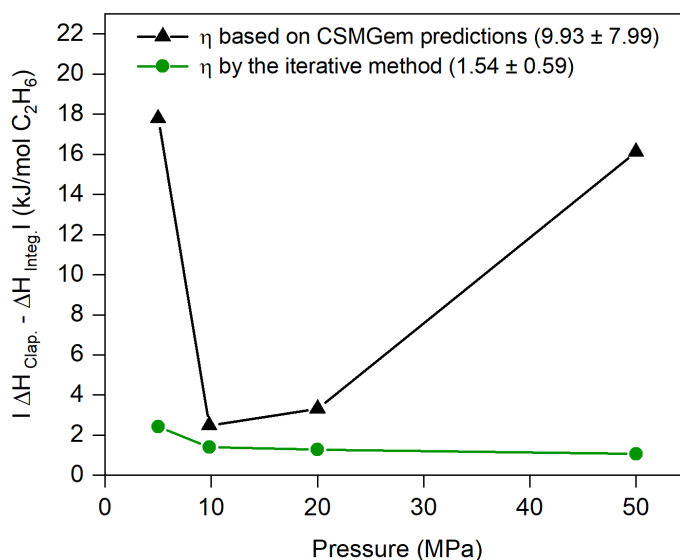


Figure 4.26 – Absolute deviations between enthalpies of C_2H_6 hydrate dissociation calculated by the Clapeyron equation and through the integration of the hydrate dissociation curve (multicycles method).



No values of enthalpies were found in the literature at similar conditions to this work. It is worth to mention that the analyses presented herein were performed above the upper quadruple point (Q_2), which connects $L_{W-H-L_{HC}}$ and $L_{W-H-V_{HC}}$ equilibrium lines. Therefore, it is reasonable that the enthalpies' changes obtained in this work are slightly lower than from the literature (below Q_2) since the hydrate dissociation delivers ethane in form of compressed liquid instead of vapor. The latent heat of ethane vaporization is about 5 kJ/mol (NIST Webbook), and this value agrees to the difference of enthalpies obtained in this work (above Q_2) and from the literature (below Q_2), shown in Table 4.12

Table 4.12 – Enthalpies of C_2H_6 hydrates obtained in this work and found in the literature.

Reference	Method	T (K)	ΔH (kJ/mol C_2H_6)
This work	HP- μ DSC	288.35 – 294.49	64.92 \pm 1.45
	Clapeyron	287.96 - 296.00	65.23 \pm 0.85
Nakagawa et al. (2008)	Calorimeter	283.00 - 286.00	71.10
Yoon et al. (2003)	Clausius-Clapeyron	273.15	71.34
Handa (1986)	Calorimeter	273.15	71.80

4.5 CARBON DIOXIDE-WATER SYSTEM

4.5.1 Equilibrium Data for CO_2 Hydrates by High Pressure Microcalorimetry

The last single guest hydrate-forming system studied was composed of water and carbon dioxide. Table 4.13 and Figure 4.27 show the data obtained by HP- μ DSC (standard method) and the respective absolute deviations. Multiflash predictions deviate noticeably from CSMGem predictions (up to 0.9 K in the range covered by Figure 4.27). The onset temperatures result in the lowest deviations from CSMGem predictions, and their lower values again may be related to the greater presence of empty cavities in the synthesized hydrates. The high discrepancy of peak and endset temperatures can be attributed to the amount of hydrate formed, significantly larger in this system even when applying the standard method. Considering there is no mixing inside the system, the hydrate formation is mainly limited by mass transfer, as already mentioned. In this context, the CO_2 solubility and diffusivity in water play a crucial role in the kinetics of hydrate formation and explains the large amount of hydrate formed (POKHAREL et al., 2018; SCHARLIN et al., 1998; TAMIMI et al., 1994;).

Table 4.13 – Dissociation data of CO₂ hydrates by HP- μ DSC and the respective absolute deviations (AD) from computational predictions.

P (MPa)	HP- μ DSC – CO ₂ Hydrate – T _{DISSOCIATION} (K)								
	Onset	AD		Peak	AD		Endset	AD	
		CSMGem	Multiflash		CSMGem	Multiflash		CSMGem	Multiflash
9.8	283.70	0.05	0.35	285.41	1.76	1.36	286.88	3.23	2.83
20	284.87	0.12	0.18	286.72	1.97	1.67	288.70	3.95	3.65
30	285.45	0.10	0.60	287.65	2.10	1.60	289.15	3.60	3.10
40	286.15	0.20	0.70	287.99	1.64	1.14	289.53	3.18	2.68
50	286.74	0.31	0.81	288.17	1.12	0.62	289.66	2.61	2.11
60	287.37	0.28	0.88	288.89	1.24	0.63	290.48	2.83	2.23
70	287.94	0.21	1.01	289.57	1.42	0.62	291.79	3.64	2.84
80	288.45	0.20	1.10	289.93	1.28	0.38	292.05	3.40	2.50

Figure 4.27 - Dissociation data of CO₂ hydrates obtained by HP- μ DSC: (\blacktriangle) onset temperatures; (\bullet) peak temperatures; (\blacklozenge) endset temperatures. Black lines refer to CSMGem predictions and Red lines, to Multiflash.

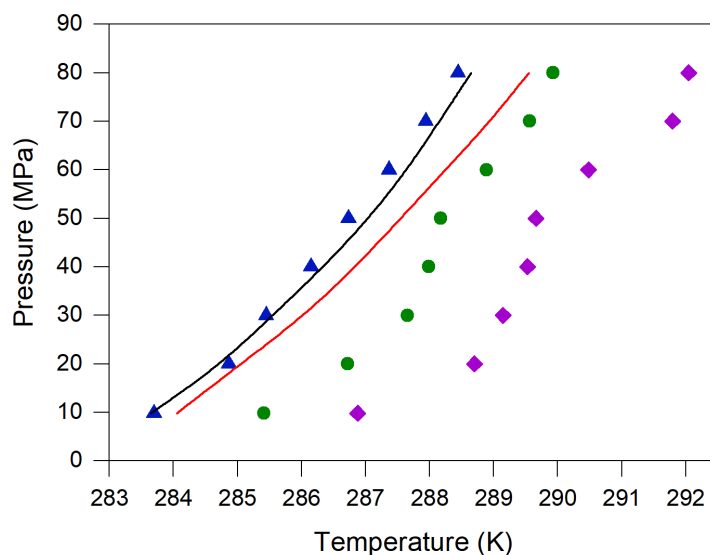
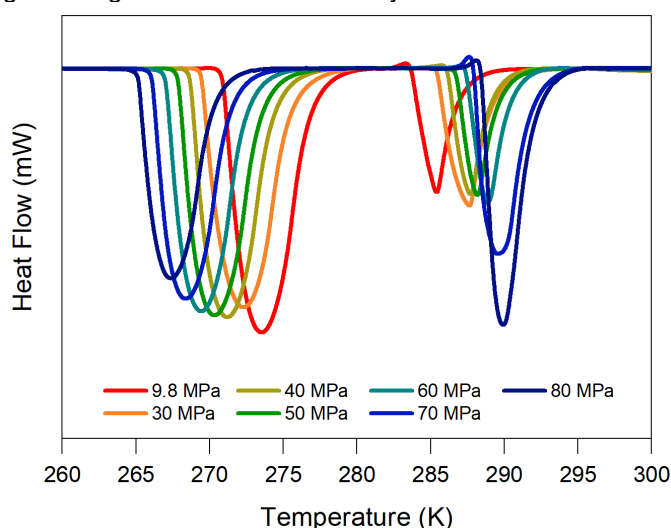


Figure 4.28 shows the thermograms obtained for carbon dioxide hydrates at different pressures by the standard method. Increasing pressure tends to form large amounts of hydrate, as observed for methane hydrates.

Figure 4.28 – Heating thermograms of the CO₂-H₂O system at 1 K·min⁻¹ and at different pressures.

4.5.2 Effect of Multicycles

Table 4.14 shows the dissociation data for carbon dioxide hydrates by standard and multicycles methods. Although the last run of multicycles analyses in the previous systems was performed at 0.2 K·min⁻¹ for better enthalpy estimations, in this case was used 1 K·min⁻¹. This was because carbon dioxide at critical conditions showed to affect the elastomer seal inside the pressure gauge so that shorter analyses were required.

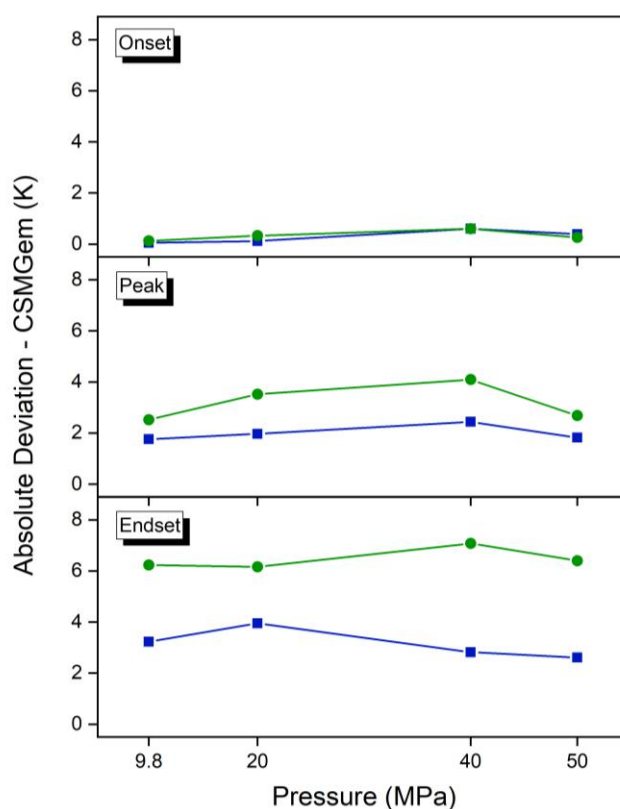
Table 4.14 – Dissociation data of CO₂ hydrates by standard and multicycles methods, and their respective absolute deviations (AD) from computational predictions.

P (MPa)	n° Cycles	Ø (K·min ⁻¹)	H ₂ O (mg)	Ice Conv. (%)	HP-μDSC – CO ₂ Hydrate – T _{DISSOCIATION} (K)					
					Onset	AD (CSMGem)	Peak	AD (CSMGem)	Endset	AD (CSMGem)
9.8	1	1	48.9	-	283.70	0.05	285.41	1.76	286.88	3.23
	25	1	48.9	99.51	283.52	0.13	286.17	2.52	289.88	6.23
20	1	1	48.9	-	284.87	0.12	286.72	1.97	288.70	3.95
	25	1	48.9	99.91	284.42	0.33	288.27	3.52	290.91	6.16
40	1	1	53.4	-	286.15	0.60	287.99	2.44	289.53	2.82
	32	1	53.4	~100	286.15	0.60	289.64	4.09	292.63	7.08
50	1	1	48.9	-	286.74	0.39	288.17	1.82	289.66	2.61
	19	1	53.4	~100	286.61	0.26	289.03	2.68	292.75	6.40

On the other hand, the effect of multiple cycles on broadening the width of dissociation curves and the influence of the methodology on the dissociation

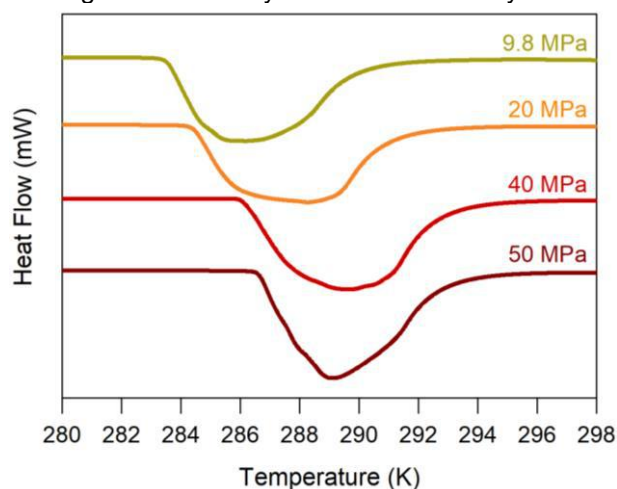
temperatures can be discussed more convincingly in this system, considering that the heating rate was the same for both methods. The onset temperatures for multicycle analyses tend to be slightly lower than for standard experiments. This supports that the heterogeneity degree is slightly higher when applying multiple cycles. As discussed for methane and ethane hydrates, deeper hydrate layers may contain more empty cavities than layers close to the interface. Such difference in cage-occupancy degrees may lead to lower onset temperatures. It is worth to remember, however, that this phenomenon does not restrict the use of multicycles method, since the results are very similar, and the onset deviations are within the experimental uncertainty. Figure 4.29 shows the absolute deviations of dissociation temperatures with respect to CSMGem predictions. Higher deviations are found for peak and endset temperatures, as expected. However, the deviations from multicycle analyses are higher than for previous systems because the experiments, in this case, were run at $1 \text{ K}\cdot\text{min}^{-1}$. Besides, the amount of hydrate formed is higher than in the standard analysis, leading to a wider dissociation curve.

Figure 4.29 – Absolute deviations of dissociation temperatures with respect to predictions for CO_2 hydrates: (■) standard method (●) multicycles method.



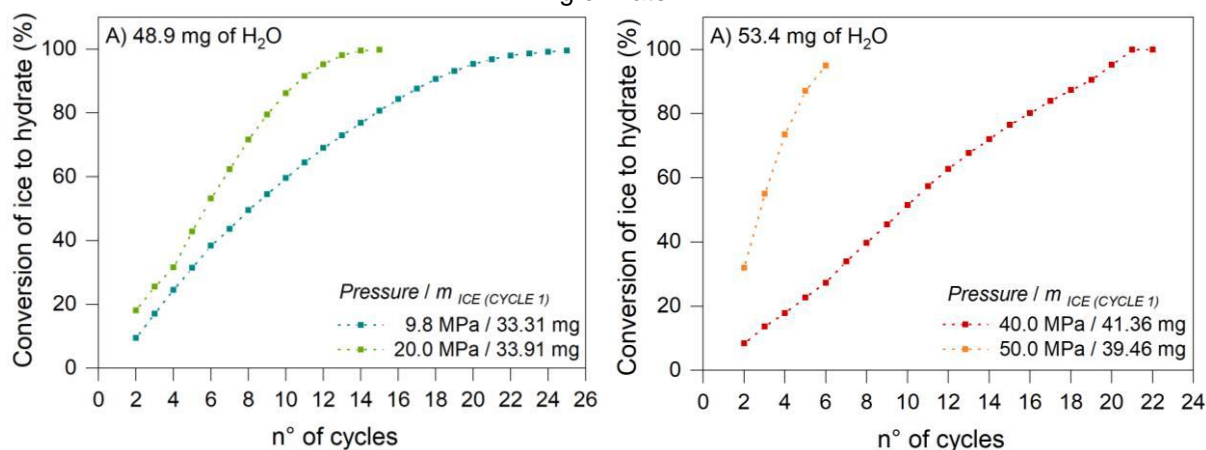
Thermograms of CO₂ hydrates dissociation obtained by the multicycles method are shown in Figure 4.30 and seem to be smoother than methane and ethane thermograms (Figures 4.9 and 4.21, respectively). This could be explained by two factors: i) Multicycles analyses of CO₂ hydrate were run at higher heating rate than multicycles performed for methane and ethane hydrates, which enlarge the dissociation curves and reduce the resolution for small transitions; ii) The CO₂ hydrates may be more homogeneous. The high solubility and diffusivity of CO₂ contribute to a higher occupancy of the hydrate cavities in deeper layers. Thereby, such distinct peaks are not as evident as they are for methane and ethane hydrates, although some discontinuities and asymmetry still can be observed in the dissociation curves.

Figure 4.30 – Thermograms of CO₂ hydrate dissociation by the multicycles method.



Finally, the ice conversion evolution over multiple cycles is shown in Figure 4.31 for samples initially containing 48.9 and 53.4 mg. Similar to methane hydrates, higher pressures led to higher conversion rates in both cases. On the other hand, it was expected faster conversion rates in this system than for methane and ethane hydrates, considering the chemical features of CO₂ mentioned above. In fact, this can be observed at 20 and 50 MPa, once only 11 and 6 cycles were enough to reach 90% of conversion. However, the same behavior is not observed for 9.8 and 40 MPa, whose ice conversion took longer than methane hydrate samples. Although pressure and H₂O sample size are factors that seem to affect the ice conversion rate to hydrate, this process may also depend on stochastic factors.

Figure 4.31 – Effect of pressure on the ice conversion to CO₂ hydrate: A) 48.9 mg of water and B) 53.4 mg of water.



4.5.3 Enthalpy of Dissociation and Hydration Number

Enthalpies of dissociation were calculated for CO₂ hydrates, similarly to the previous systems. The results from standard and multicycles methods are presented in Table 4.15 and 4.16, respectively. In this case, two reference states were used to calculate the hydration number through the iterative method: i) calorimetric data at 273.65 K from Kang et al. (2001); ii) data from the Clapeyron equation calculated by Anderson (2003) at the upper quadruple point (283.1 K and 4.45 MPa).

Table 4.15 – Enthalpies of CO₂ hydrates based on experimental data obtained by the standard method. The hydration number (n) was estimated based on the fractional occupancy degree provided by CSMGem software and by the iterative method.

P (MPa)	T (K)	CSMGem		Iterative method (ΔH^*_{Kang})		Iterative method ($\Delta H^*_{\text{And.}}$)	
		n	$\Delta H_{\text{Clapeyron}}$ (kJ/mol CO ₂)	n	$\Delta H_{\text{Clapeyron}}$ (kJ/mol CO ₂)	n	$\Delta H_{\text{Clapeyron}}$ (kJ/mol CO ₂)
9.8	283.70	6.29	48.12	5.80	53.94	6.30	47.97
20	284.87	6.20	54.37	6.23	54.03	6.62	47.75
30	285.45	6.14	54.60	6.18	53.83	6.52	47.59
40	286.15	6.08	56.21	6.20	53.76	6.50	47.52
50	286.74	6.03	56.74	6.17	53.37	6.44	47.45
60	287.37	5.99	57.45	6.15	53.61	6.39	47.41
70	287.94	5.96	57.46	6.10	53.54	6.33	47.37
80	288.45	5.93	56.91	6.05	53.45	6.25	47.32

Table 4.16 – Enthalpies of CO₂ hydrates based on experimental data obtained by the multicycles method. The hydration number (n) was estimated based on the fractional occupancy degree provided by CSMGem software and by the iterative method.

P (MPa)	T (K)	CSMGem				Iterative method (ΔH^*_{Kang})				Iterative method ($\Delta H^*_{And.}$)			
		n	$\Delta H_{Clap.}$	$\Delta H_{Int.}$	AD	n	$\Delta H_{Clap.}$	$\Delta H_{Int.}$	AD	n	$\Delta H_{Clap.}$	$\Delta H_{Int.}$	AD
			(kJ/mol CO ₂)				(kJ/mol CO ₂)				(kJ/mol CO ₂)		
9.8	283.52	6.3	52.58	47.05	5.53	6.2	54.17	46.16	8.01	6.6	47.97	49.67	1.70
20	284.42	6.2	51.44	46.62	4.82	6.1	53.82	45.49	8.33	6.5	47.72	48.50	0.78
40	286.15	6.1	53.38	45.92	7.47	6.1	53.65	45.84	7.81	6.4	47.57	48.18	0.61
50	286.61	6.0	52.27	46.08	6.19	6.0	53.50	45.70	7.80	6.3	47.48	47.84	0.36

The hydration numbers are presented in Figure 4.32, and it is observed that n tends to decrease as the pressure increases. The volumetric κ_T is found to be 3E-4, 3E-7 and 3E-5 for methane, ethane and carbon dioxide, respectively (BALLARD, 2001). Therefore, the effect of the compressibility factor on the lattice parameter is lower for ethane and carbon dioxide hydrates, and the effect of thermal expansivity probably prevails and favors the cages occupancy, decreasing the hydration number. The lower value of n observed at 9.8 MPa in Figure 4.32A could be related to the uncertainty of dP/dT at this point, since it is very close to Q₂.

Figure 4.32 – Hydration number (n) for CO₂ hydrates calculated through the iterative method: A) standard method; B) multicycles method. The black line regards to the hydration number (n) calculated from the cages occupancy obtained by CSMGem predictions.

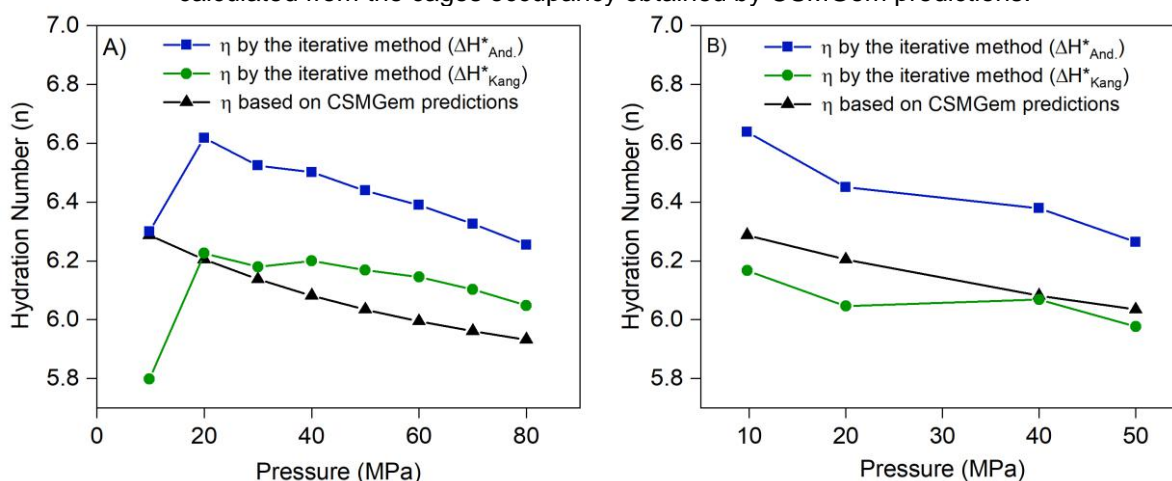
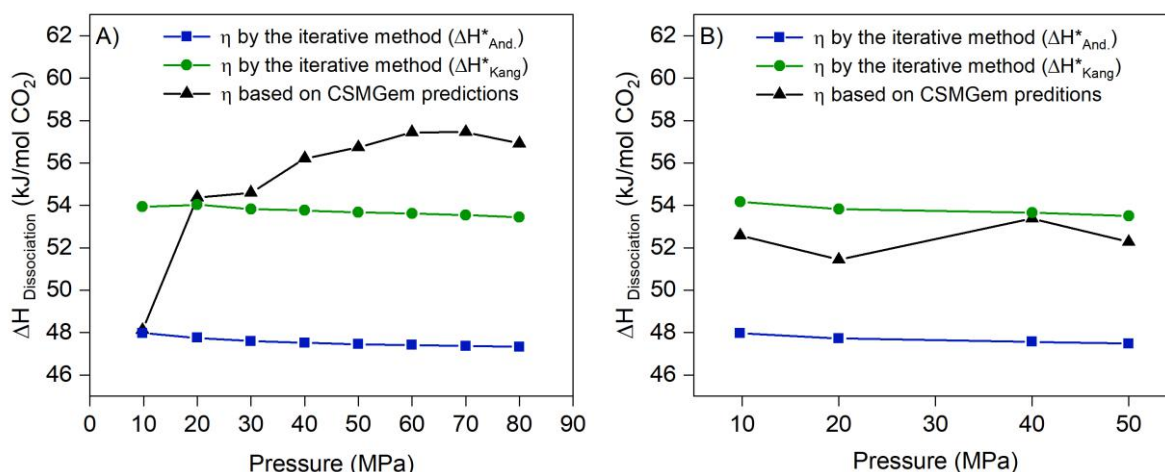


Figure 4.33 shows enthalpies of dissociation calculated by the Clapeyron equation. A notable difference is observed by using the reference enthalpies reported by Kang et al. (2001) and Anderson (2003). The latter author also found a difference

of about $5 \text{ kJ}\cdot\text{mol}^{-1}$ for the enthalpies calculated on the $L_W\text{-H-V}_{\text{HC}}$ equilibrium lines and indicates that a systematic error could have occurred in the calorimetric measurement from Kang et al. (2001). It was suggested because the calorimetric result for methane hydrate reported by Kang et al. also presents a significant deviation from enthalpies obtained by Handa (1986) using a direct method.

Figure 4.33 – Enthalpies of CO_2 hydrates dissociation by the Clapeyron equation based on experimental data: A) standard method; B) multicycles method. The black line regards to the calculus of hydrate dissociation using n calculated from the cages occupancy obtained by CSMGem predictions.



The enthalpies of dissociation obtained by the integration of thermograms are shown in Figure 4.34. Regardless the hydration number method applied, the results approach to the ones obtained by Clapeyron equation in which the Anderson enthalpy was used as the reference. In this case, the results from integrations and Clapeyron equation ($\Delta H_{\text{And.}}^*$) provides very good agreement. Figure 4.35 shows the absolute deviations from results obtained by Clapeyron equation and integration method. The average deviations and the respective confidence intervals (95%) indicate that using n from the iterative method ($\Delta H_{\text{And.}}^*$) provides the most reliable results.

As for ethane hydrates, no data were found in the literature for CO_2 hydrate dissociation above Q_2 . Moreover, the previous reported results vary in a broad temperature range, as shown in Table 4.17. However, considering that the latent heat of CO_2 vaporization is around 9 kJ/mol (NIST Webbook), it is reasonable that the enthalpy changes found in this work are lower than in the literature.

Figure 4.34 – Enthalpies of CO₂ hydrates dissociation determined by the integration of curves from calorimetric thermograms obtained by the multicycles method. (*) η by the iterative method.

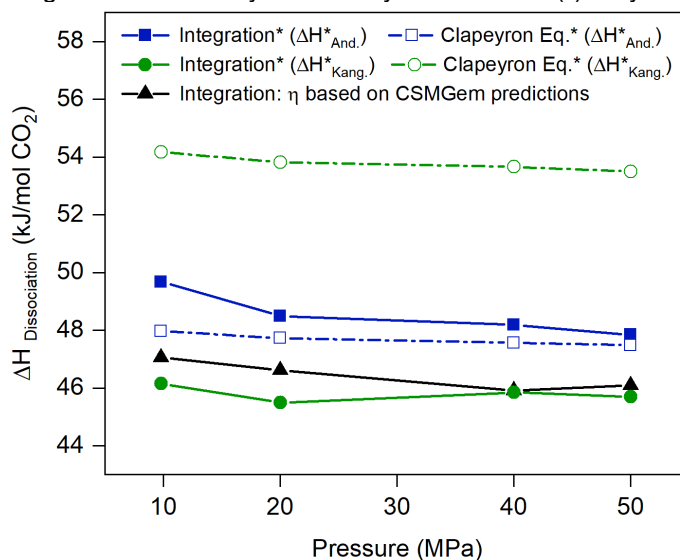


Figure 4.35 – Absolute deviations of CO₂ dissociation enthalpies calculated by the Clapeyron equation and integration of curves from thermograms.

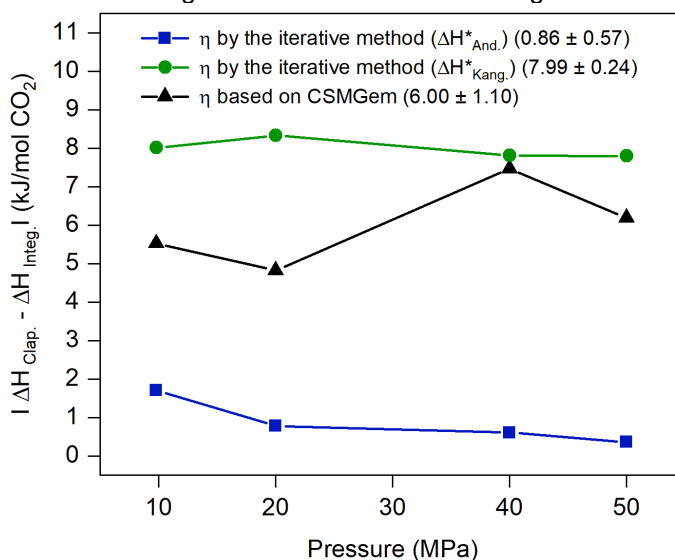


Table 4.17 – Enthalpies of CO₂ hydrates obtained in this work and found in the literature.

Reference	Method	T (K)	ΔH (kJ/mol CO ₂)
This work	HP-μDSC	283.52 - 286.61	48.55 ± 0.78
	Clapeyron	283.70 - 288.45	47.69 ± 0.21
Nasir et al. (2014)	Clausius-Clapeyron	Q ₁	53.29
Sabil (2010)	Clausius-Clapeyron	273.15 - 282.06	75.37 - 56.85
Yoon et al. (2003)	Clausius-Clapeyron	273.15	57.66
Anderson (2003)	Clapeyron	271.8 - 283.1 *	63.6 - 57.6 *
Kang et al. (2001)	Microcalorimeter	273.65	65.22
Bozzo et al. (1975)	Clausius-Clapeyron	273.15	58.99
Vlahakis et al. (1972)	Clausius-Clapeyron	273.20	59.90

* Corresponding to Q₁ (1.256 MPa) and Q₂ (4.499 MPa)

4.6 CONCLUSIONS

This chapter presents new thermodynamic data based on high-pressure microcalorimetry for single hydrates of methane, ethane and carbon dioxide. Predictions from CSMGem and Multiflash software were evaluated according to the experimental results. Onset temperatures are the most reliable for estimating hydrate equilibrium by HP- μ DSC and tend to be closer to CSMGem predictions. In fact, multiflash predictions are far from CSMGem ones, especially for ethane and carbon dioxide hydrates, and the discrepancy is greater as pressure increases. As expected, the increase in pressure led to higher hydrate dissociation temperatures. On the other hand, the ice melting temperatures are diminished with an increase in pressure, in agreement with the phase diagram of water. The influence of some experimental factors on hydrates dissociation by HP- μ DSC was also studied. The main results are summarized below for each system addressed:

- Results from methane hydrates showed reproducible and accurate onset temperatures, within the experimental uncertainty. Standard deviations of the onset temperatures corresponding to the ice melting are slightly lower than those of the hydrate dissociation due to the probable structural irregularities and cages occupancy on the latter;
- The onset temperatures in binary systems (one gas and water) seem not to be substantially affected by the amount of water added into the cell. On the other hand, dynamic effects play a role in the kinetics of hydrate formation, and hence the water-sample size affects the proportion of ice and hydrate formed. A higher amount of water favored the methane hydrate formation likely by increasing the interfacial areas between gas and aqueous phase;
- Unlike pure substances, the cooling/heating rate slightly affects the onset temperature of the hydrate dissociation. A higher cooling rate implies the formation of a more heterogeneous structure by inducing more empty cavities and intergranular defects, thus leading to lower dissociation temperatures. Onset temperatures of methane hydrates obtained at $1 \text{ K}\cdot\text{min}^{-1}$ resulted in higher deviations from predictions than at 0.5 and $0.2 \text{ K}\cdot\text{min}^{-1}$. Moreover, methane and ethane hydrates analyzed at $1 \text{ K}\cdot\text{min}^{-1}$ by the standard method presented slightly lower onset temperatures than analyses based on the multicycles method performed at $0.2 \text{ K}\cdot\text{min}^{-1}$. Despite all this evidence, the analysis time by running

at $0.2 \text{ K}\cdot\text{min}^{-1}$ can be significantly longer, and the results at $1 \text{ K}\cdot\text{min}^{-1}$ are still accurate with deviations within the experimental accuracy;

- A method of multicycles was applied in order to increase the ice conversion to hydrate. Lower onset temperatures were observed for methane and carbon dioxide hydrates after multiple cycles when the same cooling / heating rate was applied in both methods. This may be related to a slightly higher degree of heterogeneity when performing the multicycles method. The relatively low cage occupancy degree of inner hydrate layers formed during subsequent cycles should reduce the onset dissociation temperature. The heterogeneity of hydrates obtained by the multicycles method is evident in thermograms of dissociation. Nevertheless, the results of onset temperatures are still accurate and satisfactory;
- High pressures and a large amount of water seem to contribute to a faster ice conversion to methane hydrate over subsequent cycles;
- Ethane systems noticeably required more cycles to reach 90% of ice conversion to hydrate than methane and carbon dioxide systems. The larger size of ethane molecules makes geometrically harder the diffusion and incorporation of these molecules into hydrate structures. This phenomenon also contributes to a more heterogeneous structure;
- The fractions of carbon dioxide hydrate formed in the first cycle are much higher than hydrate fractions in methane and ethane systems. The high solubility and diffusivity of CO_2 contribute to the hydrate formation. These factors may also promote more homogeneous hydrate structures;
- Although the multicycles method may imply a slightly higher heterogeneity on hydrate structures, it has shown to be much more accurate to estimate enthalpies, by integrating the dissociation curves, than the standard method. The determination of baselines is much easier when no recrystallization process is observed and most of the ice is converted to hydrate. The deviations between enthalpies of CH_4 dissociation calculated by integrations and the Clapeyron equation are considerably lower by applying the multicycles method than the standard method;
- An iterative method is presented in this work to calculate the enthalpy of hydrate dissociation using the Clapeyron equation. This method accounts for the finite

volumes of all phases, the non-ideality of the vapor phase and the solubility of hydrocarbons in water. In addition, the hydrate volume was estimated by considering the effect of isobaric thermal expansivity and isothermal compressibility factors on the lattice parameter. These factors affect the hydration number and hence the enthalpy of dissociation. Although the equation chosen to describe the equilibrium data may slightly affect the term dP/dT from the Clapeyron equation, the results for both n and ΔH_{diss} obtained through iterations are consistent for all single hydrates studied;

- Although ΔH_{diss} is almost constant along the same equilibrium line, this property varies depending on the phases involved. No data was found in literature for dissociation enthalpy of single ethane and carbon dioxide hydrates at the same thermodynamic equilibrium conditions addressed in this work (above the upper quadruple point);
- Dissociation enthalpy of singles hydrates determined by the Clapeyron equation (n from iterations) based on standard and multicycles data present excellent agreement. On the other hand, the use of hydration numbers based on CSMGem predictions of fractional cages occupancy does not provide consistent results. The enthalpies of dissociation from the Clapeyron equation are compared to the ones determined by integrations, and the average deviations, along with their respective confidence intervals (95%), indicate that the multicycles method and the use of n from the iterative method provide the most reliable results.

REFERENCES

ANDERSON, G.K. Enthalpy of dissociation and hydration number of carbon dioxide hydrate from the Clapeyron equation. *Journal of Chemical Thermodynamics*, v. 35, p. 1171-1183, 2003.

ANDERSON, G.K. Enthalpy of dissociation and hydration number of methane hydrate from the Clapeyron equation. *Journal of Chemical Thermodynamics*, v. 36, p. 1119-1127, 2004.

BALLARD, A.L. A non-ideal hydrate solid solution model for a multi-phase equilibria program. Ph.D. Thesis, Colorado School of Mines, Golden, Colorado, USA, 2001.

BOZZO, A.T.; CHEN, H.-S.; KASS, J.R.; BARDUHN, A.J. The proprieties of Hydrate of chlorine and carbon dioxide. *Desalination*, v. 16, p. 303-320., 1975.

CONLEY, J.G.; HUANG, J.; ASADA, J.; AKIBA, K. Modeling the effects of cooling rate, hydrogen content, grainrefiner and modifier on microporosity formation in Al A356 alloys. *Materials Science and Engineering A*, v. 285, p. 49 – 55, 2000.

CHROSTEK, T. The influence of the heating and cooling rates on the temperature of the phase transitions. *Oficyna Wydawnicza Stowarzyszenia Menedżerów Jakości i Produkcji (SMJiP)*, Chapter 6, p.87-98, 2016.

DAVIES, S.R.; HESTER, K.C.; LACHANCE, J.W.; KOH, C.A.; SLOAN, E.D. Studies of hydrate nucleation with high pressure differential scanning calorimetry. *Chemical Engineering Science*, v. 64, p. 370-375, 2009.

DENYS S., SCHLÜTER O., HENDRICKX M.E.G., KNORR D. Effects of High Pressure on Water-Ice Transitions in Foods. In: Hendrickx M.E.G., Knorr D., Ludikhuyze L., Van Loey A., Heinz V. (eds) *Ultra High Pressure Treatments of Foods*, chapter 8, p. 242. Food Engineering Series. Springer, Boston, MA, 2001.

GUPTA, A. Methane Hydrate Dissociation Measurements and Modeling: The Role of Heat Transfer and Reaction Kinetic, Ph.D. thesis, Colorado School of Mines, Golden, Colorado, USA, 2007.

GUPTA, A.; LACHANCE, J.; SLOAN, E. D.; KOH, C. A. Measurements of methane hydrate heat of dissociation using high pressure differential scanning calorimetry. *Chemical Engineering Science*, v. 63, p. 5848-5853, 2008.

HANDA, Y.P. Compositions, enthalpies of dissociation, and heat capacities in the range 85 to 270 K for clathrate hydrates of methane, ethane, and propane, and enthalpy of dissociation of isobutane hydrate, as determined by a heat-flow calorimeter. *Journal of Chemical Thermodynamics*, v. 18, p. 915- 921, 1986.

KANG, S.P.; LEE, H.; RYU, B.J. Enthalpies of dissociation of clathrate hydrates of carbon dioxide, nitrogen, (carbon dioxide + nitrogen), and (carbon dioxide + nitrogen + tetrahydrofuran). *Journal of Chemical Thermodynamics*, v. 33, p. 513–521, 2001.

KE, W.; SVARTAAS, T.M. Effects of stirring and cooling on methane hydrate formation in a high pressure isochoric cell. Proceedings of the 7th International Conference on Gas Hydrates (ICGH), Edinburgh, Scotland, United Kingdom, July 17-21, 2011.

KERKAR, P.B.; HORVAT, K.; MAHAJAN, D.; JONES. K.W. Formation and dissociation of methane hydrates from seawater in consolidated sand: mimicking methane hydrate dynamics beneath the seafloor. *Energies*, v. 6, p. 6225-6241, 2013.

NAKAGAWA, R.; HACHIKUBO, A.; SHOJI, H. Dissociation and specific heats of gas hydrate under submarine and sublacustrine environments. Proceedings of the 6th International Conference on Gas Hydrates (ICGH), Vancouver, British Columbia, Canada, July 6-10, 2008.

NASIR, Q.; LAU, K.K.; LAL, B. Enthalpies of dissociation of pure methane and carbon dioxide gas hydrate. *International Journal of Chemical and Molecular Engineering*, v. 8, p. 840-843, 2014.

LINSTROM, P.J.; MALLARD, W.G. (Eds.). NIST Chemistry WebBook, NIST Standard Reference Database Number 69, July 2001, National Institute of Standards and Technology, Gaithersburg MD, 20899 (<http://webbook.nist.gov>).

POKHAREL, S. ARYAL, N.; NIRLAULA, B.R.; SUBEDI, A.; ADHIKARI, N.P. Transport properties of methane, ethane, propane, and n-butane in water. *Journal of Physics Communication*, v. 2, 065003, 2018.

SABIL, K.M.; WITKAMP, G-J.; PETERS, C.J. Estimations of enthalpies of dissociation of simple and mixed carbon dioxide hydrates from phase equilibrium data. *Fluid Phase Equilibria*, v. 290, p. 109-114, 2010.

SAHLE, C.J.; STERNEMANN, C.; SCHMIDT, C.; LEHTOLA, S.; JAHN, S.; SIMONELLI, L.; HUOTARI, S.; HAKALA, M.; PYLKKÄNEN, T.; NYROW, A.; MENDE, K.; TOLAN, M.; HÄMÄLÄINEN, K.; WILKE, M. Microscopic structure of water at elevated p, T. *Proceedings of the National Academy of Sciences*, v. 110, p. 6301-6306, 2013.

SANZ, E.; VEGA, C.; ABASCAL, J.L.F.; MACDOWELL, L.G. Phase Diagram of Water from Computer Simulation. *Physical Review Letters*, v. 92, 255701, 2004.

SCHARLIN, P.; BATTINO, R.; SILLA, E.; TUÑÓN, I.; PASCUAL-AHUIR, J.L. Solubility of gases in water: correlation between solubility and the number of water molecules in the first solvation shell. *Pure and Applied Chemistry*, v. 70, p. 1895-1904, 1998.

SLOAN E.D.; KOH, C. Clathrate hydrates of natural gases, 3rd ed. Boca Raton: CRC Press, 2008.

SLOAN, E.D.; FLEYFEL, F. Hydrate dissociation enthalpy and guest size. *Fluid Phase Equilibria*, v. 76, p. 123-140, 1992.

SLOAN, E.D.; FLEYFEL, F. Reply to "comments on: hydrate dissociation enthalpy and guest size", *Fluid Phase Equilibria*, v. 96, p. 233-235, 1994.

SUN, S.; HAO, Y.; ZHAO, J. Analysis of gas source for the replacement of CH₄ with CO₂ in gas hydrate production from the perspective of dissociation enthalpy. *Journal of Chemical and Engineering Data*, v. 63, p. 684-690, 2018.

TAMIMI, A.; RINKER, E.B.; SANDALL, O.C. Diffusion coefficients for hydrogen sulfide, carbon dioxide, and nitrous oxide in water over the temperature range 293-368 K. *Journal of Chemical & Engineering Data*, v. 39, p. 330-332, 1994.

VLAHAKIS, J.G.; CHEN, H.-S.; SUWANDI, M.S.; BARDUHN, A.J. The growth rate of ice crystals: Properties of carbon dioxide hydrate, a review of properties of 51 gas hydrates, Syracuse University. *Research and development report 830 prepared for US Department of Interior*, 1972.

ZHANG, X.; YANG, W.; XU, H.; ZHANG, L. Effect of cooling rate on the formation of nonmetallic inclusions in X80 pipeline steel. *Metals*, v. 9, 392, 2019.

WELLEN, R.M.R; RABELLO, M.S.; ARAUJO JUNIOR, I.C.; FECHINE, G.J.M; CANEDO, E.L. Melting and crystallization of poly(3-hydroxybutyrate): effect of heating/cooling rates on phase transformation. *Polímeros*, v. 25, p. 296-304, 2015.

CHAPTER 5

THERMODYNAMIC STUDY OF DOUBLE-GUEST GAS HYDRATES

ABSTRACT

Dissociation data of double-guest gas hydrates are presented in this chapter for systems composed of $\text{CH}_4\text{-C}_2\text{H}_6\text{-H}_2\text{O}$, $\text{CH}_4\text{-C}_3\text{H}_8\text{-H}_2\text{O}$, and $\text{CH}_4\text{-CO}_2\text{-H}_2\text{O}$. The results obtained by HP- μ DSC are compared to CSMGem and Multiflash predictions up to 100 MPa. Ternary phase diagrams were also designed for these gas hydrate-forming systems based on computational simulations to study the influence of overall and gas-phase compositions on gas hydrate dissociation temperatures. The suitability of structures I and II to host different types of molecules and the occupancy degree of the cages are addressed in order to explain the dissociation temperature profiles according to the composition. The quaternary system composed of $\text{CH}_4\text{-C}_2\text{H}_6\text{-C}_3\text{H}_8\text{-H}_2\text{O}$ was also studied through computational simulations.

5.1 INTRODUCTION

The influence of different experimental factors on mass transfer inside the microcalorimeter cell was evaluated in the last chapter. For multiple-guest systems, the dynamic effects on hydrates properties have to be considered much more carefully in this case. Considering that the diffusion of molecules in water varies with gas species, inner regions of the hydrate layer may be more filled with gas that has a higher diffusion coefficient. On the other hand, the structure should be more ideally occupied at layers close to the surface since the interface facilitates the incorporation of any gas-phase molecules into the hydrate structure. Gas solubility is another factor that should also affect the concentration of gas molecules in the liquid phase. Therefore, a heterogeneous structure can be formed in unstirred systems containing gas mixtures due to the gas concentration gradient throughout the aqueous phase, and this should influence hydrate properties, including dissociation temperature.

The type of the crystalline structure to be formed also depends on the size and composition of the guest molecules involved (NIXDORG; OELLRICH, 1997). The main types of structures formed during crystallization are sI, sII, and sH. These structures

present different equilibrium properties, such as formation and dissociation temperature, enthalpy, and heat capacity, as mentioned in previous chapters. All these data are essential for applying gas hydrates technology for the transportation of natural gas, to develop inhibition strategies, or even using hydrates in other applications. Subramanian et al. (2000) studied methane-ethane-water system by Raman spectroscopy at different gas compositions and pressures not higher than 1.6 MPa. The group verified a sudden change from the structure I to structure II as the amount of methane increased. The structure I prevailed in the samples containing up to 72.2 mol% of methane, whereas structure II was predominant in samples with larger fractions of methane. They suggested that the proximity between the host molecules size and the cavity diameter may explain the higher stability of structure II in a broad range of gas composition. For the system methane-propane-water, it has also been evidenced the coexistence structures I and II, although the formation of sI is not predicted by all commercial software programs. Klapproth et al. (2019) and other groups have also reported the formation of methane hydrate along with methane-propane hydrate in such systems. The discussion about this system is extended to Chapter 6, where a complementary technique based on a PVT cell is used to determine equilibrium properties.

This chapter presents enlightening results obtained exclusively by high-pressure microcalorimetry and computational simulations for different hydrate-forming systems composed of methane-ethane-water, methane-propane-water, methane-carbon dioxide-water, and methane-ethane-propane-water (the latter only by computational analysis). Ternary diagrams and dissociation temperature profiles as a function of gas-phase composition were built based on simulations using the CSMGem software. The purpose of modeling was to study the effect of both overall and gas-phase compositions on the type of hydrate structure formed and its dissociation temperature. Then, experimental data obtained at specific conditions were used to evaluate the reliability of predictions. In addition to the guest-molecules species, this chapter also discusses the effect of the cage occupancy degree on the hydrate properties, and how this may contribute to a structural transition in some cases.

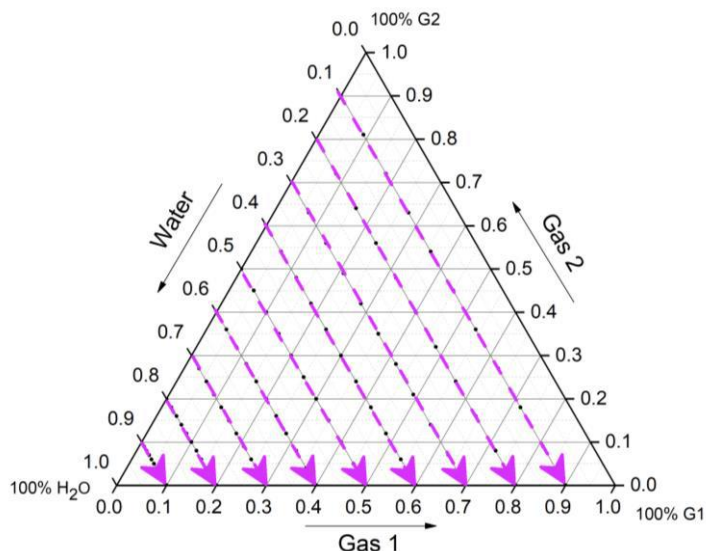
5.2 SPECIFIC EXPERIMENTAL CONDITIONS

Experimental Configuration: Systems containing gas mixtures were studied by HP- μ DSC. Two operational modes are possible: constant pressure or isochoric mode. During the isochoric mode the system is kept closed so that the volume and overall composition was kept constant throughout the experiment. This method was selected herein in order to make feasible the comparison between experimental results to computational predictions. However, the experimental pressure is not strictly constant during the analysis when using the isochoric mode due to temperature variation, unlike the constant pressure mode applied for single hydrates presented previously. For this reason, the dissociation pressure was determined from the onset point of the hydrate dissociation curve to increase accuracy of results. However, it is worth to mention that the pressure variation concerned to the hydrate dissociation is relatively low due to the small amount of sample in the cell. In addition, the temperature range covered during the dissociation process is also short. Thus, pressure can be considered approximately constant during this reaction.

Computational Analysis: In this chapter, the microcalorimetric results are compared to CSMGem and Multiflash predictions. The overall composition used as input in simulations was established according to the results obtained from estimations by using the Peng-Robinson EoS, as studied in Chapter 3. The compositions indicated in any figure or table in this chapter refer to water-free compositions.

Ternary diagrams were built based on 116 equilibrium points obtained at different compositions for the hydrate-forming systems: CH₄-C₂H₆-H₂O, CH₄-C₃H₈-H₂O, CH₄-CO₂-H₂O, and CH₄-C₂H₆-C₃H₈-H₂O. Temperature-gas composition plots, $T(P, x_{CH_4})$, have also been analyzed at constant water fraction (0.5) for these systems. In fact, the temperature profiles look very similar for any water fraction illustrated in Figure 5.1. Although only the diagrams using CSMGem predictions are presented in this chapter, profiles obtained using Multiflash predictions were very similar.

Figure 5.1 – Cross-sections of ternary phase diagrams at constant water fractions. The temperature profiles are similar, following either trajectory.



5.3 INFLUENCE OF CAGE OCCUPANCY ON STRUCTURAL STABILITY OF HYDRATES

The dissociation temperature of a specific system is related to its structural stability, and it can be explained by the cavities occupancy. Table 5.1 shows the ratios of guest molecule size by cavities diameter for structures I and II, reported by Sloan and Koh (2008). It is assumed that the structure stability depends on the ratio between guest molecule size and the cavity diameter. The typical values for this ratio vary between 0.76 and 1, and the structure becomes more stable as this ratio approaches to the unit. A proportion greater than 1 means that the host molecule is larger than the cavity and therefore such configuration is unlikely to form. For pure methane, for example, although the molecules are more stable in cavity 5¹² of sII than sI ($\Theta_{sII-SC} = 0.868$; $\Theta_{sI-SC} = 0.855$), the latter prevails due to their better fit in the large cavities of structure I than in large cavities of structure II ($\Theta_{sI-LC} = 0.744$; $\Theta_{sII-LC} = 0.655$). In fact, large cavity is more predominant in sI (3 LC : 1 SC) than small cavity in sII (2 SC : 1 LC). On the other hand, ethane tends to form structure I due to higher stability in larger cavities ($\Theta_{sI-LC} = 0.939$) when compared to sII ($\Theta_{sII-LC} = 0.826$), considering that ethane molecules are not preferentially hosted in smaller cavities since the ratio is higher than 1 in both structures. This approach based on molecules fit inside cages added to the occupancy degree (considering the probable presence of empty cavities), are factors addressed in this work to explain the diagrams obtained by simulations for the following systems: CH₄-C₂H₆-H₂O, CH₄-C₃H₈-H₂O, CH₄-CO₂-H₂O, and CH₄-C₂H₆-C₃H₈-H₂O.

Table 5.1 – Ratio of guest and cavities diameters for structures sI and sII.

Guest Molecules	guest molecule diameter / cavity diameter (Θ)			
	sI		sII	
	small cage (SC) 5 ¹²	large cage (LC) 5 ¹² 6 ²	small cage (SC) 5 ¹²	large cage (LC) 5 ¹² 6 ⁴
CH ₄	0.855	0.744	0.868	0.655
C ₂ H ₆	1.080	0.939	1.100	0.826
C ₃ H ₈	1.230	1.070	1.250	0.943
CO ₂	1.000	0.834	1.020	0.769

Source: Adapted from Sloan and Koh (2008)

5.4 METHANE-ETHANE-WATER SYSTEM

5.4.1 Equilibrium Data for CH₄-C₂H₆ Hydrates by Microcalorimetry

Table 5.2 presents experimental data for hydrates obtained from methane-ethane-water system. The first column refers to the methane content of the gas mixture injected into the cell (water-free composition). The onset and peak temperatures are compared to predictions performed by CSMGem and Multiflash software programs, as in the previous chapter. Onset temperatures approach to CSMGem predictions, whereas peak temperatures to Multiflash ones.

Table 5.2 – Dissociation data of CH₄-C₂H₆ hydrates obtained by HP- μ DSC and the respective absolute deviations (AD) from computational predictions.

CH ₄ (g) (mol%)	P _{Onset} (MPa)	T _{CSMGem} (K)	T _{Multiflash} (K)	T _{ONSET} (K)			T _{PEAK} (K)		
				HP- μ DSC	AD CSMGem	AD Multiflash	HP- μ DSC	AD CSMGem	AD Multiflash
21.0	19.3	295.67	296.00	295.62	0.05	0.38	297.70	2.03	1.70
	39.8	299.64	300.30	299.56	0.08	0.74	301.66	2.02	1.36
	60.1	302.80	303.87	303.00	0.20	0.87	304.25	1.45	0.38
	80.2	305.39	306.89	305.78	0.39	1.11	306.99	1.60	0.10
	100.3	307.67	309.66	307.94	0.27	1.72	309.43	1.76	0.23
32.8	20.5	296.32	296.84	296.36	0.04	0.48	297.65	1.33	0.81
	40.6	300.24	301.11	300.54	0.30	0.57	301.90	1.66	0.79
	60.4	303.26	304.52	303.67	0.42	0.85	304.78	1.52	0.26
	80.2	305.83	307.52	306.36	0.53	1.16	307.62	1.79	0.10
	100.5	308.14	310.35	308.93	0.79	1.42	309.98	1.84	0.37

Continues

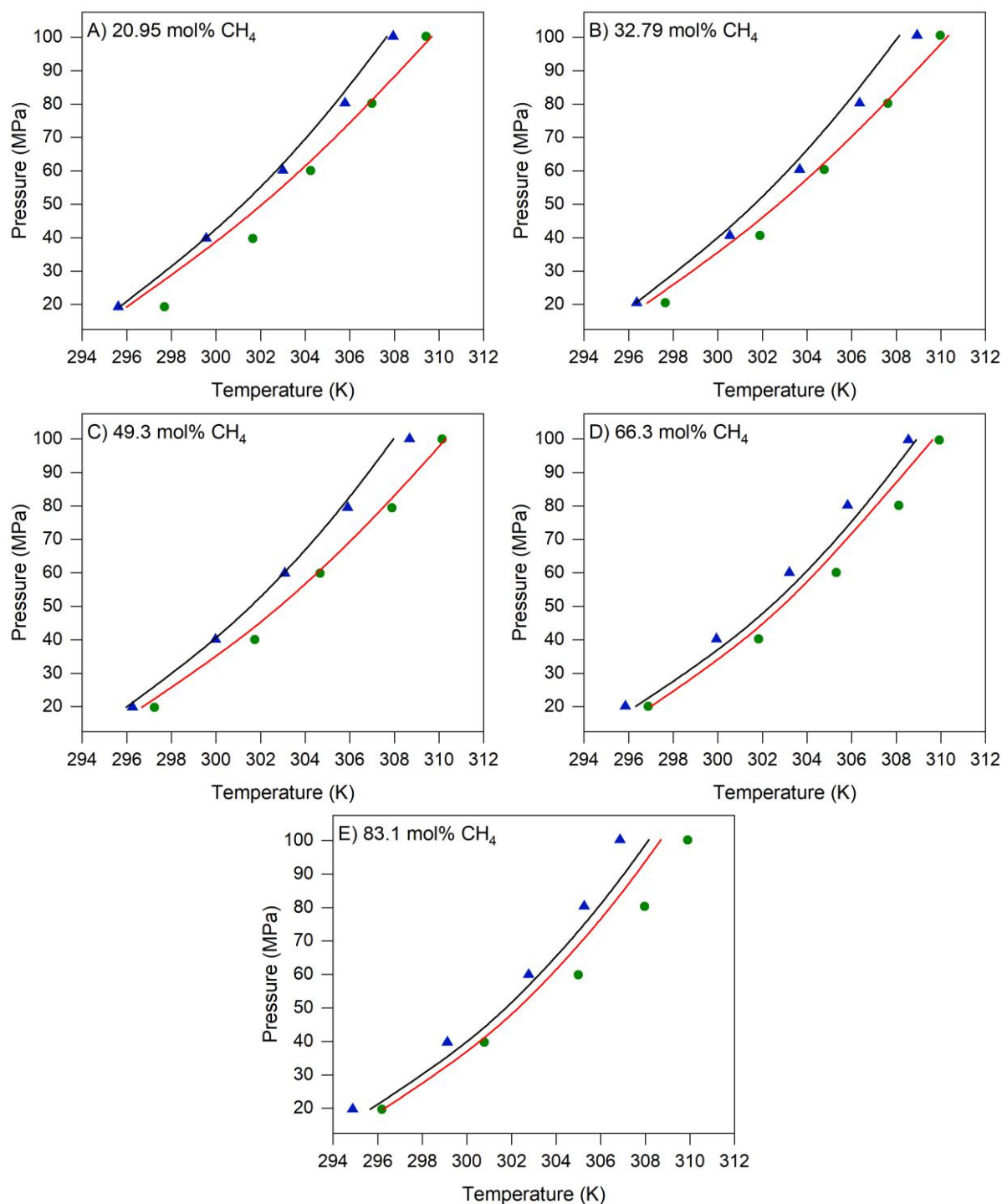
Continuation

CH ₄ (g) (mol%)	P _{Onset} (MPa)	T _{CSMGem} (K)	T _{Multiflash} (K)	T _{ONSET} (K)			T _{PEAK} (K)		
				HP- μ DSC	AD CSMGem	AD Multiflash	HP- μ DSC	AD CSMGem	AD Multiflash
49.3	19.8	295.98	296.68	296.26	0.28	0.42	297.25	1.27	0.57
	40.0	300.06	301.16	299.98	0.08	1.18	301.74	1.68	0.58
	59.8	303.11	304.59	303.08	0.03	1.51	304.67	1.57	0.08
	79.5	305.67	307.53	305.90	0.23	1.63	307.89	2.22	0.36
	100.0	307.96	310.31	308.68	0.72	1.63	310.14	2.18	0.17
66.3	20.1	296.32	297.02	295.85	0.47	1.17	296.89	0.57	0.13
	40.2	300.83	301.39	299.94	0.89	1.44	301.84	1.01	0.45
	60.1	304.01	304.47	303.21	0.80	1.26	305.31	1.30	0.85
	80.1	306.65	307.12	305.82	0.83	1.30	308.12	1.47	1.01
	99.7	308.89	309.63	308.54	0.34	1.09	309.94	1.06	0.31
83.1	19.7	295.66	296.25	294.88	0.78	1.37	296.20	0.54	0.05
	39.7	300.21	300.77	299.12	1.09	1.64	300.78	0.57	0.01
	59.9	303.30	303.86	302.77	0.53	1.09	305.00	1.70	1.14
	80.4	305.99	306.53	305.26	0.73	1.27	307.97	1.98	1.44
	100.2	308.16	308.70	306.86	1.30	1.84	309.90	1.74	1.20

Conclusion

Figure 5.2 shows the data from Table 5.2 according to the initial composition (water free) of the gas phase inside the cell. Interestingly, onset temperatures tend to come after the CSMGem predictions at plots A, B, and C, but they precede the equilibrium line at plots D and E. In fact, this system has a particularity of forming sI or sII depending on the gas composition. In general, sII forms when the methane content is higher than 50 mol%, the case of plots D and E. Thereby, one reason for higher onset temperatures in A, B and C, and lower onset temperatures in D and E is the coexistence of both structures I and II during the hydrate formation. Thus, a fraction of sII in the systems A, B and C may lead to higher onset temperatures than predictions, while a fraction of sI in the systems D and E may imply a lower onset temperatures. Another hypothesis is related to the difference of solubility and diffusion coefficients of methane and ethane (POKHAREL et al., 2018). These properties may affect the homogeneity and occupancy degree of the hydrate. Both hypothesis are also mentioned by Hachikubo et al. (2008), who found that the dissociation process of methane-ethane hydrates occurred in two stages, indicating the coexistence of both sI and sII and/or a presence of a ethane-rich fraction in the hydrate structure.

Figure 5.2 – Dissociation data of CH₄-C₂H₆ hydrates obtained by HP- μ DSC at different methane concentrations: (\blacktriangle) onset temperatures; (\bullet) peak temperatures. Black lines refer to CSMGem predictions and red lines, to Multiflash.

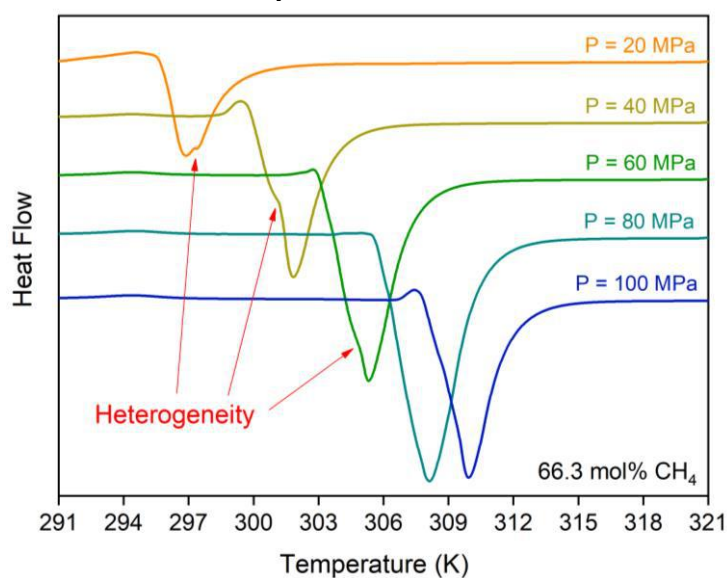


The issue of heterogeneity caused by different cage occupancy degrees will be resumed later, as this phenomenon was also observed for methane-propane and methane-carbon dioxide hydrates. Another observation from Figure 5.2 is that

Multiflash predictions are farther from CSMGem in the plots of A, B, and C, mainly as pressure increases. Since these data correspond to sI and the data of D and E to sII, one can assume that the predictions concerning to structure I implies the most significant discrepancies between both software.

As mentioned above, the hydrate structure type to be formed in methane-ethane-water systems depends on the gas phase composition. In fact, both structures I and II are predicted to be formed at compositions higher than 50 mol% CH₄, as will be discussed in the next section. These structures have similar dissociation temperatures, and thereby it is not possible to clearly distinguish each dissociation curve in the thermograms. Nevertheless, overlapped transitions can be observed during the dissociation of some methane-ethane hydrates, as shown in Figure 5.3.

Figure 5.3 – Overlapping transitions in thermograms, evidencing the heterogeneity of CH₄-C₂H₆ hydrate structures.



It is also believed that sII may coexist with sI at lower methane concentrations as a metastable phase. Two hypotheses are assumed herein: I) Both structures I and II may be formed during the process of nucleation and crystal growth; II) the metastable structure (sII) should transit to the stable one after a while, which perhaps takes longer than the time used in the analyses of this work. These hypotheses are supported by Ohno et al. (2009), who studied the transition between metastable and stable structures in methane-ethane hydrate through Raman spectroscopy. The hydrates were synthesized from gas mixtures containing 65 and 93 mol% CH₄ at 5.3 and 8.4

MPa, respectively. The group found that sI and sII initially formed in all the experiments and transitions from metastable to stable configuration occurred over time. It was also observed that the conversion rate from metastable to stable structure was significantly higher for the sample with 65% CH₄, since the complete transition from sII to sI took about 1 week and the transition from sI to sII in the sample with 93 mol% took only 3 hours. This fact was addressed considering two main factors: a) the driving force that induces phase transition; b) kinetics of transition. The driving force was considered to be the difference in water chemical-potential between sI and sII. For the sample with 65 mol% CH₄, such difference calculated using CSMGem was 36 J/mol, while it was 66 J/mol for the sample with 93% CH₄, indicating that the driving force plays a role in the conversion rate between the two structures. Regarding kinetics, the group also estimated that sI of the 65 mol% CH₄ sample was composed of 40 mol% methane, and sII of 66 mol% methane. In the 93 mol% CH₄ sample, sI was composed of 78 mol% methane, and sII of 76 mol%. Thus, it was concluded that in the first case there were many more molecules to be rearranged during the structural transition than in the latter, indicating that kinetics also contributed to a lower conversion rate for the sample with 65 mol% CH₄. Although the conversion rate was not addressed in this thesis (referring to hypothesis II), the results from this work and the ones reported by Ohno et al. (2009) strongly support that both sI and sII form simultaneously at the initial stage of hydrate formation, regardless of gas composition (referring to hypothesis I).

5.4.2 Thermodynamic and Structural Analysis of CH₄-C₂H₆ Hydrates by Simulations

Ternary diagrams of dissociation temperatures for methane-ethane hydrates are shown in Figure 5.4 at three different pressures. All cross-sections with constant water content have very similar temperature profiles, which mainly depend on the gas phase composition. The profiles vary slightly according to the pressure, as illustrated in the plots shown in Figure 5.5 for several pressures. As expected, higher pressures lead to higher dissociation temperatures, which are represented by warmer colors in the diagrams.

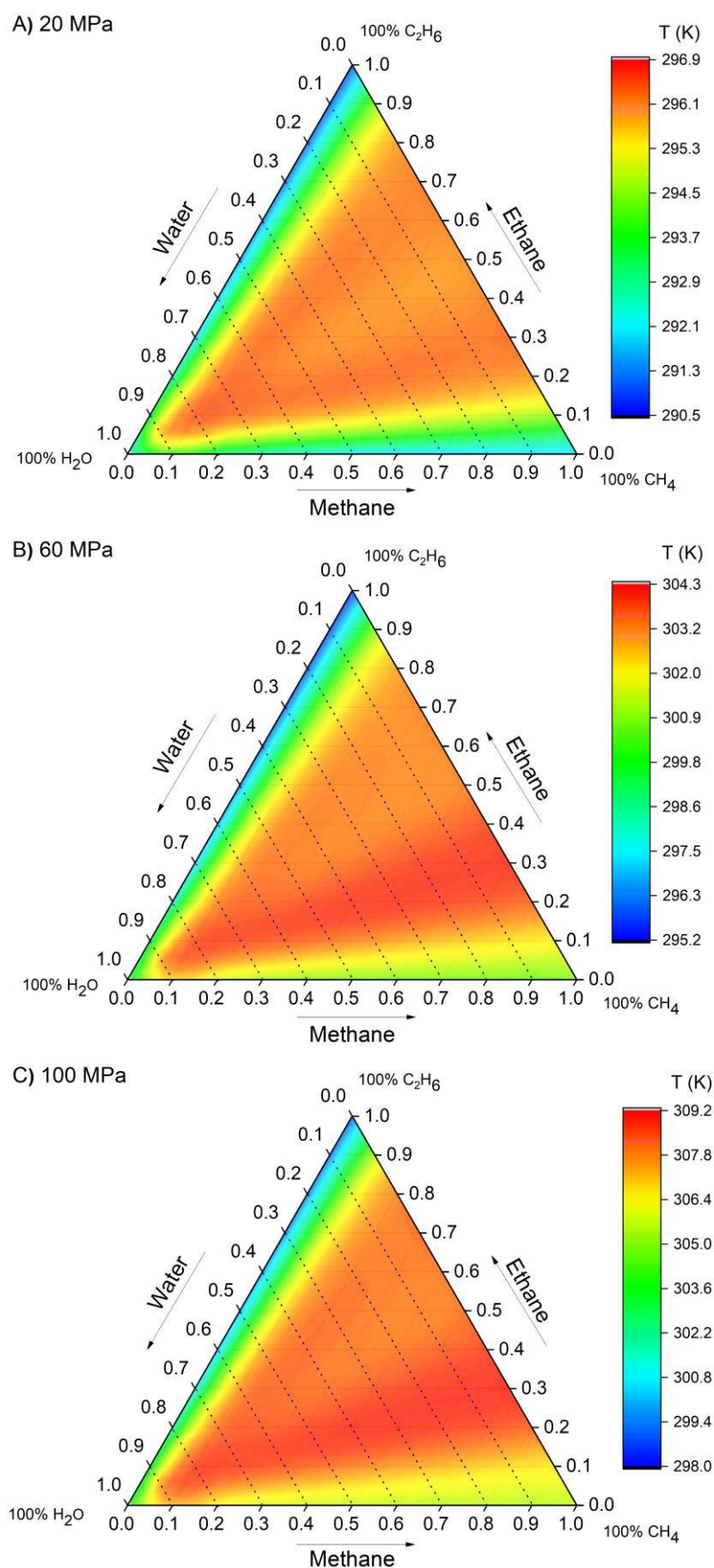
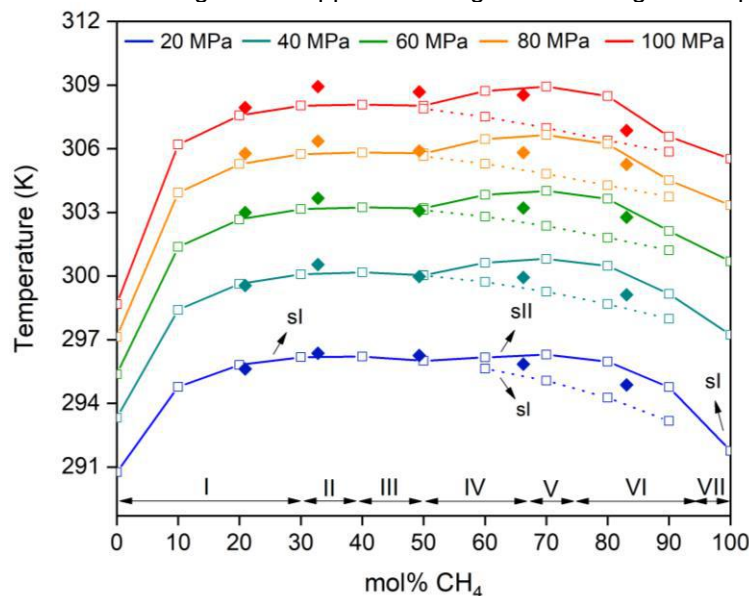
Figure 5.4 – Ternary diagrams of dissociation temperatures for CH₄-C₂H₆ hydrates.

Figure 5.5 – Dissociation temperature profiles of CH₄-C₂H₆ hydrates according to the gas phase composition: (◆) onset temperatures from thermograms; (□) CSMGem predictions. Dashed lines refer to the secondary structure (sl) predicted by simulations. Roman numerals refer to the regions established according to the supposed configuration of cages occupancy.



The predictions from CSMGem shown above confirm that the excess of methane leads to a secondary structure (sl) formed only by methane molecules. It means that there is a composition range in which two different structures coexist, but the software determines the dissociation temperature of the system by considering the more stable structure. Therefore, the onset temperatures above 50% molar of methane (Figure 5.5) are between the values of predictions for sl and sII likely due to the coexistence of these both structures, which have relatively close dissociation temperatures. Similarly, the onset temperatures below 50 mol% CH₄ tend to be slightly higher than predictions probably due to the presence of a metastable fraction of sII. In any case, the experimental data show good agreement with the computational simulations.

Regarding the structural stability for this hydrate system, structure II is formed at high methane concentrations due to the proximity of CH₄ molecules and small-cage sizes ($\Theta_{sII-SC} = 0.868$), which results in stronger interactions than structure I, added to the abundance of small cavities in sII. Besides, considering that ethane molecules can be hosted in large cavities of both structures, it is convenient to form a structure in which the number of large cavities is proportional to the ethane content. Thus, structure II provides a proper condition for hosting both methane and ethane molecules, avoiding the 'competition' to large-cage occupancy occurring in sl.

According to predictions, the dissociation temperature still changes according to the gas composition, even when only one structure should be present. As methane concentration increases in Figure 5.5, the equilibrium temperature profile is probably governed by the occupancy degree of the cavities in the respective structure. When the methane amount is sufficient to occupy most of the smaller cavities (either sI or sII), the maximum occupation of the structure is reached, i.e., most of larger cavities by ethane and most of smaller ones by methane molecules. Such configuration leads to the maximum dissociation temperature due to the high stability implied by guest-lattice interactions. Therefore, one can imagine two peaks related to maximum dissociation temperatures regarding the greatest occupancy degree for sI and sII. By following the temperature profile, it is possible to distinguish seven different regions, indicated by roman numerals in Figure 5.5. Figures 5.6 and 5.7 illustrate possible occupancy configurations of these regions as methane concentration increases in structures I and II, respectively.

Figure 5.6 – Evolution of the cages occupancy for sI hosting CH_4 (blue) and C_2H_6 molecules (yellow) as methane fraction increases.

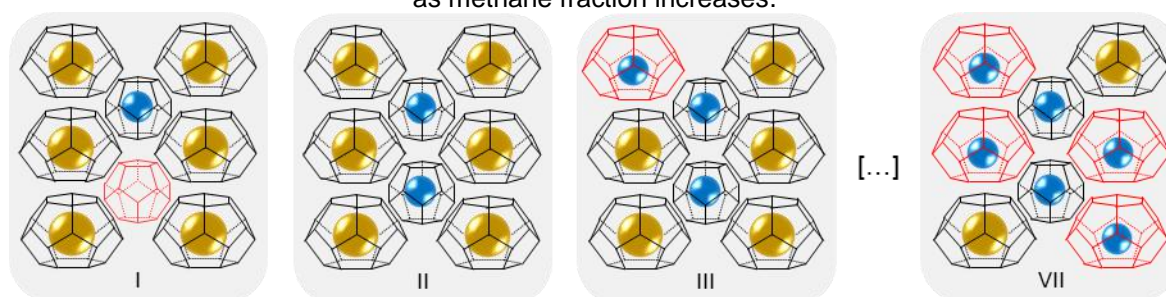
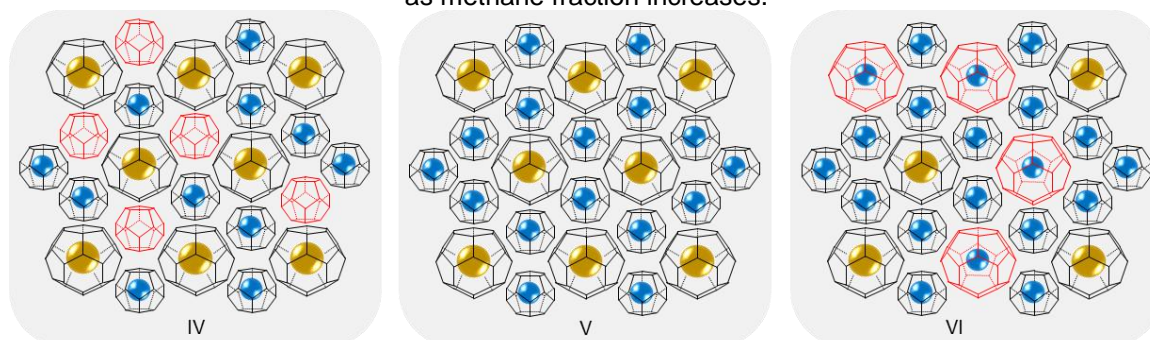


Figure 5.7 – Evolution of the cages occupancy for sII hosting CH_4 (blue) and C_2H_6 (yellow) molecules as methane fraction increases.



The illustrations do not represent real arrangement in the hydrate crystalline structure but do indicate the proportion between small and large cavities in a unit cell

for each structure. Blue and yellow balls represent methane and ethane molecules, respectively. Red cages point out empty or less stable cavities occupied by a smaller molecule, thus facilitating the dissociation of the structure. In the first region (I), low methane concentration increases the likelihood of small cavities (5^{12}) are empty or occupied by ethane, leading to less energy required to dissociate the hydrate. When methane content is sufficient to fill most of these small cavities (II), the maximum occupation of this structure is reached, requiring the highest temperature to dissociate this type of structure, depicted by the first peak observed in Figure 5.5. Thus, the temperature decreases slightly due to the occupation of large cavities ($5^{12}6^2$) by methane instead of ethane molecules (III). Subsequently, higher methane concentrations lead to the formation of sII instead of sI (IV), and by going on, a new maximum dissociation temperature is achieved when most of the cavities are occupied (V). Thereby, the temperature profile in Figure 5.5 describes two overlapping curves referring to sI and sII, in which the peaks represent the maximum occupation for each one, as mentioned before and similarly described by Larionov et al. (2006). After the second peak, the temperature decreases again (VI), because the increase in methane concentration implies the occupation of large cavities ($5^{12}6^4$) by methane instead of ethane molecules. This leads to a less stable configuration since guest and cavity diameters ratio (Θ) is just 0.665, ergo guest-lattice interaction is weaker, and the hydrate dissociation easier. Finally, sI turns back as the most favorable since ethane is scarce (about 90 mol% of CH_4) and methane molecules fill both cavities of this structure (VII).

5.5 METHANE-PROPANE-WATER SYSTEM

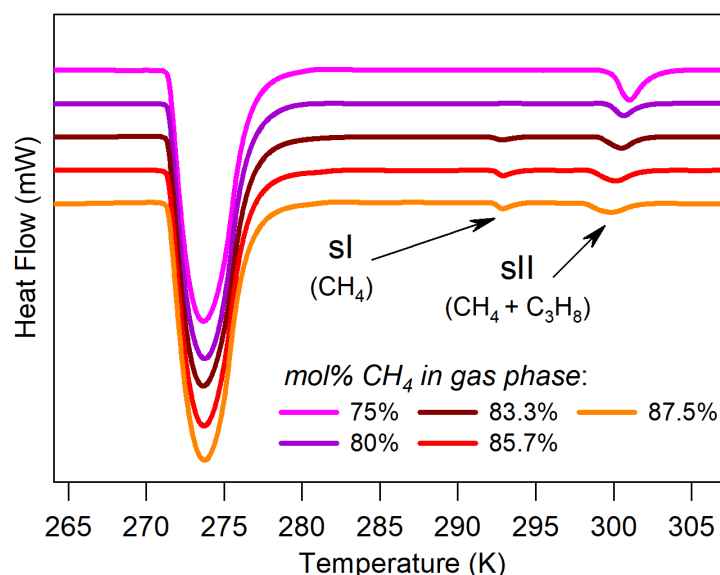
5.5.1 Coexistence of Structures I and II on $\text{CH}_4\text{-C}_3\text{H}_8$ Hydrates

Before presenting the dissociation data for methane-propane hydrates, it is convenient to elucidate a phenomenon observed during these analyses and reported by Menezes et al. (2019). The system composed of methane-propane-water is known to form structure II since the propane molecules fit the large cavities of this structure. CSMGem allows estimating the hydrate cage occupancy, and one could verify through calculations that methane molecules are hosted by both small and large cavities of sII.

However, the formation of different structures for this system is not predicted for any gas-phase composition range. In contrast, the results in this work reveal the formation of two different hydrate structures, both by microcalorimetry and by using a PVT-cell, discussed in the next chapter. Structures I and II are formed simultaneously during the cooling process, and probably sI is a pure methane hydrate, considering the similarity between calorimetric and predicted data.

Figure 5.8 shows the heating thermograms obtained by HP- μ DSC at different gas phase compositions. The first peak on the left corresponds to the ice melting. The structure I is observed only from 83.3 mol% CH₄ onwards, which suggests that the gas phase composition affects the type of structures initially formed in this hydrate-forming system. The proportion between sI and sII, in turn, seems not to differ significantly at different methane concentrations (20 MPa). However, this fact is detailed in Chapter 6 (section 6.4.3.4), where several experiments performed at different fractions of methane and propane at higher pressures by using a PVT cell will be presented.

Figure 5.8 – Thermograms of CH₄-C₃H₈ hydrates (20 MPa) at different gas phase compositions.

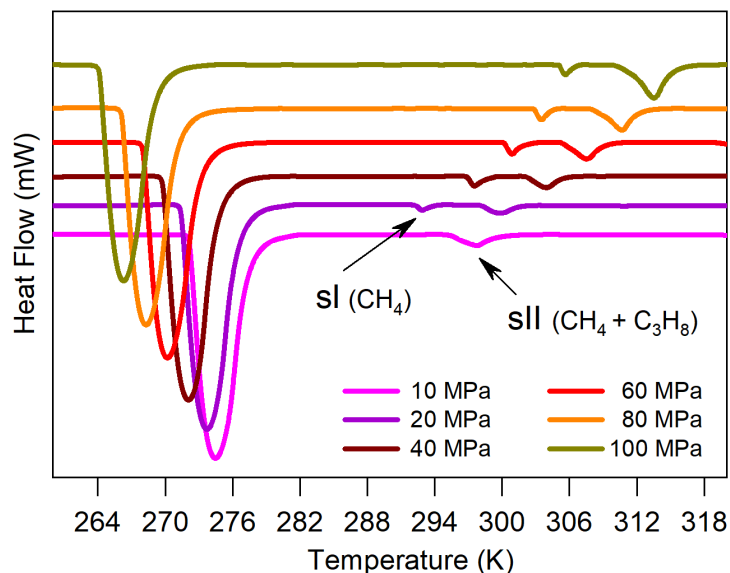


Source: Adapted from Menezes et al. (2019)

A series of thermograms are presented in Figure 5.9 at different pressures. There is no evidence for sI formation at 10 MPa, which agrees with the results from Uchida et al. (2004). At higher pressure, however, a new dissociation is verified just right on the methane hydrate (sI) dissociation range. The integration of the curves revealed similar areas for the supposed sI structure, but the areas for structure II are intensified

by increasing the pressure. Pressure does play a role in hydrate formation kinetics: the rate of diffusion of a gas depends on its partial pressure, as already stated. Thereby higher pressures lead to higher crystal growth rates.

Figure 5.9 – Thermograms of CH₄-C₃H₈ hydrates (87.5 mol% CH₄) at different pressures.



Source: Adapted from Menezes et al. (2019)

5.5.2 Equilibrium Data for CH₄-C₃H₈ Hydrates by Microcalorimetry

The onset and peak dissociation temperatures for CH₄-C₃H₈ hydrates (sII) previously shown in Figures 5.8 and 5.9 are presented in Table 5.3, as well as the deviations from predictions. Table 5.4, in turn, presents the data regarding the supposed methane hydrate (sI) formed along with sII at different pressures and methane fractions. In this case, the data are compared with simulations performed for single methane hydrates, since simulations for methane-propane system do not predict the formation of structure I. In all the systems studied in this work so far, the onset temperatures generally presented the lowest deviations when compared to CSMGem predictions. However, the deviations do not follow this tendency for this system and have to be studied separately to each hydrate dissociation curve. For structure II (Table 5.3), deviations from peak temperatures are lower than from onset temperatures, even when just sII was formed. For structure I (Table 5.4), in turn, the lowest deviation alternates between onset and peak temperatures. This may be because the amount of hydrate formed is too small so that peak temperatures approach predictions.

Table 5.3 – Dissociation data of CH₄-C₃H₈ hydrates (sII) obtained by HP- μ DSC and the respective absolute deviations (AD) from computational predictions. Bold data refer to analyses that presented a secondary structure non-predicted by computational simulations.

CH ₄ (g) (mol%)	P _{Onset} (MPa)	T _{CSMGem} (K)	T _{Multiflash} (K)	T _{ONSET} (K)			T _{PEAK} (K)		
				HP- μ DSC	AD CSMGem	AD Multiflash	HP- μ DSC	AD CSMGem	AD Multiflash
67.0	10.02	297.85	297.31	297.42	0.43	0.12	298.18	0.33	0.88
75.0	9.99	297.78	297.23	297.25	0.53	0.02	298.34	0.56	1.11
	19.71	300.95	300.24	299.93	1.02	0.31	301.03	0.08	0.79
80.0	10.00	297.65	297.10	296.88	0.77	0.22	298.17	0.52	1.07
	19.93	300.81	300.09	299.53	1.28	0.56	300.64	0.17	0.55
83.3	9.98	297.30	296.73	296.05	1.25	0.68	297.97	0.67	1.24
	19.96	300.59	299.86	298.88	1.70	0.98	300.51	0.07	0.65
	39.94	304.82	303.91	302.87	1.95	1.03	304.43	0.39	0.53
85.7	10.03	297.05	296.47	295.55	1.50	0.92	297.74	0.69	1.27
	19.92	300.40	299.66	298.45	1.95	1.21	300.13	0.27	0.47
	39.95	304.63	303.71	302.37	2.26	1.34	303.90	0.73	0.19
	60.10	307.94	306.91	305.67	2.27	1.24	307.68	0.26	0.77
87.5	10.03	296.64	296.04	295.34	1.30	0.70	297.77	1.13	1.73
	19.93	300.17	299.43	298.16	2.01	1.27	299.83	0.34	0.40
	39.89	304.38	303.47	302.09	2.29	1.38	303.93	0.45	0.47
	60.06	307.68	306.65	305.53	2.15	1.12	307.55	0.13	0.90
	80.26	310.53	309.42	308.78	1.75	0.64	310.68	0.15	1.26
	100.35	313.35	312.18	311.97	1.38	0.21	313.55	0.20	1.37

Table 5.4 – Dissociation data of likely CH₄ hydrates (sI) formed in CH₄-C₃H₈-H₂O systems by HP- μ DSC and the respective absolute deviations (AD) from computational predictions. In this case, simulations in CMSGem were performed for single methane hydrates.

mol% CH ₄ (g)	P _{Onset} (MPa)	T _{CSMGem} (K)	T _{Multiflash} (K)	T _{ONSET} (K)			T _{PEAK} (K)		
				HP- μ DSC	AD CSMGem	AD Multiflash	HP- μ DSC	AD CSMGem	AD Multiflash
83.3	19.94	291.74	291.94	292.13	0.39	0.19	292.82	1.08	0.88
	39.89	297.21	297.49	296.80	0.41	0.69	297.61	0.40	0.12
85.7	19.91	291.73	291.92	292.30	0.57	0.38	292.89	1.16	0.97
	39.90	297.21	297.49	296.92	0.29	0.57	297.56	0.35	0.07
	60.04	300.69	301.03	300.14	0.55	0.89	300.89	0.20	0.14

Continues

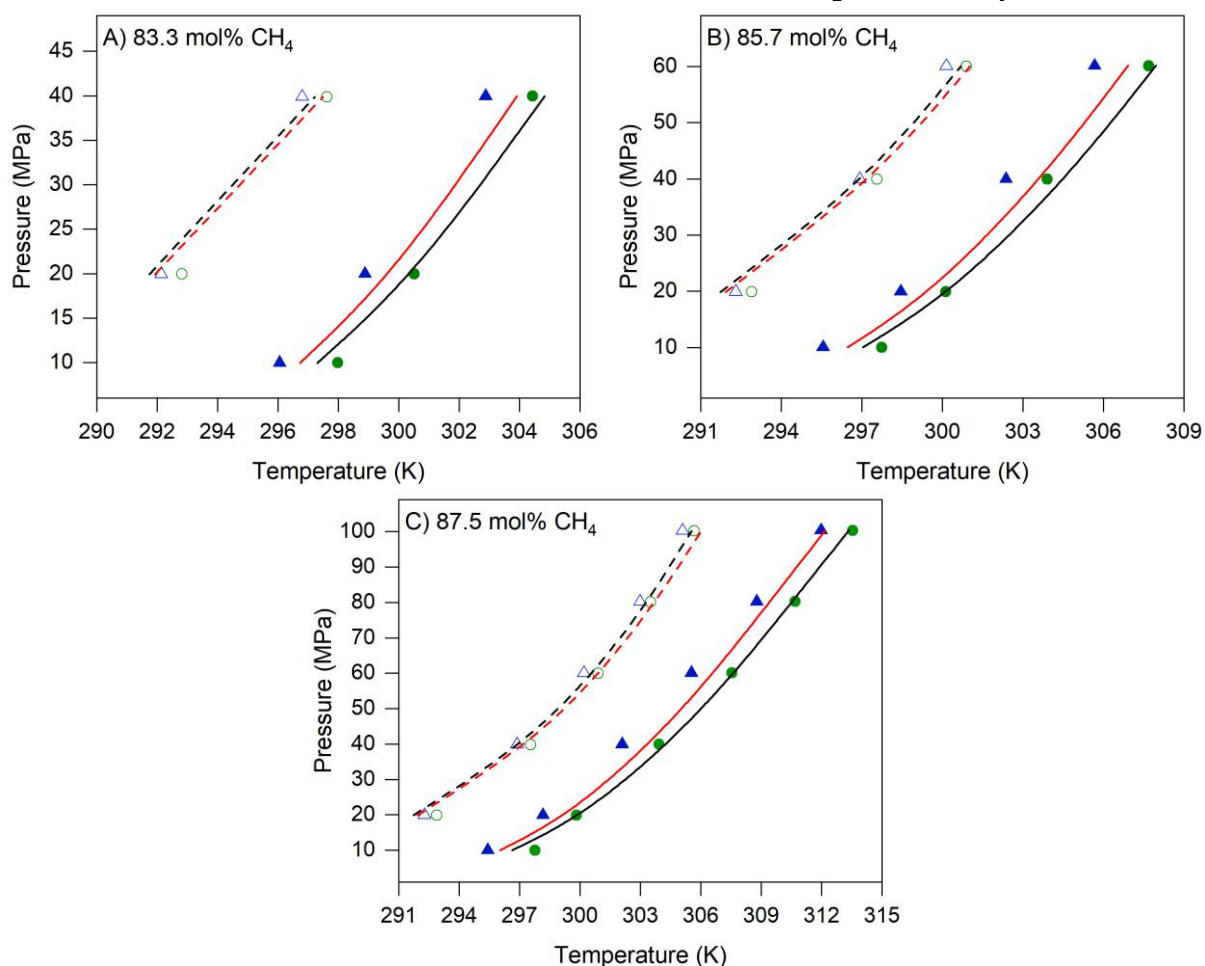
Continuation

CH ₄ (g) (mol%)	P _{Onset} (MPa)	T _{CSMGem} (K)	T _{Multiflash} (K)	T _{ONSET} (K)			T _{PEAK} (K)		
				HP- μ DSC	AD CSMGem	AD Multiflash	HP- μ DSC	AD CSMGem	AD Multiflash
	19.92	291.73	291.93	292.27	0.54	0.34	292.89	1.16	0.96
	39.86	297.21	297.48	296.87	0.33	0.61	297.54	0.34	0.06
87.5	60.01	300.69	301.02	300.19	0.50	0.83	300.91	0.22	0.11
	80.17	303.36	303.76	302.98	0.38	0.78	303.51	0.15	0.25
	100.24	305.55	306.03	305.09	0.46	0.94	305.66	0.11	0.37

Conclusion

Surprisingly, Multiflash predictions are lower than CSMGem ones for CH₄-C₃H₈ hydrates, unlike the other systems. For this reason, the experimental data seem to fit better to Multiflash predictions according to Figure 5.10. However, it does not guarantee

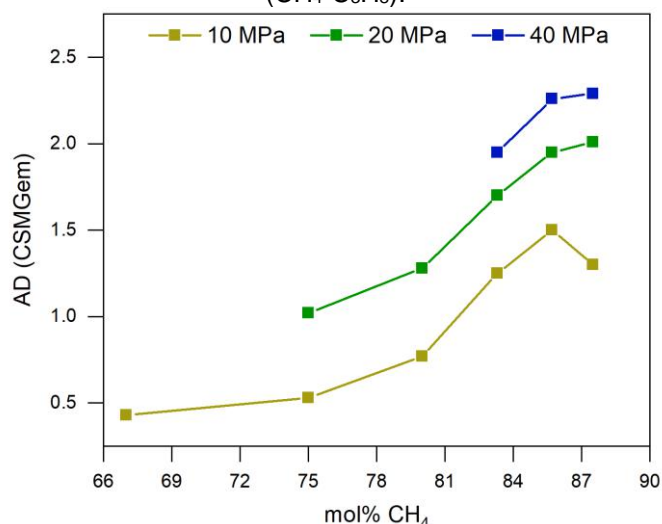
Figure 5.10 – Dissociation data of CH₄-C₃H₈ hydrates obtained by HP- μ DSC at different methane concentrations: (\blacktriangle) onset temperatures of sII; (\bullet) peak temperatures of sII; (\triangle) onset temperatures of sI; (\circ) peak temperatures of sI. Black lines refer to CSMGem predictions and red lines, to Multiflash. Solid lines refer to sII, and dashed lines to sI obtained for single methane hydrates.



that Multiflash provides the most reliable results in this case. In fact, the noticeably lower onset temperatures deviations from predictions, may be related to molecular dynamic issues. Although the solubility of propane is slightly higher than methane in water (SCHARLIN et al., 1998), the diffusion coefficient of methane in water is higher than propane (OELKERS, 1991; POKHAREL et al., 2018).

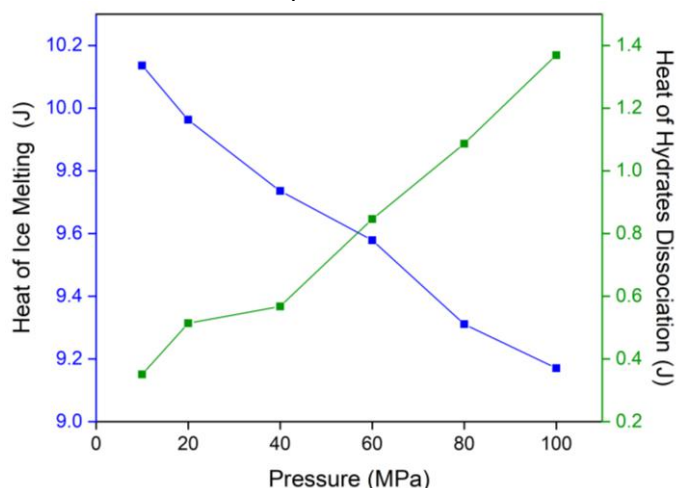
Figure 5.11 shows the tendency of higher deviations of onset temperatures (sII) from CSMGem predictions as the methane content increases. The higher mobility of methane molecules may lead to the formation of CH₄ rich fractions in deeper layers of the hydrate. This contributes to the structural heterogeneity and implies lower temperatures dissociation, as observed in Figure 5.14 addressed in the next section. The deviations are still higher when sI coexist to sII. In such cases, methane consumption by sI formation should imply a structure II rich in C₃H₈, also leading to lower dissociation temperatures.

Figure 5.11 – Evolution of absolute deviations (AD) of onset temperatures corresponding to structure II (CH₄-C₃H₈).



Finally, Figure 5.12 shows the evolution of these heats as the pressure increases in the system composed of 87.5 mol% CH₄. The heats involved during ice melting and hydrates dissociation were obtained by integrating the respective curves. The heat absorbed during ice melting decreases while the total heat concerned to sI and sII dissociations increases. This confirms that the increase in pressure favored the hydrate formation rather than ice, since the gas diffusion in water depends on the applied pressure.

Figure 5.12 – Heat absorbed during ice melting and CH₄-C₃H₈ hydrate dissociation according to the pressure.



5.5.3 Thermodynamic and Structural Analysis of CH₄-C₃H₈ Hydrates by Simulations

The equilibrium temperature profiles for CH₄-C₃H₈ hydrates at 20, 60 and 100 MPa are presented in Figure 5.13. Analogous to the methane-ethane hydrates, all cross-sections at fixed water fractions obtained from ternary diagrams, shown in Figure 5.14, give temperature contours similar to those in the figure below.

Figure 5.13 – Dissociation temperature profiles of CH₄-C₃H₈ hydrates according to the gas phase composition: (♦) onset temperatures from thermograms; (□) CSMGem predictions. Roman numerals refer to the regions established according to the supposed configuration of cages occupation.

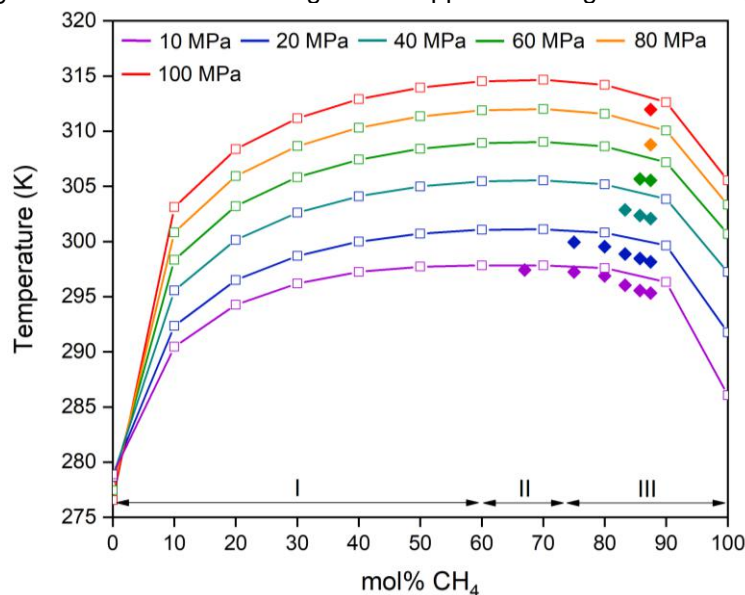
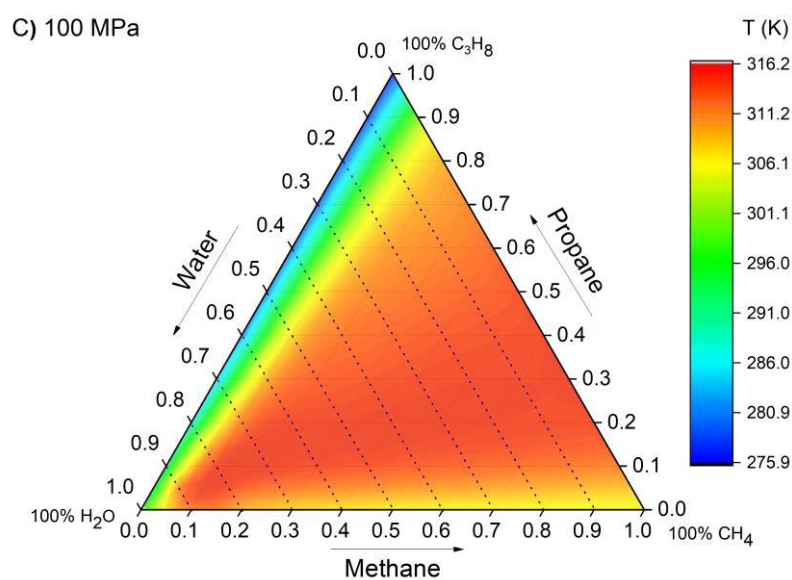
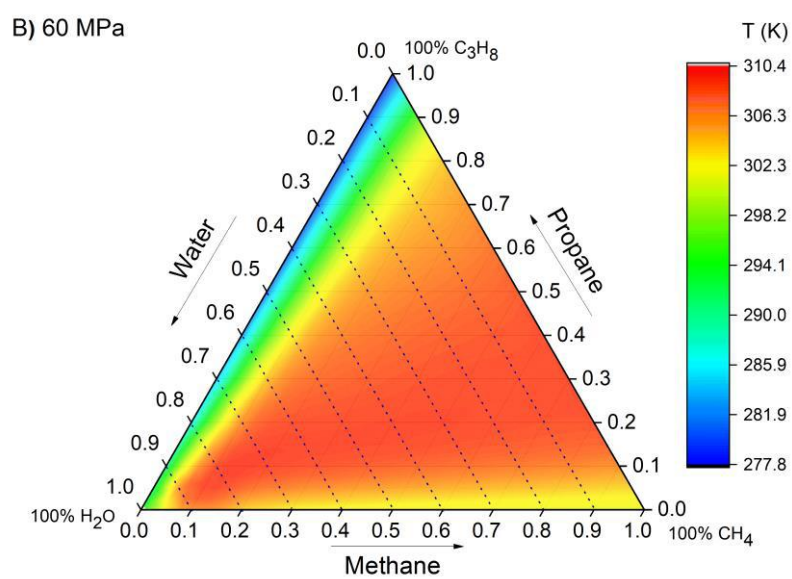
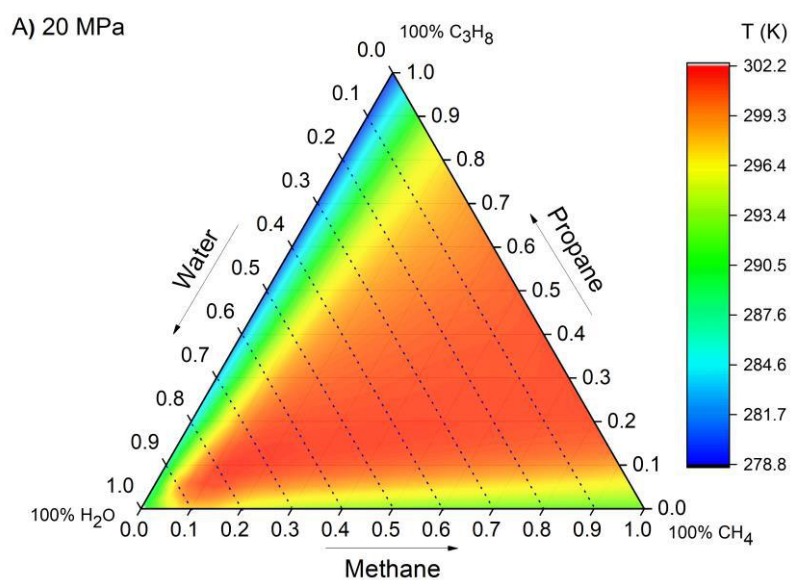
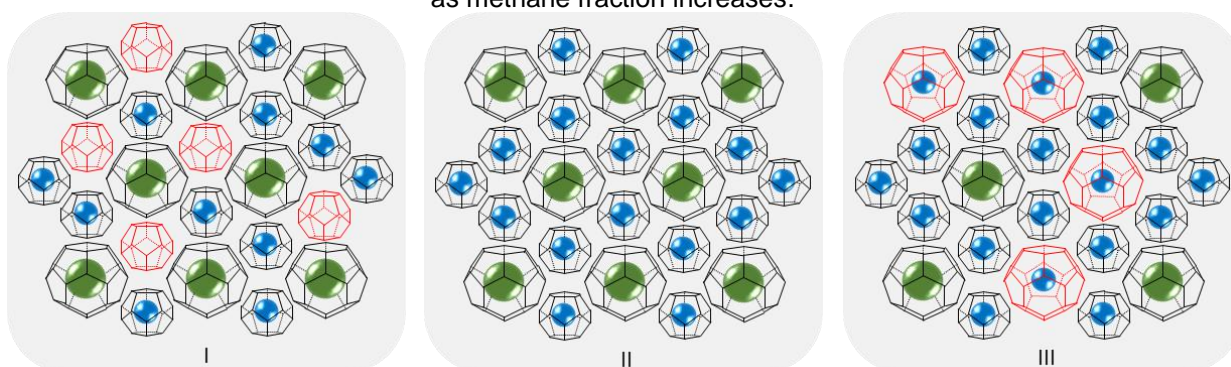


Figure 5.14 – Ternary diagrams of dissociation temperatures of CH₄-C₃H₈ hydrates.

The experimental data are in agreement with the predictions and the lower values of onset temperatures can be explained by the existence of more empty cavities throughout the hydrate structure than considered by predictions. Still in Figure 5.13, there is no evidence of overlapping curves in the temperature profiles, as observed in the ones regarding methane-ethane hydrates (Figure 5.5). This must be because just structure II can be formed in this case, since the propane molecules do not fit into any cavity of structure I. Similar dissociation temperature profiles were found for methane-propane hydrates at 100, 300 and 800 MPa (ALADKO et al. 2002).

In this case, the maximum temperature is achieved when the proportion of methane in the gas phase is about two thirds (67% mol CH_4). This fact also may be due to the occupation in cavities of structure II. The propane molecules occupy only the larger cavities of this structure ($5^{12}6^4$) while the methane molecules tend to be allocated into the smaller ones (5^{12}). Therefore, the maximum dissociation temperature is obtained when most of the cavities are filled (II), which corresponds to the most thermodynamically stable configuration. It happens when the methane / propane proportion is about 2:1, and coincides with the proportion of large and small cavities in the unit cell of sII ($5^{12}6^4 : 5^{12} = 2:1$). If the methane fraction in the gas phase is lower than two thirds (I), part of the small cavities (5^{12}) are empty, considering they do not fit propane molecules, and thereby the dissociation of the hydrate is facilitated. On the other hand, if the methane fraction is larger than $2/3$, both species compete to occupy the large cages ($5^{12}6^4$). This means that some of these cavities should host methane instead of propane molecules, forming a structure that again requires less energy to dissociate (III). In the illustration of Figure 5.15, blue balls represent methane while the green ones the propane molecules.

Figure 5.15 – Evolution of the cages occupancy for sII hosting CH_4 (blue) and C_3H_8 molecules (green) as methane fraction increases.



Although the onset temperatures are lower than predictions by the reasons already discussed, the experimental data plotted in Figure 5.14 follow the trend traced by predictions as the methane content increases. Finally, the non-predicted structure observed in the experiments reinforces the importance of obtaining experimental data in the most varied conditions in order to validate and improve mathematical models. Unfortunately, it was not possible to perform experiments at lower methane concentrations and at higher pressures due to experimental limitations.

5.6 METHANE-CARBON DIOXIDE-WATER SYSTEM

5.6.1 Equilibrium Data for CH₄-CO₂ Hydrates by Microcalorimetry

The third and last ternary system used to study double-guest hydrates is composed of methane, carbon dioxide, and water. The dissociation temperatures are indicated in Table 5.5 and plotted in Figure 5.16. In this case, similar gas phase compositions and different water content were used.

A peculiar phenomenon is observed for this system: the onset temperatures are noticeably lower than predictions when a small amount of water was added to the cell. Two factors are believed to have contributed to the lower onset temperatures mainly for 3 and 11.7 mg of water: i) the solubility and diffusivity of carbon dioxide in water; ii) the effect of H₂O sample size on the hydrate heterogeneity. The first factor may have led to a heterogenous hydrate with a significant fraction rich in CO₂. Considering the high solubility of CO₂ in water (SCHARLIN et al., 1998) and its higher diffusivity than methane (TAMIMI et al., 1994; POKHAREL et al., 2018), deeper layers of the hydrate likely present a high content of carbon dioxide. Next section shows in detail that low contents of CH₄ lead to lower dissociation temperatures, similarly to the methane-propane system.

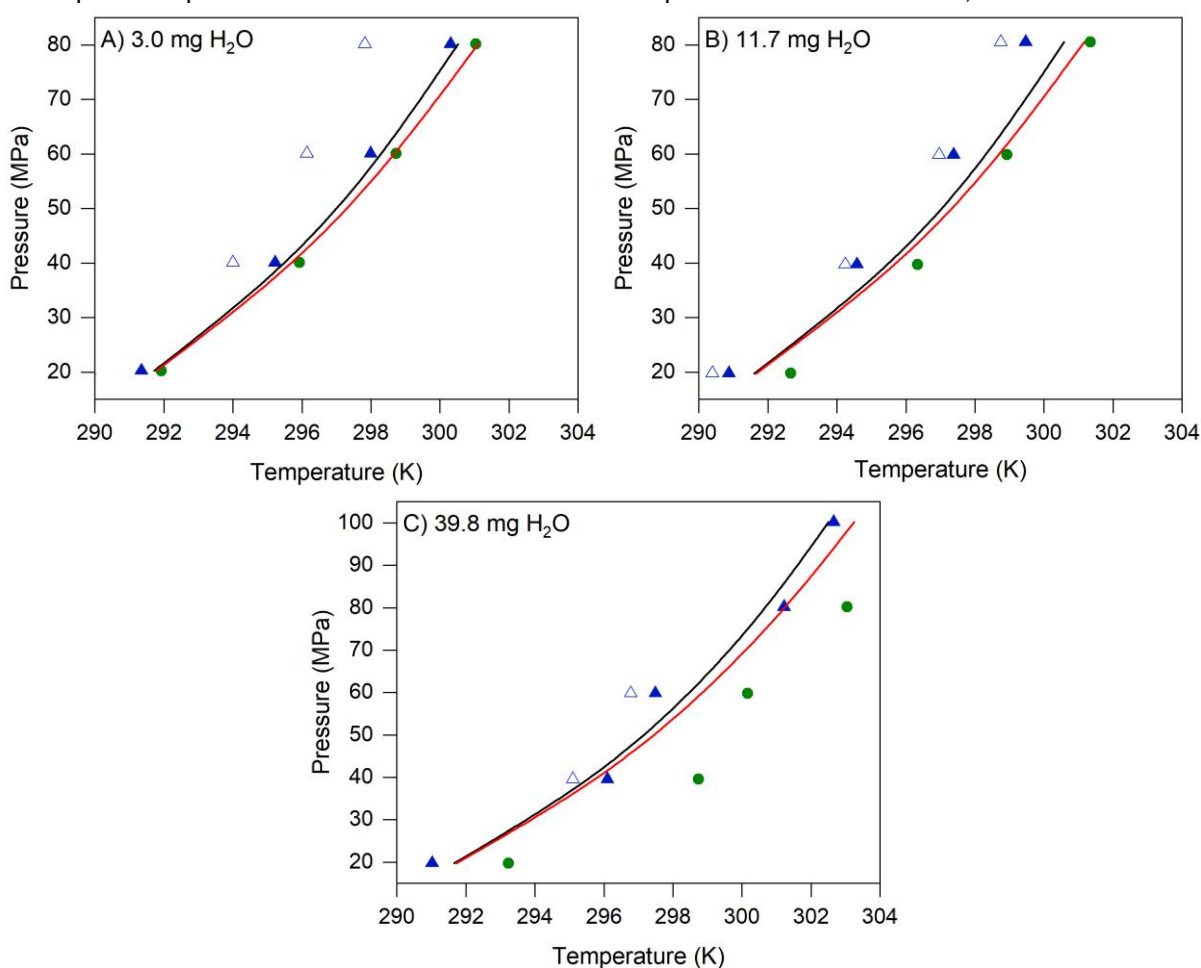
On the other hand, this occurred mainly for samples with low amount of water. It was mentioned in Chapter 4 that large water sample sizes might increase the interfacial area between aqueous and gas phases. This effect should contribute to both guest-molecules incorporations in CH₄-CO₂ hydrate structure. In other words, the sample initially containing 39.8 mg H₂O may have favored a more homogeneous hydrate formation, thus leading to more reliable dissociation temperatures. In contrast, lower

Table 5.5 – Dissociation data of CH₄-CO₂ hydrates obtained by HP- μ DSC and the respective absolute deviations (AD) from computational predictions.

H ₂ O (liq) (mg)	CH ₄ (g) (mol%)	P _{Onset} (MPa)	T _{CSMGem} (K)	T _{Multiflash} (K)	T _{ONSET – PEAK 1} (K)			T _{ONSET – PEAK 2} (K)			T _{PEAK 2} (K)		
					HP- μ DSC	AD CSMGem	AD Multiflash	HP- μ DSC	AD CSMGem	AD Multiflash	HP- μ DSC	AD CSMGem	AD Multiflash
3.0	55.5	20.2	291.72	291.78	289.85	1.87	1.93	291.35	0.37	0.43	291.93	0.21	0.15
		40.1	295.72	295.93	294.00	1.72	1.93	295.22	0.50	0.71	295.93	0.20	0.00
		60.1	298.38	298.76	296.14	2.24	2.62	297.99	0.39	0.77	298.73	0.34	0.03
		80.2	300.52	301.10	297.82	2.70	3.28	300.31	0.21	0.79	301.04	0.52	0.06
11.7	55.7	19.8	291.61	291.66	290.39	1.22	1.27	290.87	0.74	0.79	292.66	1.05	0.99
		39.7	295.69	295.89	294.24	1.45	1.65	294.58	1.11	1.31	296.34	0.65	0.45
		59.9	298.41	298.78	296.96	1.44	1.82	297.38	1.02	1.40	298.93	0.52	0.15
		80.5	300.57	301.16	298.75	1.82	2.41	299.47	1.10	1.69	301.34	0.77	0.19
39.8	57.6	19.8	291.67	291.73	-	-	-	291.02	0.65	0.71	293.24	1.57	1.51
		39.5	295.74	295.95	295.10	0.64	0.85	296.10	0.36	0.15	298.74	3.00	2.79
		59.8	298.55	298.93	296.78	1.77	2.15	297.49	1.06	1.44	300.16	1.61	1.23
		80.2	300.75	301.32	-	-	-	301.22	0.47	0.10	303.05	2.30	1.73
100.2	302.50	303.25	-	-	-	302.66	0.16	0.59	304.45	1.95	1.20		

amounts of water (3 and 11.7 mg) may have implied a smaller interfacial area. In these cases, a substantial fraction of hydrate rich in CO_2 (indicated in Figure 5.17) may have formed in the regions below the interface due to the higher disposal of CO_2 than CH_4 molecules dissolved in water. Therefore, low water content and high diffusivity of CO_2 in water could explain the lower dissociation temperatures shown in Figures 5.16A and 5.16B.

Figure 5.16 – Dissociation data of $\text{CH}_4\text{-CO}_2$ dioxide hydrates obtained by HP- μDSC at different methane concentrations: (Δ) onset temperatures of peak 1; (\blacktriangle) onset temperatures of peak 2; (\bullet) peak temperatures. Black lines refer to CSMGem predictions and Red lines, to Multiflash.



In fact, it can be distinguished at least two overlapped peaks in the wide dissociation curves obtained, shown in Figure 5.17. The intersection of the extrapolated baseline and the inflectional tangent at the most energetic peak (corresponding to peak 2) provides a dissociation temperature closer to the prediction.

Figure 5.17 – Overlapping transitions in HP- μ DSC thermograms, evidencing the heterogeneity of CH_4 - CO_2 hydrate structures (3 mg H_2O).

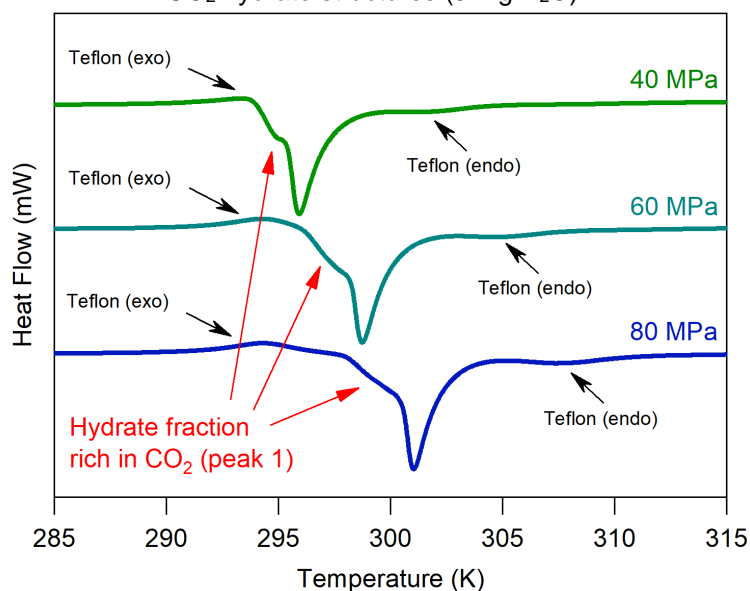
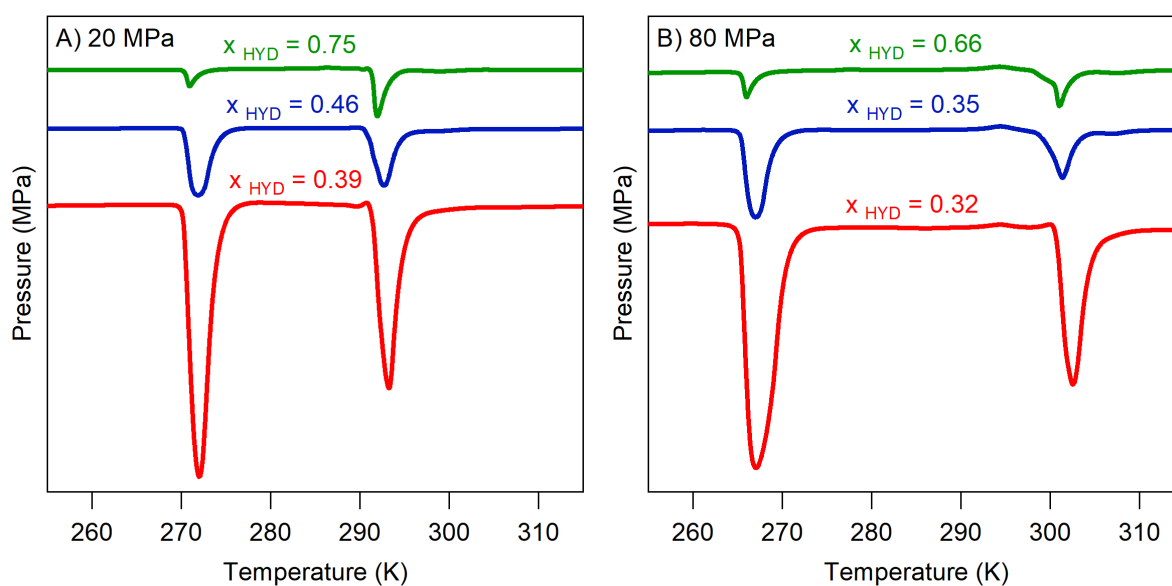


Figure 5.18 shows that the H_2O sample size added in the cell is directly related to the fractions of ice and hydrate formed during the cooling. As observed for methane hydrates in section 4.3.2, samples containing different amounts of water (39 and 56.4 mg, in that case) presented changes in the kinetic and growth of both ice and hydrate.

Figure 5.18 – Influence of H_2O sample size on the hydrate fraction: (—) 3 mg H_2O (—) 11.7 mg H_2O (—) 39.8 mg H_2O . The larger the H_2O sample size, higher the hydrate homogeneity, slower the crystals growth and hence lower the hydrate fraction.



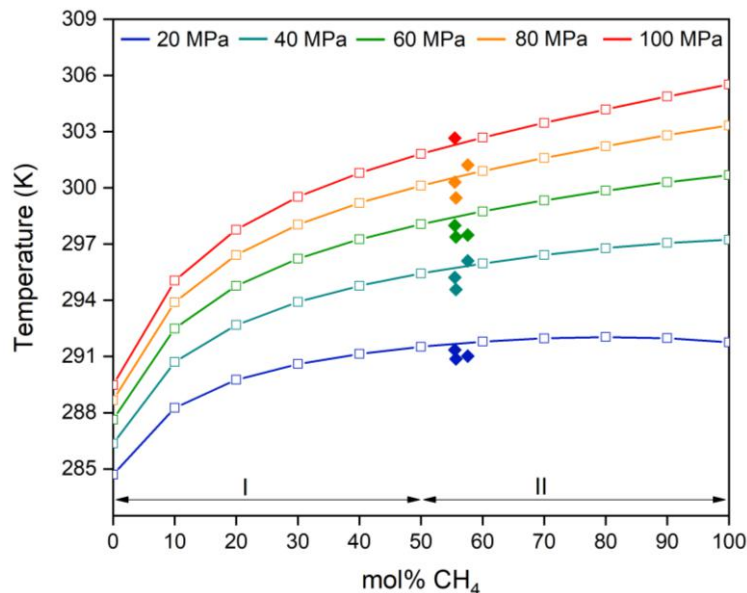
In this system – methane, carbon dioxide, and water – the predominance of ice or hydrate seems to depend on the size of the water sample. As discussed before, the

hydrate becomes more homogeneous as larger the water sample size. Therefore, it is reasonable to suppose that the hydrate growth rate also changes according to the sample size, i.e., a more homogeneous structure should form slower than a more heterogeneous one. In other words, hydrate rich in CO₂, favored by smaller samples, may present higher growth rate than ice, and on the other hand, the opposite should occur for hydrate rich in CH₄, favored by larger samples. This could explain the decrease of hydrate fraction in Figure 5.18.

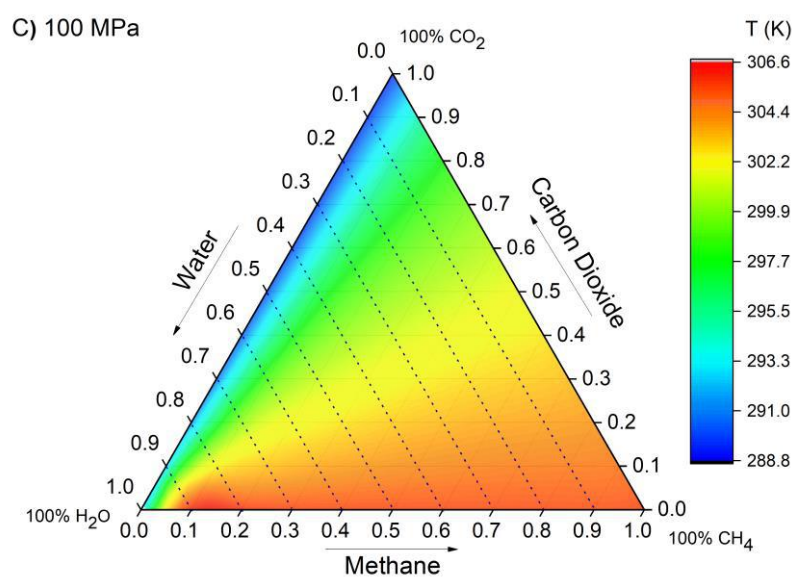
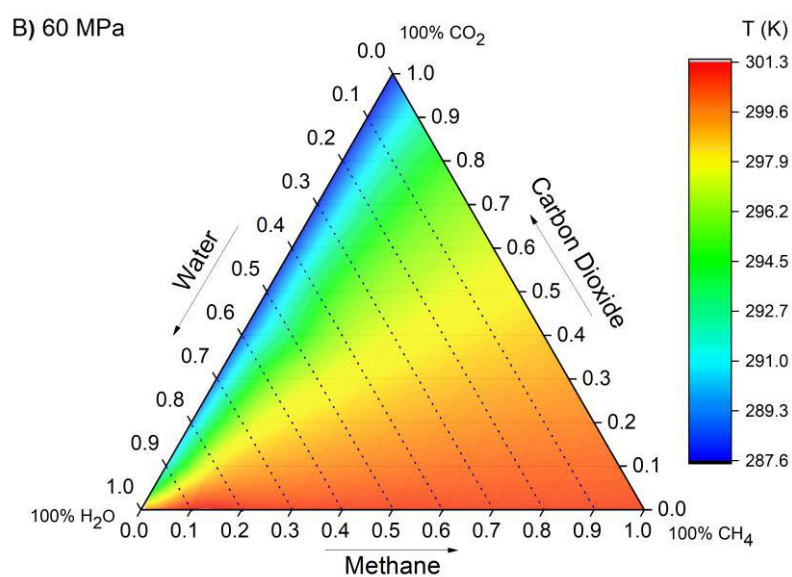
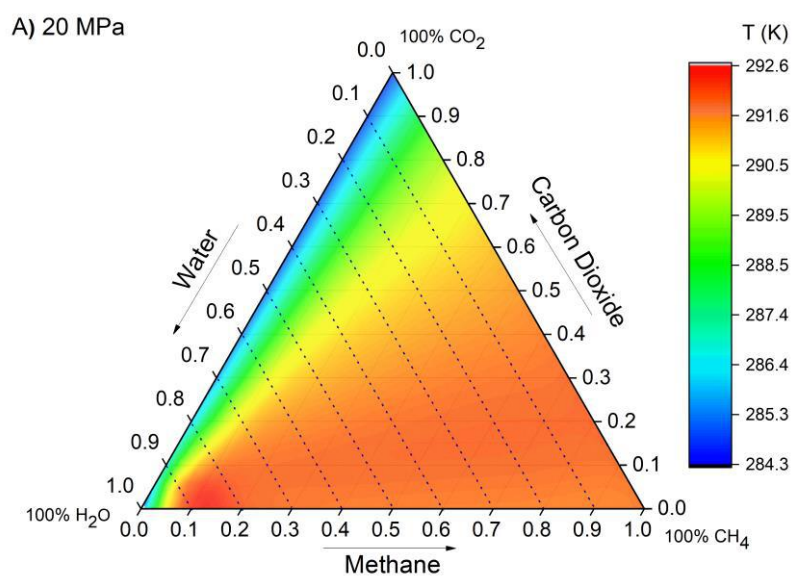
5.6.2 Thermodynamic and Structural Analysis of CH₄-CO₂ Hydrates by Simulations

Dissociation temperature profiles of CH₄-CO₂ hydrates are shown in Figure 5.19, and the ternary diagrams at 20, 60 and 100 MPa are presented in Figure 5.20.

Figure 5.19 – Dissociation temperature profiles of CH₄-CO₂ hydrates according to the gas phase composition: (♦) onset temperatures of peak 2 from thermograms; (□) CSMGem predictions. Roman numerals refer to the regions established according to the supposed configuration of cages occupation.



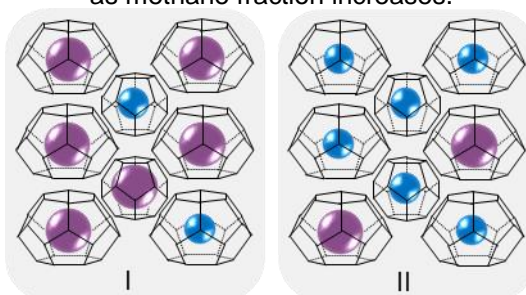
The experimental data are in relative accordance with the predictions, and the discrepancies between onset temperatures should be related to the heterogeneity of the hydrate structures. Moreover, the formation of real hydrates with higher CO₂ fraction than in the gas phase is reasonable, considering the higher diffusivity of these molecules in water than methane. This also could explain the lower dissociation temperatures.

Figure 5.20 – Ternary diagrams of dissociation temperatures of CH₄-CO₂ hydrates.

Unlike previous systems, the CH₄-CO₂ hydrate dissociation temperature continuously increases according to higher methane concentrations, except to the slightly cooler temperatures at 20 MPa with 90 and 100 mol% CH₄. Both methane and carbon dioxide form structure I and can be hosted by any cavities of this structure, unlike the first system in which ethane just fills properly in the largest cavity of sI. Therefore, the dissociation temperature may not be significantly affected by the presence of empty cavities, as in previous cases, but mainly by the proportion of guest molecules trapped in the structure.

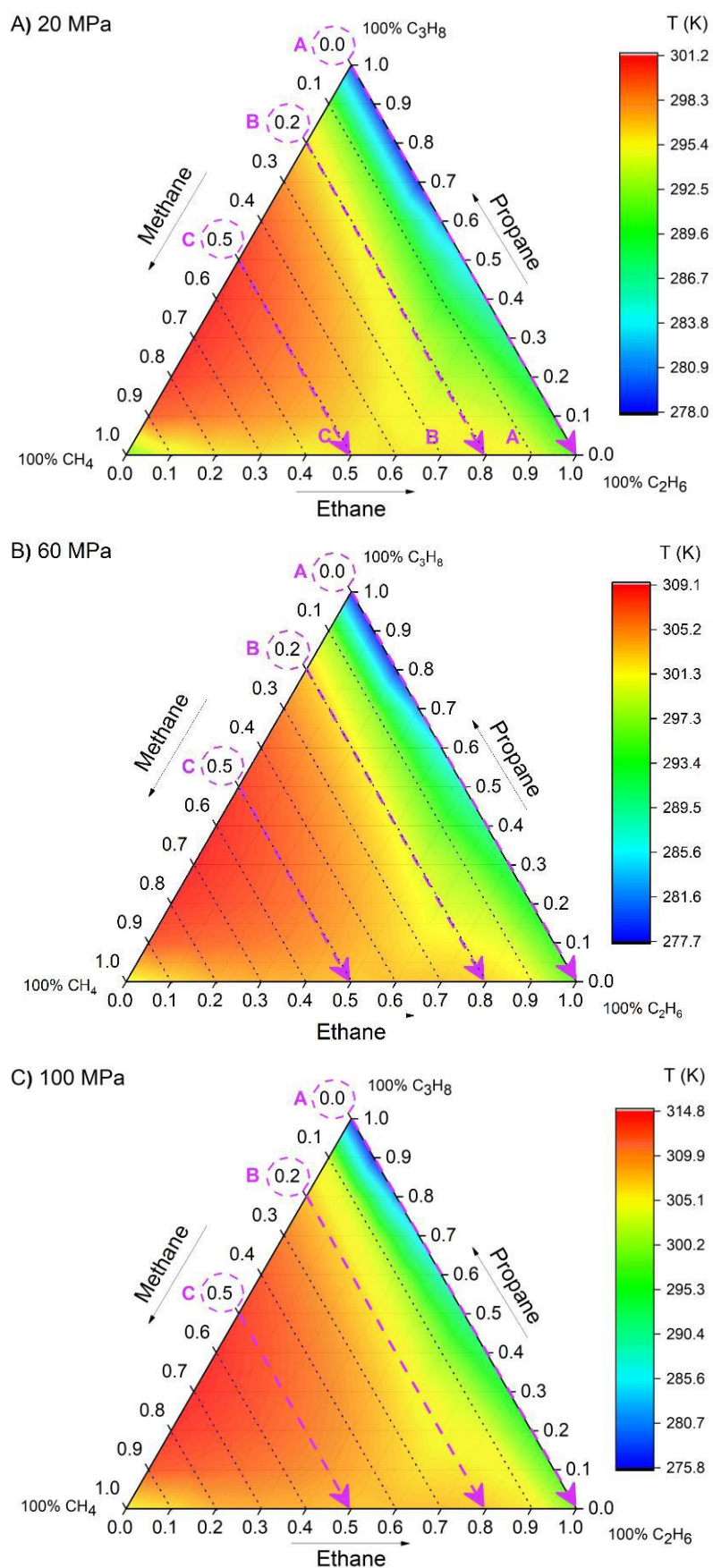
According to Table 5.1, CO₂ molecules fit better on cavities of structure I than CH₄ molecules. However, the hydrate rich in CH₄ is more stable because methane molecules tend to withstand dissolution in the aqueous phase during dissociation, considering that the CH₄ has different chemical nature and it is less soluble in water than CO₂. It means that the second configuration illustrated in Figure 5.21, containing higher methane content, should present higher dissociation temperature. It is worth to mention that the difference in solubility between methane and carbon dioxide is higher as the pressure increases and, thereby, the hydrate composition has a stronger effect on dissociation temperature at higher pressures, as can be observed in Figure 5.19. No more experimental data were obtained for this system due to technical issues.

Figure 5.21 – Evolution of the cages occupancy for sI hosting CH₄ (blue) and CO₂ molecules (purple) as methane fraction increases.



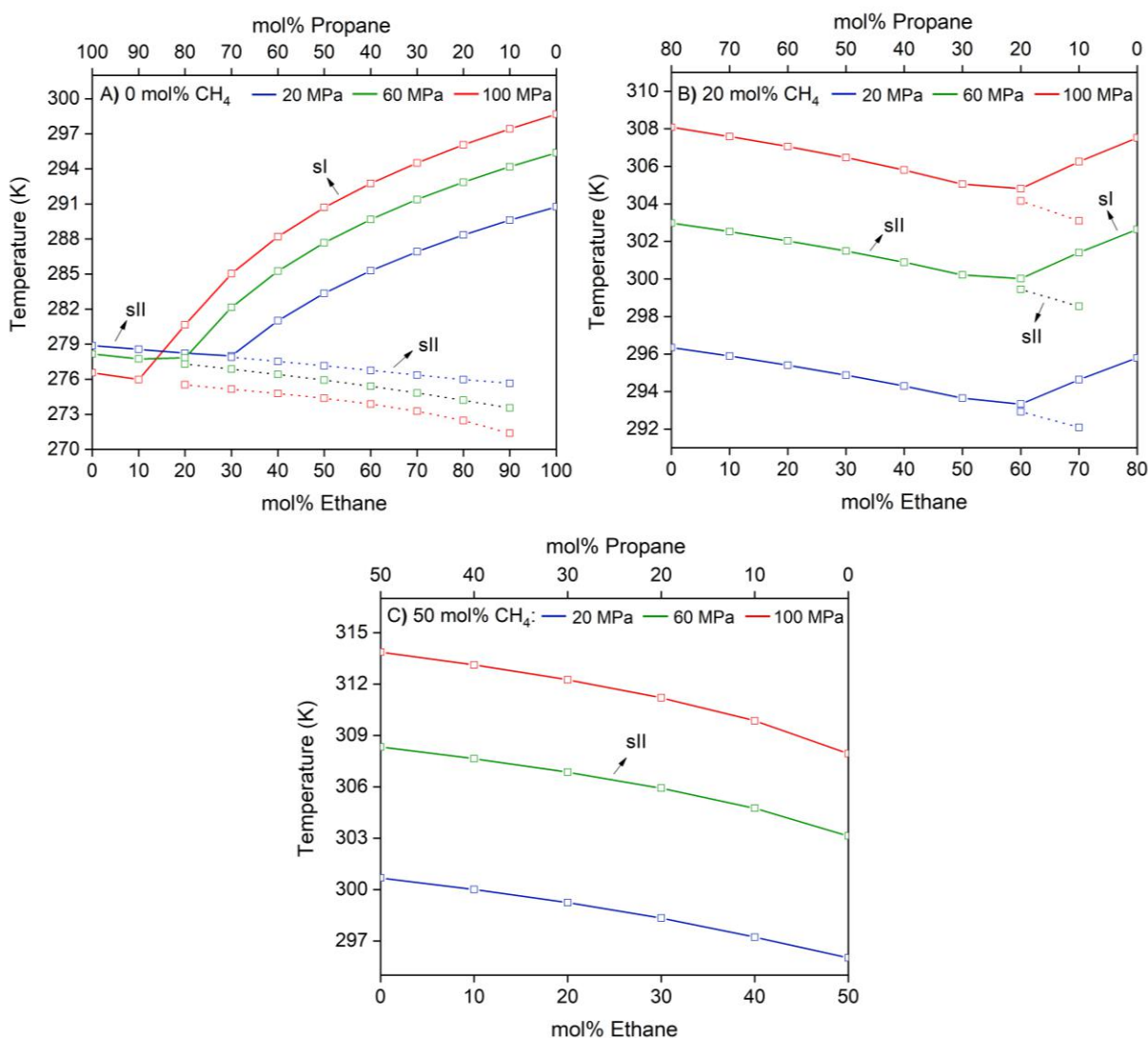
5.6.3 Methane-Ethane-Propane-Water System

The last system studied, only through simulations, was composed of methane-ethane-propane-water. Ternary diagrams in Figure 5.22 point out that the most thermodynamically stable regions are formed by hydrates rich in methane and propane (sII).

Figure 5.22 – Ternary diagrams of dissociation temperatures of $\text{CH}_4\text{-C}_2\text{H}_6\text{-C}_3\text{H}_8$ hydrates.

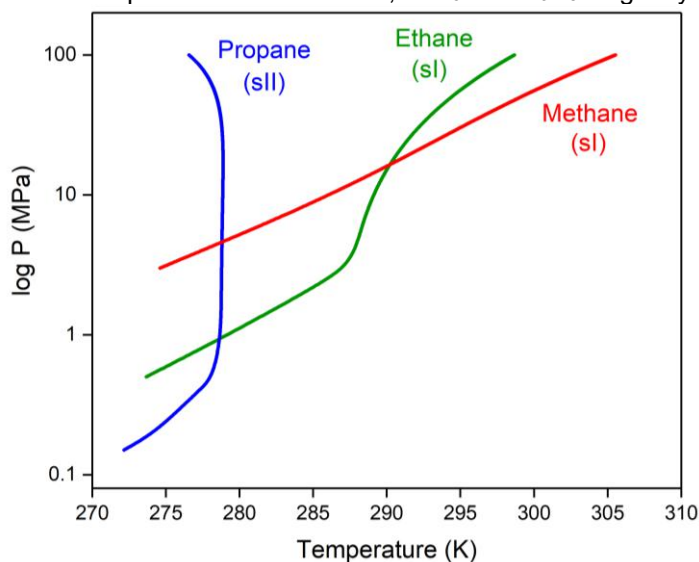
In order to verify the effect of ethane-propane ratio, $T(P,x)$ diagrams are shown at three different methane fractions in Figure 5.23. The concentrations used in the figure below are indicated by A, B and C in the ternary diagrams shown in Figure 5.22. The predictions indicate that both sI and sII coexist, depending on the gas composition. The system tends to form structure I preferentially at high ethane contents (0% and 20% CH_4), but structure II should also be formed due to the presence of propane, considering again that these molecules just fit on large cavities of sII. Structure I, in turn, requires higher temperatures to dissociate, and it is probably occupied by both methane and ethane.

Figure 5.23 – Dissociation temperature profiles of $\text{CH}_4\text{-C}_2\text{H}_6\text{-C}_3\text{H}_8$ hydrates according to the ethane-propane ratio. Each plot presents a constant fraction of methane.



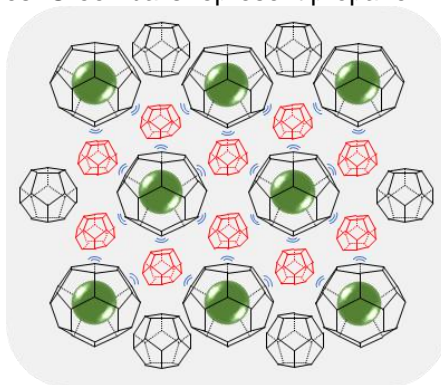
In all cases addressed by now, one can note higher dissociation temperatures as the pressure increases, as expected. Nevertheless, the opposite effect is observed for structure II in Figure 5.22A, in which the methane concentration is null. The same reverse phenomenon happens to the single propane hydrate, as shown in Figure 5.24.

Figure 5.24 – Equilibrium lines for CH₄, C₂H₆ and C₃H₈ single hydrates.



Unlike single methane and ethane hydrates, dissociation temperature of propane hydrate starts to decrease after 17 MPa as the pressure increases. This may be because most of the small cavities of sII should be empty in single propane and propane-ethane hydrates, since ethane and propane molecules fit preferentially in large cavities of this structure ($\Theta_{sII-SC} > 1$). Although the hydrate stability is known to be higher according to increasing the pressure, the opposite effect is observed when small cavities are empty likely because they are tightened by large cavities occupied by propane or ethane/propane molecules. This could lead to a structural deformation according to the pressure, as illustrated by red cages in Figure 5.25, and hence a less stable configuration is obtained. Another reason is that the compressibility factor (κ_T) may overcome the effect of the thermal expansivity coefficient (β) on the lattice parameter, decreasing the hydrate volume and the filling of the large cavities by ethane/propane molecules. Thus, low cages occupancy can also lead to higher hydration numbers and lower dissociation temperatures.

Figure 5.25 – Structural deformation of small cavities from sII due to the absence of methane molecules. Green balls represent propane molecules.



Finally, a second opposite behavior can be observed between sI and sII for all cases of Figure 5.23: the dissociation temperature increases for sI and decreases for sII as ethane concentration increases. It is because sII becomes less stable when large cavities are occupied by ethane instead of propane, as illustrated in Figure 5.26. Once ethane molecules are smaller, the intermolecular interactions become weaker. This does not happen with structure I because it becomes more stable as the large cavities are occupied by the ethane molecules. Although Figure 5.27 only represents empty or ethane-occupied large cages, some of them could be filled by methane molecules as well.

Figure 5.26 – Evolution of the cages occupancy for sII hosting CH_4 (blue), C_2H_6 (yellow) and C_3H_8 molecules (green) as ethane fraction increases.

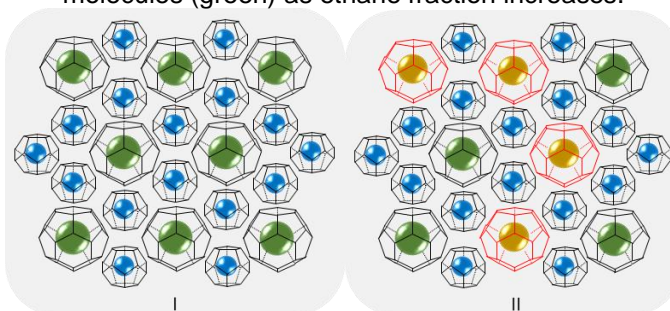
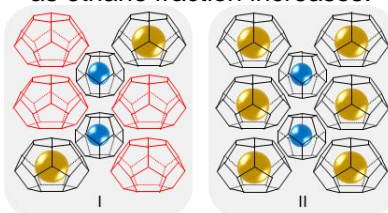


Figure 5.27 – Evolution of the cages occupancy for sI hosting CH_4 (blue) and C_2H_6 molecules (yellow) as ethane fraction increases.



5.7 CONCLUSIONS

This chapter presents new dissociation data for double-guest gas hydrates obtained by HP- μ DSC. In general, the experimental onset temperatures of dissociation curves from thermograms usually show a good agreement to predictions, especially from CSMGem. However, they deviated noticeably in some cases indicating the formation of a heterogeneous hydrate phase. It is suggested that dynamic effects significantly influence the filling of cages in the cases of systems containing a gas mixture. Differences in solubility and diffusivity in water between gas species are factors that likely imply gradients of gas concentrations through the solid phase so that the hydrate phase should consist of different occupancy degrees. Ternary diagrams and temperature profiles based on computational predictions were also built to elucidate the influence of gas composition on the type of structure (s) formed and on the cavities occupancy.

- Two approaches were used in this work to explain the preferential type of structure in different gas mixtures and the dissociation temperature profiles according to the gas phase composition: i) the influence of the ratio between guest molecules size and cages diameter on the hydrate stability; ii) the cages occupancy degree, including the existence of empty cavities throughout the hydrate lattice. These factors play a role in the hydrate thermodynamic properties and should contribute to structural transitions. The dissociation temperature, for example, is said to be affected according to the stability provided by these factors;
- Equilibrium data obtained by predictions for methane-ethane hydrates revealed the coexistence of two different structures at methane concentrations higher than 50 mol%. Although thermograms did not evidence a distinct curve regarding the secondary structure, some overlapped transitions were observed during the hydrate dissociation, supporting the probable coexistence of sI and sII with similar dissociation temperatures. It is believed that a secondary structure (sII) is also formed as a metastable phase at low methane concentrations. The onset temperatures presented lower absolute deviations with respect to CSMGem predictions than peak and endset temperatures;
- Experiments for methane-propane systems showed evidence of two structures, sI and sII, at high methane contents. The first dissociates at lower temperatures

and is likely occupied only by methane molecules, since the dissociation temperatures approach to that of methane hydrates (sI). The other structure, sII, is the only predicted by computational simulations through all the methane-propane composition range. According to predictions, the most stable configuration occurs close to 67 mol% CH₄, and either lower or higher concentrations lead to lower dissociation temperatures.

- Methane-carbon dioxide hydrates were experimentally studied at similar gas phase compositions and varying the H₂O sample size. In cases of a small amount of water added into the cell, the onset temperatures deviate significantly from predictions. It is believed that low content of water do not favor the interfacial area between gas molecules and the aqueous phase. In addition, the high solubility and diffusion coefficient of CO₂ in water could also imply hydrate fractions rich in CO₂. These factors should contribute to a more heterogeneous phase and explain the lower dissociation temperatures, mainly for smaller H₂O samples. Unlike single guest systems, therefore, the amount of water in 'static' systems (no mixing) containing gas mixtures could have a moderate effect on the hydrate equilibrium due to different chemical properties in water of the gas species involved.
- Although carbon dioxide molecules fit better in cavities of sI, the increase of methane fraction provides more stable structures according to predictions. It could be explained by the hardest dissolution of methane molecules into aqueous phase during hydrate dissociation due to the low solubility of methane in water.
- A quaternary system composed of methane-ethane-propane-water was studied by computational simulations. For hydrates in absence of methane (single propane or ethane/propane hydrates), structure II likely presents a structural deformation since most of the small cavities are empty. In addition, the increase in the pressure may reduce the hydrate volume if the compressibility factor overcomes the thermal expansivity, leading to a lower occupancy degree. These factors are believed to decrease the hydrate stability and the dissociation temperature as the pressure increases. Structure II also seems to be less stable when ethane content increases and propane decreases, probably because molecular interactions between ethane and the lattice are weaker.

- In general, CSMGem showed a better approach to experimental results, except for methane-propane hydrates. As, observed for singles hydrates, Multiflash predictions become distant from CSMGem as pressure increases, especially for methane-ethane hydrates with low methane fractions.

REFERENCES

ALADKO, E. Y.; DYADIN, Y. A.; MANAKOV, A. Y.; ZHURKO, F. V.; LARIONOV, E. G. Phase diagrams of the ternary gas hydrate forming systems at high pressures. Part 1. Propane–Methane–Water System. *Journal of Supramolecular Chemistry*, v. 2, p. 369–376, 2002.

HACHIKUBO, A.; NAKAGAWA, R.; KUBOTA, D.; SAGAKAMI, H.; TAKAHASHI, N.; SHOJI, H. Dissociation heat of mixed-gas hydrate composed of methane and ethane. *Proceedings of the 6th International Conference on Gas Hydrates (ICGH 2008)*, Vancouver, British Columbia, Canada July 6-10, 2008.

KLAPPROTH, A.; PILTZ, R.O.; KENNEDY, S.J.; KOZIELSKI, K.A. Kinetics of sII and Mixed sI/sII, Gas Hydrate Growth for a Methane/Propane Mixture Using Neutron Diffraction. *The Journal of Physical Chemistry C*, v. 123 (5), p. 2703-2715, 2019.

LARIONOV, E.G.; DYADIN, YU.A.; ZHURKO, F.V.; MANAKOV., A.YU. Phase Diagrams of the Ternary Gas Hydrate Forming Systems at High Pressures. Part II. Ethane–Methane–Water System. *Journal of Inclusion Phenomena and Macrocyclic Chemistry*, v. 56, p. 303–308, 2006.

MENEZES, D.E.S.; SUM, A. K.; DESMEDT, A.; PESSOA FILHO, P. A.; ROBUSTILLO, M. D. Coexistence of sI and sII in methane-propane hydrate former systems at high pressures. *Chemical Engineering Science*, v. 208, article 115149, 2019.

NIXDORF, J.; OELLRICH, L.R. Experimental determination of hydrate equilibrium conditions for pure gases, binary and ternary mixtures and natural gases. *Fluid Phase Equilibria*, v. 139 (1), p. 325-333, 1997.

OELKERS, E.H. Calculation of diffusion coefficients for aqueous organic species at temperatures from 0 to 350°C. *Geochimica et Cosmochimica Acta*, v. 55, p. 3515-3529, 1991.

OHNO, H.; STROBEL, T.A.; DEC, S.F.; SLOAN, E.D.; KOH, C.A. Raman Studies of Methane–Ethane Hydrate Metastability, *The Journal of Physical Chemistry A*, v. 113 (9), p. 1711–1716, 2009.

POKHAREL, S.; ARYAL, N.; NIRLAULA, B.R.; SUBEDI, A.; ADHIKARI, N.P. Transport properties of methane, ethane, propane, and n-butane in water. *Journal of Physics Communications*, v. 2, 065003, 2018.

SCHARLIN, P.; BATTINO, R.; SILLA, E.; TUÑÓN, I.; PASCUAL-AHUIRC, J.L. Solubility of gases in water: Correlation between solubility and the number of water molecules in the first solvation shell. *Pure and Applied Chemistry*, v. 70, p. 1895-1904, 1998.

SLOAN E.D.; KOH, C. Clathrate hydrates of natural gases, 3rd ed. Boca Raton: CRC Press, 2008.

SUBRAMANIAN, S.; BALLARD, A.L.; KINI, R.A.; DEC, S.F; SLOAN, E.D. Structural transitions in methane+ethane gas hydrates — Part I: upper transition point and applications. *Chemical Engineering Science*, v. 55, p. 5763-5771, 2000.

TAMIMI, A.; RINKER, E.B.; SANDALL, O.C. Diffusion Coefficients for Hydrogen Sulfide, Carbon Dioxide, and Nitrous Oxide in Water over the Temperature Range 293-368 K. *Journal of Chemical Engineering Data*, v. 39, p. 330-332, 1994.

UCHIDA, T.; MOORIWAKI, M.; TAKEYA, S.; IKEDA, I.Y.; OHMURA, R.; NAGAO, J.; MINAGAWA, H.; EBINUMA, T.; NARITA, H.; GOHARA, K.; MAE, S. Two-step formation of methane-propane mixed gas hydrates in a batched-type reactor. *American Institute of Chemical Engineers*, v. 50, p. 518-523, 2004.

CHAPTER 6

GAS HYDRATES STUDIES BY ISOCHORIC METHOD IN A PVT CELL

ABSTRACT

Hydrate-forming systems composed of methane-water and methane-propane-water are studied in this chapter through isochoric measurements using a PVT cell. The experiments were reproduced by HP- μ DSC at constant pressure in order to compare both techniques. New equilibrium data at high-pressure conditions (up to 100MPa) were obtained considering the experimental features and limitations of both methods. Results reveal evidence of the simultaneous formation of structures I and II for systems containing CH₄ and C₃H₈, although only sII was expected at such conditions at equilibrium. Although most of sI is formed as a metastable structure, a small fraction of it seems to provide a more stable system, mainly in conditions of excess methane. The effects of heating rate, mixing, multiple cycles and initial gas phase composition on the hydrates formation were evaluated by both experimental methods. These factors affect the kinetics of formation, the type and the proportion of each hydrate structure and hence the thermodynamic profile during dissociation.

6.1 INTRODUCTION

Apart from microcalorimetry, the isochoric method applied on PVT cells is a usual method to study hydrate phase equilibria (CHA, et al., 2016; DALMAZZONE et al., 2002; HU et al. 2017a,b; MASOUDI et al., 2004; MOHAMMADI et al., 2005; MOHHAMAD-TAHERI et al., 2013; WARD et al., 2015). Both microcalorimetry and the isochoric method in the PVT cell feature advantages and drawbacks. The latter configuration allows bulk phases mixing, resulting in faster equilibration and more homogeneous sampling. The hydrate growth inside the high-pressure cells of the microcalorimeter is limited by mass transfer, since the hydrate is formed in the interfacial area between the gas and liquid phases. Nevertheless, microcalorimetry is relevant not only for determining equilibrium points but also for different thermodynamic properties of hydrates such as enthalpy and heat capacity (GUPTA et al., 2008; KANG et al., 2001; ZHANG et al., 2004). This method has other advantages such as shorter analysis time, simpler experimental procedures, and smaller samples.

In addition, the apparatus is allowed to operate in the isochoric or the isobaric modes, unlike most of PVT cells, in which the hydrate formation and dissociation are detected from pressure changes. This chapter presents analogous studies on the formation and dissociation of methane and methane-propane hydrates performed by both methods.

The formation and dissociation of methane-propane hydrates are particularly approached in this chapter, since the coexistence of sI and sII structures was observed by both microcalorimetry and PVT-isochoric method for such hydrates. In fact, metastable states may occur under specific thermodynamic conditions in various gas hydrates such as carbon monoxide (PETUYA et al., 2017; ZHU et al., 2014), nitrogen (PETUYA et al., 2018a,b), or methane-based hydrates (ALADKO et al., 2002; KLAPPROTH et al., 2019; KUMAR et al., 2008; SHIN et al., 2012). Shin et al. (2012) confirmed the formation of a metastable structure (sII) during methane-hexamethyleneimine hydrate formation. The group assessed the kinetic and thermodynamic competition and phase transition during the process of hydrate growth, indicating that all sI, sII and sH coexist in this case. For systems composed by methane, propane and water, a simultaneous formation of hydrate types sI (methane hydrate) and sII (methane-propane hydrate) has been observed. Klapproth et al. (2019) studied the kinetics of hydrate formation for methane-propane mixtures through neutron diffraction. They reported the coexistence of both structures I and II and affirmed that the kinetic of sI can be faster even when the driving force for sII is higher. Aladko et al. (2002) also reported data evidencing single methane hydrate coexisting with double methane-propane hydrate above 75 mol% CH₄ at 100, 300 and 800 MPa. Even though thermodynamic models should be able to calculate metastable equilibrium states, commercial packages usually search the global minimum of the Gibbs energy and do not predict these states. Thus, the study of the coexistence of sI and sII in methane-propane hydrates is important as it likely occurs in real conditions, such as in hydrate reservoirs and hydrocarbon flowlines.

In short, this chapter includes the results previously reported by Menezes et al. (2019) and presents new equilibrium data for CH₄ and CH₄-C₃H₈ hydrates based on microcalorimetry at constant pressure mode and the isochoric method in a PVT cell. Evidence of sI and sII formation in methane-propane-water systems is also discussed. Moreover, the solid phase in a hydrate forming system may present different properties depending on the experimental protocol (SLOAN et al., 2010). In fact, the results obtained from microcalorimetry at constant pressure mode and by performing isochoric

measurements in a PVT cell are not strictly identical, which evidences the influence of the methodology on the hydrate formation, especially concerning the mixing. Thus, some relevant experimental factors that affect hydrate structural properties are discussed. These factors should be considered when comparing literature data or planning experimental procedures.

6.2 SPECIFIC EXPERIMENTAL CONDITIONS

Microcalorimetry: The experimental configuration based on HP- μ DSC is described in section 2.1 and the procedures applied in this chapter vary according to the topic concerned (standard or multicycles methods). In each of the experiments presented below, about 30 mg of Milli-Q water was placed in the sample cell so that the bottom surface was totally covered. Then the sample was pressurized with either pure gas (methane or propane, both 99.5 mol%) or a mixture, while the reference cell was kept empty. As previously mentioned, two operational modes can be used: isobaric and isochoric. In the experiments presented in this chapter, the isobaric mode was chosen for comparison with PVT results, as will be explained in section 6.4.1.

PVT- Isochoric method: The setup used for isochoric analysis by using a PVT cell was made available by the Phases to Flow Laboratory at the Colorado School of Mines (USA) and it is described in detail in section 2.3 of this work. Methane (99.99% purity, General Air), propane (98% purity, General Air) and a commercial mixture of 92:8 mol% methane and propane (99% purity, General Air) were used to form double-guest hydrates. Other two mixtures of methane-propane (85:15 and 95:5 mol%) were prepared in the lab by gravimetry using a balance shown in figure 2.12.

Modeling: Equilibrium phase data were obtained through calculations by using the software CSMGem code Version 1.10, which implements the van der Waals and Platteeuw model with the SRK equation of state.

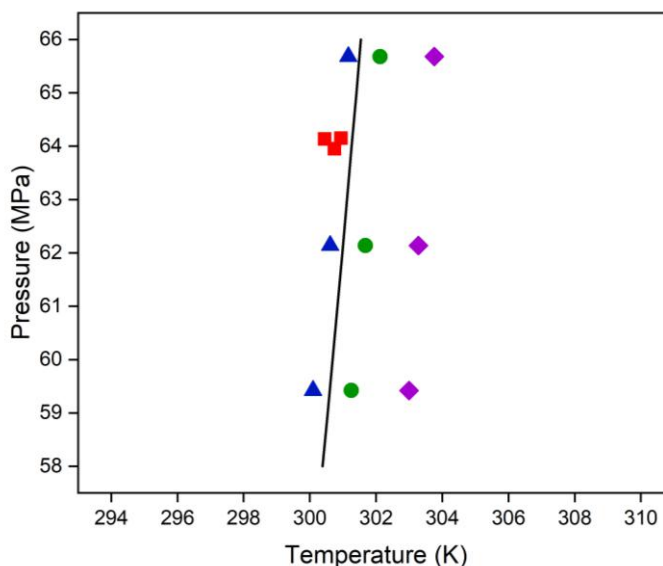
6.3 METHANE HYDRATE

6.3.1 Equilibrium Data for CH₄ Hydrates: PVT-Isochoric Method vs Microcalorimetry

Figure 6.1 shows experimental points for methane hydrate dissociation obtained by the PVT-isochoric method and in the microcalorimeter at constant pressure.

Although the experiments were not performed at exactly the same pressure, it is possible to verify by extrapolation that the PVT measurements coincide with the onset values obtained by HP- μ DSC.

Figure 6.1 – Dissociation data of CH₄ hydrates by PVT-isochoric method and microcalorimetry: (■) PVT-isochoric search; (▲) onset points, (●) peak points, and (◆) endset points by HP- μ DSC; black line corresponds to the predictions from CSMGem.



The equilibrium point determined from the PVT-isochoric method represents the complete dissociation of the solid phase (hydrate crystals). In this way, one could expect similar values for PVT measurements and endset points obtained by HP- μ DSC, since both represent the ending of the dissociation process. However, as mentioned before, the pressure changes along the experiments performed through the PVT-isochoric method, whereas it is constant along the microcalorimetric measurements. Hence, the quality, size, shape and structure of formed crystals vary accordingly to the changes in the thermodynamic conditions of the system. Thereby, the last crystal dissolved during the PVT- isochoric method is considered to be equivalent to the first crystal dissolved through HP- μ DSC method, since it is subjected to the same pressure and supposed to present similar properties.

Table 6.1 shows the numeric values for the dissociation data plotted in the figure above. Each point was obtained in a distinct experiment and both PVT-isochoric data and onset points present good agreement with the prediction.

Slightly lower temperatures are observed for such experimental data likely due to the presence of empty cavities in real hydrate structures, leading to less stable configuration with lower dissociation temperatures. The onset temperature is expected to present more accurate results than peak and endset temperatures for the same reasons mentioned in section 4.3.1.

Table 6.1 – Dissociation data of CH₄ hydrates by HP- μ DSC at constant pressure and the PVT-isochoric method. AD corresponds to the average absolute deviation.

HP- μ DSC					UHP system (PVT-Isochoric method)		
P (MPa)	CSMGem (K)	T _{ONSET} (K) (AD)	T _{PEAK} (K) (AD)	T _{ENDSET} (K) (AD)	P (MPa)	CSMGem (K)	T (K) (AD)
59.4	300.60	300.10 (0.5)	301.25 (0.65)	303.00 (2.4)	64.26	301.30	300.45 (0.85)
62.1	300.99	300.62 (0.02)	301.68 (1.08)	303.28 (2.68)	64.15	301.29	300.95 (0.35)
65.7	301.50	301.16 (0.56)	302.12 (1.52)	303.76 (3.16)	63.95	301.26	300.75 (0.55)

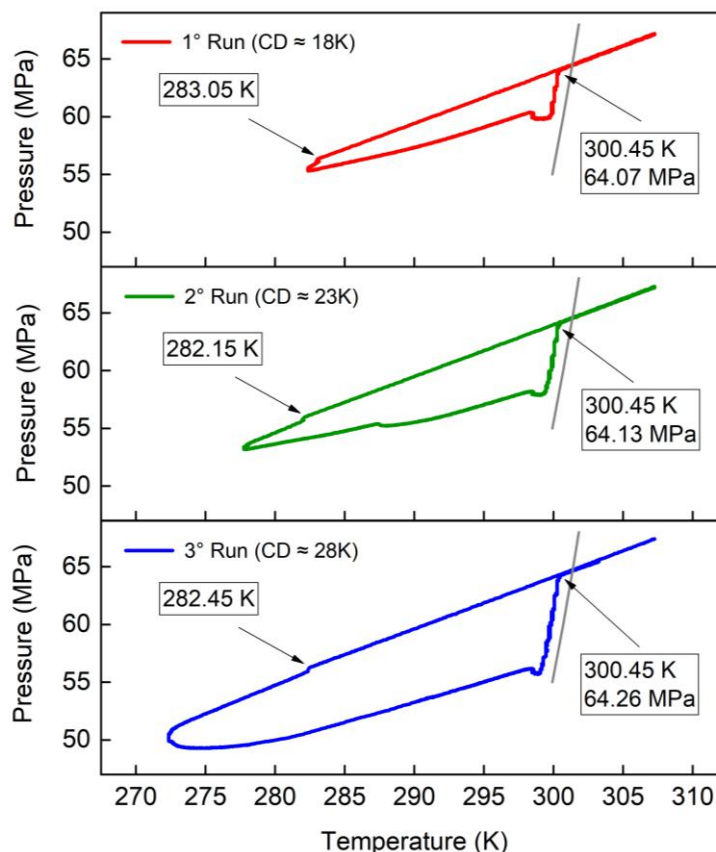
6.3.1.1 Effect of the Cooling Degree

Three runs were carried out in the PVT cell using the same sample in order to verify possible effects of applying different cooling degrees (CD) – the difference between the dissociation temperature and the minimum temperature reached during the cooling process. The analyses are shown in Figure 6.2 and a very good reproducibility is observed through this method. Higher cooling degrees seem to slightly increase the equilibrium pressure. Although this change is not very significant, higher cooling degrees increase the driving force of the hydrate formation and this may favor the gas molecules filling the cavities, reducing the empty cages on the lattice and thus approaching the hydrate equilibrium point to the one predicted by modeling.

Moreover, the cooling does affect the amount of the solid phase, as one can see by checking the pressure drop during the cooling, since the residence time of the sample in the hydrate zone is longer.

Finally, it is noted that the crystallization temperatures are similar for all three experiments, although it is a stochastic phenomenon.

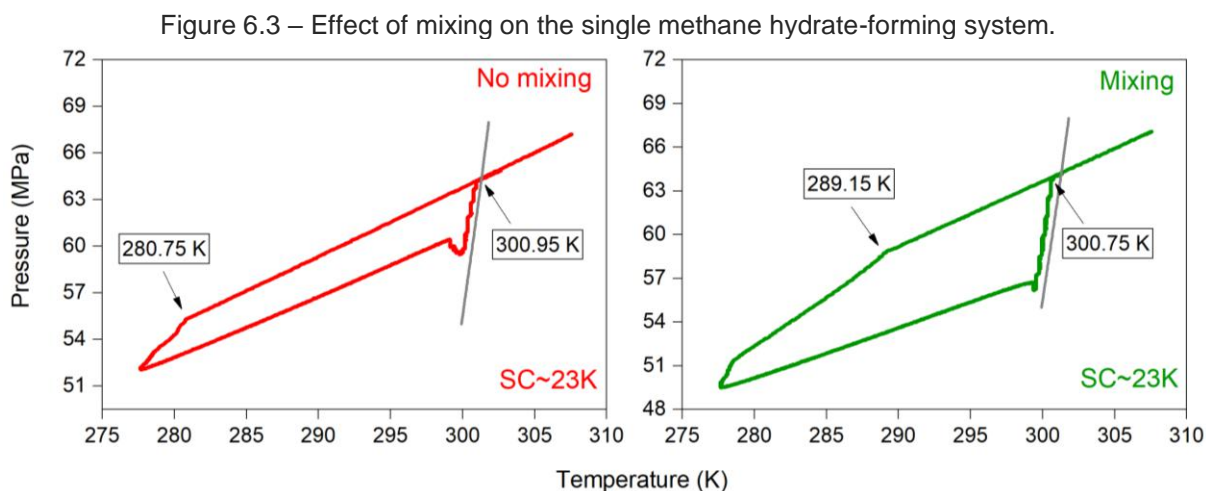
Figure 6.2 – Effect of cooling degree (CD) on the equilibrium point and the amount of methane hydrate formed.



6.3.1.2 Effect of Mixing

The influence of mixing the system is a substantial factor considered in this work. Considering there is no mixing inside the high-pressure cell coupled to the microcalorimeter, it is important to gather evidence about how much the equilibrium point may be affected by stirring. Figure 6.3 shows two PVT-isochoric experiments performed in the presence and absence of mixing. The equilibrium points given by these analyses were: 300.95K and 64.15 MPa for the first case, without mixing, and 300.75K and 63.95 MPa with magnetic stirring inside the PVT cell. The difference seems to be not relevant since both temperature and pressure decreased slightly by mixing the system. The experimental observation throughout the analyses shows that mixing the system leads to a decrease in pressure, probably due to the higher transfer of gas molecules to the liquid phase. So, the decrease in dissociation temperature may be a result of the lower pressure in the system and not because mixing would lead to a hydrate with different properties. In contrast, the crystallization temperature is significantly different in absence or presence of stirring. Mixing the bulk contributes to

the crystallization process as it favors the gas dissolution in the aqueous phase and increases the number of molecular collisions and their energy intensity, facilitating the overcoming of the activation energy barrier required for the hydrate formation.



Even though the effect of mixing could be negligible in a single gas system, the phenomenon still needs to be studied by checking the structure of the hydrate formed. Such study becomes more relevant when a gas mixture is applied. It is possible to obtain different hydrate compositions by working at different dynamic conditions. Thus, the equilibrium point may be affected in such cases, as indicated in Chapter 5.

6.4 METHANE-PROPANE HYDRATE

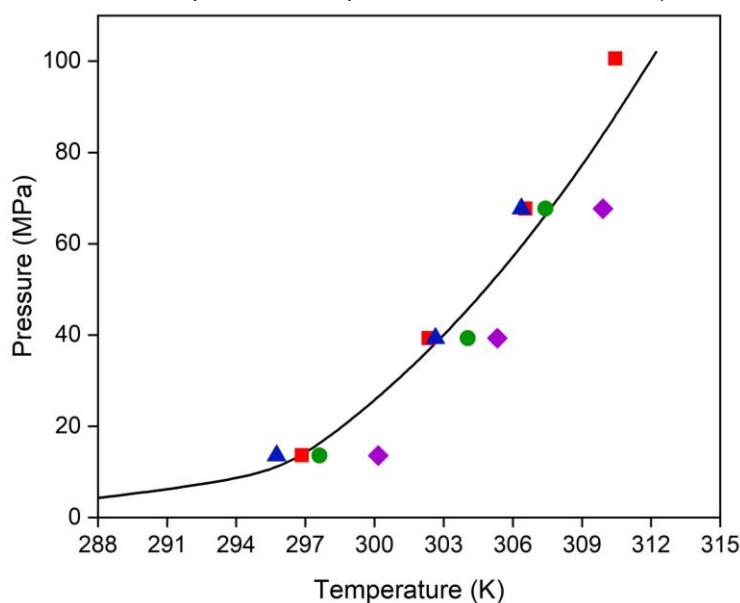
6.4.1 Equilibrium Data for $\text{CH}_4\text{-C}_3\text{H}_8$ Hydrates: PVT - Isochoric Method vs Microcalorimetry

New equilibrium data for methane-propane hydrates were obtained by both microcalorimetry (at constant pressure) and isochoric search in a PVT cell. The hydrate equilibrium conditions in the PVT-isochoric method change throughout the experiment, as mentioned before. Consequently, it is not possible to accurately predict the pressure at which the hydrate dissociation will end. For this reason, the calorimetric analyses in this case were subsequently performed at the same equilibrium pressures obtained by the PVT-isochoric method, in order to compare similar data from both methods. On the other hand, the use of the isochoric method in the HP- μ DSC also implies a pressure variation (although much smaller than in PVT cell) due to the thermodynamic issue

(temperature ramping) and the hydrate formation/dissociation. In this case, the equilibrium pressure from the onset point does not exactly match the PVT measurements. Thus, the use of isobaric mode in HP- μ DSC was preferred to perform the experiments described in this section, as it allows one to fix a specific pressure and compare results with the thermodynamic properties obtained by the PVT method. It worth mentioning herein that the experiments carried out throughout the work showed that the variation of the gas phase composition in the isobaric method is not relevant to change the hydrate equilibrium as initially thought, considering the low amount of hydrate formed.

Figure 6.4 presents the experimental data obtained from PVT measurements and microcalorimetric method, and the predictions from CSMGem modeling.

Figure 6.4 – Dissociation data of $\text{CH}_4\text{-C}_3\text{H}_8$ hydrates (92 mol% CH_4) by the PVT-isochoric method and microcalorimetry: (■) isochoric search; (▲) onset points, (●) peak points and (◆) endset points by HP- μ DSC; black line corresponds to the prediction from CSMGem (92 mol% CH_4).

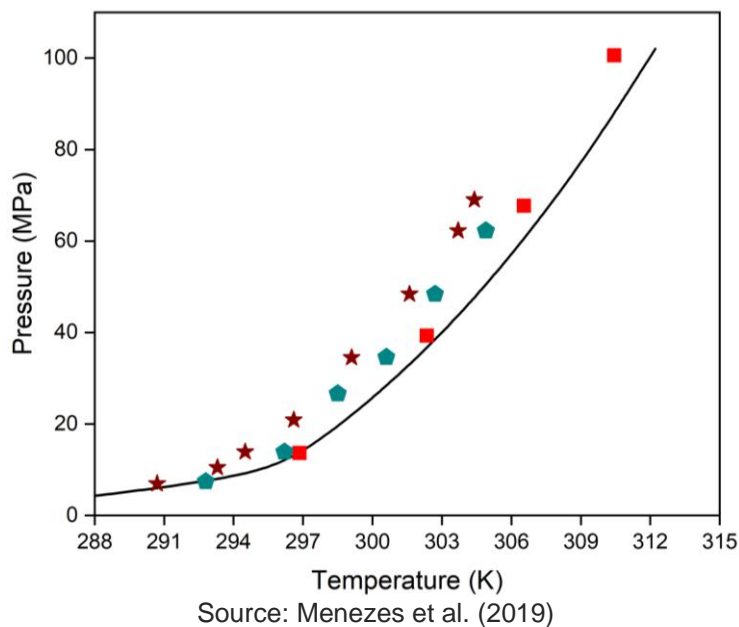


Source: Menezes et al. (2019)

As observed in the results previously discussed for methane hydrates, the isochoric data again approach to the onset values, as observed in Chapter 4 and section 5.3.1. The figure above also shows the effect of pressure on hydrate dissociation temperature and indicates that predictions deviate more significantly from experimental data at higher pressures. Isochoric data obtained in this study are shown in Figure 6.5 along with data from the literature with approximate compositions. The

results obtained in this study at 92 mol% CH₄ follow the trend of the curves obtained by the data published in the literature.

Figure 6.5 – Equilibrium data obtained by the PVT-isochoric method at different compositions: (★) 96.5 mol% CH₄ (MCLEOD; CAMPBELL, 1961); (◆) 94.5 mol% CH₄ (MCLEOD; CAMPBELL, 1961); (■) 92 mol% CH₄ (this work.); black line corresponds to the prediction from CSMGem (92 mol% CH₄).



Tables 6.2 and 6.3 show the dissociation data obtained by microcalorimetry and PVT-isochoric method, respectively. The PVT measurements also indicate the dissociation of two different structures concerned to a single methane hydrate and a double methane-propane hydrate, as will be discussed in detail in the next section (6.4.2). Although Table 6.2 shows good agreement for prediction and onset values of sI, a higher discrepancy is observed for some onset values of sII, in agreement to the results previously presented in section 5.5.2. The onset determination for structure II can be more difficult when occurs a small exothermic peak right before the dissociation curve, likely related to a rearrangement in the crystalline structure or a recrystallization process, as indicated in Figure 6.6. On the other hand, Table 6.3 also indicates higher deviation of equilibrium data obtained through the PVT-isochoric method as the pressure increases. Although the amount of empty cavities in real hydrates may also lead to lower dissociation temperatures, such deviations should also be related to the effect of sI formation on the gas phase composition change.

Table 6.2 – Dissociation data of CH₄-C₃H₈ hydrates obtained by HP- μ DSC. AD corresponds to the average absolute deviation from prediction (CSMGem).

CH ₄ (mol%)	P (MPa)	Temperature (K) – sI (CH ₄)			Temperature (K) – sII (CH ₄ + C ₃ H ₈)				
		CSMGem	Onset (AD)	Peak (AD)	Endset (AD)	CSMGem	Onset (AD)	Peak (AD)	Endset (AD)
	13.6	288.55	288.39 (0.16)	289.14 (0.59)	290.36 (1.81)	297.22	295.75 (1.47)	297.61 (0.39)	300.16 (2.94)
92	39.3	297.05	296.94 (0.11)	297.55 (0.50)	298.60 (1.55)	303.14	302.65 (0.49)	304.05 (0.91)	305.33 (2.19)
	67.7	301.75	301.10 (0.65)	301.64 (0.11)	302.66 (0.91)	307.71	306.37 (1.34)	307.42 (0.29)	309.91 (2.20)

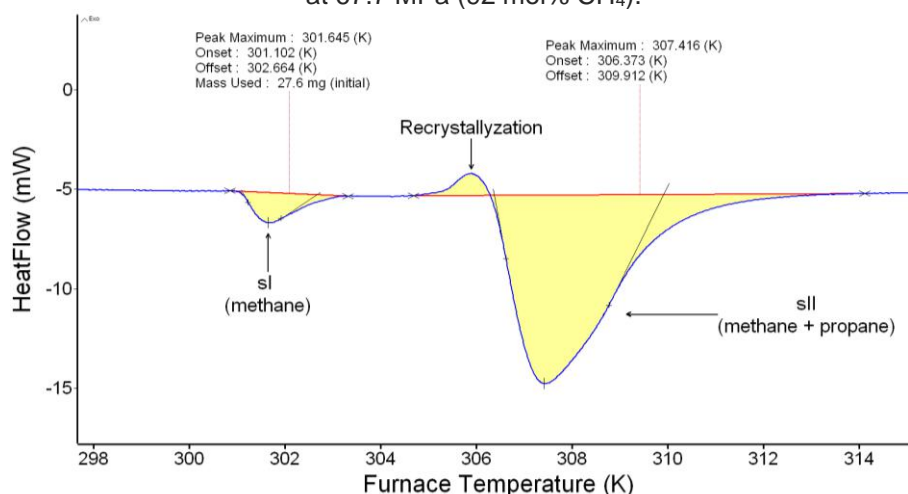
Source: Adapted from Menezes et al. (2019)

Table 6.3 – Dissociation data of CH₄-C₃H₈ hydrates obtained by the PVT-isochoric method. AD corresponds to the average absolute deviation from prediction (CSMGem).

CH ₄ (mol%)	P (MPa)	CSMGem (K)	T (K)	AD
	13.6	297.29	296.85	0.44
92	39.3	303.18	302.35	0.83
	67.7	307.71	306.55	1.16
	100.5	312.045	310.45	1.6

Source: Adapted from Menezes et al. (2019)

Figure 6.6 – Phenomenon of recrystallization just before the dissociation of sII in the CH₄-C₃H₈ system at 67.7 MPa (92 mol% CH₄).



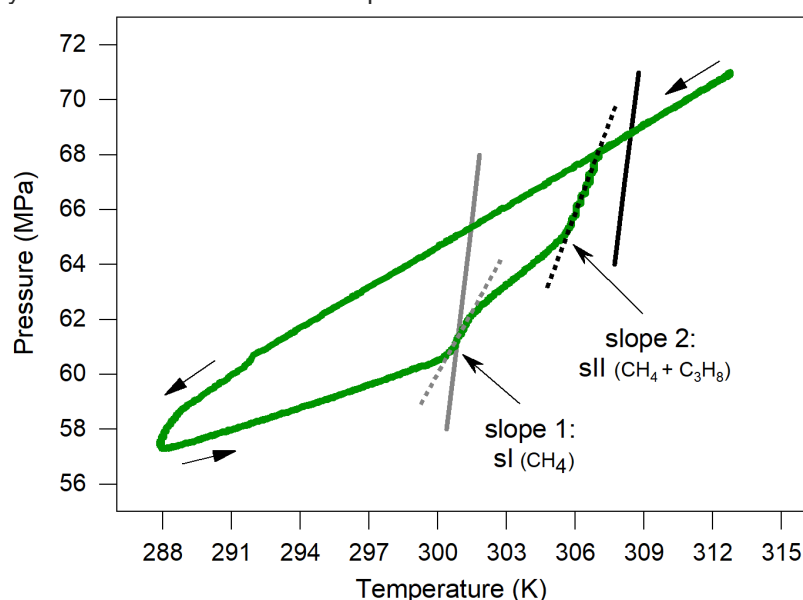
Source: Menezes et al. (2019)

6.4.2 Coexistence of Structures I and II on CH₄-C₃H₈ Hydrates Obtained by the PVT-Isochoric Method

A pressure-temperature plot obtained through the PVT-isochoric method is shown in Figure 6.7. It reveals the formation of both structures I and II at higher

pressures, in agreement with the results by HP- μ DSC previously shown in Chapter 5, section 5.1. One can clearly identify two regions in which the increase in pressure is accentuated. This occurs due to the release of gas from different hydrate phases leading to an increase of pressure caused by gas phase compression. Moreover, the first slope indicated in the figure takes place much earlier than sII equilibrium line predicted by CSMGem, indicated by the black solid line. In fact, it appears just before methane hydrate equilibrium (grey solid line), indicating that the first slope concerns to structure I dissociation, formed along with sII during cooling. This phenomenon is discussed below by considering different factors that may influence the formation of structures I and II.

Figure 6.7 – Diagram P vs T for the system $\text{CH}_4\text{-C}_3\text{H}_8\text{-H}_2\text{O}$ (92 mol% CH_4) by the PVT-isochoric method: black and gray solid lines correspond to the predicted results through CSMGem for sII and sI, respectively. Dashed lines refer to the slopes related to the dissociation of such structures.



Source: Adapted from Menezes et al. (2019)

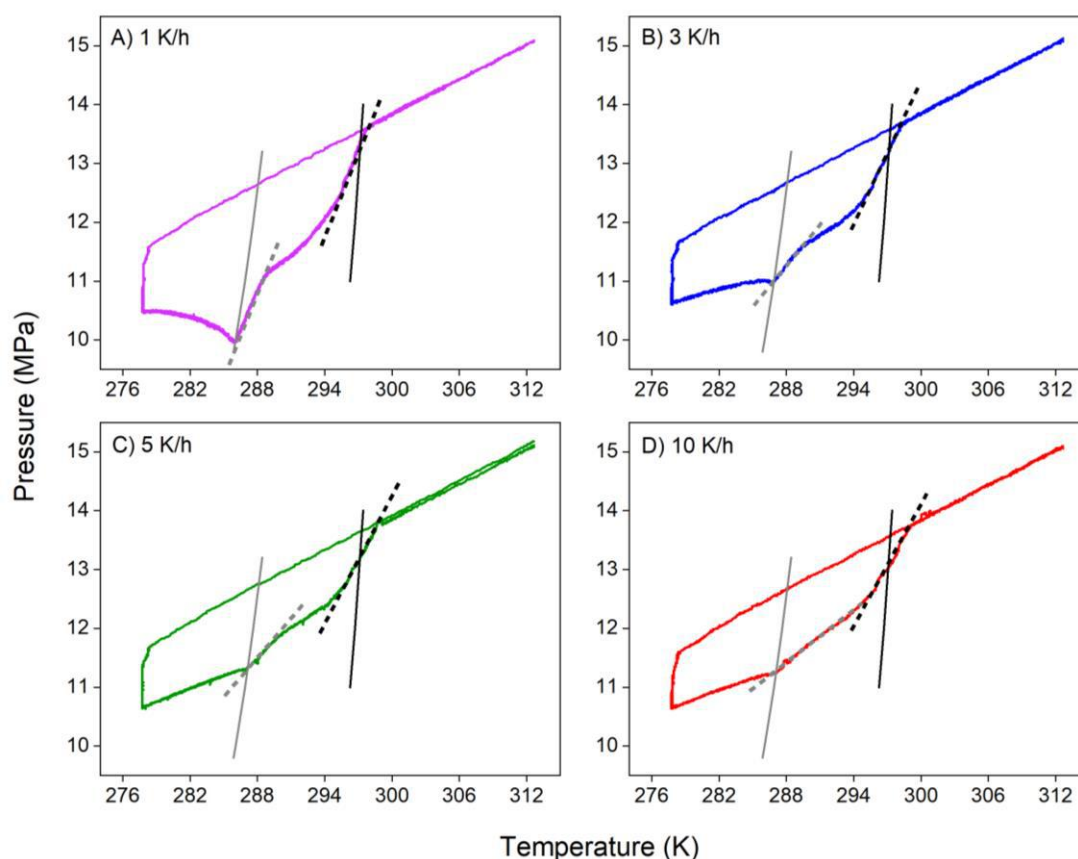
6.4.3 Impact of Experimental Factors on the Formation of sI and sII

6.4.3.1 Effect of Heating Rate

A set of experiments at different heating rates was performed to verify the effect of heating rate in the methane + propane hydrate thermodynamic profile. Figure 6.8 shows PVT-isochoric diagrams at four different heating rates at 15 MPa. Even during the heating, the hydrate formation still may occur before the system reaches the equilibrium line. If the heating rate is low, the pressure drop effect caused by hydrate

formation prevails over the pressure rise effect caused by temperature ramping. In this case, a profile similar to that observed in Figure 6.8A is obtained, where the pressure initially falls during heating due to the high rate of hydrate formation. On the other hand, if the heating rate is so fast, the slopes are not sufficiently separated from each other, as in Figure 6.8D. Therefore, better-defined profile was obtained at 5 K per hour (Figure 6.8C), since two slopes referring sI and sII can be clearly distinguished, indicating that each structure dissociates close to their respective equilibrium lines.

Figure 6.8 – Dissociation profiles for CH₄-C₃H₈ hydrate-forming systems (92 mol% CH₄) at different heating rates by the PVT-isochoric method. Black and gray solid lines correspond to the predicted results through CSMGem for sII and sI structures, respectively. Dashed lines refer to the slopes related to the dissociation of such structures.

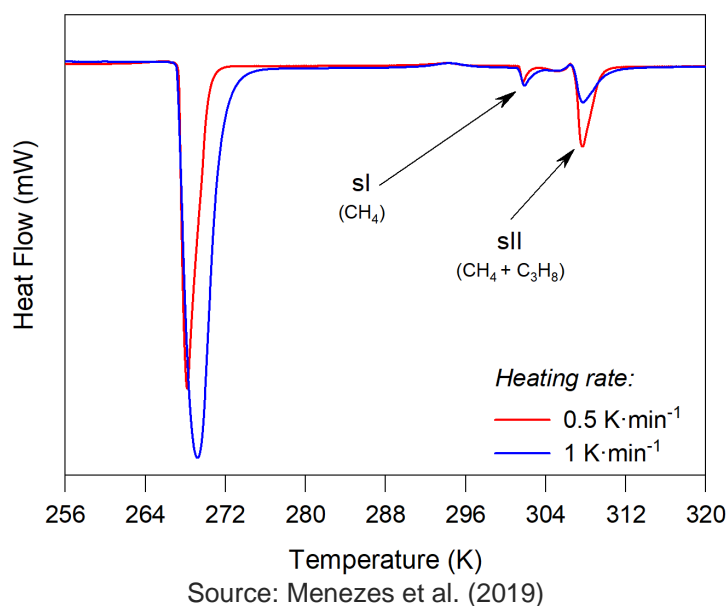


Source: Adapted from Menezes et al. (2019)

Although the PVT-isochoric method allows observing both dissociation stages, this is not appropriate to estimate the proportion between structures I and II. In fact, the microcalorimetric method is more appropriate for estimating the fractions of sI and sII. In this case, the pressure is kept constant and thereby the hydrate equilibrium does not move as in the PVT-isochoric method, making it possible the integration of area for

each dissociation curve separately. Figure 6.9 presents thermograms at two cooling-heating rates.

Figure 6.9 – Thermograms of CH₄-C₃H₈ hydrates (92.1 mol% CH₄, 67 MPa) at different heating rates.

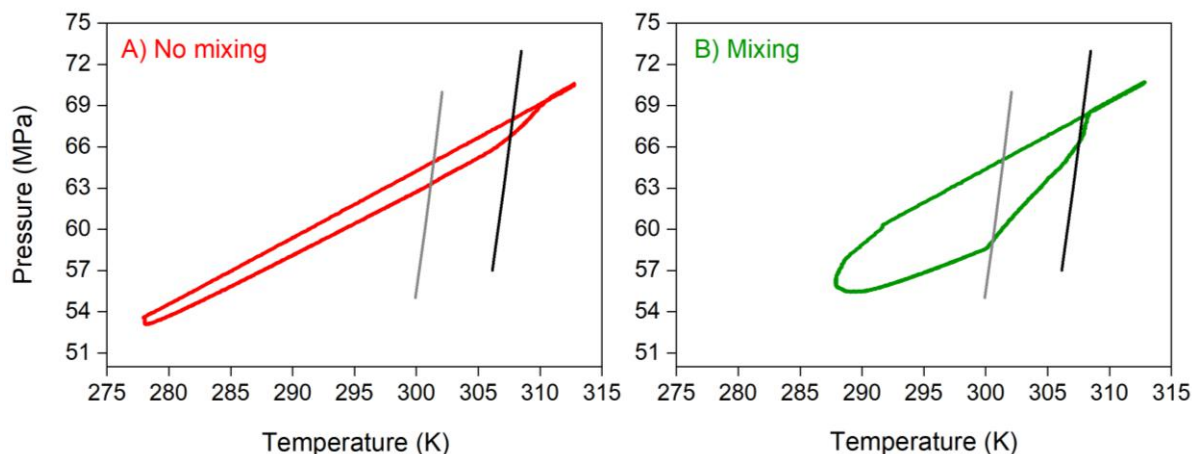


The area for the first curve (sI) does not seem to be affected by the heating rate. On the other hand, the fraction of structure II is higher at lower heating rates (0.92 at 0.5 K·min⁻¹, and 0.78 at 1 K·min⁻¹). The residence time in the hydrate zone is higher at 0.5 K·min⁻¹ and hence more ice is converted to the preferential hydrate structure during the experiment.

6.4.3.2 Effect of Mixing

Heterogeneous hydrate structures can be obtained by working at static conditions, especially when gas mixtures are involved. Hence, the dissociation point may also be affected, as previously mentioned in the section 6.3.1.2. Figure 6.10 shows diagrams obtained via the PVT-isochoric method to verify the mixing effect. Although stepwise stages were not applied in these runs, the dissociation points for sII taken in these plots are 308.25 K and 68.27 MPa with no mixing and 307.15 K and 68.12 MPa with mixing. These data are very similar, and the lower values obtained for the experiment with mixing are mainly related to the higher gas dissolution in the liquid phase, which leads to lower pressure and hence a lower dissociation temperature.

Figure 6.10 – Effect of stirring on the dissociation profiles of CH₄-C₃H₈ hydrates (92 mol% CH₄) by the PVT-isochoric method, initially at 70 MPa. Black and gray lines correspond to the predicted results through CSMGem for sII and sI structures, respectively.



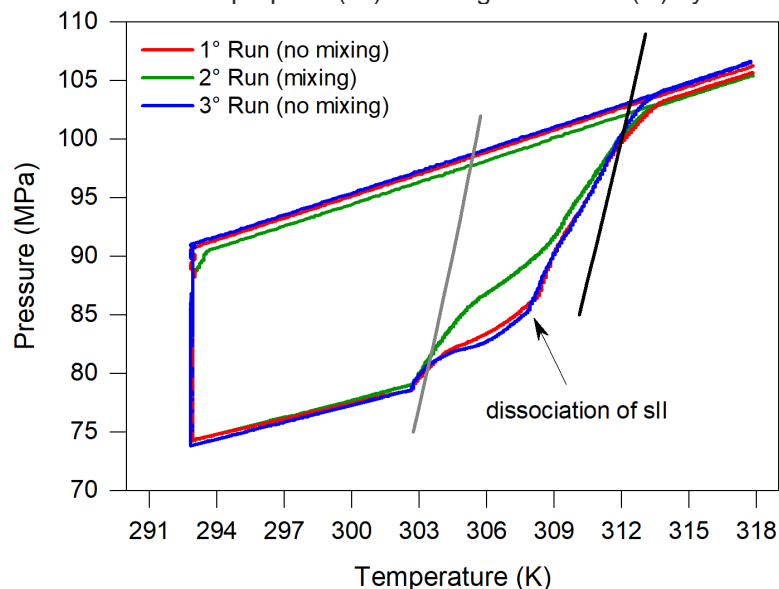
Source: Menezes et al. (2019)

Although no definitive conclusion can be drawn about the effect of the dynamic condition inside the cell on hydrate structures, two observations should be highlighted: the amount of hydrate formed is very small in the experiment performed without stirring and the formation of sI is not even observed, whereas a large amount of sI seems to have been formed in the presence of stirring. These phenomena are related to mass transfer issues, considering that no mixing implies in lower availability of gas molecules in the proper sites for interactions with water in order to form the hydrate crystals. On the other hand, the presence of mixing favors even the formation of the supposedly metastable structure I. The mechanical stirring provides enough energy so that such molecular interactions overcome the activation barrier, allowing the nucleation and crystals growth. Even though sII is the thermodynamically stable structure for this system, its kinetics of formation may be significantly slower than for sI, which may explain the large amount of sI when mixing the system (KLAPPROTH et al., 2019).

The mixing effect was also studied at a higher pressure to favor the hydrate formation so that the profiles could be easily compared. Figure 6.11 presents three consecutive runs using the same sample, where only the second run was carried out with mixing. The dissociation profiles obtained in the first and third runs are similar, which suggests that the fractions of sI and sII are similar. The arrow indicates the moment in which sII dissociation changes significantly the compression line. On the other hand, the second run presents a different profile, which indicates a different proportion between sI and sII. Structure I was favored in the presence of mixing since a higher increase in pressure is observed right after the sI equilibrium line. This finding

agrees with the previous results regarding the addition of mechanical energy. Nonetheless, the higher pressure, in this case, was enough to induce the formation of a notable fraction of sl even in the absence of mixing. Better solubility and diffusivity of methane into water than propane may have contributed to sl formation.

Figure 6.11 – Effect of stirring on the dissociation profile of CH₄-C₃H₈ hydrate (92 mol% CH₄) by the PVT-isochoric method, initially at 105 MPa. Black and gray lines correspond to the prediction from CSMGem software for methane-propane (sII) and single methane (sl) hydrates, respectively.



Source: Adapted from Menezes et al. (2019)

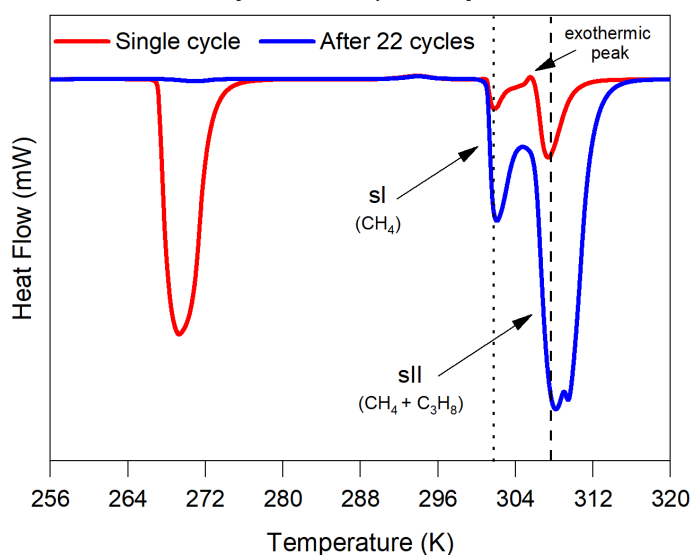
6.4.3.3 Effect of Multicycles

The fact that the hydrate kinetics contributes to sl formation does not imply that this structure is thermodynamically stable when coexisting with sII. Thereby, some experiments were performed to verify possible changes in structural fractions by subjecting the sample to multicycles. The conversion rate for synthetic hydrates depends on experimental conditions, and the final product usually presents a small fraction of free water or ice due to incomplete conversion. In the first method studied through microcalorimetry, shown in Figure 6.12, the subsequent cycles were heated up to 283.15 K in order to melt the ice repeatedly and increase its conversion to hydrate, either sl or sII.

According to the integration of the dissociation areas in the figure below, 98.5% of the ice initially formed in the first cycle was converted to hydrate after 22 cycles, and the final hydrate was composed of 81.35% of sII. The percentage of sII obtained for the single cycle run by using the same sample at the same pressure was 78.6%,

revealing that sII structure is indeed preferentially formed throughout the multiple cycles. This indicates that although sI presents better kinetics of formation, part of it should be converted to sII, the most thermodynamically stable structure.

Figure 6.12 – Effect of multicycles heated up to ice melting, on CH₄-C₃H₈ system at 67.7 MPa (92.3 mol% CH₄). Dotted and dashed lines refer to CSMGem predictions for methane and methane-propane hydrates, respectively

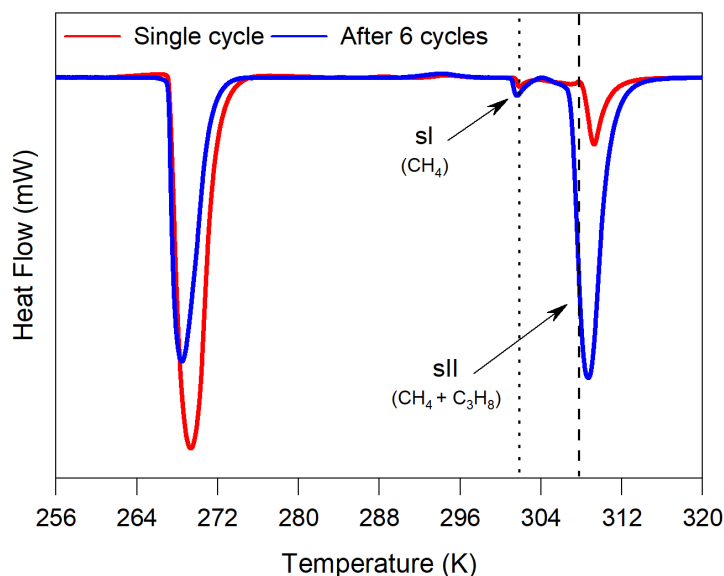


The dissociation process in the single cycle presents a recrystallization peak, similar to the one illustrated in Figure 6.6, and the sII dissociation curve after 22 cycles reveals the presence of two overlapped peaks. As discussed throughout chapter 4, the multicycles method may induce greater heterogeneity in the hydrate structure. This phenomenon is believed to occur due to the limitations of mass transfer implied by the hydrate layer formed in the early cycles, that may increase the amount of empty cavities in deeper regions of aqueous phase. Considering that the system herein is composed of CH₄ and C₃H₈, the difference in diffusivity of these molecules through the initial hydrate layer may further affect the heterogeneity of the final structure.

A second method was applied for studying these structures by applying multicycles, presented in Figure 6.13. In this case, the system was heated up to a temperature above the dissociation point for sI, but below that for sII, in order to check whether sI continues to form even if sII is already present in the system. Due to experimental issues, it was not possible to keep running cycles until the maximum conversion of water. According to the thermograms presented in the figure below, 31.29% of the ice formed in the first run was converted to hydrate after 6 cycles, and 97.41% of the final hydrate was constituted of structure sII, which may indicate the

metastability of structure I. The first method resulted in a smaller amount of sII (81.35%) even after 22 cycles because sl was not dissociated throughout the multiple cycles.

Figure 6.13 – Effect of multicycles heated up to sl dissociation on $\text{CH}_4\text{-C}_3\text{H}_8$ system at 68 MPa (92.1 mol% CH_4) by microcalorimetry. Dotted and dashed lines refer to CSMGem predictions for methane and methane-propane hydrates, respectively.



Source: Adapted from Menezes et al. (2019)

Although the fraction of sII increases in subsequent cycles, it is possible to observe that sl continues to be formed but surely not at the same proportion as sII. On the one hand, the formation of sl may be due to mass transfer issues due to the absence of mixing inside the cell, limiting the availability of propane molecules required to form sII in deeper regions of the aqueous phase. On the other hand, the formation of a small fraction of methane hydrate (sl) could lead to a more stable system, as resumed below in this section, even though sII is the preferential structure.

One can also observe that Figure 6.13 (method II) presents a discrepancy between onset temperatures (~ 1.2 K) for sII concerning single run and after multiple cycles. Two factors should contribute to this phenomenon: i) greater heterogeneity degree implied by the multicycles method, as mentioned above; ii) changes in gas phase composition due to sl dissociation. With regards to the greater heterogeneity caused by the multicycle method, one should note that although the onset temperatures in single guest systems were slightly lower than the ones obtained by the standard method, the difference between both methods were not as higher as in this case. The difference in diffusivity of methane and propane through the hydrate layer formed during earlier cycles also may contribute to a more heterogeneous final

structure. Therefore, it seems that the multicycle method in the absence of mixing may affect more significantly the homogeneity and the thermodynamic properties of hydrates formed in the presence of different guest species. On the other hand, the second factor that may have affected the onset temperature after 6 cycles in Figure 6.13 is a possible change in gas composition, since the dissociation of sI during the heating in method II increases the fraction of methane available to form hydrate in the subsequent cycle. As explained in chapter 5.5.3, the increase in the methane fraction (for methane-propane systems whose methane content is higher than 67 mol%) leads to hydrates with lower dissociation temperatures as methane molecules occupy large cavities of sII due to propane scarcity. Methane molecules do not fit into large cavities as well as propane molecules and the interaction between guest molecules and the water lattice is weaker in this case, favoring structure dissociation.

Table 6.4 shows the onset and peak temperatures for each experiment shown above and the absolute deviation from prediction calculated by CSMGem.

Table 6.4 – Dissociation data for CH₄-C₃H₈ hydrates obtained by single runs and after multiple cycles by HP- μ DSC. AD corresponds to the average absolute deviation from prediction (CSMGem).

Method	mol% CH ₄	P (MPa)	n° of cycles	sI (CH ₄) Temperature (K)			sII (CH ₄ + C ₃ H ₈) Temperature (K)			
				CSMGem	Onset (AD)	Peak (AD)	CSMGem	Onset (AD)	Peak (AD)	(area%)
I ^a	92.3	67.7	Single	301.78	301.09 (0.69)	301.84 (0.06)	307.62	306.1 (1.52)	307.39 (0.23)	78.55
			After 22		301.11 (0.67)	302.06 (0.28)		305.66 (1.96)	308.15 (0.53)	81.35
II ^b	92.1	68	Single	301.82	301.49 (0.33)	301.88 (0.06)	307.74	308.19 (0.45)	309.27 (1.53)	94.60
			After 6		301.11 (0.71)	301.61 (0.21)		306.98 (0.76)	308.70 (0.96)	97.41

Cycles before the last one: ^a Heating up to complete ice melting; ^b Heating up to complete sI dissociation.

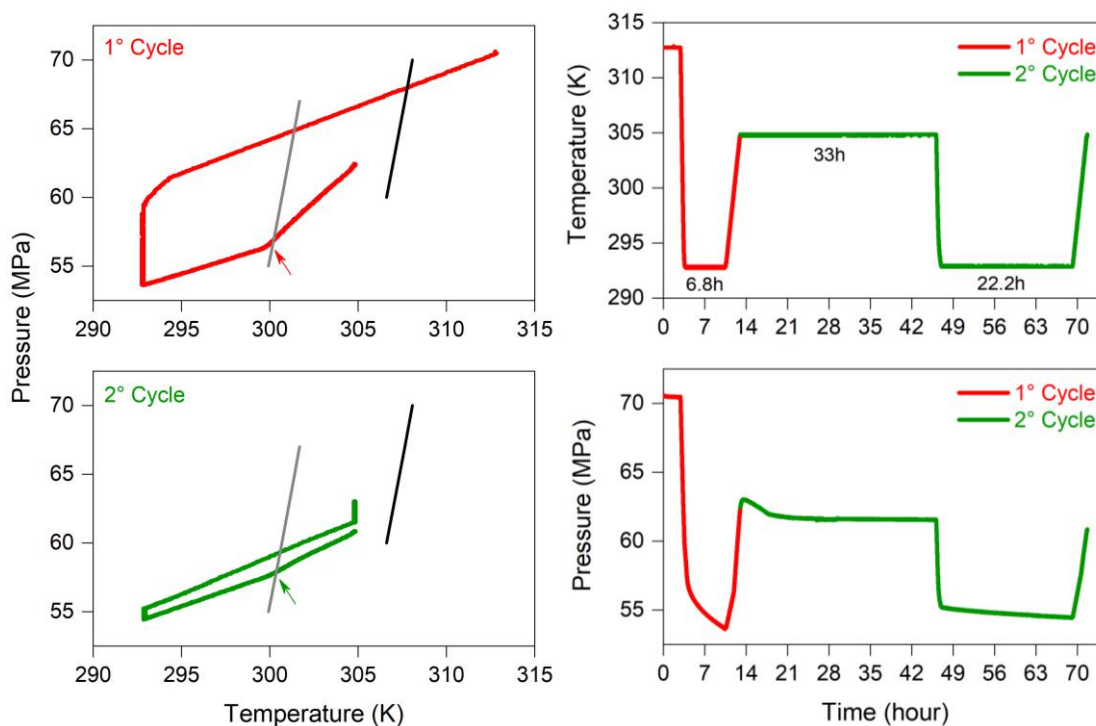
In most cases, equilibrium points obtained after multiple cycles tend to present lower dissociation temperatures and greater deviations from predictions than those obtained in single runs, in agreement to the results found throughout chapter 4. It is believed that the main reason for this is the absence of mixing and hence the limitation of gas diffusion through the liquid phase as an initial hydrate layer is formed on the gas-liquid interface, acting as a hindrance of mass transfer. The scarcity of gas molecules in deeper regions of the sample may lead to an increase of empty cavities

during hydrate crystal growth over multiple cycles, thus affecting structural stability. Such difference is more evident for sII when applying method II, for the reason explained previously.

Better agreement between peak temperatures and predictions can also be noted in most cases of Table 6.4.1. The presence of empty cavities in real hydrates and the fact that sI formation is not evidenced by predictions could justify such deviation of onset temperatures. Finally, it is worth to remember that the overlapping of dissociation curves (sI and sII) and structural rearrangement make less accurate the determination of the onset points for sII.

Figure 6.14 shows an experiment in the PVT cell similar to the second method of multicycles performed by HP- μ DSC. The first cycle was interrupted before the equilibrium line regarding structure II, and then a new cycle was run.

Figure 6.14 – Effect of multicycles on the dissociation profile for $\text{CH}_4\text{-C}_3\text{H}_8$ hydrate (92 mol% CH_4) by the PVT-isochoric method. Black and gray lines correspond to the predicted results through CSMGem for sII and sI, respectively.



Source: Adapted from Menezes et al. (2019)

The first cycle (red) presents hydrate formation during cooling (slight slope change at 294.0 K) and at the isotherm at 292.85 K, as verified by the drop in pressure over 6.8 h. A notable inflection point due to the a hydrate dissociation close to sI equilibrium line is observed during heating. A new isotherm was carried out for 33 h

preceding the second cooling so that most of sl could be dissociated. In this period, hydrate (sII) was still formed at a similar rate as in the first isotherm over the first 5 hours, then the formation was slowed down and the pressure remained almost constant. This behavior indicates that there was still propane to induce the formation of sII during the first cooling, but nevertheless, sl was formed simultaneously. During the second cycle (green), one can verify hydrate formation in the last isotherm at 292.85 K by over 22.2 h at a slower rate. Even after such a long time kept at this temperature, the pressure dropped about 1 MPa less than during the first cycle, which lasted 6.8 h. This suggests that more gas was consumed during the first cycle probably due to the high amount of sl formed along with sII, thereby reinforcing the faster kinetics for sl formation. Indeed, the subsequent cycle presents a smaller slope change close to sl equilibrium line, evidencing that the amount of sl formed was significantly lower in this case. Although the kinetics of formation of sl is faster, sII is likely the most stable structure for this system, as mentioned before, and it may be favored in the latter cycle due to the presence of crystals formed in the previous one.

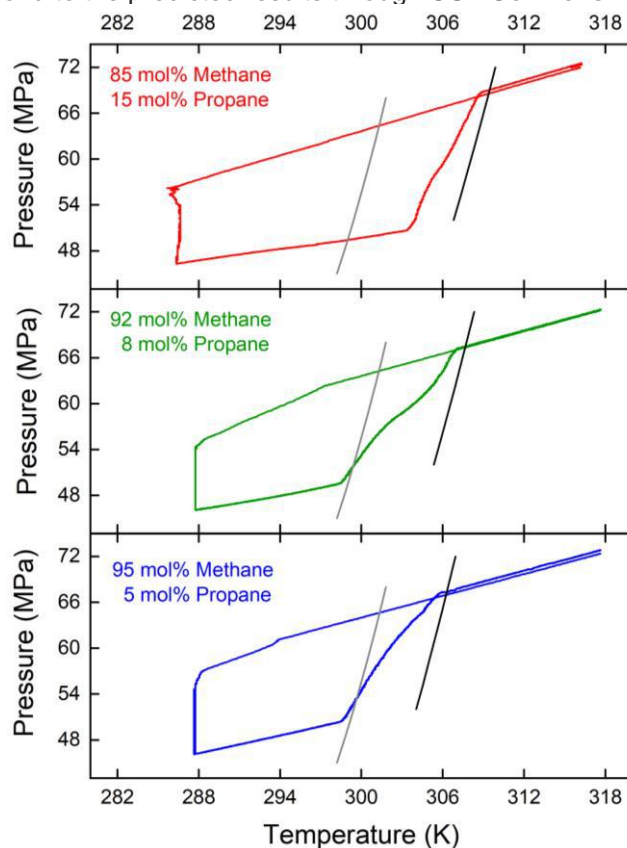
According to the results above obtained by both methods, sl does not totally disappear from the systems. It is not ruled out that stable $\text{CH}_4\text{-C}_3\text{H}_8$ systems at high methane content present a small fraction of sl due to the better structural conformation of methane molecules in both cages of sl than in large cages of sII. As shown in Table 5.1, methane molecules fit better in small cavities of sII (ratio of guest molecule diameter to cavity diameter equal to 0.868), but the diameter ratio is substantially lower for the large cage of sII (0.655) than for any cage of sl (0.855 and 0.744). It means that a system containing a single structure II, hosting methane molecules in large cages due to the shortage of propane, could be less stable than a system composed by both sl and sII.

6.4.3.4 Effect of Gas phase composition

Gas composition plays an important role in the type of structures formed and their proportion (NIXDORF; OELLRICH, 1997). The first experiment shown in Figure 6.15, carried out by the PVT-isochoric method, presented the highest propane content (85 mol% of CH_4). The plot suggests no sl was formed at this gas phase composition, since hydrate dissociation appears 4 K far from sl equilibrium line predicted by the model. This result differs from the previous one showed on the thermograms presented

in Figure 5.8 from chapter 5, in which sl is observed at 83.3 mol% CH₄ at 20 MPa. This is attributed to the higher subcooling applied on HP- μ DSC, that favor sl formation by increasing the driving force. The second plot in Figure 6.15 (92 mol% of CH₄) shows that dissociation started immediately before sl equilibrium line, evidencing the presence of sl besides slI. The last experiment (95 mol% of CH₄) resulted in a different profile, in which the dissociation looks like a continuous process. This profile is consistent with the fact that most of the hydrate formed in this case likely constitutes structure sl.

Figure 6.15 – Effect of gas phase composition on dissociation profile of CH₄-C₃H₈ hydrates. Black and gray lines correspond to the predicted results through CSMGem for slI and sl, respectively.

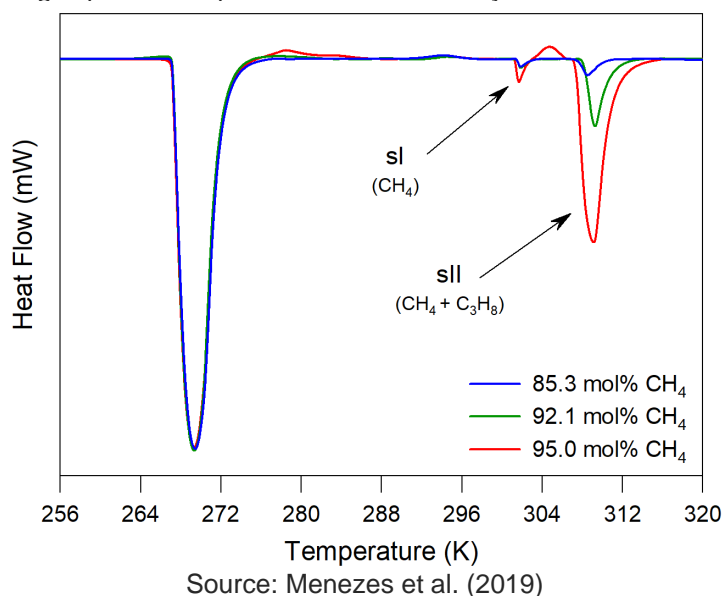


Source: Menezes et al. (2019)

Figure 6.16 shows three thermograms obtained by the calorimetric method using gas phase compositions similar to the ones used in the PVT-isochoric method. Even though these experiments were conducted with no mixing, sl is still observed for all the three compositions, in agreement to that observed in Figure 5.8 (chapter 5). As mentioned before, this is likely a result of the greater subcooling degree in those experiments compared to PVT measurements: the system was cooled down further from the equilibrium point in the calorimetric experiments. The thermograms also

indicate that the initial proportion between sI and sII changes significantly according to the methane content in the gas phase. However, structure II seems to be favored by increasing methane content in the calorimetric analysis, which apparently contradicts the results obtained by the PVT-isochoric method. The ratios between the areas corresponding to the dissociation curves (sII/sI) are 3.0 (85.3 mol% CH₄), 16.1 (92.1 mol% CH₄) and 25.5 (95.0 mol% CH₄). Hydrate formation depends on the availability of molecules for hydrate crystal growth. Considering that, a higher concentration of methane implies better gas dissolution on liquid phase, contributing to the fulfillment of sII small cavities, which firstly form according to Schicks and Luzi-Helbing (2013). Thereby, the kinetics of formation for sII is improved, even though part of large cavities probably hosts methane instead of propane molecules. This may explain the larger hydrate amount by increasing the methane content in the gas phase. Recrystallization processes are observed right after ice melting and sI dissociation at 95 mol% CH₄, confirming that hydrate formation is facilitated at such higher composition.

Figure 6.16 – Effect of gas phase composition on CH₄-C₃H₈ hydrate at 67.5 MPa by microcalorimetry.



Structure I is poorly favored by increasing methane fraction in the gas phase in this case: the higher methane dissolution in aqueous phase seems to favor sII but not sI. The results obtained through the PVT-isochoric method are different due to the presence of mixing, that contributes not just to the formation of sI, by improving methane solubility and providing enough mechanical energy to form this secondary

structure, but also to the arrangement of molecules that allows the growth of both sI and sII hydrate crystals. Therefore, even though the greater subcooling degree in the microcalorimetric method contributes to sI formation as mentioned, it does not have the same effect as stirring the system.

6.5 CONCLUSIONS

Hydrate-forming systems composed of methane-water and methane-propane-water were investigated through microcalorimetric analysis and PVT-isochoric method search. This chapter brings together evidence of the simultaneous formation of sI and sII at high pressures and high methane contents, considering that computational predictions do not reveal this phenomenon. The effects of experimental factors on these structures were evaluated according to the methodology applied since the results were not strictly the same when using the PVT Cell and the microcalorimeter. Thereby, the results are discussed according to the experimental limitations of each technique and considering their specific features.

- Dissociation data were obtained for methane and methane-propane hydrates. Equilibrium points obtained by the PVT-isochoric method approach to the onset temperatures of dissociation curves from thermograms in both systems. In some cases, the peak temperatures are closer to predictions, although the onset point should approach to the equilibrium more accurately since it represents the beginning of the hydrate dissociation process. However, empty cavities and higher heterogeneity degree may occur in real hydrates mainly in absence of mixture, affecting structural stability and implying in lower dissociation temperatures. Besides, results from predictions do not reveal the formation of sI in CH₄-C₃H₈ systems, thus disregarding methane molecules trapped in structure I, which may change the gas composition. Finally, the overlapping of dissociation curves (sI and sII) and structural rearrangement, such as recrystallization process, make less accurate the determination of the onset points of sII;
- High cooling degrees affect mainly the amount of hydrate formed and may lead to slightly higher dissociation temperatures as the increased driving force and higher residence time in the hydrate stable zone should favor the filling of the hydrate structure;

- The absence of mixing in the PVT-isochoric method does not seem to affect the equilibrium point but has a major influence on crystallization temperature and crystal growth. It indicates that no mixing in the μ DSC cells indeed does not invalidate the equilibrium data by HP- μ DSC. According to the results, sI was favored in $\text{CH}_4\text{-C}_3\text{H}_8$ systems when mixing likely due to the addition of the mechanical energy and the better diffusivity of methane in water compared to propane;
- Lower heating rate contributed mainly to sII hydrate formation, considering the residence time in the hydrate stable zone is longer;
- PVT-Isochoric results indicate that sI and sII form simultaneously in the methane-propane system, with a higher kinetic of formation for sI, although sII is the most thermodynamically stable. Applying multiple cycles in the PVT-isochoric method reveals sI mainly as a metastable structure since most of it is converted to sII in subsequent cycles. However, both microcalorimetric and PVT-isochoric methods indicate that a small fraction of sI remains a stable configuration even after multicycles, suggesting that a single structure II could be less stable than a system composed by both sI and sII;
- Dissociation data deviate from prediction mainly after subsequent cycles likely due to the scarcity of gas molecules in deeper regions of the sample, that lead to an increase of empty cavities (CH_4 systems) or most methane-occupied ($\text{CH}_4\text{-C}_3\text{H}_8$ systems) during the hydrate crystals growth, thus affecting the structural stability. Although the multicycles method did not imply significant deviations in the case of single guest systems by HP- μ DSC, it is believed that larger deviations were obtained for methane-propane systems due to the difference in diffusivity of these molecules through the hydrate layer formed in the first cycles.
- While sI was favored in $\text{CH}_4\text{-C}_3\text{H}_8$ systems by mixing in the PVT- isochoric method, this structure was also favored by using microcalorimetry due to the greater subcooling degree required to induce hydrate crystallization in this case;
- Increasing the methane fraction in $\text{CH}_4\text{-C}_3\text{H}_8$ systems revealed the opposite effect on the results obtained by the two experimental methods. A larger amount of sI was obtained in the PVT cell whereas sII structure formation was favored by using the microcalorimeter, probably because of mixing effect in the PVT cell.

REFERENCES

ALADKO, E.Y.; DYADIN, YU.A.; MANAKOV, A.YU.; ZHURKO, F.V.; LARIONOV, E.G. Phase Diagrams of the Ternary Gas Hydrate Forming Systems at High Pressures. Part 1. Propane–Methane–Water System. *Journal of Supramolecular Chemistry*, v. 2, p. 369-376, 2002.

CHA, M., HU, Y., SUM, A.K. Methane hydrate phase equilibrium for systems containing NaCl, KCl, and NH₄Cl. *Fluid Phase Equilibria*, v. 413, p. 2-9, 2016.

DALMAZZONE, D.; KHARRAT, M.; LACHET, V.; FOUCONNIER, B.; CLAUSSE, D. DSC and PVT measurements, *Journal of Thermal Analysis and Calorimetry*, v. 70 (2), p. 493-505, 2002.

GUPTA, A.; LACHANCE, J.; SLOAN, E.D.; KOH, C.A. Measurements of methane hydrate heat of dissociation using high pressure differential scanning calorimetry. *Chemical Engineering Science*, v. 63 (24), p. 5848-5853, 2008.

HU, Y.; LEE, B.R.; SUM, A.K. Insight into increased stability of methane hydrates at high pressure from phase equilibrium data and molecular structure. *Fluid Phase Equilibria*, v. 450, p. 24-29, 2017a.

HU, Y.; LEE, B.R.; SUM, A.K. Phase equilibrium data of methane hydrates in mixed brine solutions. *Journal of Natural Gas Science and Engineering*, v. 46, p. 750-755, 2017b.

KANG, S.P.; LEE, H.; RYU, B.J. Enthalpies of dissociation of clathrate hydrates of carbon dioxide, nitrogen, (carbon dioxide + nitrogen), and (carbon dioxide + nitrogen + tetrahydrofuran). *Journal of Chemical Thermodynamics*, v. 33, p. 513-521, 2001.

KLAPPROTH, A.; PILTZ, R.O.; KENNEDY, S.J.; KOZIELSKI, K.A. Kinetics of sII and Mixed sI/sII, Gas Hydrate Growth for a Methane/Propane Mixture Using Neutron Diffraction. *The Journal of Physical Chemistry C*, v. 123 (5), p. 2703-2715, 2019.

KUMAR, R.; LINGA, P.; MOUDRAKOVSKI, I.; RIPMEESTER, J. A.; ENGLEZOS, P. Structure and kinetics of gas hydrates from methane/ethane/propane mixtures relevant to the design of natural gas hydrate storage and transport facilities. *American Institute of Chemical Engineers Journal*, v. 54 (8), p. 2132-2144, 2008.

MASOUDI, R.; TOHIDI, B.; ANDERSON, R.; BURGASS, R.W.; YANG, J. Experimental measurement and thermodynamic modelling of clathrate hydrate equilibria and salt solubility in aqueous ethylene glycol and electrolyte solutions, *Fluid Phase Equilibria*, v. 219 (2), p. 157-163, 2004.

MCLEOD, H. O. J. AND CAMPBELL, J. M. Natural Gas Hydrates at Pressures to 10,000 psia. *Journal of Petroleum Technology*, v. 13, p. 590-594, 1961.

MENEZES, D.E.S.; SUM, A. K.; DESMEDT, A.; PESSOA FILHO, P. A.; ROBUSTILLO, M. D. Coexistence of sl and sII in methane-propane hydrate former systems at high pressures. *Chemical Engineering Science*, v. 208, article 115149, 2019.

MOHAMMADI, A.H.; ANDERSON, R.; TOHIDI, B. Carbon monoxide clathrate hydrates: equilibrium data and thermodynamic modeling, *American Institute of Chemical Engineers*, v. 51 (10), p. 2825-2833, 2005.

MOHAMMAD-TAHERI, M.; MOGHADDAM, A.Z.; NAZARI, K.; ZANJANI, N.G. The role of thermal path on the accuracy of gas hydrate phase equilibrium data using isochoric method, *Fluid Phase Equilibria*, v. 338, p. 257-264, 2013.

NIXDORF, J.; OELLRICH, L.R. Experimental determination of hydrate equilibrium conditions for pure gases, binary and ternary mixtures and natural gases. *Fluid Phase Equilibria*, v. 139 (1), p. 325-333, 1997.

PETUYA, C.; DAMAY, F.; DESPLANCHE, S.; AUPETIT, C.; DESMEDT, A. Ageing and Langmuir Behavior of the Cage Occupancy in the Nitrogen Gas Hydrate. *Crystals*, v. 8 (4), p. 145-158, 2018b.

PETUYA, C.; DAMAY, F.; DESPLANCHE, S.; TALAGA, D.; DESMEDT, A. Selective trapping of CO₂ gas and cage occupancy in CO₂-N₂ and CO₂-CO mixed gas hydrates. *Chemical Communications*, v. 54, p. 4290-4293, 2018a.

PETUYA, C.; DAMAY, F.; TALAGA, D.; DESMEDT, A. Guest Partitioning in Carbon Monoxide by Raman Spectroscopy. *The Journal of Physical Chemistry C*, v. 121, p. 13798-13802, 2017.

SCHICKS, J.M.; LUZI-HELBING, M. Cage occupancy and structural changes during hydrate formation from initial stages to resulting hydrate phase. *Spectrochimica Acta Part A: Molecular and Biomolecular Spectroscopy*, v. 115, p. 528-536, 2013.

SHIN, W.; PARK, S.; RO, H.; KOH, D.Y.; SEOL, J.; LEE, H. Spectroscopic confirmation of metastable structure formation occurring in natural gas hydrates. *Chemistry – An Asian Journal*, v. 7, p. 2235-2238, 2012.

SLOAN, E.D. Gas hydrates: review of physical/chemical properties. *Energy & Fuels*, v. 12, p. 191-196, 1998.

SLOAN, E.D.; KOH, C.A.; SUM, A.K. Gas hydrate stability and sampling: the future as related to the phase diagram. *Energies*, v. 3, p. 1991-2000, 2010.

UCHIDA, T.; MOORIWAKI, M.; TAKEYA, S.; IKEDA, I.Y.; OHMURA, R.; NAGAO, J.; MINAGAWA, H.; EBINUMA, T.; NARITA, H.; GOHARA, K.; MAE, S. Two-step formation of methane-propane mixed gas hydrates in a batched-type reactor. *American Institute of Chemical Engineers*, v. 50, p. 518-523, 2004.

WARD, Z.T.; MARRIOTT, R.A.; SUM, A.K.; SLOAN, E.D.; KOH, C.A. Equilibrium Data of Gas Hydrates containing Methane, Propane, and Hydrogen Sulfide. *Journal of Chemical & Engineering*, v.60 (2), p.424-428, 2015.

ZHANG, Y.; DEBENEDETTI, P.G.; PRUD'HOMME, R.K.; PETHICA, B.A. Differential Scanning Calorimetry Studies of Clathrate Hydrate Formation. *The Journal of Physical Chemistry B*, v. 108 (43), p. 16717-16722, 2004.

ZHU, J.; DU, S.; YU, X.; ZHANG, J.; XU, H.; VOGEL, S. C.; GERMANN, T. C.; FRANCISCO, J. S.; IZUMI, F.; MOMMA, K.; KAWAMURA, Y.; JIN, C.; ZHAO, Y. Encapsulation kinetics and dynamics of carbon monoxide in clathrate hydrate. *Nature Communications*, v. 5, 4128, 2014.

CHAPTER 7

STUDIES OF GAS HYDRATES BY RAMAN SPECTROSCOPY

ABSTRACT

Although the techniques applied in the previous chapters are useful to determine thermodynamic properties and equilibrium data, they do not provide intrinsic information about the gas hydrate structure formed. In this chapter, Raman spectroscopy is one of the most used techniques for structural analyses at real-time or time-independent measurements. The main method used was based on *ex situ* analyses in order to evaluate the composition of stable structures. Besides, two different methods based on *in situ* analyses were applied to visualize and evaluate the gas hydrate formation and growth processes. The results present Raman signatures for single methane and propane hydrates and for methane-propane hydrates. The predominance of structure II is observed for such double hydrates and the increase of methane content in the gas phase led to a higher occupation of large cavities by methane molecules. The real-time measurements indicate the prior formation of the small cavities and the progression of the cages occupancy according to the location in the aqueous phase and the time elapsed from the hydrate nucleation.

7.1 INTRODUCTION

Raman spectroscopy is a usual technique applied for hydrate characterization, that generates useful information on the structure, composition and cage occupancy (SCHICKS et al., 2005). The analyses can provide time-dependent or time-independent spectra depending on the methodology employed. Long (1994) firstly studied tetrahydrofuran (THF) clathrates through real-time Raman measurements. Sum et al. (1997) published time-independent Raman signatures for three structures (sI, sII and sH) of different gas hydrates by analyzing samples prepared *ex situ*. Subramanian and Sloan (1999) report methane hydrate spectra applying both time-independent and real-time measurements. Uchida et al. (1999) studied the hydration number for methane hydrates prepared *ex situ* by using Raman spectroscopy. Thenceforth, several groups have applied this technique to study the formation and dissociation of distinct phases of gas hydrates through *in situ* measurements (HESTER

et al., 2006; TANG et al., 2018; ZHONG et al., 2016), as well as to investigate time-independent signatures for several gas molecules trapped in hydrate cavities, the hydration number and the cages occupancy (BOURRY et al., 2009; CHAZALLON et al., 2017; KUMAR et al., 2019; QIN; KUHS, 2013; UCHIDA et al., 2007). Other groups have studied the effect of the equilibrium conditions, such as pressure and temperature, on hydrates structural features (MAGNOTTI et al., 2015; PETUYA et al., 2017; PETUYA et al, 2018). Thereby, this chapter presents three methods for the preparation of gas hydrates samples in order to analyze them by means of Raman measurements and includes results recently published (MENEZES et al., 2019).

7.2 SPECIFIC EXPERIMENTAL CONDITIONS

Details about Raman spectroscopy features applied in this work are described in section 2.4. Raman spectra were obtained through a HR Evo micro-spectrometer (Horiba Jobin Yvon, France), coupled to a confocal microscope allowing to reach micrometric spatial resolution. *Ex situ* analyses were performed on previously prepared methane and methane-propane samples for studying their structural composition. On the other hand, *in situ* measurements were performed on samples of methane hydrate in order to study the structural changes throughout the formation process.

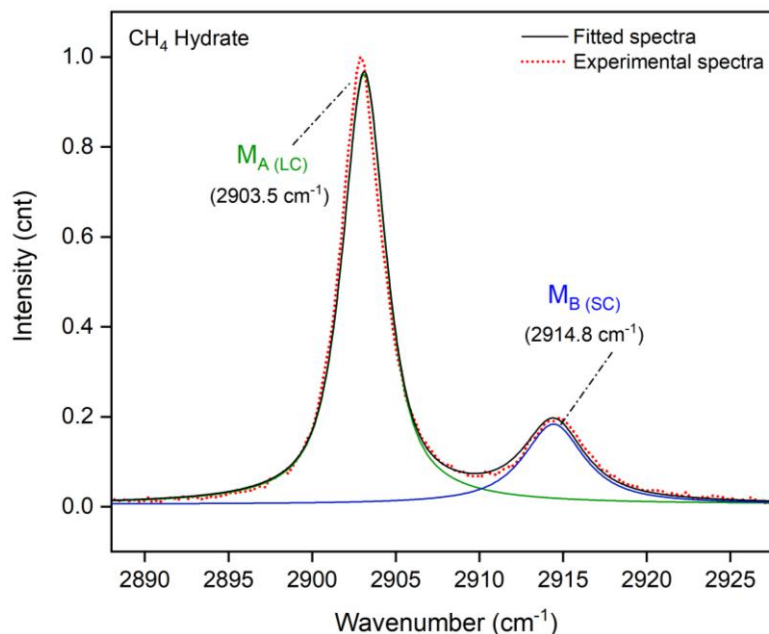
7.3 EX SITU ANALYSES

Among the methods employed in this work, the analysis of the hydrate prepared *ex situ* is the most indicated for the preparation of gas hydrates when it is desired to obtain the Raman spectra of stable structures. This is because the samples are prepared from ice powder, which favors the ice conversion to hydrate due to higher diffusivity of gas molecules through the ice crystalline lattice. In addition, different samples can be prepared previously by this method and analyzed one at a time according to the availability of the spectrometer, considering that the complete conversion to a stable structure may last for a few days. Therefore, Raman spectra for methane and methane-propane hydrates prepared *ex situ* are presented in this section.

7.3.1 Methane Hydrate

Figure 7.1 presents the deconvolution of the peaks concerning to the methane hydrate sample prepared *ex situ* at 10 MPa. The vibrational band for methane hydrate is composed of two peaks related to the incorporation of CH₄ in large cavities (M_A , 2903.5 cm⁻¹) and small cavities (M_B , 2914.8 cm⁻¹) of sI. Sum et al. (1997) reported similar wavenumbers for large and small cages of methane hydrate: 2905 and 2915 cm⁻¹, respectively. The group also mentioned that the intensities of these bands agree to the density of cavities per unit cell of sI (two small and six large cavities). Thereby, the larger band at lower frequency was assigned to methane molecules inserted in large cavities ($M_{A(SC)}$), while the smaller band was related to the same molecules trapped in small cavities ($M_{B(LC)}$). In this work, the ratio between large and small bands is also very similar to the proportion between large and small cavities in the unit cell of sI (~3.5).

Figure 7.1 - Deconvolution of the peaks related to the CH₄ molecules hosted in large and small cavities of structure I.

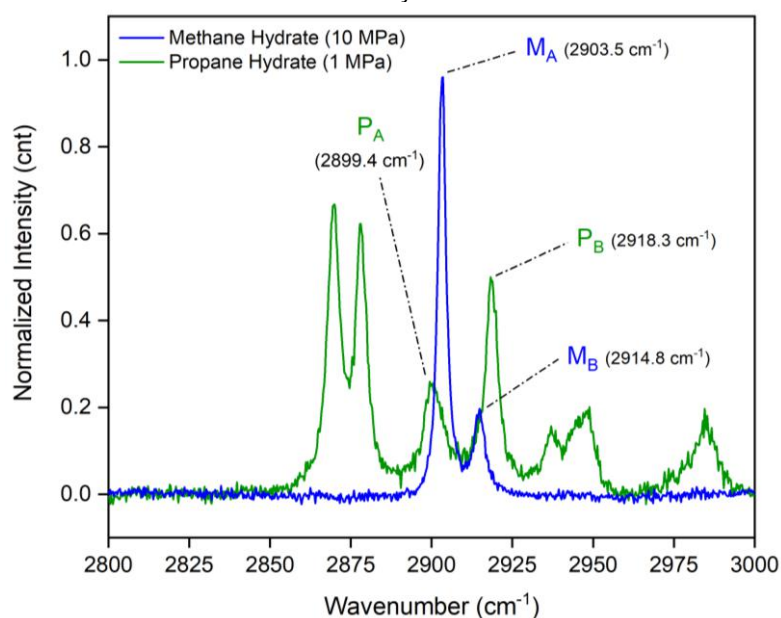


7.3.2 Methane-propane Hydrates

As mentioned throughout this work, gas composition plays an important role on the structural properties of gas hydrates. In the previous chapter, CH₄-C₃H₈ hydrates were studied at three different compositions by both PVT-isochoric method and

microcalorimetry. The results obtained by the first indicate that sI is favored by increasing the methane content in the gas phase, while the calorimetric thermograms, in turn, indicate that sII is favored. It is important to remind that the system in the first method is maintained under mixing conditions, unlikely in the microcalorimetric cells. It has shown in earlier chapters that lack of mixing can increase the hydrate phase heterogeneity, especially in the case of double guest systems. Thus, in order to complement the results obtained by microcalorimetry and PVT-isochoric method, a similar study was carried out by Raman spectroscopy analyses, in which methane-propane hydrates were prepared *ex situ* by applying three gas mixtures with different compositions. The characteristic peaks from Raman spectroscopy for the single-guest gas hydrates are indicated in Figure 7.2. They were used as Raman signatures for single hydrates to further compare the structures of the double-hydrate samples.

Figure 7.2 – Raman spectra of single CH₄ and C₃H₈ hydrates: assigned peaks for characterization of double hydrates.



Source: Menezes et al. (2019)

Among the various CH₃ and CH₂ stretching and bending modes of the propane molecules trapped in the sII cavities, the ones observed at 2899.4 cm⁻¹ (*P_A*) and 2918.3 cm⁻¹ (*P_B*) are remarkable bands for investigating the mixed gas hydrate. Raman spectra were then obtained for the three methane-propane hydrates prepared at 68.7, 79.8 and 95 mol% CH₄ in the gas phase. The spectra for methane-propane hydrates are shown in Figure 7.3. The bands for methane and propane molecules indicated in Figure 7.2 can be obtained separately by decomposing the spectra, thanks to the high

spectral resolution (of the order of 1 cm^{-1}). For this, four pseudo-Voigt peaks were fitted to the experimental spectra in order to obtain the partial contributions and to measure the peak intensities. Figure 7.4 shows the deconvolution of the peaks concerning to the hydrate prepared with 79.8 mol% CH_4 , indicating an excellent agreement between the fitted spectra and the experimental one.

Figure 7.3 – Raman spectra of CH_4 - C_3H_8 hydrate samples prepared under different gas compositions.

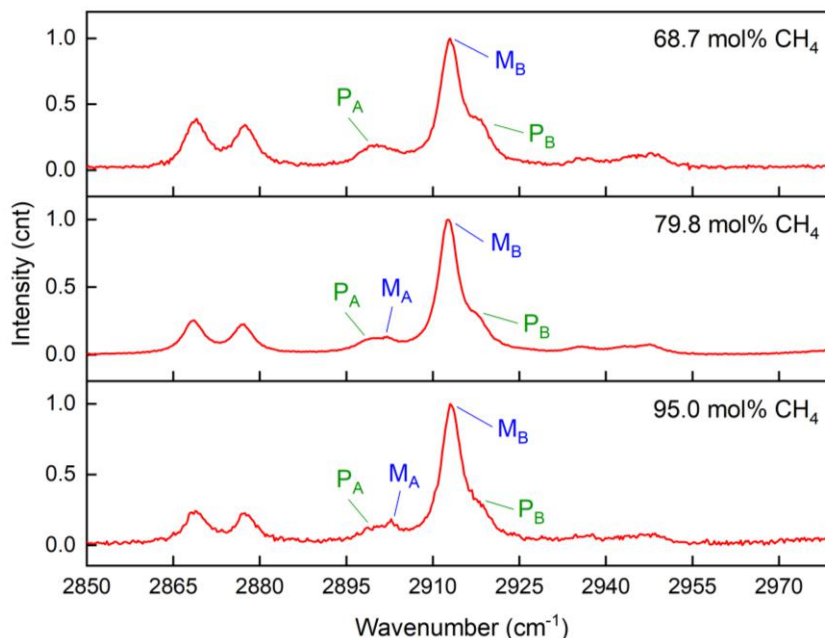


Figure 7.4 – Deconvolution of the peaks from the CH_4 - C_3H_8 hydrate (79.8 mol% CH_4 in gas phase) formed at 8.7 MPa.

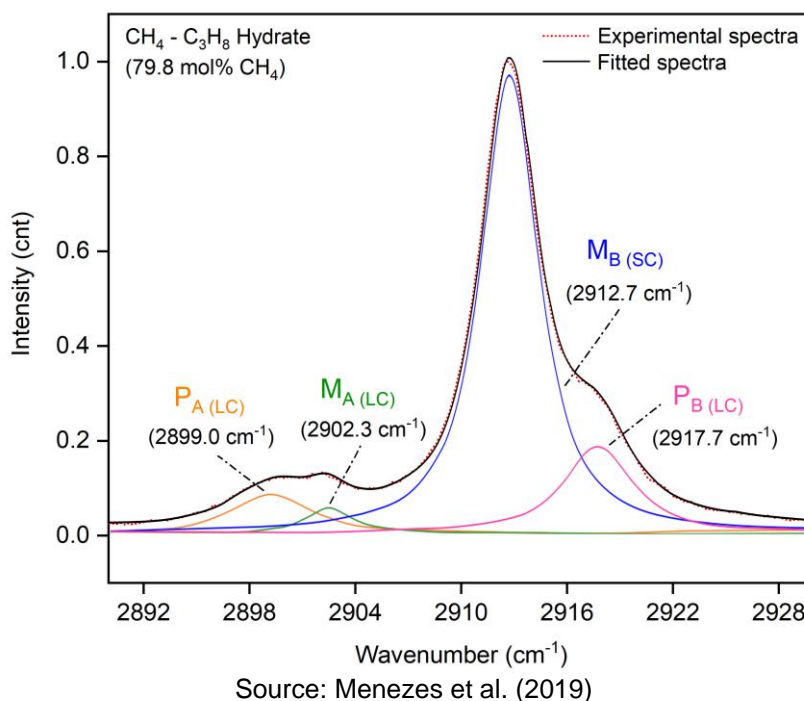
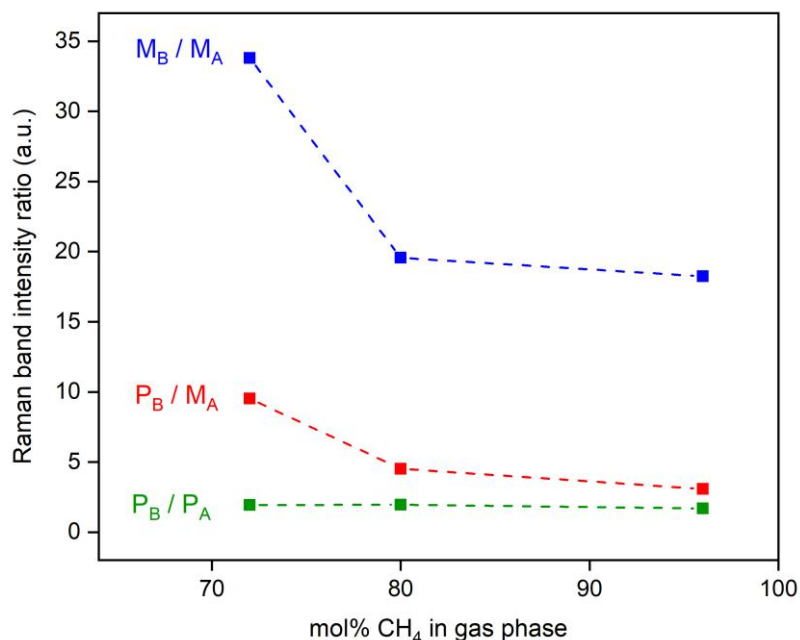


Figure 7.5 shows some intensity ratios (P_B/P_A , M_B/M_A and P_B/M_A) for the three samples of CH₄-C₃H₈ hydrates so that sI and sII can be studied according to the gas composition. The intensity ratios P_B/P_A are similar for all compositions, including for the single propane hydrate (~2.1), which is expected since both peaks concern to the propane encapsulated in large cavities of sII. Although it is not possible to conclude that sI coexists with sII only by analyzing these bands, since the signatures for methane encaged in sI and sII are very similar (SUM et al., 1997), the hydrate is inferred to be constituted mostly by sII. This assumption is supported by the considerable high methane content in small cages indicated by M_B/M_A , considering that the proportion LC : SC for the single methane hydrate (sI) is about 0.3. Therefore, much more large cavities are hosting methane molecules than allowed by sI. The predominance of sII, which presents a higher density of small cavities per unit cell, may explain the elevated ratios M_B/M_A obtained in these double-guest hydrates. However, M_B/M_A and P_B/M_A decrease substantially by increasing the methane fraction in the gas phase, indicating that a greater part of methane molecules ends up to be hosted in large cavities (either from sI or sII). This can be observed visually in Figure 7.3, in which M_A becomes evident as methane content increases. This could be due to either an increase in the fraction of structure I, which contains two small and six large cavities per unit cell, or because methane partially occupied large cavities of sII in place of propane molecules.

Figure 7.5 – Ratios between intensities of Raman bands corresponding to propane (P_A and P_B) and methane (M_A and M_B) in CH₄-C₃H₈ hydrates with different gas compositions.



Source: Menezes et al. (2019)

7.4 IN SITU ANALYSES

In situ analyses performed by using capillary or cylindrical cells were performed by Raman spectroscopy in order to evaluate the compositional evolution of the structures according to the gas hydrate formation. Considering that the complete hydrate conversion can last for a couple of days, these techniques are not the most suitable for the characterization of stable structures. Such analyses depend on the availability of the spectrometer and demand a larger amount of liquid nitrogen for maintaining the system at low temperature. Besides, the hydrate may not be as homogeneous as the ones prepared from ice powders (*ex situ*) due to the diffusivity limitations. Therefore, only the initial stages of methane hydrate formation and growth are presented in this section.

7.4.1 Capillary Cell

The capillary cell allows monitoring the hydrate growth in an axial perspective. The hydrate crystals grow from the meniscus towards the aqueous phase, as shown in Figure 7.6. On the side of the gas phase, some crystals can be noted along the inner walls due to moisture in the cell.

Figure 7.6 – Gas hydrate growth towards the aqueous phase in capillary cell visualized through the microscope coupled to the Raman spectrometer. Time elapsed after the first visually observed hydrate crystals: A) 2 min; B) 2min 17s; C) 3min 5s.

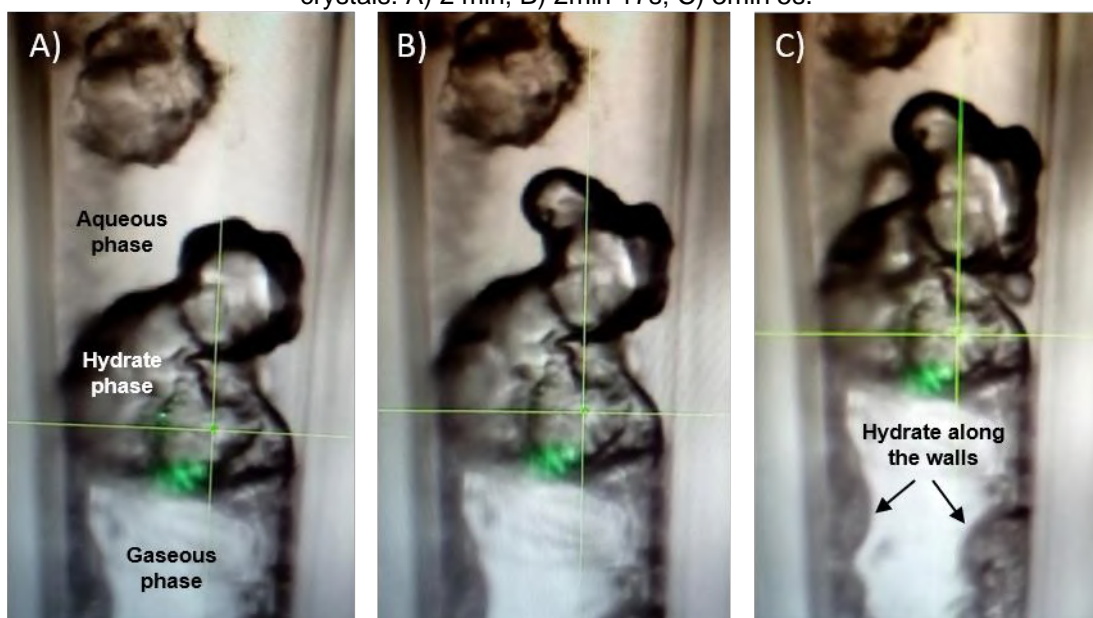
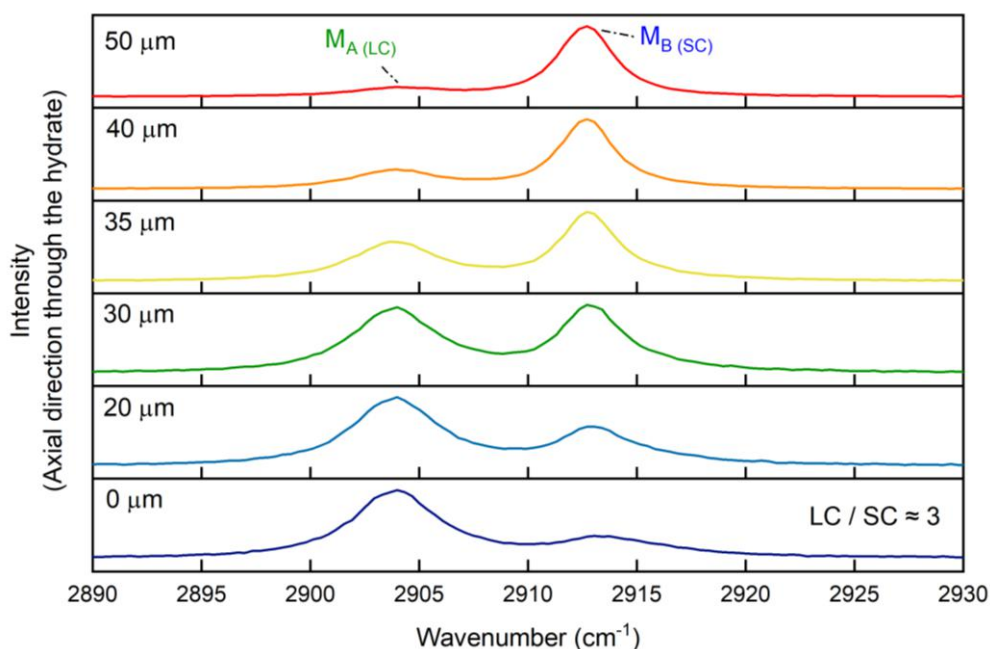


Figure 7.7 presents the Raman spectra for the solid phase at different axial positions. One can verify both peaks corresponding to methane molecules in large and small cages of sl. However, the intensity corresponding to small cages increases as the green laser of the Raman spectrometer is moved towards the aqueous phase. This is an evidence that, in fact, small cavities occupied by methane present a higher kinetic of formation than the large ones (SCHICKS; LUZI-HELBING, 2013; SUBRAMANIAN; SLOAN, 1999). It is reasonable to say that the hydrate crystals close to the meniscus present a more stable configuration since both large and small cages in this region are firstly formed and occupied by methane molecules. Thereby, the proportion between the cavities at the point established as 0 μm is close to 3 and agree to the density of cavities per unit cell of sl, as mentioned before. On the other hand, the growth of crystals at upper positions depends on the methane molecules diffusion on the aqueous phase and thus still do not present a stable configuration at the time of the Raman analysis.

Figure 7.7 – Raman spectra of CH_4 hydrate (20 MPa) at different axial positions in the capillary cell.



7.4.2 Cylindrical Cell

The second method applied for hydrate analysis *in situ* is based on a cylindrical cell equipped with an optical visor. In this case, since the volume of the sample is considerably larger than in the capillary cell, the temperature is decreased below the

melting point of ice in order to favor the nucleation and crystals growth. It makes possible the formation of ice along with the gas hydrate, implying a more heterogeneous solid phase. Images that compose Figure 7.8 show the evolution of the solid phase over time. The first visible clue to the crystallization process can be seen in the second image (19 min), in which droplets of water crystallize on the walls of the cell. From 35 min onwards, one can note that the aqueous phase becomes turbid, indicating the formation of small crystals. Hydrate growth within the aqueous phase is observed only in the last image since the process is limited by the diffusion of the methane molecules and can take several hours to complete the hydrate crystallization process.

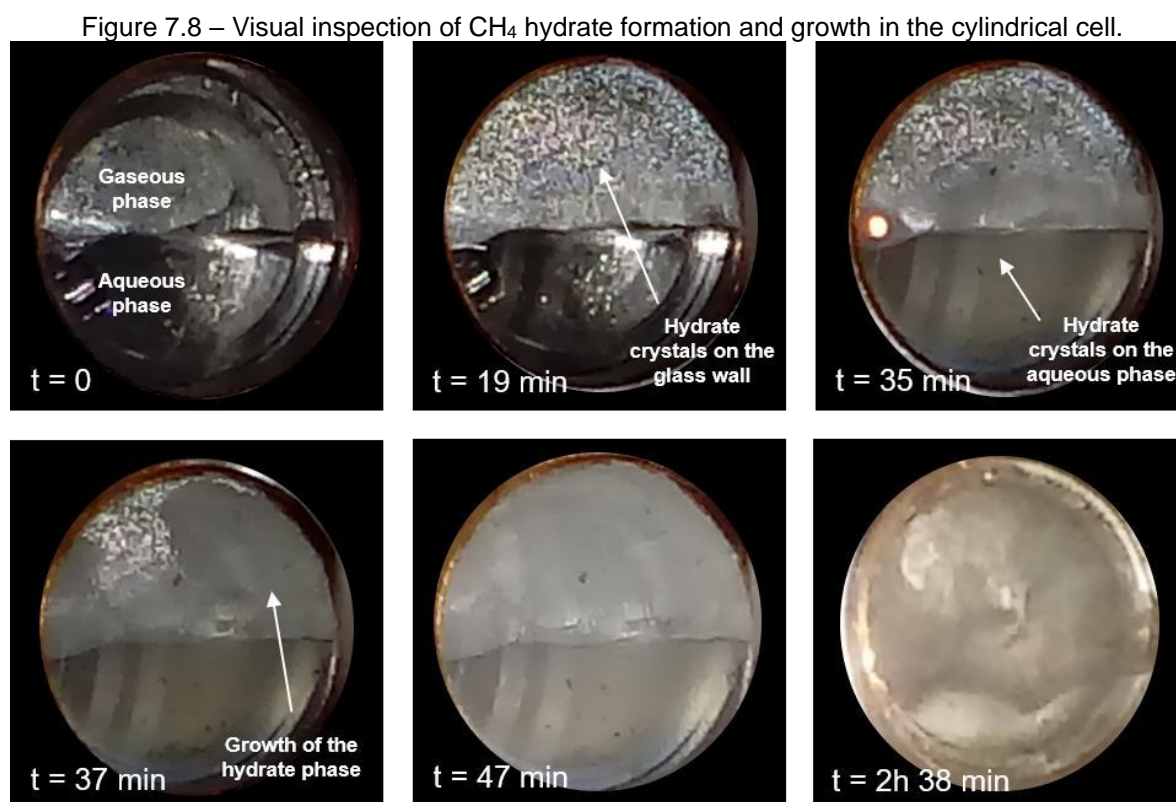
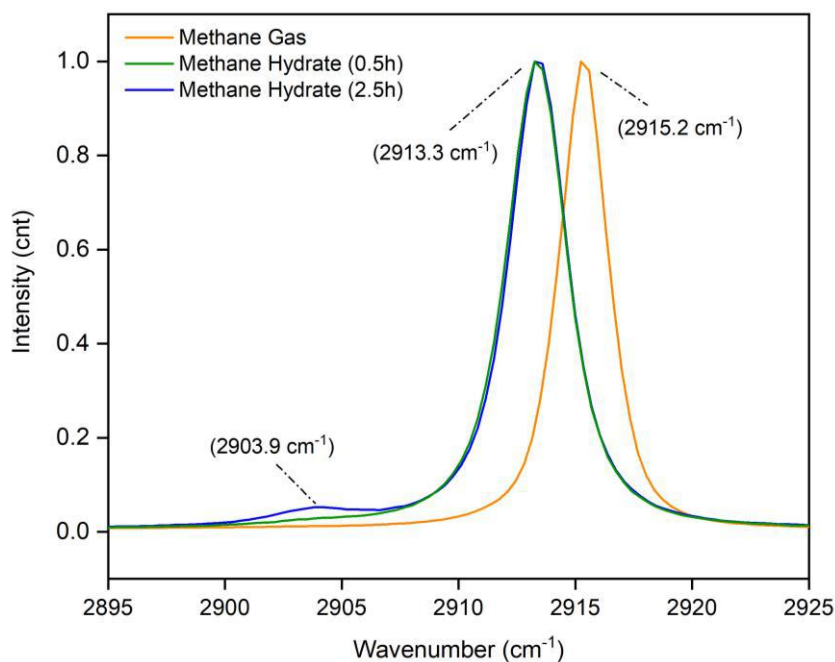


Figure 7.9 shows the peaks concerned to CH₄ molecules trapped inside large (2903.9 cm⁻¹) and small cavities (2913.3 cm⁻¹) of sl, obtained by applying this method. The peak at 2903.9 cm⁻¹ increases slowly over time and it is again evidence for the prior formation of small cavities, confirming the results observed in the capillary cell.

Figure 7.9 – Raman spectra of CH₄ hydrate in the cylindrical cell at 16.4 MPa.

Nevertheless, it is worth to mention that Schicks and Ripmeester (2004) reported a similar behavior for methane hydrates monitored *in situ* by Raman spectroscopy and assumed that this phenomenon is related to a prior formation of a metastable structure (sII). According to the authors, the change in peak intensities indicates the transition from sII to sI, a thermodynamically more stable configuration, thereby, the ratio of large to small cages shown in their spectra changes from about 1:2 to 3:1. However, the spectra showed in Figures 7.7 and 7.9 do not indicate an initial rate even close to 1:2. Therefore, it is supported in this work that the phenomena observed in both cases above have to do with the cages occupancy, considering that the occupation of large cavities is the rate-limiting factor for the formation of sI, as reassessed by Shicks and Luzi-Helbing (2013) in a more recent work.

Finally, the peak observed at 2915.2 cm⁻¹ in Figure 7.9 refers to the methane in the gas phase. Methane molecules hosted in small cavities are reported at slightly lower frequencies than free methane molecules in gas phase (SUM et al., 1997). Therefore, checking this peak is important to ensure that the peak at 2913.3 cm⁻¹ indeed is related to methane in the hydrate phase and not in the gas phase.

7.5 CONCLUSIONS

This chapter presents some Raman spectra for gas hydrates based on the main methods used for structural studies of these compounds. The most remarkable points are presented below:

- *Ex situ* analyses are more suitable for characterization of hydrate stable structures than *in situ* analyses. Once samples are based on ice powder, the diffusivity of gas molecules through the water-bonded lattice is favored, implying in a faster conversion to hydrate and a more homogeneous solid phase. Methane hydrate and methane-propane hydrates were characterized through this method;
- The results for methane hydrate agree to the literature data whereas the ones for methane-propane hydrates reveals the complexity of determining their structural composition and the cages occupancy;
- Despite the difficulties faced due to overlapping peaks, it is stated that sII is predominant in the three methane-propane hydrates evaluated, prepared from different gas phase compositions;
- The increase of the methane content in CH₄-C₃H₈ systems led to a higher occupation of large cavities by methane molecules, either due to the formation of a larger fraction of structure I or because methane molecules were hosted on large cavities of sII;
- *In situ* analyses are interesting for studying the hydrate formation and crystal growth process. The initial stage of methane hydrate formation was studied by two different methods based on a capillary and a cylindrical cell. The results evidence the prior formation of the small cavities and the progression of the cages occupancy towards the aqueous phase;
- Finally, this chapter is of relevant importance not only for the new perspectives provided by the results but also for describing in detail the most applied methods in the study of gas hydrates through Raman spectroscopy.

REFERENCES

BOURRY, C.; CHAZALLON, B.; CHARLOU, J.L.; DONVAL, J.P.; RUFFINE, L.; HENRY, P.; GELI, L.; ÇAGATAY, M.N.; İNAN, S.; MOREAU, M. Free gas and gas

hydrates from the Sea of Marmara, Turkey: Chemical and structural characterization. *Chemical Geology*, v. 264, p. 197-206, 2009.

CHAZALLON, B.; NOBLE, J.; DESMEDT, A. Spectroscopy of Gas Hydrates: From Fundamental Aspects to Chemical Engineering, Geophysical and Astrophysical Applications. In *Gas Hydrates 1: Fundamentals, Characterization and Modeling*, Wiley-ISTE: London, p. 63-112, 2017.

HESTER, K.C.; WHITE, S.N.; PELTZER, E.T.; BREWER, P.G.; SLOAN, E.D. Raman spectroscopic measurements of synthetic gas hydrates in the ocean. *Marine Chemistry*, v. 98, p. 304-314, 2006.

KUMAR, A.; KUMAR, R.; LINGA, P. Sodium Dodecyl Sulfate Preferentially Promotes Enclathration of Methane in Mixed Methane-Tetrahydrofuran Hydrates. *iScience*, v. 14, p.136-146, 2019.

LONG, X.P. Master Thesis T-4458, Colorado School of Mines, 1994.

MAGNOTTI, G.; KC, U.; VARGHESE, P.L.; BARLOW, R.S. Raman spectra of methane, ethylene, ethane, dimethyl ether, formaldehyde and propane for combustion applications. *Journal of Quantitative Spectroscopy and Radiative Transfer*, v. 163, p. 80-101, 2015.

MENEZES, D.E.S.; SUM, A. K.; DESMEDT, A.; PESSOA FILHO, P. A.; ROBUSTILLO FUENTES, M. D. Coexistence of sl and sII in methane-propane hydrate former systems at high pressures. *Chemical Engineering Science*, v. 208, article 115149, 2019.

PETUYA, C.; DAMAY, F.; CHAZALLON, B.; BRUNEEL, J.-L.; DESMEDT, A. Guest Partitioning and Metastability of the Nitrogen Gas Hydrate. *The Journal of Physical Chemistry C*, v. 122, p. 566-573, 2018.

PETUYA, C.; DAMAY, F.; TALAGA, D.; DESMEDT, A. Guest Partitioning in Carbon Monoxide by Raman Spectroscopy. *The Journal of Physical Chemistry C*, v. 121, p. 13798-13802, 2017.

QIN, J.; KUHS, W.F. Quantitative analysis of gas hydrates using raman spectroscopy. *American Institute of Chemical Engineers Journal*, v. 59, p. 2155-2167, 2013.

SCHICKS, J.M.; LUZI-HELBING, M. Cage occupancy and structural changes during hydrate formation from initial stages to resulting hydrate phase. *Spectrochimica Acta Part A: Molecular and Biomolecular Spectroscopy*, v. 115, p. 528-536, 2013.

SCHICKS, J.M.; RIPMEESTER, J.A. The Coexistence of Two Different Methane Hydrate Phases under Moderate Pressure and Temperature Conditions: Kinetic versus Thermodynamic Products. *Angewandte Chemie International Edition*, v. 43, p. 3310-3313, 2004.

SCHICKSA, J.M.; ERZINGERA, J.; ZIEMANN, M.A. Raman spectra of gas hydrates-differences and analogies to ice 1h and (gas saturated) water. *Spectrochimica Acta Part A*, v. 61, p. 2399–2403, 2005.

SUBRAMANIAN, S.; SLOAN, E.D. Molecular measurements of methane hydrate formation. *Fluid Phase Equilibria*, v. 158–160, p. 813–820, 1999.

SUM, A.K.; BURRUSS, R.C.; SLOAN, E.D. Measurement of Clathrate Hydrates via Raman Spectroscopy. *The Journal of Physical Chemistry B*, v. 101 (38), p. 7371-7377, 1997.

TANG, C.; ZHOU, X.; LI, D.; ZHAO, X.; LIANG, D. In situ Raman investigation on mixed CH₄-C₃H₈ hydrate dissociation in the presence of polyvinylpyrrolidone. *Fuel*, v. 214, p. 505-511, 2018.

UCHIDA, T.; HIRANO, T.; EBINUMA, T.; NARITA, H.; GOHARA, K.; MAE, S.; MATSUMOTO, R. Raman Spectroscopic Determination of Hydration Number of Methane Hydrates. *American Institute of Chemical Engineers Journal*, v. 45, p. 2641-2645, 1999.

UCHIDA, T.; TAKEYA, S.; KAMATA, Y.; OHMURA, R.; NARITA, H. Spectroscopic Measurements on Binary, Ternary, and Quaternary Mixed-Gas Molecules in Clathrate Structures. *Industrial and Engineering Chemistry Research*, v. 47, p. 5080-5087, 2007.

ZHONG, J.-R.; ZENG, X.-Y.; ZHOU, F.-H.; RAN, Q.-D.; SUN, C.-Y.; ZHONG, R.-Q.; YANG, L.-Y.; CHEN, G.-J.; KOH, C.A. Self-preservation and structural transition of gas hydrates during dissociation below the ice point: an in situ study using Raman spectroscopy. *Scientific Reports*, v. 6, 38855, 2016.

CHAPTER 8

USE OF 1-BUTYL-3-METHYLIMIDAZOLIUM-BASED IONIC LIQUIDS AS HYDRATE INHIBITORS AT HIGH PRESSURE CONDITIONS

ABSTRACT

Ionic liquids (ILs) are fluids constituted by ions that present peculiar features as solvents. Among many other applications, these materials have been studied as innovative and promising compounds for the prevention of hydrate formation in oil and gas flowlines. The performance of 1-Butyl-3-methylimidazolium chloride ([BMIM][Cl]) and 1-Butyl-3-methylimidazolium bromide ([BMIM][Br]) as methane hydrate inhibitors is evaluated in this chapter at pressures from 9.8 to 100 MPa by high-pressure microcalorimetry. New hydrate dissociation data were obtained for aqueous systems containing 1, 5, 10 and 15 % molar fractions of inhibitors. The inhibitory effect is clearly better as the concentration of the IL in aqueous solution increases and tends to be slightly enhanced at higher pressures. Previous studies in literature indicate that these ionic liquids act simultaneously as thermodynamic and kinetic inhibitors (dual function inhibitors) for pressures up to 20 MPa and concentrations of 10 wt% (approximately 1% molar). In this chapter, it is shown that [BMIM][Cl] and [BMIM][Br] also work as thermodynamic inhibitors even at higher pressures, but they surprisingly act as hydrate growth promoters at concentrations of 1% and 5% molar. Phase equilibrium curves are also presented to evaluate the effectiveness of these ionic liquids as thermodynamic inhibitors at high pressures and to compare experimentally their efficiency to methanol, a commercial inhibitor commonly applied in oil and gas exploitations. [BMIM][Cl] showed to be a more efficient inhibitor than [BMIM][Br] and methanol, considering equimolar aqueous solutions, even though methanol is more effective for solutions with the same mass fraction. The results are also compared to predictions from Multiflash software by applying NaCl and NaBr as gas hydrate inhibitors.

8.1 INTRODUCTION

As mentioned throughout this work, gas hydrates form at high pressure and low temperature, which are typical conditions of the subsea surface. In this context, thermodynamic and kinetic studies related to the formation and dissociation of gas

hydrates play an important role in determining proper conditions to extract oil in offshore wells, since hydrates can obstruct oil and gas flowlines during these operations (SLOAN; KOH, 2008). Different techniques are used to avoid blocking flowlines in these regions (KINNARI et al. 2015). The most effective ones involve the addition of substances that act as hydrate inhibitors. These additives are usually classified as thermodynamic and kinetic inhibitors. Thermodynamic inhibitors, such as salts, methanol or ethylene glycol, are substances that move the hydrate-liquid-vapor equilibrium (HLVE) curve to lower temperatures and higher pressures. Large amounts of these inhibitors may be required when working in deeper water conditions, sometimes making this choice uneconomical (HAGHIGHI et al., 2009; HU et al, 2017; MOHAMMADI; RICHON, 2010). Thus, the oil and gas industry has started developing low-dosage hydrate inhibitors (LDHIs), such as kinetic inhibitors (KHIs) and anti-agglomerants (AAs). Kinetic hydrate inhibitors (KHIs) retard hydrate formation: if the residence time of the fluid is shorter than that required for the hydrate nucleation and growth, the blockage is avoided (KELLAND, 2006; KOH et al., 2002; TARIQ et al., 2014). Anti-agglomerants (AAs) allow hydrate formation but prevent particle agglomeration (KIM et al., 2011).

Ionic Liquids (ILs) are salt-like substances with melting temperatures below 373 K. These substances present properties such as good stability and low volatility and are used as green solvents (ANGELL et al., 2007). They have recently been considered as promising hydrate inhibitors. The great advantage of using ILs as gas hydrates inhibitors is that they may act as both thermodynamic and kinetic inhibitors, therefore being more efficient than inhibitors currently used in oil industry (QURESHI et al., 2016; RICHARD; ADIDHARMA, 2013; TARIQ et al.; 2016). Xiao and Adidharma (2009) proposed that this dual function is related to the strong electrostatic charge and to the hydrogen bond interactions with water. These properties affect the equilibrium curve (HLV), shrinking the risk zone for hydrate formation and slowing hydrate nucleation/growth rates. Some imidazolium-based ILs were studied by Sabil et al. (2015) as methane hydrate inhibitors, for pressures from 3.6 to 11.2 MPa. These results showed the effectiveness of nine ILs at 10 wt% in shifting the equilibrium curve toward low dissociation temperatures and highlight the promising role that ionic liquids may play as hydrate inhibitors.

This chapter is based on a recent work published by Menezes et al. (2020) and presents new equilibrium data for methane hydrates at pressures up to 100 MPa using

two ionic liquids as inhibitors: 1-butyl-3-methylimidazolium chloride [BMIM][Cl] and 1-butyl-3-methylimidazolium bromide [BMIM][Br]. Inhibitors performance at high pressures and different concentrations is also evaluated. These compounds were previously studied by Xiao et al. (2010) at pressures up to 20 MPa. They showed a good performance as both thermodynamic and kinetic inhibitors for a composition of 10 wt.%. In this work, thermograms of the methane-water system are compared to those containing either an ionic liquid or methanol, a commonly used hydrate thermodynamic inhibitor. Most of the works found in literature regarding hydrate inhibitors present the results in weight concentration (wt%). This is important to evaluate the proper amount of inhibitor, since large amounts cause storage, handling and separation problems in offshore environments. However, this work also considers molar concentrations to indicate the chemical efficiency of both ILs studied. Experimental results are also compared with literature data (at lower pressures) and thermodynamic models.

8.2 SPECIFIC EXPERIMENTAL CONDITIONS

Methane gas (99.5%) was provided by White Martins and employed for pressurization and hydrate formation in all experiments. The ionic liquids chosen to be studied as promising hydrate inhibitors were 1-butyl-3-methylimidazolium bromide (97%) and 1-butyl-3-methylimidazolium chloride (99%). Both ionic liquids and methanol (99.8%) were provided by Sigma Aldrich. Milli-Q water was used in all experiments.

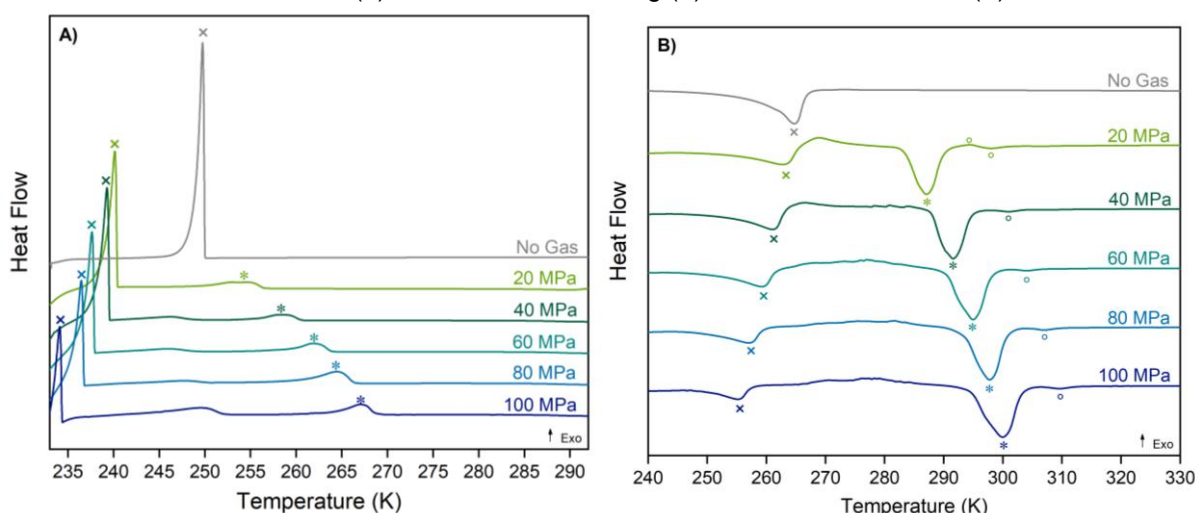
The thermal procedure applied on the microcalorimeter oven is the same as that mentioned on chapter 2 of this work (see Figure 2.6). In all cases, the reference cell was kept empty and the sample cell was pressurized with methane, after addition of the aqueous solution (~35 mg). The experiments were planned to evaluate and compare ionic liquid efficiency by determining hydrate dissociation temperatures at constant pressure. Data were obtained for samples with water (no inhibitor) and those containing ILs ([BMIM][Br], [BMIM][Cl]), or methanol (CH₃OH). The efficiency of each ionic liquid was studied considering different molar fractions (5.0%, 10.0%, and 15.0%). Although chemical efficiency is based on molar amounts, the inhibition effectiveness should also be assessed in terms of mass fractions, since the volume of inhibitor to be stored is a severe restriction in offshore platforms. Thereby, three further

experiments were performed considering the same mass fraction (~10 wt%) of each inhibitor.

8.3 EFFECT OF PRESSURE ON THE FORMATION AND DISSOCIATION OF SOLID PHASES

Crystallization and dissociation peaks are pointed out in Figure 8.1 for systems containing 5.0 mol% of [BMIM][Br], for both cooling (A) and heating (B) processes.

Figure 8.1 – Cooling (A) and heating (B) thermograms of hydrate-forming systems composed of 5 mol% [BMIM][Br] at different pressures. The indicated transitions correspond to hydrate crystallization / dissociation (*), ice formation / melting (x) and Teflon transitions (o).



Source: Menezes et al. (2020)

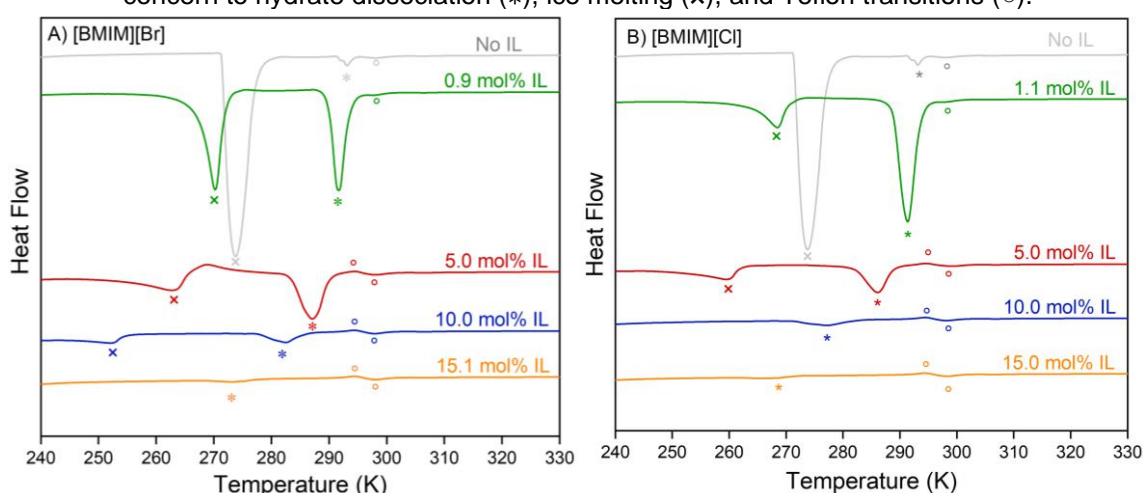
As observed for non-inhibited systems, the increase in pressure shifts the hydrate thermodynamic equilibrium to higher crystallization and dissociation temperatures. The ice melting point presents an anomalous behavior due to a crystalline rearrangement, as discussed in section 4.3.1. Because of that, the crystallization and melting points of ice in this region decrease as the pressure increases.

8.4 EFFECT OF IONIC LIQUID CONTENT IN GAS HYDRATES FORMATION

Thermodynamic inhibitors act by reducing the amount of water molecules available to form the hydrate structures by binding to them through hydrogen bonds. Thus, large amounts are required for hydrate inhibition. On the other hand, kinetic inhibitors prevent hydrate nucleation and are needed in smaller amounts. In this work, relatively high molar concentrations are also studied for the ionic liquids based on

[BMIM][Br] and [BMIM][Cl] to evaluate the behavior of these compounds in a more comprehensive concentration range. In the thermograms shown in Figure 8.2, all the IL concentrations shifted the hydrate dissociation curve to lower temperatures, confirming their efficiency as thermodynamic inhibitors (TARIQ et al., 2014). The figure also shows that the ice formation and melting peaks either diminished or are not observed at higher concentrations of ionic liquid for the temperature range analyzed.

Figure 8.2 – Effect of ionic liquid concentration on CH₄ hydrate formation and dissociation (20 MPa): A) Ionic liquid based on [BMIM][Br] B) Ionic liquid based on [BMIM][Cl]. The indicated transitions concern to hydrate dissociation (*), ice melting (x), and Teflon transitions (o).



Source: Menezes et al. (2020)

Xiao et al. (2010) studied the kinetic inhibition induced by the same ILs up to 20 MPa. According to their results, the induction time for methane hydrate nucleation at 261 K and 11.4 MPa was about 1.5 and 2.1 hours later when adding 1 mol% [BMIM][Cl] and [BMIM][Br], respectively. However, the integration of the areas corresponding to dissociation curves in Figure 8.2 reveals that the amount of hydrate formed is significantly greater at 1.0 mol% and 5.0 mol% for both ILs. This fact suggests that these compounds promote hydrate growth at low fractions, even though they act as thermodynamic inhibitors simultaneously.

In fact, the same compound may act as both hydrate kinetic promoter and thermodynamic inhibitor at low concentrations, as discussed in previous works involving the following inhibitors: methanol for carbon dioxide and methane hydrates (BOBEV; TAIT, 2004; KE et al., 2013); monoethylene glycol for natural gas hydrate (CHA et al., 2013); salt solutions for methane-propane and tetrahydrofuran hydrates (SOWA et al., 2014; SOWA et al., 2015); and ionic liquid 1-hydroxyethyl-1-methylmorpholinium for methane hydrate (LEE et al., 2016). According to Amtawong

et al. (2016), low dosages of methanol enhance propane hydrate formation substantially, increasing the maximum uptake and conversion rates and decreasing the initial pressure required to initiate the reaction. McLaurin et al. (2014) observed the acceleration of methane uptake to form hydrate from powdered frozen solutions at 253 K (initially at 12.5 MPa), containing methanol at concentrations within 0.6 to 10 wt%.

On the other hand, the area of hydrate dissociation curves decreases as the IL concentration further increases. These curves are barely observed at 15.0 mol%, and the intensities are as low as those of the Teflon transition phenomenon. Indeed, the performance of ionic liquids as dual function inhibitors (kinetic and thermodynamic) is observable at high concentrations of IL. The hydrate equilibrium is shifted to lower temperatures, diminishing substantially the amount of hydrate formed. Sowa et al. (2014) suggest that the thermodynamic inhibition effect is likely to be dominant and masks the kinetic promotion effect when the inhibitor is present at high concentrations. These results highlight the complexity of the action of ionic liquids: it depends on the design of the molecules (the type of cation and anion) and the concentration of IL in aqueous solution.

Although ionic liquids have been studied as hydrate inhibitors by many researchers, their kinetic promotion effect and the mechanisms involved in nucleation and growth of hydrates are barely addressed. Zare et al. (2015) evaluated the use of some imidazolium-based ionic liquids and indicated some of them as hydrate promoters since they decrease the induction time and accelerate gas-consumption during hydrate growth. They explained the phenomenon considering the similarity between imidazolium based ILs and cationic surfactants, both capable of forming micelles in aqueous solutions (BLESIC et al., 2007; DUPONT, 2004). The presence of surfactants reduces the surface tension, thus favoring the gas solubilization and providing better conditions for hydrate nucleation and growth (CHEN et al., 2008; DI PROFIO et al., 2005; SHEN et al., 2016). Kumar et al. (2015) conducted a comprehensive literature review of the role of surfactants in the formation and dissociation studies of clathrate hydrates. The anionic surfactant sodium dodecyl sulfate (SDS) is the most efficient hydrate promoter. Zhong et al. (2000) stated that the use of SDS to form ethane and natural gas hydrates reduces the induction time, resulting in a high rate of formation without the need for agitation. These authors also verified the reproducibility of the induction time in the presence of surfactant, which contrasts with the non-surfactant randomness. According to them, it may be due to the

spatial uniformity of micellar nuclei, which may act as carriers of ethane molecules to the bulk of the aqueous phase, favoring the formation of the hydrate. However, some works pointed out that the presence of micelles is not restrictive for gas hydrate promotion since many surfactants cannot form micelles at normal hydrate formation temperatures, i.e., below 283 K, and different mechanisms of formation may be effective in the presence of surfactants (OKUTANI et al., 2008; ZHANG, 2007; WATANABE et al., 2005). Watanabe et al. (2005) reported the promoting effect of SDS in hydrofluorocarbon hydrate formation, even though no micelles were formed in aqueous solutions. Zhang et al. (2007) suggested that SDS promotes hydrate nucleation at temperatures below the normal Krafft point because it adsorbs on hydrate crystals and reduces the energy barrier. However, Watanabe et al. (2005) also recognized that micelles might influence the formation of hydrates since Krafft temperature has always been obtained under atmospheric pressure and not under hydrate conditions. Bhattacharjee et al. (2017) developed a new surfactant (based on the combination of SDS and a zwitterionic surfactant) that micellizes at the temperature of clathrate hydrate formation in a methane-pressurized system. This study confirms that the presence of surfactant micelles increases the kinetics of methane hydrate formation.

According to Sun et al. (2003, 2004), the concentration of surfactant in a solution that gives the highest methane storage capacity in hydrates is the critical micellar concentration (CMC) – above such concentration, gas solubility is reduced. Thus, although the mechanisms by which ionic liquids promote the formation of gas hydrates are yet to be better understood, the amount of hydrate observed in Figure 8.2 may be significantly higher at 1 mol % for both ILs because the CMC has not been reached.

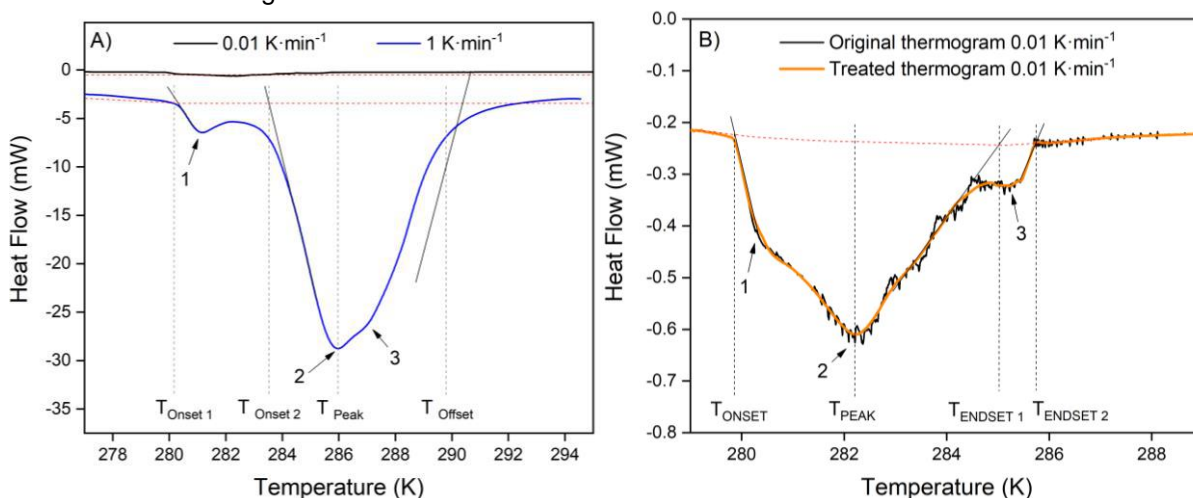
8.4.1 Distance between onset and peak temperatures

The onset temperature of the dissociation peak is less influenced by the heating rate and the sample mass (MENEZES et al., 2019). However, some authors (SABIL et al., 2015; XIAO et al., 2010) use the endset of hydrate dissociation to define the equilibrium temperature at a certain pressure to study gas hydrate formation and dissociation in the presence of inhibitors. In those cases, a slower heating rate ($0.01 \text{ K}\cdot\text{min}^{-1}$) is required to ensure that the equilibrium condition can always be approximated during the process. The concentration of inhibitor in the liquid phase is

known only at the endpoint of the dissociation peak, which is equivalent to the initial concentration of the inhibitor loaded in the cell at the beginning of the experiment. However, if the amount of hydrate formed is small and the mutual solubility of hydrate formers and inhibitor is low, it is frequently considered that the concentration of inhibitor in the liquid phase at the onset of the dissociation peak would be approximately the same as that at the beginning of the experiment.

In this work, a sample of methane hydrate-forming system in the presence of [BMIM][Cl] at 9.6 MPa was analyzed at $1 \text{ K}\cdot\text{min}^{-1}$ and $0.01 \text{ K}\cdot\text{min}^{-1}$ for comparison. Figure 8.3 shows the hydrate dissociation peak obtained in both cases.

Figure 8.3 – Dissociation peak of CH_4 hydrate in the presence of [BMIM][Cl] at 10% wt. and 9.6 MPa: A) Comparison of both thermograms obtained at $0.01 \text{ K}\cdot\text{min}^{-1}$ and $1 \text{ K}\cdot\text{min}^{-1}$; B) Comparison of original thermogram obtained at $0.01 \text{ K}\cdot\text{min}^{-1}$ and the treated one to reduce noise.



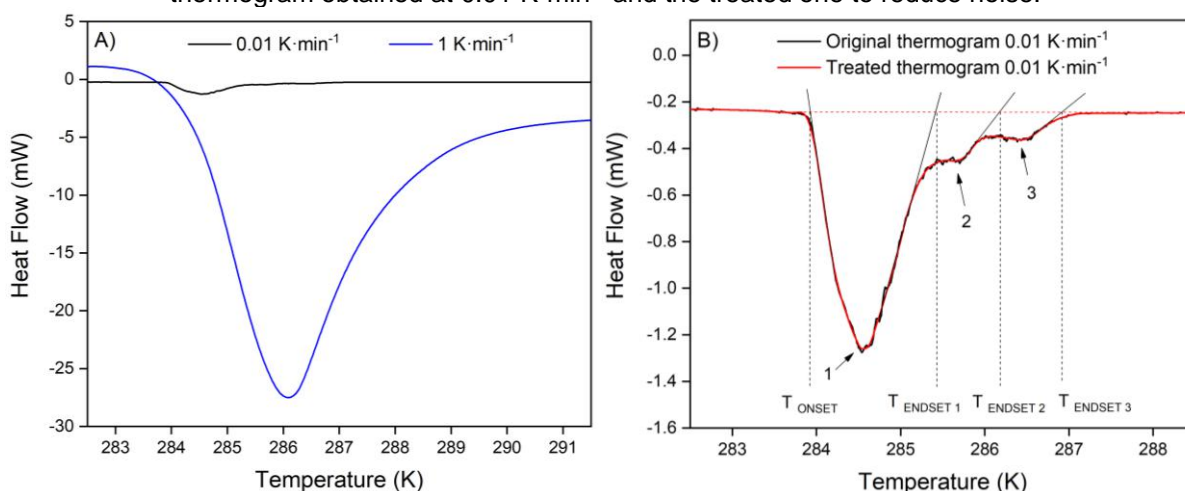
Source: Menezes et al. (2020)

As observed in the figure above, the use of a lower heating rate improves the instrument resolution, which leads to narrower dissociation peaks. Transitions and thermal events become shorter, but the lower rate also reduces sensitivity and increases noise. Consequently, the thermogram must be treated to eliminate noise. The heating rate affects peak and endset temperatures. The onset temperature is not significantly affected by the heating rate. However, the determination of onset and endset temperatures is not evident when overlapped transitions are observed during the dissociation. In Figure 8.3A, two possible onset temperatures are observed for overlapped peaks named as 1 and 2 (onset 1, 280.2 K, and onset 2, 283.6 K). The onset of methane hydrate dissociation peak might be considered as that belonging to the most energetic transition (i.e., onset 2, 283.6 K). Nevertheless, when results

presented in Figure 8.3B for $0.01 \text{ K}\cdot\text{min}^{-1}$ are compared (onset 279.9 K), the real onset value at $1 \text{ K}\cdot\text{min}^{-1}$ from Figure 8.3A would be that obtained from the small peak (i.e., onset 1, 280.2 K). The small difference ($\sim 0.3 \text{ K}$) in onset values is within experimental uncertainty.

A similar analysis can be applied to endset temperatures. In Figure 8.3A only one endset is observed for the peak named as 3, but in Figure 8.3B two endset values are observed for overlapped peaks, named as 2 and 3 (endset 1, 284.90 K , and endset 2, 285.70 K , respectively). Xiao et al. (2010) determined an endset value of 284.92 K , which agrees with our results for endset 1, which corresponds to the most energetic transition. Although an overlapped peak close to the end of the curve is also observed in the thermogram presented by Xiao et al. (2010), those authors do not provide any information about it, neither the onset nor the peak or endset temperatures, which makes difficult to compare results. Thermograms obtained for methane hydrate in the presence of 10 wt.% of [BMIM][Br] at 9.6 MPa and different rates are shown in Figure 8.4. In Figure 8.4B, it is also evidenced that different endset values can be considered.

Figure 8.4 – Dissociation peak of CH_4 hydrate in the presence of [BMIM][Br] at 10% wt. and 9.6 MPa: A) Comparison of both thermograms obtained at 0.01 and $1 \text{ K}\cdot\text{min}^{-1}$; B) Comparison of original thermogram obtained at $0.01 \text{ K}\cdot\text{min}^{-1}$ and the treated one to reduce noise.



Source: Menezes et al. (2020)

The peak temperature may be considered as an estimate when curves overlap or the onset or endset are not well-defined, although it does not strictly represent an equilibrium point (MENEZES et al., 2019). In this work, peak temperatures representing the dissociation of the methane hydrate are those corresponding to the minimum heat flow (transition 2 in both Figure 8.3A and 8.3B). Overlapped peaks observed in Figure 8.3 and numbered by 1 and 3 might be due to crystalline

heterogeneity caused by a non-uniform distribution of nuclei and different growth rates. Those peaks did not appear in the thermograms at 20 MPa. Further analysis based on X-Ray diffraction or polarized light optical microscopy would be necessary to determine the origin of those transitions, but they do not affect the interpretation of high-pressure thermograms concerning the inhibition effect, and hence are out of the scope of this work.

Table 8.1 shows a comparison between our experimental data obtained up to 20 MPa and literature values by using high-pressure microcalorimetry. For higher pressures, experimental data corresponding to our work conditions were not found in literature. The onset temperatures for systems containing inhibitors obtained in this work at $1.0 \text{ K}\cdot\text{min}^{-1}$ and $0.01 \text{ K}\cdot\text{min}^{-1}$ are very similar (experiments 6 and 7 for [BMIM][Cl], 13 and 14 for [BMIM][Br]). Likewise, a very good agreement was also observed for peak temperatures obtained in this work at $1 \text{ K}\cdot\text{min}^{-1}$ and endset temperatures obtained at $0.01 \text{ K}\cdot\text{min}^{-1}$ in the literature for $\sim 20 \text{ MPa}$ (experiments 11 and 12 for [BMIM][Cl], 18 and 19 for [BMIM][Br]). Differences between these temperatures are slightly higher ($\sim 1 \text{ K}$) at 9.6 MPa (experiments 6 and 8 for [BMIM][Cl], 13 and 15 for [BMIM][Br]). However, at this pressure several possible endset temperatures were found, due to the existence of overlapped transitions (experiments 7 and 14 for [BMIM][Cl] and [BMIM][Br], respectively), which would match perfectly with peak temperatures obtained at $1 \text{ K}\cdot\text{min}^{-1}$ in experiments 6 and 13 for both ionic liquids, but were not considered in literature.

A good agreement was also observed between experimental dissociation temperatures of methane hydrate in the absence of inhibitor and literature data obtained from PVT measurements and model predictions. Thus, considering a) the ambiguity of determining onset and endset temperatures previously described, which can lead to misinterpreted results, b) the necessity of using a smoothing function to treat data at $0.01 \text{ K}\cdot\text{min}^{-1}$ to reduce noise, c) the necessary compromise between the time of analysis and quality of the results, and d) the need to minimize the wear of the high-pressure cells at extreme conditions, the peak temperatures obtained at $1.0 \text{ K}\cdot\text{min}^{-1}$ are considered to represent conveniently the equilibrium temperature of methane hydrate dissociation in the presence of inhibitors. A standard deviation of $\sim 0.3 \text{ K}$ for peak temperatures by HP- μDSC at $1.0 \text{ K}\cdot\text{min}^{-1}$ in the determination of methane hydrate dissociation temperature at 21 MPa was presented in a previous work

(MENEZES et al., 2018). Xiao and Adidharma (2009) used a dissociation rate of $0.3 \text{ K}\cdot\text{min}^{-1}$ and admitted that no improvement of accuracy is observed at lower rates.

Table 8.1 – Comparison between experimental data of CH_4 hydrates dissociation in the absence and in the presence of ionic liquids obtained in this work and found in the literature.

Experiment	Reference	X_{IL} (wt%)	P (MPa)	\emptyset ($\text{K}\cdot\text{min}^{-1}$)	Temperature (K)					
					Onset 1	Onset 2	Peak	Endset 1	Endset 2	Endset 3
No inhibitor	1 <i>This work</i>	0	9.6	1	281.47	285.12	286.08	290.43	-	-
	2 Literature ^a	0	9.58	-	-	285.7*	-	-	-	-
	3 Literature ^b	0	9.54	-	-	285.7*	-	-	-	-
	4 Literature ^c	0	9.55	-	-	285.8*	-	-	-	-
	5 Multiflash	0	9.6	-	-	285.77#	-	-	-	-
[BMIM][Cl]	6 <i>This work</i>	10	9.6	1	280.2	283.6	285.9	289.7	-	-
	7 <i>This work</i>	10	9.6	0.01	279.9	-	282.2	284.9	285.7	-
	8 Literature ^d	10	9.6	0.01	-	-	-	284.92	-	-
	9 Literature ^e	10	10.7	0.01	-	-	-	285.98	-	-
	10 Literature ^e	10	14.7	0.01	-	-	-	289.01	-	-
	11 <i>This work</i>	10	20	1	288.73	-	291.37	-	293.7	-
	12 Literature ^e	10	20.7	0.01	-	-	-	291.25	-	-
[BMIM][Br]	13 Literature ^d	9.7	9.6	1	284.29	-	286.08	288.2	-	-
	14 <i>This work</i>	9.7	9.6	0.01	283.96	-	284.54	285.36	286.18	286.9
	15 Literature ^d	10	9.6	0.01	-	-	-	285.13	-	-
	16 Literature ^e	10	10.6	0.01	-	-	-	285.87	-	-
	17 Literature ^e	10	14.5	0.01	-	-	-	288.79	-	-
	18 <i>This work</i>	9.7	20	1	289.87	-	291.67	-	293.58	-
	19 Literature ^e	10	20.4	0.01	-	-	-	291.59	-	-

^a Mohammadi et al. (2005); ^b Nakamura et al. (2003); ^c Yang (2000); ^d Sabil et al. (2015); ^e Xiao et al. (2010); * These data were obtained in a PVT cell by isochoric method; # Model prediction.

Source: Menezes et al. (2020)

Tables 8.2 and 8.3 present the equilibrium data obtained for ice and methane hydrate, respectively, formed in the absence and in the presence of each inhibitor at different concentrations and pressures. For the sake of completeness, both onset and peak temperatures are presented. Model predictions without inhibitor show slightly higher equilibrium temperatures than those represented by onset points. As previously mentioned in this work, this may be due to a more significant presence of empty cavities in real hydrate structures, leading to a less stable configuration with lower dissociation temperatures (MENEZES et al., 2019). Likewise, since literature data in the absence of inhibitor were obtained by an isochoric method in a PVT cell, they are also slightly higher than onset temperatures obtained by HP- μ DSC, where no mixing is possible, and consequently mass transfer is less favored to fill cavities.

The difference between onset and peak dissociation temperatures is notable for inhibited systems and increases when pressure increases. Such difference is not so significant for non-inhibited hydrates, since the dissociation curves are narrower in these cases. Ionic liquids can compose hydrate structures by both hosting cationic chains as “guest” inside cages and incorporating anionic molecules in the hydrate framework, instead of water molecules (DESCHAMPS; DALMAZZONE, 2010; DYADIN; UDACHIN, 1987; JEFFREY, 1984; KOBORI et al., 2015; LI et al., 2010). A similar phenomenon may happen by using methanol as a hydrate inhibitor (MCLAURIN et al., 2014; SHIN et al., 2013; WALLQVIST, 1992). Therefore, the incorporation of the inhibitor molecules either in the hydrate lattice or trapped in cavities could affect the structural heterogeneity and hence the characteristic properties of the hydrate, shifting the equilibrium point and extending the dissociation process or leading to overlapped transitions that difficult onset determination, as observed in samples containing about 10 and 15 mol% of [BMIM][Br], for instance, in which two onset points can be established in most thermograms.

Table 8.2 – Ice melting temperatures (onset and peak) in the absence and presence of different inhibitors.

Inhibitor	Inhibitor concentration		Pressure (MPa)									
			20		40		60		80		100	
	mol%	wt%	T _{ONSET}	T _{PEAK}								
No Inhibitor	0	0	271.38	273.8	269.77	272.1	268.01	270.3	266.13	268.4	264.12	266.5
Literature*	0	0	271.68		269.82		267.8		265.69		263.53	
[BMIM][Br]	0.9	9.7	267.37	270.3	265.42	268.3	263.51	266.4	261.73	264.5	259.56	262.5
	5	39.1	254.41	263.1	252.36	261.2	250.56	259.3	249.19	257.1	249.91	255.3
	10	57.4	245.72	252.3	245.31	250.4	242.63	247.8	NA	245	NA	243.7
	15.1	68.3	NA	NA								
[BMIM][Cl]	1.1	10	263.66	268.5	262.11	266.5	259.47	264.5	257.91	262.8	256.43	261
	5	33.8	250.9	259.5	248.45	257.9	247.36	255.6	246.85	253.6	242.54	251.2
	10	51.8	NA	NA								
	15	63.1	NA	NA								
Methanol	5.63	9.6	255.9	264.8	NA	NA	NA	NA	NA	NA	NA	NA
	5	8.6	257.45	265.6	NA	NA	NA	NA	NA	NA	NA	NA

* Dunaeva et al. (2010)
Source: Menezes et al. (2020)

Table 8.3 – Dissociation temperatures (onset and peak) of CH₄ hydrates in the absence and presence of different inhibitors.

Inhibitor	[Inhibitor]		Pressure (MPa)									
			20		40		60		80		100	
			mol%	wt%	T _{ONSET}	T _{PEAK}	T _{ONSET}	T _{PEAK}	T _{ONSET}	T _{PEAK}	T _{ONSET}	T _{PEAK}
No inhibitor	0	0	291.4	293.13	296.88	298.04	300.39	301.3	303.01	304.15	305.19	306.25
Literature	0	0	291.86 (20.2 MPa) ^a		297.3 (42.2 MPa) ^b		300.6 (62.76 MPa) ^b		303.6 (84 MPa) ^c		305.08 (98 MPa) ^d	
No inhibitor (Multiflash)	0	0	291.96		297.51		301.02		303.74		306.01	
No inhibitor (CSMGem)	0	0	291.76		297.23		300.69		303.34		305.53	
[BMIM][Br]	0.9	9.7	289.87	291.67	294.84	297.11	297.96	300.38	300.63	303.14	302.77	305.16
	5	39.1	283.31	287.1	287.83	291.59	290.4	294.94	293.14	297.76	294.47	299.98
	10	57.4	274.32 277.74	282.5	277.94 281.10	286.46	279.57 283.63	289.84	281.04 285.61	292.26	286.84 288.33	295.11
	15.1	68.3	265.20 268.20	273.33	271.22 273.63	280.45	275.21	283.32	277.25	285.52	278.56	287.53
[BMIM][Cl]	1.1	10	288.73	291.37	292.99	296.27	296.34	299.51	299	302.19	301.3	304.41
	5	33.8	281.93	286.09	285.9	290.56	288.57	293.89	291.32	296.59	293.42	298.57
	10	51.8	271.38	277.2	275.02	281.65	278.57	286.57	281.05	287.78	282.83	289.84
	15	63.1	261.44	266.64	263.97	272.59	267.69	275.91	268.57	278.71	271.92	280.76
Methanol	5.63	9.6	284.64	288.27	287.31	293.61	291.45	297.14	293.32	299.79	295.53	301.81
	5	8.6	285.36	289.11	287.95	294.27	291.86	297.65	294.19	300.26	296.83	302.49
Methanol (Multiflash)	5.63	9.6	287.33		292.79		296.27		298.97		301.23	
Methanol (Multiflash)	5	8.6	287.85		293.32		296.8		299.5		301.76	
Methanol (CSMGem)	5.63	9.6	287.23		292.55		295.94		298.54		300.7	
Methanol (CSMGem)	5	8.6	287.74		293.08		296.47		299.08		301.24	

^aJager and Sloan (2001); ^bJager (2001); ^cDyadin and Aladko (1996); ^dNakano et al. (1999).

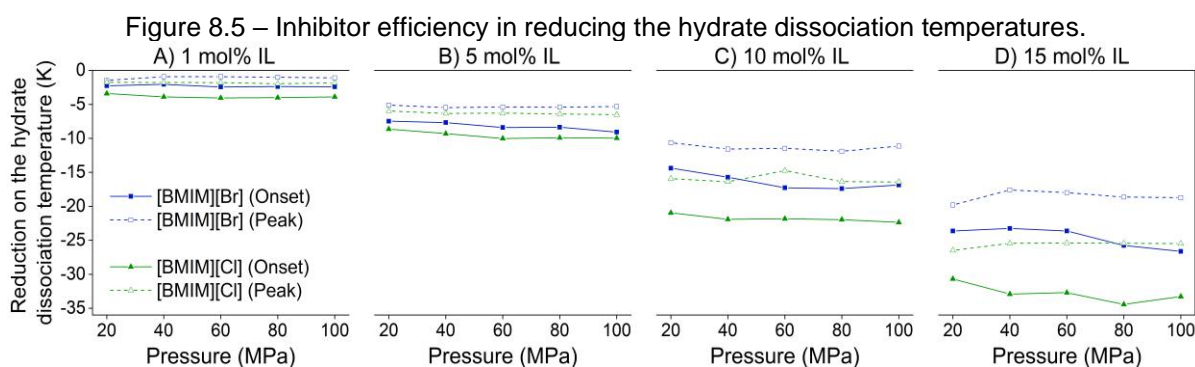
Source: Menezes et al. (2020)

8.4.2 Thermodynamic inhibition efficiency of [BMIM][Br] and [BMIM][Cl]

Figure 8.3 compares the dissociation temperature reduction resulting from the addition of both ionic liquids, considering the non-inhibited methane hydrate as reference. [BMIM][Cl] presents a better inhibitory effect, considering both the onset and peak temperatures. Hydrates formed in the presence of this chloride-based IL present lower dissociation temperatures. The inhibition efficiency is even better as the IL content increases, i.e., the inhibitory effect of [BMIM][Cl] is more significant than [BMIM][Br] at higher IL fractions. Similar results are found in previous studies with Cl- and Br- as IL anions (RICHARD; ADIDHARMA, 2013; XIAO et al., 2010). Some works

indicate that the electrical conductivity of [BMIM][Cl] in aqueous solutions is higher than for [BMIM][Br], which may be correlated to the thermodynamic effectivity of the IL as gas hydrate inhibitor (SABIL et al., 2015; XIAO et al., 2010). Xiao et al. (2010) report that chloride ionic liquids form stronger hydrogen bonds with water molecules, according to infrared spectra results. Therefore, both phenomena may be related to the better performance of [BMIM][Cl] as a gas hydrate inhibitor.

The difference between onset and peak temperatures also increases for higher contents of IL, which was expected since the presence of ILs leads to broader hydrate dissociation curves, as previously mentioned. Considering onset temperatures, a slight trend of greater inhibition efficiency is observed at higher pressures for the same composition, as shown in Figure 8.5. This phenomenon was also observed by Richard and Adidharma (2013) for 1-ethyl-3-methylimidazolium chloride [EMIM][Cl] and 1-ethyl-3-methylimidazolium bromide [EMIM][Br].



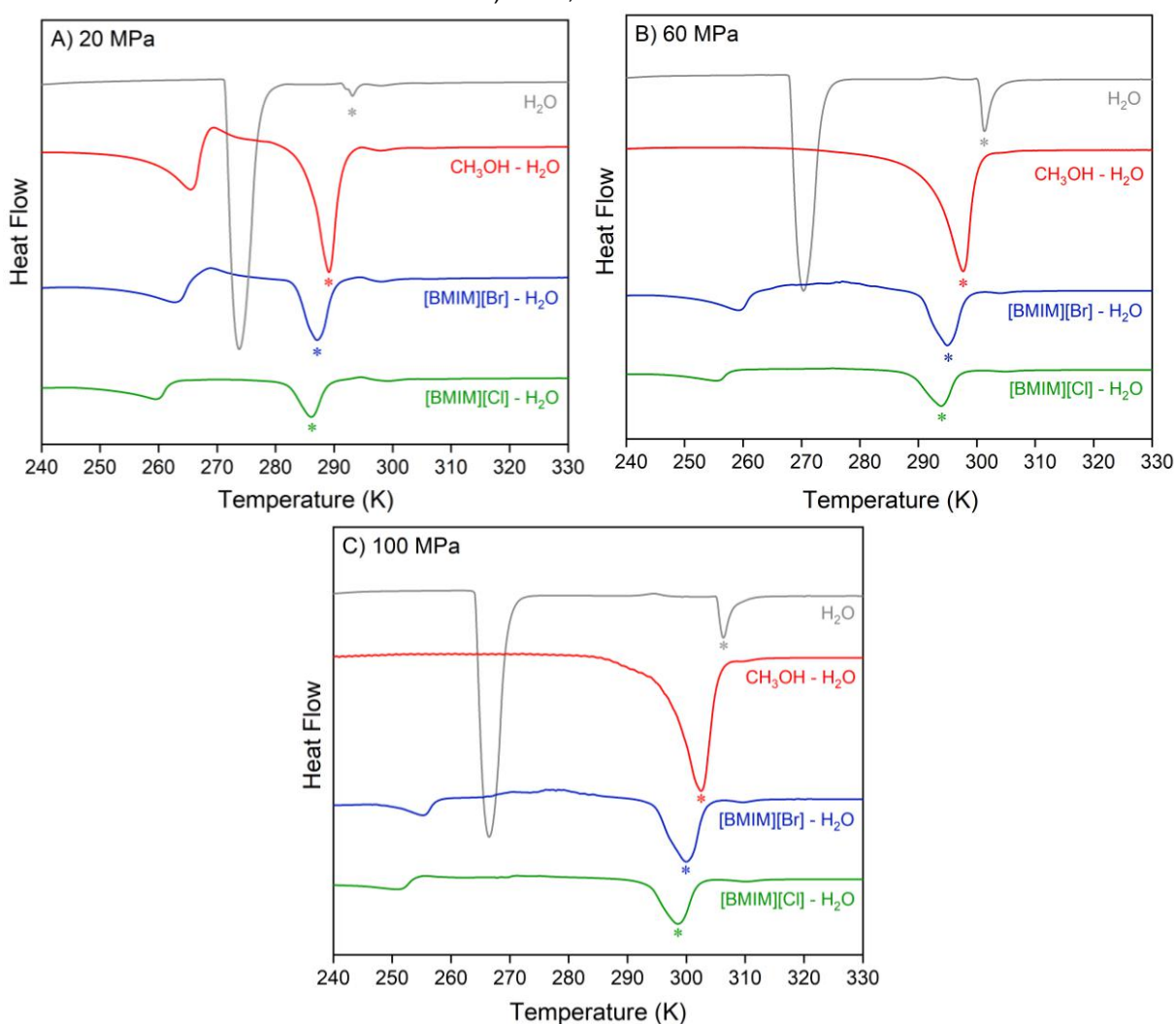
Source: Menezes et al. (2020)

8.4.3 Comparison with methanol

Considering that methanol is the most applied commercial inhibitor of hydrates, thermograms of methane hydrate dissociation are compared in Figure 8.6 by using both ionic liquids and methanol at the same molar fraction (5 mol%). The non-inhibited systems present smaller fractions of hydrate at 5 mol% than using both ILs and methanol. As previously mentioned, the acceleration of hydrate formation by employing usual thermodynamic inhibitors and ionic liquids has been reported in the literature (AMTAWONG et al., 2016; BOBEV; TAIT, 2004; CHA et al., 2013; KE et al., 2013; LEE et al., 2016; MCLAURIN et al., 2014; SOWA et al., 2014; SOWA et al., 2015;). Therefore, the inhibitors investigated in this work seem to contribute to hydrate

formation and growth at low concentrations. Nevertheless, both [BMIM][Br] and [BMIM][Cl] are more efficient thermodynamic inhibitors than methanol in terms of molar concentrations. The [BMIM][Cl] is the most effective one, shifting the hydrate dissociation curve about 7.0 K in all cases (5 mol%). Moreover, it presents the lowest promoting effect on hydrate formation, since its hydrate dissociation curves at 20, 60, and 100 MPa are smaller than the [BMIM][Br] and methanol ones, considering that the amounts of aqueous solutions inside the cell were similar. The lower amounts of hydrate formed in the presence of [BMIM][Cl] indicate a slower hydrate growth. Thus, this IL seems to be the least effective kinetic promoter, and therefore the most interesting hydrate inhibitor in terms of molar concentrations.

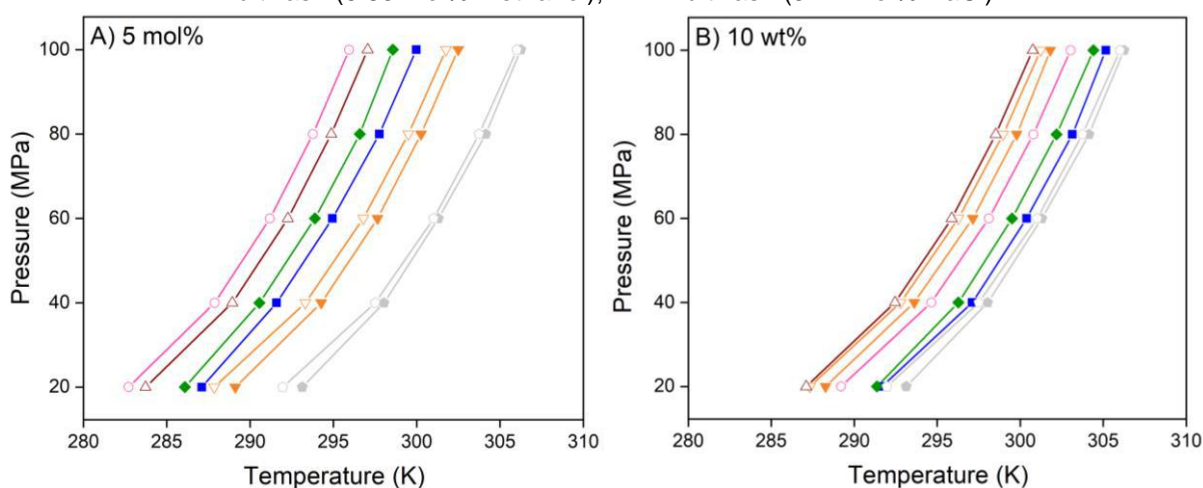
Figure 8.6 – Comparison of CH₄ hydrate dissociation (*) by using different inhibition solutions (5 mol% inhibitor) at 20, 60 and 100 MPa.



Source: Menezes et al. (2020)

Figure 8.7 indicates the equilibrium curves by using inhibitors at 10 wt% (corresponding about 1 mol% IL) and 5 mol%. The curves were drawn from experimental data by considering the peak temperatures, since the onset points for methanol-inhibited systems are difficult to determine due to the existence of overlapped transitions, as previously mentioned. Predictions for methane hydrate forming systems in the presence of NaCl and NaBr were also included to compare the performance of these common salts with the one provided by the studied ILs.

Figure 8.7 – Comparison of CH₄ hydrate equilibrium lines by using different inhibitors (experimental data and predictions using Multiflash): **A) Constant molar fraction:** ● Experimental (No inhibitor); ○ Multiflash (No inhibitor); ▼ Experimental (8.5 wt% Methanol); ▽ Multiflash (8.5 wt% methanol); ■ Experimental (39.1 wt% [BMIM][Br]); ◆ Experimental (33.8 wt% [BMIM][Cl]); ▲ Multiflash (14.6 wt% NaCl); ○ Multiflash (23.1 wt% NaBr); **B) Constant mass fraction:** ● Experimental (No inhibitor); ○ Multiflash (No inhibitor); ■ Experimental (0.9 mol% [BMIM][Br]); ◆ Experimental (1.1 mol% [BMIM][Cl]); ○ Multiflash (1.83 mol% NaBr); ▼ Experimental (5.63 mol% Methanol); ▽ Multiflash (5.63 mol% methanol); ▲ Multiflash (3.17 mol% NaCl).



Source: Menezes et al. (2020)

Despite the good performance of [BMIM][Cl] and [BMIM][Br] as hydrate inhibitors compared to methanol at the same molar fraction, the amount of 5 mol% represents a high content of inhibitor in terms of mass fraction (30-40 wt%) when compared to the usually employed concentrations, either using methanol or ethylene glycol. Although in some cases up to 50 wt% of inhibitors are required to avoid hydrate formation, about 10 wt% is the fraction of thermodynamic inhibitors typically used in industrial applications and scientific studies (SLOAN; KOH, 2008; TARIQ et al., 2014; ZARE et al., 2013). This mass fraction corresponds to about 1 mol% of ILs studied in this work. For this concentration, the equilibrium curve is shifted by about 2.0 K, according to Table 8.3, while methanol shifts the curve in 4.0-5.0 K, according to the literature (SLOAN; KOH, 2008), and to the results presented in this work. Comparing mass

fractions, NaCl presents similar performance to methanol, and NaBr is slightly better than the studied ILs. However, NaCl is not recommended for oil and gas pipelines as it increases corrosion rate (RUSTANDY et al., 2012), and some oilfield tubular materials are susceptible to pitting and localized corrosion in the presence of NaBr (KE et al., 2004).

To sum up, considering the mass fraction, methanol could be still selected as the best option for hydrate thermodynamic inhibition. Moreover, the expensive processes of ILs synthesis still make them economically unfeasible compared to methanol, although new perspectives have arisen for cheaper IL-based inhibitors (ALTAMASH et al., 2018). Methanol acts as a stronger catalyst for hydrate formation reactions but, as previously mentioned, the cost-benefit ratio must be assessed when choosing a gas hydrate inhibitor and the feasibility of IL-methanol mixtures as inhibition solutions.

8.5 CONCLUSION

New experimental hydrate dissociation data are presented in this chapter by using inhibition additives at pressures from 9.6 to 100 MPa via microcalorimetric measurements. Two ionic liquids, [BMIM][Cl] and [BMIM][Br], were evaluated as methane hydrate inhibitors. Their performance was compared to methanol in terms of molar and mass fractions and to predictions made for other salts (NaCl and NaBr).

- A rigorous analysis of thermograms interpretation has been carried out to compare experimental hydrate dissociation temperatures obtained herein with literature data. Although the results indicate that these additives promote the hydrate growth when at low concentrations, all of them act as thermodynamic inhibitors for methane hydrates, shifting the phase equilibrium curves to lower temperatures.
- The increase in the content of these ILs improves the thermodynamic inhibition effect considerably, mainly for [BMIM][Cl], but methanol presents better results in terms of mass fractions. However, one must consider the dual inhibition effect observed at high concentrations (~ 15 mol%), characteristic of the studied ionic liquids, which allows not only to shift the hydrate equilibrium curve to lower temperatures but also to retard nucleation and reduce hydrate growth rate. This effect is especially relevant for the production, processing, and transportation of

oil and gas in offshore platforms, where extreme pressure conditions and low temperatures are favorable for hydrate formation.

REFERENCES

- ALTAMASH, T.; KHRAISHEH, M.; QURESHI, M.F.; SAAD, M.A.; APARICIO, S.; ATILHAN, M.; Cost-effective alkylammonium formate-based protic ionic liquids for methane hydrate inhibition. *Journal of Natural Gas Science and Engineering*, v. 58, p. 59-68, 2018.
- AMTAWONG, J.; GUO, J.; HALE, J.S.; SENGUPTA, S.; FLEISCHER, E.B.; MARTIN, R.W.; JANDA, K.C. Propane Clathrate Hydrate Formation Accelerated by Methanol. *Journal of Physical Chemistry Letters*, v. 7, p. 2346–2349, 2016.
- ANGELL, C.A.; BYRNE, N.; BELIERES, J.-P. Parallel developments in aprotic and protic ionic liquids: physical chemistry and applications. *Accounts of Chemical Research*, v. 40 (11), p. 1228–1236, 2007.
- BHATTACHARJEE, G.; KUSHWAHA, O. S.; KUMAR, A.; KHAN, M. Y.; PATEL, J. N.; KUMAR, R. Effects of micellization on growth kinetics of methane hydrate. *Industrial and Engineering Chemistry Research*, v. 56 (13), p. 3687-3698, 2017.
- BLESIC, M.; MARQUES, M.H.; PLECHKOVA, N.V.; SEDDON, K.R.; REBELO, L.P.N.; LOPES, A. Self-aggregation of ionic liquids: micelle formation in aqueous solution. *Green Chemistry*, v. 9, p. 481-490, 2007.
- BOBEV, S.; TAIT, K.T. Methanol - inhibitor or promoter of the formation of gas hydrates from deuterated ice? *American Mineralogist*, 89 (8–9), p. 1208–1214, 2004.
- CHA, M., HU, Y., SUM, A.K. Methane hydrate phase equilibrium for systems containing NaCl, KCl, and NH₄Cl. *Fluid Phase Equilibria*, v. 413, p. 2-9, 2016.
- CHA, M.; SHIN, K.; KIM, J.; CHANG, D.; SEO, Y.; LEE, H.; KANG, S. P. Thermodynamic and kinetic hydrate inhibition performance of aqueous ethylene glycol solutions for natural gas. *Chemical Engineering Science*, v. 99, p. 184–190, 2013.
- CHEN, Q.; YU, Y.; ZENG, P.; YANG, W.; LIANG, Q.; PENG, X.; LIU, Y.; HU, Y. Effect of 1-butyl-3-methylimidazolium tetrafluoroborate on the formation rate of CO₂ hydrate. *Journal of Natural Gas Chemistry*, v.17 (3), p. 264-267, 2008.
- CHONG, Z. R.; YANG, S.H.B.; BABU, P.; LINGA, P.; LI, X.S. Review of natural gas hydrates as an energy resource: Prospects and challenges. *Applied Energy*, v. 162, p. 1633-1652, 2016.
- DALMAZZONE, D.; HAMED, N.; DALMAZZONE, C. DSC measurements and modelling of the kinetics of methane hydrate formation in water-in-oil emulsion. *Chemical Engineering Science*, v. 64, p. 2020-2026, 2009.

DALMAZZONE, D.; SALES SILVA, L. P.; DELAHAYE, A.; FOURNAISON, L. Calorimetric Characterization of Clathrate and Semiclathrate Hydrates. Chapter 4 in book "Gas Hydrates: Fundamentals, Characterization and Modeling", First Edition. Edited by Daniel Broseta, Livio Ruffine and Arnaud Desmedt. ISTE Ltd 2017. Published by ISTE Ltd and John Wiley & Sons, Inc.

DARABOINA, N.; MALMOS, C.; SOLMS, N. Investigation of kinetic hydrate inhibition using a high pressure micro differential scanning calorimeter. *Energy and Fuels*, v. 27 (10), p. 5779–5786, 2013.

DESCHAMPS, J.; DALMAZZONE, D. Hydrogen storage in semi clathrate hydrates of tetrabutyl ammonium chloride and tetrabutylphosphonium bromide. *Journal of Chemical and Engineering Data*, v. 55, p. 3395–3399, 2010.

DI PROFIO, P.; ARCA, S.; GERMANI, R.; SAVELLI, G. Surfactant promoting effects on clathrate hydrate formation: are micelles really involved?. *Chemical Engineering Science*, v. 60 (15), p. 4141-4145, 2005.

DUNAEVA, A. N.; ANTSYSHKIN, D. V.; KUSKOV, O. L. Phase diagram of H₂O: thermodynamic functions of the phase transitions of high-pressure ices. *Solar System Research*, v. 44 (3), p. 202–222, 2010.

DUPONT, J. On the solid, liquid and solution structural organization of imidazolium ionic liquids. *Journal of the Brazilian Chemical Society*, v. 15 (3), p. 341-350, 2004.

DYADIN, Y. A.; ALADKO, E. Y. Decomposition of the methane Hydrate up to 10 kbar. International Conference on Natural Gas Hydrates (1996) Toulouse, France, June 2-6, p. 67-70, 1996.

DYADIN, Y.A.; UDACHIN, K.A. Clathrate polyhydrates of peral kylonium salts and their analogs. *Journal of Structural Chemistry*, v. 28, 394-432, 1987.

FARHADIAN, A.; KUDBANOV, A.; VARFOLOMEEV, M. A.; DALMAZZONE, D. Waterborne Polyurethanes as a New and Promising Class of Kinetic Inhibitors for Methane Hydrate Formation. *Nature Scientific Reports*, v. 9, 9797, 2019.

GUPTA, A.; LACHANCE, J.; SLOAN, E.D.; KOH, C.A. Measurements of methane hydrate heat of dissociation using high pressure differential scanning calorimetry. *Chemical Engineering Science*, v. 63 (24), p. 5848-5853, 2008.

HAGHIGHI, H.; CHAPOY, A.; BURGESS, R.; TOHIDI, B. Experimental and thermodynamic modelling of systems containing water and ethylene glycol: application to flow assurance and gas processing. *Fluid Phase Equilibria*, v. 276 (1), p. 24–30, 2009.

HU, Y.; MAKOGON, T.Y.; KARANJKAR, P.; LEE, K.; LEE, B.; SUM, A.K. Gas hydrates phase equilibria and formation from high concentration NaCl brines up to 200 MPa. *Journal of Chemical & Engineering Data*, v. 62 (6), p. 1910–1918, 2017.

JAGER, M. D. High pressure studies of hydrate phase inhibition using raman spectroscopy. *Ph.D. Thesis*, Colorado School of Mines, Golden, Colorado, USA, 2001.

JAGER, M. D., SLOAN, E. D. The effect of pressure on methane hydration in pure water and sodium chloride solutions. *Fluid Phase Equilibria* v. 185, p. 89-99, 2001.

JEFFREY, G.A. Hydrate inclusion compounds. *Journal of Inclusion Phenomena*, v. 1 (3), p. 211-222, 1984.

KE, M.; JAVORA, P. H.; QU, Q. Application of pH buffer as corrosion inhibitor in nabr brine packer fluids at high temperatures. *Society of Petroleum Engineers*, 87563-MS, 2004.

KE, W.; SVARTAAS, T. M.; ABAY, H.K. Effects of Low Concentration Methanol, PVP and PVCap on Structure-I Methane Hydrate Formation. *Journal Energy and Power Engineering*, v. 7, p. 432-439, 2013.

KELLAND, M.A. History of the development of low dosages hydrate inhibitors. *Energy and Fuels*, v. 20 (3), p. 825-847, 2006.

KIM, K. S.; KANG, J. W.; KANG, S. P. Tuning ionic liquids for hydrate inhibition. *Chemical Communications*, v. 47 (2011) 6341-6343.

KINNARI, K.; HUNDSEID, J.; LI, X.; ASKVIK, K.M. Hydrate Management in Practice. *Journal of Chemical & Engineering Data*, v. 60 (2), p. 437-446, 2015.

KOBORI, T.; MUROMACHI, S.; YAMASAKI, T.; TAKEYA, S.; YAMAMOTO, Y.; ALAVI, S.; OHMURA, R. Phase Behavior and Structural Characterization of Ionic Clathrate Hydrate Formed with Tetra-n-butylphosphonium Hydroxide: Discovery of Primitive Crystal Structure. *Crystal Growth and Design*, v. 15 (8), p. 3862-3867, 2015.

KOH, C.A.; SLOAN, E.D.; SUM, A.K.; WU, D.T. Fundamentals and applications of gas hydrates. *Annual Review of Chemical and Biomolecular Engineering*, v. 2, p. 237-257, 2011.

KOH, C.A.; WESTACOTT, R.E.; ZHANG, W.; HIRACHAND, K.; CREEK, J.L.; SOPER, A.K. Mechanisms of gas hydrate formation and inhibition. *Fluid Phase Equilibria*, v. 194-197, p. 143-151, 2002.

KOUAKOU, A.C.; MAPIHAN, K.L.; PAULY, J. Solid-liquid equilibria under high pressure of pure fatty acid methyl esters. *Fuel*, v. 109, p. 297-302, 2013.

KUMAR, A.; BHATTACHARJEE, G.; KULKARNI, B. D.; KUMAR, R. Role of surfactants in promoting gas hydrate formation. *Industrial and Engineering Chemistry Research*, v. 54, p. 12217-12232, 2015.

LE PARLOUËR, P.; DALMAZZONE, C.; HERZHAFT, B.; ROUSSEAU, L.; MATHONAT, C. Characterization of gas hydrates formation using a new high pressure micro-DSC. *Journal of Thermal Analysis and Calorimetry*, v. 78, p. 165-172, 2004.

LEE, W.; SHIN, J.Y.; KIM, K.S.; KANG, S.P. Kinetic Promotion and Inhibition of Methane Hydrate Formation by Morpholinium Ionic Liquids with Chloride and Tetrafluoroborate Anions. *Energy and Fuels*, v. 30 (5), p. 3879-3885, 2016.

LI, S.; FAN, S.; WANG, J.; LANG, X.; WANG, Y. Semicathrate hydrate phase equilibrium for CO₂ in the presence of tetra-n-butyl ammonium halide (bromide, chloride, or fluoride). *Journal of Chemical Engineering Data*, v. 55, 3212–3215, 2010.

LINJUN, W.; XUEMIN, Z.; HONGHUI, LI.; SHAO, L.; ZHANG, D.; JIAO, L. Theory research on desalination of brackish water using gas hydrate method. *Advanced Materials Research*, v. 616-618, p. 1202-1207, 2013.

MCLAURIN, G.; SHIN, K.; ALAVI, S.; RIPMEESTER, J.A. Antifreezes act as catalysts for methane hydrate formation from ice. *Angewandte Chemie International Edition*, v. 53 (39), p. 10429-10433, 2014.

MENEZES, D.E.S.; RALHA, T.W.; FRANCO, L.F.M., PESSÔA FILHO, P.A.; ROBUSTILLO, M.D. Simulation and experimental study of methane-propane hydrate dissociation by high pressure differential scanning calorimetry. *Brazilian Journal of Chemical Engineering*, v. 35, p. 403-414, 2018.

MENEZES, D.E.S.; SUM, A. K.; DESMEDT, A.; PESSOA FILHO, P. A.; ROBUSTILLO, M.D. Coexistence of sl and sll in methane-propane hydrate former systems at high pressures. *Chemical Engineering Science*, v. 208, article 115149, 2019.

MENEZES, D.E.S.; PESSÔA FILHO, P.A.; ROBUSTILLO, M.D. Use of 1-Butyl-3-methylimidazolium-based ionic liquids as methane hydrate inhibitors at high-pressure conditions. *Chemical Engineering Science*, v. 212, 115323, 2020.

MISKOLCZY, Z.; SEBOK-NAGY, K.; BICZOK, L.; GOKTURK, S. Aggregation and micelle formation of ionic liquids in aqueous solution. *Chemical Physics Letters*, v. 400 (4-6), p. 296-300, 2004.

MOHAMMADI, A. H.; ANDERSON, R.; TOHIDI, B. Carbon monoxide clathrate hydrates: experimental equilibrium data and thermodynamic modeling. *American Institute of Chemical Engineers*, v. 51, p. 2825 – 2833, 2005.

MOHAMMADI, A.H., RICHON, D. Phase equilibria of methane hydrates in the presence of methanol and/or ethylene glycol aqueous solutions. *Industrial and Engineering Chemistry Research*, v. 49 (2), p. 925–928, 2010.

NAKAMURA, T.; MAKINO, T.; SUGAHARA, T.; OHGAKI, K. Stability boundaries of gas hydrates helped by methane - structure-H hydrates of methylcyclohexane and cis-1,2-dimethylcyclohexane. *Chemical Engineering Science*, v. 58, p. 269–273, 2003.

NAKANO, S.; MORITOKI, M.; OHGAKI, K. High-Pressure Phase Equilibrium and Raman Microprobe Spectroscopic Studies on the Methane Hydrate System. *Journal of Chemical and Engineering Data*, v. 44, p. 254-257, 1999.

NISHIKAWA, K.; WANG, S.; KATAYANAGI, H.; HAYASHI, S.; HAMAGUCHI, H.O.; KOGA, Y.; TOZAKI, K. Melting and Freezing Behaviors of Prototype Ionic Liquids, 1-Butyl-3-methylimidazolium Bromide and Its Chloride, Studied by Using a Nano-Watt Differential Scanning Calorimeter. *Journal of Physical Chemistry B*, v. 111 (18), p. 4894-4900, 2007.

OKUTANI, K.; KUWABARA, Y.; MORI, Y.H. Surfactant effects on hydrate formation in an unstirred gas/liquid system: An experimental study using methane and sodium alkyl sulfates. *Chemical Engineering Science*, v. 63 (1), p. 183–194, 2008.

QURESHI, M.F.; ATILHAN, M.; ALTAMASH, T.; TARIQ, M.; KHRAISHEH, M.; APARICIO, S.; TOHIDI, B. Gas hydrate prevention and flow assurance by using mixtures of ionic liquids and synergent compounds: combined kinetics and thermodynamic approach. *Energy and Fuels* 30 (4), 3541–3548, 2016.

RAE, P.J.; DATTELBAUM, D.M. The properties of poly(tetrafluoroethylene) (PTFE) in compression. *Polymer*, v. 45, p. 7615-7625 (2004).

RICHARD, A. R.; ADIDHARMA, H. The performance of ionic liquids and their mixtures in inhibiting methane hydrate formation. *Chemical Engineering Science*, v. 87, p. 270–276, 2013.

RIGBY, H.A.; BUNN, C.W. A room-temperature transition in polytetrafluoroethylene. *Nature*, v. 164, p. 583, 1949.

RUSTANDY A.; ADYUTATAMA, M.; FADLY, E.; SUBEKTI, N. Corrosion rate of carbon steel for flowline and pipeline as transmission pipe in natural gas production with CO₂ content. *Makara Journal of Technology*, v. 16:1, p. 57-62, 2012.

SABIL, K.M.; NASHED, O.; LAL, B.; ISMAIL, L.; JAPPER-JAAFAR, A. Experimental investigation on the dissociation conditions of methane hydrate in the presence of imidazolium-based ionic liquids. *The Journal of Chemical Thermodynamics*, v. 84, p.7-13, 2015.

SAHLE, C.J.; STERNEMANN, C.; SCHMIDT, C.; LEHTOLA, S.; JAHN, S.; SIMONELLI, L.; HUOTARI, S.; HAKALA, M.; PYLKKÄNEN, T.; NYROW, A.; MENDE, K.; TOLAN, M.; HÄMÄLÄINEN, K.; WILKE, M. Microscopic structure of water at elevated pressures and temperature. *Proceedings of the National Academy of Sciences*, v. 110 (16), p. 6301-6306, 2013.

SAMI, N.A.; SANGWAI, J.S.; SUBRAMANIAN, B. Gas hydrate Applications and problems in Oil and Gas Industry. *International Journal of Scientific & Engineering Research*, v. 4 (8), 2013.

SANTOS, L.C., ABUNAHMAN, S.S., TAVARES, F.W., AHÓN, V.R.R., KONTOGEORGIS, G.M. Cubic Plus Association Equation of State for Flow Assurance Projects. *Industrial & Engineering Chemistry Research*, v. 54, p. 6812-6824, 2015.

SANZ, E.; VEJA, C.; ABASCAL, J.L.; MACDOWELL, L.G. Phase diagram of water from computer simulation. *Physical Review Letters*, v. 92 (25): 255701, 2004.

SHEN, X.; SHI, L.; LONG, Z.; ZHOU, X.; LIANG, D. Experimental study on the kinetic effect of N-butyl-N-methylpyrrolidinium bromide on CO₂ hydrate. *Journal of Molecular Liquids*, v. 223, p. 672–677, 2016.

SHIN K.; UDACHIN, K.A.; MOUDRAKOVSKI, I.L.; LEEK, D.M.; ALAVI, S.; RATCLIFFE, C.I.; RIPMEESTER, J.A. Methanol incorporation in clathrate hydrates and the implications for oil and gas pipeline flow assurance and icy planetary bodies. *Proceedings of the National Academy of Sciences*, v. 110 (21), p. 8437–8442, 2013.

SLOAN E.D.; KOH, C. Clathrate hydrates of natural gases, 3rd ed. Boca Raton: CRC Press, 2008.

SLOAN, E.D.; KOH, C.A.; SUM, A.K. Natural Gas Hydrates in Flow Assurance. *Gulf Professional Publishing (Elsevier)*, Oxford, U.K., 2010.

SOWA, B.; ZHANG, X.H.; HARTLEY, P.G.; DUNSTAN, D.E.; KOZIELSKI, K.A.; MAEDA, N. Formation of Ice, Tetrahydrofuran Hydrate, and Methane/Propane Mixed Gas Hydrates in Strong Monovalent Salt Solutions. *Energy and Fuels*, v. 28 (11), p. 6877–6888, 2014.

SOWA, B.; ZHANG, X.H.; KOZIELSKI, K.A.; HARTLEY, P.G.; DUNSTAN, D.E.; MAEDA, N. Nucleation Probability Distributions of Methane– Propane Mixed Gas Hydrates in Salt Solutions and Urea. *Energy and Fuels*, v. 29 (10), p. 6259–6270, 2015.

SUN Z., MA R., FAN S., GUO K., WANG R. Investigation on gas storage in methane hydrate. *Journal of Natural Gas Chemistry*, v. 13, p. 107–112, 2004.

SUN, Z.; WANG, R.; MA, R.; GUO, K.; FAN, S. Natural gas storage in hydrates with the presence of promoters. *Energy Conversion and Management*, v. 44, p. 2732–2742, 2003.

TARIQ, M.; CONNOR, E.; THOMPSON, J.; KHRAISHEH, M.; ATILHAN, M.; ROONEY, D. Doubly dual nature of ammonium-based ionic liquids for methane hydrates probed by rocking-rig assembly. *Royal Society of Chemistry Advances*, v.6 (28), p. 23827–23836, 2016.

TARIQ, M.; ROONEY, D.; OTHMAN, E.; APARICIO, S.; ATILHAN, M.; KHRAISHEH, M. Gas Hydrate Inhibition: A Review of the Role of Ionic Liquids. *Industrial and Engineering Chemistry Research*, v. 53, p. 17855–17868, 2014.

VAN DER WAALS, J. H., PLATTEEUW, J.C. Clathrate solutions, *Advances in Chemical Physics*, v. 2, p. 1–57, 1959.

VOROTYNTSEV, V.M.; MALYSHEV, V.M. Gas hydrates: nanosized phases in the separation and purification of substances by crystallization. *Russian Chemical Reviews*, v. 80 (10), p. 971–991, 2011.

WALLQVIST, A. On the stability of type I gas hydrates in the presence of methanol. *The Journal of Chemical Physics*, v. 96 (7), 1992.

WATANABE, K.; IMAI, S.; MORI, Y.H. Surfactant effects on hydrate formation in an unstirred gas/liquid system: An experimental study using HFC-32 and sodium dodecyl sulfate. *Chemical Engineering Science*, v. 60 (17), p. 4846–4857, 2005.

XIAO, C.; ADIDHARMA, H. Dual function inhibitors for methane hydrate. *Chemical Engineering Science*, v. 64, p. 1522–1527, 2009.

XIAO, C.; WIBISONO, N.; ADIDHARMA, H. Dialkylimidazolium halide ionic liquids as dual function inhibitors for methane hydrate. *Chemical Engineering Science*, v. 65, p. 3080–3087, 2010.

XU, C.G.; ZHANG, S.H.; CAI, J.; CHEN, Z.Y.; LI, X.S. CO₂ (carbon dioxide) separation from CO₂ e H₂ (hydrogen) gas mixtures by gas hydrates in TBAB (tetra-n-butyl ammonium bromide) solution and Raman spectroscopic analysis. *Energy*, v. 59, p. 719-725, 2013.

YANG, S. O. Measurements and predictions of phase equilibria for water + natural gas components in hydrate-forming conditions. *PhD Thesis*, Korea University, Seoul, 2000.

ZARE, M.; HAGHTALAB, A.; AHMADI, A.N.; NAZARI, K. Experiment and thermodynamic modeling of methane hydrate equilibria in the presence of aqueous imidazolium-based ionic liquid solutions using electrolyte cubic square well equation of state. *Fluid Phase Equilibria*, v. 341, p. 61–69, 2013.

ZARE, M.; HAGHTALAB, A.; AHMADI, A.N.; NAZARI, K.; MEHDIZADEH, A. Effect of imidazolium based ionic liquids and ethylene glycol monoethyl ether solutions on the kinetic of methane hydrate formation. *Journal of Molecular Liquids*, v. 204, p. 236-242, 2015.

ZHANG, J.S.; LEE, S.; LEE, J.W. Does SDS micellize under methane hydrate-forming conditions below the normal Krafft point?. *Journal of Colloid and Interface Science*, v. 315 (1), p. 313–318, 2007.

ZHONG, Y.; ROGERS, R.E. Surfactant effects on gas hydrate formation. *Chemical Engineering Science*, v. 55, p. 4175-4187, 2000.

CHAPTER 9

CONCLUSIONS AND RECOMMENDATIONS

9.1 SUMMARY OF CONCLUSIONS

The main conclusions obtained throughout this work are summarized below. The full descriptions can be verified at the end of each chapter.

Chapter 3 presents preliminary studies related to relevant factors to be considered on planning the experiments and analyzing the thermograms. The study on phase diagrams of hydrate-forming species indicated that phase change-related transitions should occur in experiments containing C_2H_6 or CO_2 when below their respective critical pressures, which was confirmed in thermograms presented in Chapter 4. The previous study of gas mixtures diagrams allowed to avoid the coexistence of heterogeneous phases inside the cell (HP- μ DSC), by working at higher pressures than found in the liquid-vapor envelopes. Moreover, the computational predictions presented in this chapter indicate that the water fraction has a negligible effect on the hydrate dissociation temperature, considering the conditions required for practical applications of the gas hydrates. The Peng-Robinson was considered adequate to estimate the overall composition in isochoric measurements using the HP- μ DSC. Finally, this chapter introduces to the reader an unexpected transition observed in several analyzes throughout the work, related to the structural change of Teflon, especially when using hydrate inhibiting additives.

Chapter 4 presents new thermodynamic data based on microcalorimetry for single hydrates of CH_4 , C_2H_6 and CO_2 up to 100 MPa. Onset temperatures were found to be the most reliable for estimating hydrate equilibrium when in absence of overlapped transitions and approaches to CSMGem predictions. Multiflash predictions move away from CSMGem ones as pressure increases, especially for ethane and carbon dioxide hydrates. The increase in pressure led to higher hydrate dissociation temperatures, while the ice melting temperatures decreased, in agreement with the literature and the anomalous behavior of water. The influence of some experimental factors by using HP- μ DSC on the hydrate dissociation are also discussed in chapter 4. Dynamic effects play a significant role in the kinetics of hydrate formation, and hence the water-sample size affects the proportion of ice and hydrate in single-guest hydrate-

forming systems, although the thermodynamic properties are not affected. The cooling/heating rate slightly affects the onset temperatures since the structural heterogeneity may change. However, the analyses at $1 \text{ K}\cdot\text{min}^{-1}$ can be significantly shorter and are still accurate. A method based on multicycles analysis was also studied in order to maximize the ice conversion to hydrate. Ethane systems noticeably required more cycles to reach 90% of ice conversion to hydrate than methane and carbon dioxide systems, likely due to the harder diffusion of these larger molecules through the hydrate structure. On the other hand, the fraction of carbon dioxide hydrate formed in the first cycle is much higher than hydrate fraction in methane and ethane systems, due to the favored mass transfer by this molecule species. Applying the multicycles method on HP- μ DSC has shown to be much more accurate to estimate the enthalpy of hydrate dissociation than the standard method. However, a slightly higher heterogeneity seems to occur when performing multiple cycles. The hydrate layer initially formed during the first cooling may hamper the gas molecules diffusion through deeper regions of the droplet, affecting the filling of the cavities. Nevertheless, the results obtained are still accurate and satisfactory for determining the dissociation properties of single-gas hydrates.

The same chapter also shows the results of an alternative indirect method used to calculate the enthalpy of hydrate dissociation using the Clapeyron Equation. The hydrate volume was estimated by considering the effect of isobaric thermal expansivity and isothermal compressibility factors on the lattice parameter. The results of hydration number and enthalpy of dissociation obtained by the iterative method are consistent for all single hydrates studied. Unpublished data for dissociation enthalpies of single ethane and carbon dioxide hydrates, above the upper quadruple point, are also presented in this chapter. The dissociation enthalpy calculated by the Clapeyron equation is compared to the one determined by integrating the hydrate dissociation curve from thermograms. The average deviations, along with their respective confidence intervals (95%), indicate that the multicycles method and the hydration number from the iterative method provide the most reliable results.

Chapter 5 presents new dissociation data for double-guest gas hydrates obtained by HP- μ DSC up to 100 MPa. Dynamic effects play an important role in filling the cages for systems containing a gas mixture. Different solubilities and diffusivity in water between gas species are factors that likely imply gradients of gas concentrations

through the aqueous phase. Then, the cavities of the hydrate structure should have different occupancy degrees, leading to a heterogeneous phase. This phenomenon, among others, should explain the lower onset temperatures when compared to predictions. Ternary diagrams and pressure vs. temperature profiles based on computational predictions were also built to elucidate the influence of gas composition on the hydrate properties. The influence of the ratio between guest molecules size and cages diameter on the hydrate stability and the cages occupancy degree are factors addressed to explain the type (s) of structure formed and the hydrate dissociation temperature profiles according to the gas phase composition. In case of CH₄-C₂H₆ hydrate-forming systems, both sI and sII coexist at high methane concentrations, and a secondary structure (sII) may also be formed as a metastable phase at low methane concentrations. Experiments containing CH₄ and C₃H₈, in turn, unexpectedly presented the simultaneous formation of two structures, sI and sII, at high methane contents. CH₄-CO₂ hydrates were experimentally studied at similar gas phase compositions and varying the content of water. Differently from single-guest systems, the amount of water added into the cell seems to affect more considerably the onset temperatures of double-guest hydrates. Low content of water and high solubility and diffusion coefficient of CO₂ are factors that should contribute to a more heterogeneous phase and explain the lower experimental dissociation temperatures than predictions. Other factors are also referred to affect the hydrate stability and the dissociation temperature as the pressure increases, such as the absence of methane in small cavities and the reduction of the unit cell volume when the compressibility factor overcomes the thermal expansivity, leading to a lower occupancy degree.

In the next chapter (6), hydrate-forming systems composed of methane-water and methane-propane-water were investigated through the isochoric method, and compared to microcalorimetric results. Equilibrium points obtained from the PVT-isochoric method approach to onset temperatures of the hydrate dissociation curves from HP- μ DSC thermograms for both systems. Evidence are shown of the simultaneous formation of sI and sII for CH₄-C₃H₈-H₂O systems at high pressures and high methane contents. A higher kinetic of formation is found for sI, although sII is the most thermodynamically stable structure. The effects of experimental factors on these structures were also evaluated according to the methodology applied and the results are discussed according to the characteristics of each experimental technique. High

cooling degrees affect mainly the amount of hydrate formed and may lead to slightly higher dissociation temperatures as the increased driving force should favor the filling of the hydrate structure. According to PVT-isochoric measurements, sI was favored by mixing the system likely due to the addition of the mechanical energy and the better solubility of methane in water compared to propane. Lower heating rate contributed mainly to sII hydrate formation, considering the residence time in the hydrate zone is higher. Although the use of multi-cycle procedures reveals most of sI as a metastable structure, both experimental methods indicate that a small fraction of sI remains as a stable configuration even after multiple cycles. Finally, increasing the methane fraction in the gas phase showed the opposite effect on the results obtained by HP- μ DSC and the PVT-isochoric method.

Chapter 7 shows the main techniques used for structural analysis of gas hydrates based on Raman spectroscopy. *Ex situ* analyses are more suitable than *in situ* ones for characterization of stable structures, considering the faster conversion from ice to hydrate and a more homogeneous solid phase. The results obtained for the CH₄ hydrate agree to the literature data whereas the ones for CH₄-C₃H₈ hydrates reveals the complexity of determining their structural composition and the cages occupancy. In the latter system, it is observed that sII is predominant in all the three hydrates samples evaluated. The increase in methane content led to a higher occupation of large cavities by methane molecules, either due to the formation of a larger fraction of structure I or because of methane molecules were hosted in large cavities of sII. On the other hand, *in situ* analyses are interesting for studying the hydrate formation and crystals growth process. The initial stage of CH₄ hydrate formation was studied by two different methods based on a capillary and a cylindrical cell. The results evidence the prior formation of the small cavities and the progression of the cages occupancy towards the aqueous phase.

Finally, chapter 8 presents new experimental hydrate dissociation data in the presence of additives for hydrate inhibition, at pressures from 9.6 to 100 MPa via microcalorimetric measurements. Two ionic liquids, [BMIM][Cl] and [BMIM][Br], were evaluated as methane hydrate inhibitors, and their performance was compared to methanol and predictions made for other salts (NaCl and NaBr). The experimental hydrate dissociation temperatures obtained herein were also compared to literature data. Although the results indicate that the additives employed promote the hydrate

growth when at low concentrations, all of them act as thermodynamic inhibitors for CH₄ hydrates, shifting the phase equilibrium curves to lower temperatures. The increase in the content of the ionic liquids improves the thermodynamic inhibition effect considerably, mainly for [BMIM][Cl], but methanol presents better results in terms of mass fractions. However, one should consider the dual inhibition effect of ILs observed above certain concentrations, i.e., the shifting of the hydrate equilibrium curve to lower temperatures, and decreasing the kinetic of crystals nucleation and growth.

9.2 RECOMMENDATIONS

As discussed above, the experimental configuration based on HP- μ DSC, used in this work, has shown to be a very promising and convenient tool to obtain hydrate equilibrium and dissociation data. By considering the great advantages and limitations indicated herein for each method applied, several topics can be studied further, as suggested below:

- *Determination of specific heat of gas hydrates:* this thermodynamic property is also important for predicting gas production from hydrate reservoirs and to managing the operating conditions during exploitation. Improvements in the thermal insulation of the system and the recent relocation of pressure gauge in the experimental setup should allow to determine accurately the specific heats based on information provided by thermograms. Both isochoric and isobaric methods can be applied to determine C_v and C_p , respectively.
- *Extending equilibrium data for double-guest hydrates:* It is still necessary to study different systems composed of gas mixtures. The study of CH₄-CO₂-H₂O system is of particular interest for the capture and storage of carbon dioxide in hydrate reservoirs. The proper amount of water found in this work for studying CH₄-CO₂ hydrates can be used to investigate this system at different gas phase compositions, since only mixtures containing about 55 mol% of CH₄ were investigated herein.
- *Kinetic studies of gas hydrates formation:* Several studies can be performed with respect to the kinetics of gas hydrate formation. For instance, the induction time required to form hydrate at isothermal conditions should elucidate the kinetic of formation of different structures present in double-guest systems. The multicycles

method, coupled with isothermal studies, is another interesting tool for investigating secondary or metastable structures.

- *Structural analysis of double-guest hydrates:* Raman spectroscopy is also a powerful tool for understanding the coexistence of different hydrate structures in systems composed by a gas mixture. Although the determination of occupancy degree for CH₄-C₃H₈ hydrates was not managed in this work, the structural analyses by Raman spectroscopy were relevant for the conclusions obtained. Thus, similar studies for CH₄-C₂H₆ and CH₄-CO₂ hydrates, including attempting to determine cages occupancy, are encouraged.

CHAPTER 10

SCIENTIFIC PRODUCTION

10.1 ARTICLES PUBLISHED IN SCIENTIFIC JOURNALS

- MENEZES, D. E. S.; PESSÔA FILHO, P.A.; ROBUSTILLO, M. D. Use of 1-Butyl-3-methylimidazolium-based ionic liquids as methane hydrate inhibitors at high-pressure conditions. **Chemical Engineering Science**, v. 212, 115323, 2020.
- MENEZES, D. E. S.; SUM, A. K.; DESMEDT, A.; PESSOA FILHO, P. A.; ROBUSTILLO, M. D. Coexistence of sl and sll in methane-propane hydrate former systems at high pressures. **Chemical Engineering Science**, v. 208, 115149, 2019.
- MENEZES, D. E. S.; RALHA, T.W.; FRANCO, L.F.M., PESSÔA FILHO, P.A.; ROBUSTILLO, M. D. Simulation and experimental study of methane-propane hydrate dissociation by high-pressure differential scanning calorimetry. **Brazilian Journal of Chemical Engineering**, v. 35, p. 403-414, 2018.

10.2 ARTICLE ACCEPTED FOR PUBLICATION IN SCIENTIFIC JOURNAL

- MENEZES, D. E. S.; PESSÔA FILHO, P.A.; ROBUSTILLO, M. D. Phase equilibrium for methane, ethane and carbon dioxide hydrates at pressures up to 100 MPa through high-pressure microcalorimetry: experimental data, analysis and modeling. **Fluid Phase Equilibria**. *Forthcoming 2020*.

10.3 ARTICLES IN PROGRESS

- Phase equilibrium for methane-ethane, methane-propane and methane-carbon dioxide double hydrates at pressures up to 100 MPa through high-pressure microcalorimetry: influence of gas phase composition on the dissociation temperature profiles.
- Dissociation enthalpy of methane, ethane and carbon dioxide hydrates at pressures up to 100 MPa: assessment of experimental data obtained by a multicycle method performed in a high-pressure microcalorimeter and modeling.

10.4 WORKS IN SCIENTIFIC EVENTS

10.4.1 Full works

- MENEZES, D. E. S.; SUM, A.K.; PESSÔA FILHO, P. A.; ROBUSTILLO, M. D. Effects of experimental factors on methane-propane hydrate formation through isochoric method by using a PVT cell. Oral presentation. **XXII COBEQ**, São Paulo, Brazil, 2018.
- MENEZES, D. E. S.; RALHA, T.; FERRADOR, P. R.; FRANCO, L. F. M.; PESSÔA FILHO, P. A.; ROBUSTILLO, M. D. Estudo experimental da formação e dissociação de hidratos de metano por meio da calorimetria de alta pressão. Poster. **XXI COBEQ**, Fortaleza, Brazil, 2016.
- MENEZES, D. E. S.; RALHA, T.; FERRADOR, P. R.; LAVRADOR, R. B.; PESSÔA FILHO, P. A.; ROBUSTILLO, M. D. Desenvolvimento de metodologia para determinação experimental do calor específico do metano com base na calorimetria exploratória de alta pressão. Poster. **X CBRATEC IV CPANATEC**, São Paulo, Brazil, 2016.

10.4.2 Extended Abstracts

- MENEZES, D. E. S.; SUM A. K.; PESSÔA FILHO, P. A.; ROBUSTILLO, M. D. Thermodynamic and Structural Analysis for Methane-Ethane-Propane Hydrates Through Computational Simulations. Poster. **EQUIFASE**, Córdoba, Argentina, 2018.
- MENEZES, D. E. S.; LAVRADOR, R. B.; SUM, A. K.; PESSÔA FILHO, P.A.; ROBUSTILLO, M. D. Thermodynamic properties of methane hydrates by high pressure differential scanning calorimetry. Poster. **9th ICGH**, Denver, USA, 2017.
- MENEZES, D. E. S.; PESSÔA FILHO, P. A.; ROBUSTILLO, M. D. Dissociation temperature profiles of hydrate-forming ternary systems through thermodynamic simulations. Poster. **30th ESAT**, Prague, Czech Republic, 2018.
- ROBUSTILLO, M. D.; MENEZES, D. E. S.; PESSÔA FILHO, P. A. Experimental determination of dissociation temperature, enthalpy and heat capacity of ethane

hydrates by high pressure microcalorimetry. Poster. **30th ESAT**, Prague, Czech Republic, 2018.

- MENEZES, D. E. S.; PESSÔA FILHO, P.A.; ROBUSTILLO, M. D. Estudo experimental e simulação termodinâmica de hidratos de metano e propano a elevadas pressões. Oral presentation. **I EQUIPETRO**, Salvador de Bahía, Brazil, 2017.
- ROBUSTILLO, M. D.; MENEZES, D. E. S.; PESSÔA FILHO, P. A. Estudo cinético da formação e dissociação de hidratos de metano através da calorimetria de alta pressão. Poster. **I EQUIPETRO**, Salvador de Bahía, Brazil, 2017.
- FRANCO, L. F. M.; MENEZES, D. E. S.; RALHA, T.; FERRADOR, P. R.; PESSÔA FILHO, P. A.; ROBUSTILLO, M. D. Study of phase transitions of CH₄ at 200 bar by HP-Differential Scanning Calorimetry and molecular dynamics simulations. Oral presentation. **IV ProSCiba**, Viña del Mar, Chile, 2016.

10.4.3 Abstracts

- ROBUSTILLO, M. D.; MENEZES, D. E. S.; PESSÔA FILHO, P. A. Experimental determination of equilibrium properties of methane, CO₂ and ethane hydrates by a multi-cycle HP- μ DSC procedure. Poster. **ANQUE-ICCE-CIBIQ 2019**. Santander, Spain, 2019.
- MENEZES, D. E. S.; DESMEDT, A.; PESSÔA FILHO, P. A.; ROBUSTILLO, M. D. Influence of gas diffusion on the homogeneity of hydrates by in-situ Raman analysis at 20 MPa. Oral Presentation. **56th EHPRH**, Aveiro, Portugal, 2018.
- ROBUSTILLO, M. D.; MENEZES, D. E. S.; PESSÔA FILHO, P. A. Experimental Determination of Dissociation Temperature and Enthalpy of CO₂ Hydrates by HP- μ DSC. Poster. **56th EHPRH**, Aveiro, Portugal, 2018.
- MENEZES, D. E. S.; SUM, A. K.; PESSÔA FILHO, P. A.; ROBUSTILLO, M. D. Comparison of Experimental Gas Hydrate Equilibrium Data Obtained from an Isochoric Method and High-Pressure Calorimetry for Pressures Up to 100 MPa. Oral Presentation. **20th Symposium on Thermophysical Properties**, Boulder, Colorado, USA, 2018.
- ROBUSTILLO, M. D.; MENEZES, D. E. S.; PESSÔA FILHO, P. A. Characterization of Methane and Propane Double Hydrate Obtained by Both Isobaric and Isochoric

Methods by a Multi-Cycle HP- μ DSC Procedure. Poster. **Summer School and Workshop in Calorimetry**, Lyon, France, 2018.

- MENEZES, D. E. S.; PESSÔA FILHO, P. A.; ROBUSTILLO, M. D. Study of ionic liquids as thermodynamic inhibitors of methane hydrate formation up to 1000 bar by differential scanning calorimetry. Poster. **5th IMIL**, Santos, Brazil, 2017.
- MENEZES, D. E. S.; PESSÔA FILHO, P.A.; ROBUSTILLO, M. D. Influence of ionic liquids in the kinetic of methane hydrate formation at high pressures by differential scanning calorimetry. Poster. **5th IMIL**, Santos, Brazil, 2017.
- ROBUSTILLO, M. D.; MENEZES, D. E. S.; FERRADOR, P.R.; RALHA, T.; FRANCO, L. M.; PESSÔA FILHO, P. A. Experimental study and modeling on the formation of gas hydrates of methane and CO₂ at high pressure. Poster. **14th PPEPPD**, Porto, Portugal, 2016.
- ROBUSTILLO, M. D.; MENEZES, D. E. S.; PESSÔA FILHO, P. A. Experimental study on the formation of gas hydrates of methane and ethane by high pressure differential scanning calorimetry. Poster. **17th PetroPhase**, Elsinore, Denmark, 2016.
- MENEZES, D. E. S.; PESSÔA FILHO, P. A.; ROBUSTILLO, M. D. Development of methodologies based on high pressure DSC. **Summer School and Workshop in Calorimetry**, Lyon, France, 2016.
- MENEZES, D. E. S.; PESSÔA FILHO, P. A.; ROBUSTILLO, M. D. Estudo experimental e modelagem da formação de hidratos de metano e propano por meio de calorimetria de alta pressão. Poster. **CBTermo**, Aracajú, Brazil, 2015.

APPENDIX

CALCULATION OF HYDRATE DISSOCIATION ENTHALPY BY THE CLAPEYRON EQUATION AND HIDRATION NUMBER BY THE ITERATIVE METHOD

The Clapeyron equation allows to calculate the enthalpy from the experimental thermodynamic data (P, T), according to equation A1. The main deviations are related to the derivative of the equation used to describe the data and the volume change in the system. This appendix presents the main results of the calculations required to apply the Clapeyron equation and to estimate the hydration number by the iterative method.

$$\Delta H = \frac{dP}{dT} \cdot T \cdot \Delta V \quad (\text{A.1})$$

A.1 EQUATIONS FITTED TO THE EXPERIMENTAL DATA

A.1.1 Methane hydrates

For methane hydrates, the equation A2 showed good adjustment to experimental data from both standard and multicycles methods. The data were linearized so that $\ln(P)$ and $(1/T)$ were the respective y and x from the equation below:

$$y = a + b \cdot x + c \cdot x \cdot \ln(x) + \frac{d \cdot x}{\ln(x)} + \frac{e}{x^{1.5}} \quad (\text{A.2})$$

Table A.1 – Coefficients of equations fitted to the experimental data of CH₄ hydrates.

	Standard Method		Multicycles Method
<i>a</i>	-6.76E+06	<i>a</i>	-6.00E+05
<i>b</i>	-6.28E+08	<i>b</i>	-3.55E+09
<i>c</i>	3.17E+09	<i>c</i>	-3.98E+08
<i>d</i>	-4.57E+07	<i>d</i>	-8.27E+09
<i>e</i>	7.58E+02	<i>e</i>	9.31E+00

Tables A2 and A3 show the relation (dP/dT) obtained from the identity shown by equation A3 (ANDERSON, 2004). The pressures calculated from equation A2 are also presented, as well their respective relative errors.

$$\frac{dP}{dT} \equiv \frac{-P \, d\ln(P)}{T^2 \, d(1/T)} \quad (\text{A.3})$$

Table A.2 – Results from equations fitted to the experimental data of CH₄ hydrates by the standard method.

T (K)	291.74	296.98	300.50	303.21	305.48
P (MPa)	20	40	60	80	100
dP/dT	2.69	4.98	6.58	7.99	9.54
P _{CALC.} (MPa)	20.01	39.89	60.25	79.97	99.74
Error _(REL) (%)	0.05	-0.27	0.41	-0.04	-0.26

Table A.3 – Results from equations fitted to the experimental data of CH₄ hydrates by the multicycles method.

T (K)	291.74	295.23	296.96	298.82
P (MPa)	20	31.5	40	50
dP/dT	2.71	4.16	5.05	5.92
P _{CALC.} (MPa)	19.88	31.84	39.82	50.00
Error _(REL) (%)	-0.60	1.07	-0.45	0.00

T (K)	299.99	301.83	303.13	304.33
P (MPa)	59.4	70	80	90
dP/dT	6.72	7.36	8.01	8.68
P _{CALC.} (MPa)	57.25	69.96	79.94	89.94
Error _(REL) (%)	-3.63	-0.05	-0.07	-0.06

A.1.2 Ethane hydrates

The following equations were used to fit the experimental data from standard and multicycles method, respectively:

$$y = a + \frac{b}{x^{0.5}} + c \cdot \frac{\ln(x)}{x^2} \quad (\text{A.4})$$

$$y = a + b \cdot \ln(x) + c \cdot \frac{\ln(x)}{x} \quad (\text{A.5})$$

Table A.4 – Coefficients of equations fitted to the experimental data of C₂H₆ hydrates.

Standard Method		Multicycles Method	
<i>a</i>	6.16E+04	<i>a</i>	-2.93E+05
<i>b</i>	-1.42E+06	<i>b</i>	4.30E+04
<i>c</i>	3.22E+08	<i>c</i>	2.55E+06

Table A.5 – Results from equations fitted to the experimental data of C₂H₆ hydrates by the standard method.

T (K)	287.96	288.76	290.27	291.55	292.8	293.93	294.98	296
P (MPa)	5	9.8	20	30	40	50	60	70
dP/dT	5.81	6.29	7.17	7.90	8.59	9.21	9.77	10.30
P _{CALC.} (MPa)	4.99	9.82	19.99	29.63	39.94	50.00	59.96	70.20
Error _(REL) (%)	-0.28	0.25	-0.06	-1.22	-0.14	0.00	-0.06	0.29

Table A.6 – Results from equations fitted to the experimental data of C₂H₆ hydrates by the multicycles method.

T (K)	288.35	289	290.61	294.49
P (MPa)	5	9.8	20	50
dP/dT	6.18	6.42	7.00	8.35
P _{CALC.} (MPa)	5.27	9.37	20.18	49.99
Error _(REL) (%)	5.40	-4.41	0.88	-0.03

A.1.3 Carbon dioxide hydrates

The following equations were used to fit the experimental data from standard and multicycles method, respectively:

$$y = a + b \cdot x^{0.5} + \frac{c}{\ln(x)} \quad (\text{A.6})$$

$$y = a + \frac{b}{x} + \frac{c}{x^2} + \frac{d}{x^3} \quad (\text{A.7})$$

Table A.7 – Coefficients of equations fitted to the experimental data of CO₂ hydrates.

	Standard Method		Multicycles Method
<i>a</i>	-1.82E+06	<i>a</i>	8.71E+05
<i>b</i>	2.85E+04	<i>b</i>	-7.22E+08
<i>c</i>	7.59E+06	<i>c</i>	2.00E+11
		<i>d</i>	-1.84E+13

Table A.8 – Results from equations fitted to the experimental data of CO₂ hydrates by the standard method.

T (K)	283.7	284.87	285.45	286.15	286.74	287.37	287.94	288.45
P (MPa)	9.8	20	30	40	50	60	70	80
dP/dT	9.01	11.92	13.36	15.07	16.51	18.04	19.41	20.63
P _{CALC.} (MPa)	9.95	22.20	29.53	39.48	48.80	59.68	70.36	80.57
Error _(REL) (%)	1.57	11.00	-1.56	-1.29	-2.40	-0.53	0.51	0.71

Table A.9 – Results from equations fitted to the experimental data of CO₂ hydrates by the multicycles method.

T (K)	283.52	284.42	286.15	286.61
P (MPa)	9.8	20	40	50
dP/dT	9.95	11.29	14.24	15.11
P _{CALC.} (MPa)	10.01	19.56	41.57	48.32
Error _(REL) (%)	2.16	-2.21	3.92	-3.36

A.2 ESTIMATION OF HYDRATE VOLUME

As cited in the methodology section (2.1.4.3), the hydrate volume was estimated by equation A.8 and the volume of the unit cell is obtained by the equation A.9:

$$V_{hyd}(T, P) / (m^3 \cdot mol^{-1}) = \frac{6.0221 \cdot 10^{23} \cdot V_{uc} \cdot n}{46} \quad (A.8)$$

$$V_{uc}(T, P, x) = V_{uc0} \cdot \exp \left[\begin{array}{l} \alpha_{v1} \cdot (T - T_0) + \frac{\alpha_{v2}}{2} \cdot (T - T_0)^2 + \frac{\alpha_{v3}}{3} \cdot (T - T_0)^3 \\ - \kappa_T \cdot (P - P_0) \end{array} \right] \quad (A.9)$$

A.2.1 Methane hydrates

The lattice parameter data used to obtain the linear coefficients (α_l) of equation 2.12 were reported by Gutt et al. (2000) and Klapproth et al. (2003). The reference temperature (T_0) and lattice parameter (a_0) used for methane hydrates were 271.15 K and 11.96 Å (KLAPPROTH et al., 2003). The volumetric coefficients (α_v), found to be three times the linear ones, are: $\alpha_{v1} = 2.14E-4$; $\alpha_{v2} = 5.26E-7$ and $\alpha_{v3} = -7.37E-10$. The linear expansivity ($\beta_{(l)}$) found for methane hydrates by applying equation 2.12 agree to the experimental values reported in the literature, as shown in Table A.10.

Table A.10 – Linear thermal expansivity coefficients for CH₄ hydrates found in this work and reported in the literature.

T (K)	Linear thermal expansivity, $\beta_{(l)}$ (K ⁻¹)	
	<i>Shpakov et al. (1998)</i>	<i>This work</i>
100	3.50E-05	3.42E-05
150	5.00E-05	4.66E-05
200	6.40E-05	5.77E-05

Table A.11 – Methane hydrate volume by the standard method.

T (K)	285.93	286.15	286.28	291.49	291.66
P (MPa)	20	40	60	80	100
$\beta_{(V)} (K^{-1}) \times 10^4$	2.25	2.27	2.29	2.30	2.31
$\kappa_{T(V)} (MPa^{-1}) \times 10^4$	3.00	3.00	3.00	3.00	3.00
$V_{UC} (m^3/mol uc) \times 10^{27}$	1.71	1.70	1.69	1.68	1.67
$V_{HYD} (m^3/mol CH_4) \times 10^4$	1.37	1.34	1.35	1.36	1.39

Table A.12 – Methane hydrate volume by the multicycles method.

T (K)	291.74	295.23	296.96	298.82
P (MPa)	20	31.5	40	50
$\beta_{(V)} (K^{-1}) \times 10^4$	2.25	2.27	2.27	2.28
$\kappa_{T(V)} (MPa^{-1}) \times 10^4$	3.00	3.00	3.00	3.00
$V_{UC} (m^3/mol uc) \times 10^{27}$	1.71	1.70	1.70	1.69
$V_{HYD} (m^3/mol CH_4) \times 10^4$	1.38	1.35	1.35	1.35

T (K)	299.99	301.83	303.13	304.33
P (MPa)	59.4	70	80	90
$\beta_{(V)} (K^{-1}) \times 10^4$	2.29	2.30	2.30	2.31
$\kappa_{T(V)} (MPa^{-1}) \times 10^4$	3.00	3.00	3.00	3.00
$V_{UC} (m^3/mol uc) \times 10^{27}$	1.69	1.68	1.68	1.68
$V_{HYD} (m^3/mol CH_4) \times 10^4$	1.36	1.34	1.34	1.34

A.2.2 Ethane hydrates

The lattice parameter data used to obtain the linear coefficients (α_l) of equation 2.12 were reported by Hester et al., 2007. The reference temperature (T_0) and lattice parameter (a_0) used for ethane hydrates were 217 K and 11.995 Å. The volumetric coefficients (α_v) obtained are: $\alpha_{v1} = 6.11E-5$; $\alpha_{v2} = 5.37E-8$ and $\alpha_{v3} = -3.34E-10$.

Table A.13 – Ethane hydrate volume by the standard method.

T (K)	287.96	288.76	290.27	291.55	292.8	293.93	294.98	296.00
P (MPa)	5	9.8	20	30	40	50	60	70
$\beta_{(V)} (K^{-1}) \times 10^4$	1.86	1.86	1.86	1.86	1.86	1.86	1.86	1.86
$\kappa_{T(V)} (MPa^{-1}) \times 10^7$	3.00	3.00	3.00	3.00	3.00	3.00	3.00	3.00
$V_{UC} (m^3/mol uc) \times 10^{27}$	1.75	1.75	1.75	1.75	1.75	1.75	1.75	1.75
$V_{HYD} (m^3/mol CH_4) \times 10^4$	1.88	1.78	1.73	1.71	1.69	1.68	1.66	1.65

Table A.14 – Ethane hydrate volume by the multicycles method.

T (K)	288.35	289	290.61	294.49
P (MPa)	5	9.8	20	50
$\beta_{(V)} (K^{-1}) \times 10^4$	1.86	1.86	1.86	1.86
$\kappa_{T(V)} (MPa^{-1}) \times 10^7$	3.00	3.00	3.00	3.00
$V_{UC} (m^3/mol uc) \times 10^{27}$	1.75	1.75	1.75	1.75
$V_{HYD} (m^3/mol CH_4) \times 10^4$	1.99	1.82	1.70	1.59

A.2.3 Carbon dioxide hydrates

The lattice parameter data used to obtain the linear coefficients (α_l) of equation 2.12 were reported by Ikeda et al. (1999) and Udachin et al. (2001). The reference temperature (T_0) and lattice parameter (a_0) used for carbon dioxide hydrates were 173 K and 11.893 Å (UDACHIN, et al., 2001). The volumetric coefficients (α_v) obtained are: $\alpha_{v1} = 1.91E-4$; $\alpha_{v2} = 7.23E-7$ and $\alpha_{v3} = -2E-9$.

Table A.15 – Carbon dioxide hydrate volume by the standard method.

T (K)	283.7	284.87	285.45	286.15	286.74	287.37	287.94	288.45
P (MPa)	9.8	20	30	40	50	60	70	80
$\beta_V (K^{-1}) \times 10^4$	2.47	2.47	2.47	2.47	2.48	2.48	2.48	2.48
$\kappa_{T-V} (MPa^{-1}) \times 10^5$	3.00	3.00	3.00	3.00	3.00	3.00	3.00	3.00
$V_{UC} (m^3/mol uc) \times 10^{27}$	1.72	1.72	1.72	1.72	1.72	1.72	1.72	1.72
$V_{HYD} (m^3/mol CH_4) \times 10^4$	1.42	1.49	1.47	1.47	1.45	1.44	1.43	1.41

Table A.16 – Carbon dioxide hydrate volume by the multicycles method.

T (K)	283.52	284.42	286.15	286.61
P (MPa)	9.8	20.0	40	50
$\beta_V (K^{-1}) \times 10^4$	2.47	2.47	2.47	2.48
$\kappa_{T-V} (MPa^{-1}) \times 10^5$	3.00	3.00	3.00	3.00
$V_{UC} (m^3/mol uc) \times 10^{27}$	1.72	1.72	1.72	1.72
$V_{HYD} (m^3/mol CH_4) \times 10^4$	1.50	1.46	1.44	1.41

A.3 CALCULATION OF THE VOLUME CHANGE

The calculation of the volume change was according to equation A.14. The volume of the products (V'_{CH_4} and V'_{H_2O}) correspond to the terms described in equation 2662.7 (chapter 2).

$$\Delta V = V'_{CH_4} + n \cdot V'_{H_2O} - V_{HYD} \quad (A.10)$$

A.3.1 Methane hydrates

Table A.17 – Volume change for CH₄ hydrate dissociation by the standard method.

T (K)	285.93	286.15	286.28	291.49	291.66
P (MPa)	20	40	60	80	100
X _{CH₄, H₂O} x10 ³	3.13	4.07	4.72	5.27	5.73
V' _{CH₄} (m ³ /mol) x10 ⁵	9.61	6.28	5.36	4.89	4.58
V' _{H₂O}	1.80	1.79	1.78	1.77	1.76
V _{HYD} (m ³ /mol CH ₄) x10 ⁴	1.37	1.34	1.33	1.34	1.37
ΔV (m ³ /mol) x10 ⁵	6.95	3.68	2.76	2.27	1.91

Table A.18 – Volume change for CH₄ hydrate dissociation by the multicycles method.

T (K)	291.74	295.23	296.96	298.82
P (MPa)	20	31.5	40	50
X _{CH₄, H₂O} x10 ³	3.13	3.72	4.06	4.42
V' _{CH₄} (m ³ /mol) x10 ⁵	9.61	7.06	6.27	5.72
V' _{H₂O}	1.80	1.79	1.79	1.79
V _{HYD} (m ³ /mol CH ₄) x10 ⁴	1.38	1.35	1.35	1.35
ΔV (m ³ /mol) x10 ⁵	6.93	4.43	3.63	3.09

T (K)	299.99	301.83	303.13	304.33
P (MPa)	59.4	70	80	90
X _{CH₄, H₂O} x10 ³	4.73	5.02	5.27	5.51
V' _{CH₄} (m ³ /mol) x10 ⁵	5.37	5.09	4.89	4.72
V' _{H₂O}	1.78	1.78	1.77	1.77
V _{HYD} (m ³ /mol CH ₄) x10 ⁴	1.36	1.34	1.34	1.34
ΔV (m ³ /mol) x10 ⁵	2.72	2.47	2.27	2.10

A.3.2 Ethane hydrates

Table A.19 – Volume change for C₂H₆ hydrate dissociation by the standard method.

T (K)	287.96	288.76	290.27	291.55	292.8	293.93	294.98	296.00
P (MPa)	5	9.8	20	30	40	50	60	70
X _{CH₄, H₂O} x10 ³	1.05	1.09	1.16	1.22	1.27	1.31	1.35	1.39
V' _{CH₄} (m ³ /mol) x10 ⁵	7.91	7.38	6.86	6.56	6.35	6.19	6.06	5.95
V' _{H₂O}	1.80	1.80	1.79	1.79	1.78	1.77	1.77	1.76
V _{HYD} (m ³ /mol CH ₄) x10 ⁴	1.88	1.78	1.73	1.71	1.69	1.68	1.66	1.65
ΔV (m ³ /mol) x10 ⁵	3.92	3.57	3.10	2.80	2.57	2.39	2.25	2.13

Table A.20 – Volume change for C₂H₆ hydrate dissociation by the multicycles method.

T (K)	288.35	289	290.61	294.49
P (MPa)	5	9.8	20	50
X _{CH₄, H₂O} x10 ³	1.04	1.08	1.15	1.30
V' _{CH₄} (m ³ /mol) x10 ⁵	7.93	7.39	6.87	6.20
V' _{H₂O} (m ³ /mol) x10 ⁵	1.80	1.80	1.79	1.77
V _{HYD} (m ³ /mol CH ₄) x10 ⁴	1.99	1.82	1.70	1.59
ΔV (m ³ /mol) x10 ⁵	3.71	3.51	3.17	2.61

A.3.3 Carbon dioxide hydrates

Table A.21 – Volume change for CO₂ hydrate dissociation by the standard method.

T (K)	283.7	284.87	285.45	286.15	286.74	287.37	287.94	288.45
P (MPa)	9.8	20	30	40	50	60	70	80
X _{CH₄, H₂O} x10 ²	2.96	3.10	3.18	3.28	3.38	3.48	3.58	3.67
V' _{CH₄} (m ³ /mol) x10 ⁵	3.88	3.57	3.42	3.29	3.20	3.12	3.05	2.99
V' _{H₂O} (m ³ /mol) x10 ⁵	1.91	1.91	1.90	1.90	1.90	1.90	1.89	1.89
V _{HYD} (m ³ /mol CH ₄) x10 ⁴	1.42	1.49	1.47	1.47	1.45	1.44	1.43	1.41
ΔV (m ³ /mol) x10 ⁵	1.71	1.26	1.12	0.98	0.89	0.81	0.75	0.70

Table A.22 – Volume change for CO₂ hydrate dissociation by the multicycles method.

T (K)	283.52	284.42	286.15	286.61
P (MPa)	9.8	20.0	40	50
X _{CH₄, H₂O} x10 ²	2.94	3.04	3.28	3.36
V' _{CH₄} (m ³ /mol) x10 ⁵	3.84	3.60	3.31	3.23
V' _{H₂O} (m ³ /mol) x10 ⁵	1.91	1.91	1.90	1.90
V _{HYD} (m ³ /mol CH ₄) x10 ⁴	1.50	1.46	1.44	1.41
ΔV (m ³ /mol) x10 ⁵	1.54	1.34	1.05	0.98

A.4 DETERMINATION OF THE HYDRATION NUMBER BY THE INDIRECT METHOD

Tables A.23 and A.24 shows the main values calculated during the determination of the hydration number by the iterative method, according to equation A.15.

$$n = \frac{\Delta H_1 - \Delta H_2 + (H_{HC(2)} - H_{HC(1)}) + (H_{Hyd(1)} - H_{Hyd(2)})}{(H_{H_2O(1)} - H_{H_2O(2)})} \quad (\text{A.11})$$

A.4.1 Methane hydrates

Table A.23 – Hydration number of CH₄ hydrate by the standard method.

T (K)	285.93	286.15	286.28	291.49	291.66
P (MPa)	20	40	60	80	100
ΔH_1 (kJ/mol CH ₄)	54.91	54.65	54.95	55.37	55.97
ΔH_2 (kJ/mol CH ₄)*	54.19	54.19	54.19	54.19	54.19
$\Delta H_{CH_4 (1-2)}$ (kJ/mol)	-2.39	-2.86	-2.61	-2.17	-1.66
$\Delta H_{HYD (2-1)}$ (kJ/mol CH ₄)	-7.56	-11.46	-14.94	-18.28	-21.73
H _{H₂O (1)}} (kJ/mol)	1.74	2.46	3.04	3.55	4.02
H _{H₂O (2)}} (kJ/mol) x10 ³	1.86	1.86	1.86	1.86	1.86
n ₁	6.12	6.01	6.03	6.10	6.26

*Handa (1986).

Table A.24 – Hydration number of CH₄ hydrate by the multicycles method.

T ₍₁₎ (K)	291.74	295.23	296.96	298.82
P ₍₁₎ (MPa)	20	31.5	40	50
ΔH_1 (kJ/mol CH ₄)	54.97	54.73	54.77	54.92
ΔH_2 (kJ/mol CH ₄)*	54.19	54.19	54.19	54.19
$\Delta H_{CH_4 (1-2)}$ (kJ/mol)	-2.39	-2.81	-2.86	-2.77
$\Delta H_{HYD (2-1)}$ (kJ/mol CH ₄)	-7.58	-9.95	-11.51	-13.30
H _{H₂O (1)}} (kJ/mol)	1.74	2.19	2.46	2.76
H _{H₂O (2)}} (kJ/mol) x10 ³	1.86	1.86	1.86	1.86
n ₁	6.17	6.08	6.09	6.10

T ₍₁₎ (K)	299.99	301.83	303.13	304.33
P ₍₁₎ (MPa)	59.4	70	80	90
ΔH_1 (kJ/mol CH ₄)	55.07	55.20	55.37	55.77
ΔH_2 (kJ/mol CH ₄)*	54.19	54.19	54.19	54.19
$\Delta H_{CH_4 (1-2)}$ (kJ/mol)	-2.64	-2.41	-2.17	-1.72
$\Delta H_{HYD (2-1)}$ (kJ/mol CH ₄)	-14.88	-16.64	-18.27	-19.89
H _{H₂O (1)}} (kJ/mol)	2.99	3.29	3.54	3.79
H _{H₂O (2)}} (kJ/mol) x10 ³	1.86	1.86	1.86	1.86
n ₁	6.15	6.09	6.11	6.13

*Handa (1986).

A.4.2 Ethane hydrates

Table A.25 – Hydration number of C₂H₆ hydrate by the standard method.

T (K)	287.96	288.76	290.27	291.55	292.8	293.93	294.98	296.00
P (MPa)	5	9.8	20	30	40	50	60	70
ΔH_1 (kJ/mol CH ₄)	65.74	65.06	64.78	64.76	64.85	64.91	64.95	65.00
ΔH_2 (kJ/mol CH ₄)*	71.8	71.8	71.8	71.8	71.8	71.8	71.8	71.8
$\Delta H_{CH_4(1-2)}$ (kJ/mol)	-9.89	-10.09	-10.04	-9.81	-9.50	-9.15	-8.78	-8.39
$\Delta H_{HYD(2-1)}$ (kJ/mol CH ₄)	-6.27	-7.32	-9.49	-11.52	-13.54	-15.48	-17.35	-19.19
H _{H₂O(1)}} (kJ/mol)	1.21	1.35	1.63	1.90	2.15	2.40	2.64	2.87
H _{H₂O(2)}} (kJ/mol) x10 ³	1.9E-03							
n ₁	8.22	7.79	7.56	7.45	7.40	7.33	7.26	7.19

*Handa (1986).

Table A.26 – Hydration number of C₂H₆ hydrate by the multicycles method.

T (K)	288.35	289	290.61	294.49
P (MPa)	5	9.8	20	50
ΔH_1 (kJ/mol CH ₄)	66.41	65.31	64.72	64.46
ΔH_2 (kJ/mol CH ₄)*	71.8	71.8	71.8	71.8
$\Delta H_{CH_4(1-2)}$ (kJ/mol)	-9.84	-10.06	-10.01	-9.11
$\Delta H_{HYD(2-1)}$ (kJ/mol CH ₄)	-6.46	-7.44	-9.56	-15.25
H _{H₂O(1)}} (kJ/mol)	1.24	1.37	1.66	2.44
H _{H₂O(2)}} (kJ/mol) x10 ³	1.9E-03	1.9E-03	1.9E-03	1.9E-03
n ₁	8.69	7.94	7.44	6.92

*Handa (1986).

A.4.3 Carbon dioxide hydrates

Table A.27 – Hydration number of CO₂ hydrate by the standard method.

T (K)	283.70	284.87	285.45	286.15	286.74	287.37	287.94	288.45
P (MPa)	10	20.0	30	40	50	60	70	80
ΔH_1 (kJ/mol CH ₄)	47.97	47.75	47.59	47.52	47.45	47.41	47.37	47.32
ΔH_2 (kJ/mol CH ₄)*	57.6	57.6	57.6	57.6	57.6	57.6	57.6	57.6
$\Delta H_{CH_4(1-2)}$ (kJ/mol)	-9.89	-10.09	-10.04	-9.81	-9.50	-9.15	-8.78	-8.39
$\Delta H_{HYD(2-1)}$ (kJ/mol CH ₄)	-1.53	-3.42	-4.94	-6.52	-8.01	-9.50	-10.93	-12.30
H _{H₂O(1)}} (kJ/mol)	1.21	1.35	1.63	1.90	2.15	2.40	2.64	2.87
H _{H₂O(2)}} (kJ/mol) x10 ³	1.9E-03							
n ₁	6.30	6.62	6.52	6.50	6.44	6.39	6.33	6.25

*Anderson (2003).

Table A.28 – Hydration number of CO₂ hydrate by the multicycles method.

T (K)	283.52	284.42	286.15	286.61
P (MPa)	9.8	20	40	50
ΔH_1 (kJ/mol CH ₄)	47.97	47.72	47.57	47.48
ΔH_2 (kJ/mol CH ₄)*	57.6	57.6	57.6	57.6
$\Delta H_{CH_4(1-2)}$ (kJ/mol)	-9.84	-10.06	-10.01	-9.11
$\Delta H_{HYD(2-1)}$ (kJ/mol CH ₄)	-1.53	-3.18	-6.42	-7.78
H _{H₂O(1)}} (kJ/mol)	1.24	1.37	1.66	2.44
H _{H₂O(2)}} (kJ/mol) x10 ³	1.9E-03	1.9E-03	1.9E-03	1.9E-03
n ₁	6.64	6.45	6.38	6.26

*Anderson (2003).

REFERENCES

ANDERSON, G.K. Enthalpy of dissociation and hydration number of methane hydrate from the Clapeyron equation. *Journal of Chemical Thermodynamics*, v. 36, p. 1119-1127, 2004.

GUTT, C.; ASMUSSEN, B.; PRESS, W; JOHNSON, M.R.; HANDA, Y.P.; TSE, J.S. The structure of deuterated methane-hydrate. *Journal of Chemical Physics*, v. 113, p. 4713-4721, 2000.

HESTER, K.C.; HUO, Z.; BALLARD, A.L.; KOH, C.A.; MILLER, K.T.; SLOAN, E.D. Thermal Expansivity for sI and sII Clathrate Hydrates. *Journal of Physical Chemistry B*, v. 111, p. 8830-8835, 2007.

IKEDA, T.; YAMAMURO, O.; MATSUO, T.; MORI, K.; TORII, S.; KAMIYAMA, T.; IZUMI, F.; IKEDA, S.; MAE, S. Neutron diffraction study of carbon dioxide clathrate hydrate. *Journal of Physics and Chemistry of Solids*, v. 60, p. 1527-1529, 1999.

KLAPPROTH, A.; GORESHNIK, E.; STAYKOVA, D.; KLEIN, H.; KUHS, W. Structural studies of gas hydrates. *Canadian Journal of Physics*, v. 81, p. 503–518, 2003.

SHPAKOV, V.P.; TSE, J.S.; TULK, C.A.; KVAMME, B.; BELOSLUDOV, V.R. Elastic moduli calculation and instability in structure I methane clathrate hydrate. *Chemical Physics Letters*, v. 282, p. 107-114, 1998.

UDACHIN, K.A.; RATCLIFFE, C.I.; RIPMEESTER, J.A. Structure, composition and thermal expansion of CO₂ hydrate from single crystal x-ray diffraction measurements. *Journal of Physics Chemistry B*, v. 105, p. 4200-4204, 2001.